

AD-A088 912

SRI INTERNATIONAL MENLO PARK CA  
THEORETICAL AND EXPERIMENTAL STUDY OF DEEP-BASED STRUCTURES IN -- TC(U)  
SEP 79 P E SENSENY, H E LINDBERG

F/6 1 /13

DNA001-76-C-0385

UNCLASSIFIED

DNA-5208F

NL

1 of 3  
AD-A  
0-9912



12  
2.5

LEVEL II

AD-E300895\*

DNA 5208F

AD A088912

# THEORETICAL AND EXPERIMENTAL STUDY OF DEEP-BASED STRUCTURES IN INTACT AND JOINTED ROCKS

P. E. Senseny  
H. E. Lindberg  
SRI International  
333 Ravenswood Avenue  
Menlo Park, California 94025

1 September 1979

Final Report for Period 15 September 1977-30 August 1979

CONTRACT No. DNA 001-76-C-0385

APPROVED FOR PUBLIC RELEASE;  
DISTRIBUTION UNLIMITED.

THIS WORK SPONSORED BY THE DEFENSE NUCLEAR AGENCY  
UNDER RDT&E RMSS CODE B34407T462 J34HAXSX31107 H2590D.

Prepared for  
Director  
DEFENSE NUCLEAR AGENCY  
Washington, D. C. 20305

DTIC  
ELECTE  
SEP 8 1980  
S D  
B

DUG FILE COPY

80 8 13 018

Destroy this report when it is no longer needed. Do not return to sender.

PLEASE NOTIFY THE DEFENSE NUCLEAR AGENCY,  
ATTN: STTI, WASHINGTON, D.C. 20305, IF  
YOUR ADDRESS IS INCORRECT, IF YOU WISH TO  
BE DELETED FROM THE DISTRIBUTION LIST, OR  
IF THE ADDRESSEE IS NO LONGER EMPLOYED BY  
YOUR ORGANIZATION.



UNCLASSIFIED

UNCLASSIFIED

SECURITY CLASSIFICATION OF THIS PAGE (When Data Entered)

19 REPORT DOCUMENTATION PAGE		READ INSTRUCTIONS BEFORE COMPLETING FORM	
1. REPORT NUMBER DNA 5208E AD-E300 895	2. GOVT ACCESSION NO. AD-A088912	3. RECIPIENT'S CATALOG NUMBER (9)	
4. TITLE (and Subtitle) THEORETICAL AND EXPERIMENTAL STUDY OF DEEP-BASED STRUCTURES IN INTACT AND JOINTED ROCK		5. TYPE OF REPORT & PERIOD COVERED Final Report 15 Sep 77-30 Aug 79	
7. AUTHOR(s) P. E. Senseny H. E. Lindberg		6. PERFORMING ORG. REPORT NUMBER SRI PYU-5762	8. CONTRACT OR GRANT NUMBER(s) DNA 001-76-C-0385
9. PERFORMING ORGANIZATION NAME AND ADDRESS SRI International 333 Ravenswood Avenue Menlo Park, California 94025		10. PROGRAM ELEMENT, PROJECT, TASK AREA & WORK UNIT NUMBERS Subtask J34HAXSX311-07	
11. CONTROLLING OFFICE NAME AND ADDRESS Director Defense Nuclear Agency Washington, D.C. 20305		12. REPORT DATE 1 Sept 1979	
14. MONITORING AGENCY NAME & ADDRESS (if different from Controlling Office) 12 275		13. NUMBER OF PAGES 274	15. SECURITY CLASS (of this report) UNCLASSIFIED
15a. DECLASSIFICATION/DOWNGRADING SCHEDULE			
16. DISTRIBUTION STATEMENT (of this Report) Approved for public release; distribution unlimited.			
17. DISTRIBUTION STATEMENT (of the abstract entered in Block 20, if different from Report)			
18. SUPPLEMENTARY NOTES This work sponsored by the Defense Nuclear Agency under RDT&E RMSS Code B34407T462 J34HAXSX31107 H2590D.			
19. KEY WORDS (Continue on reverse side if necessary and identify by block number) Deep Basing      Mohr-Coulomb      Rock Mechanics      Tunnels DIABLO HAWK      NONSAP      Scale Models      Underground Joints      Plasticity      Static Laboratory Tests      Reinforcement      Structures Lateral Confinement      Repeat Loading      Theory			
20. ABSTRACT (Continue on reverse side if necessary and identify by block number) Theoretical and laboratory studies were performed to investigate: (1) effects of lateral confinement and rock specimen-to-tunnel diameter ratio in laboratory testing of reinforced tunnels in rock, (2) tunnel response in jointed rock, and (3) response to repeat loading of various reinforced tunnels in intact and jointed rock.  Results of the laboratory study of effects of lateral confinement and rock specimen-to-tunnel diameter ratio show that: → over			

410281

JW

20. ABSTRACT (Continued)

- (a) Small deviations from the uniaxial strain lateral confining pressure (10% to 20% over- or underconfinement) cause correspondingly small deviations in the loading needed to produce a critical design crown-invert tunnel closure,
- (b) The specimen-to-tunnel diameter ratio has a small but measurable effect (less than 20%) on critical loads for tunnel closure in the range used in laboratory testing, *AND*
- (c) The presence of the tunnel does not cause the laboratory specimen to bulge. Specimen lateral boundaries remain straight to within the accuracy required for uniaxial strain tunnel response (to within 200 microstrain for tunnel closures of interest).

Laboratory tests performed on jointed rock show that under static loading there is no block motion, even though the joint blocks (plates) were free to slide in the test machine. The tests also show that, for some joint orientations, tunnel deformation is similar to that measured for intact specimens, while for other joint orientations, tunnel deformation is significantly greater than for intact specimens. The additional deformation is caused by local sliding along the joints and, in some cases, by fracture across the rock plates from plate bending.

Theoretical and laboratory studies of repeat loading of deep-buried structures show that both direct contact and backpacked structures can withstand repeat loading well into the yielded range in a wide variety of geologies. Little or no additional closure occurs on repeat loading until the repeat load exceeds the preceding maximum load. The theoretical analysis predicts repeat loading closures that are larger than observed experimentally, suggesting that the theory can be used for conservative design analysis.

ACCESSION for		
NTIS	White Section	<input checked="" type="checkbox"/>
DDC	Buff Section	<input type="checkbox"/>
UNANNOUNCED		<input type="checkbox"/>
JUSTIFICATION _____		
BY _____		
DISTRIBUTION/AVAILABILITY CODES		
Dist.	AVAIL.	and/or SPECIAL
A		

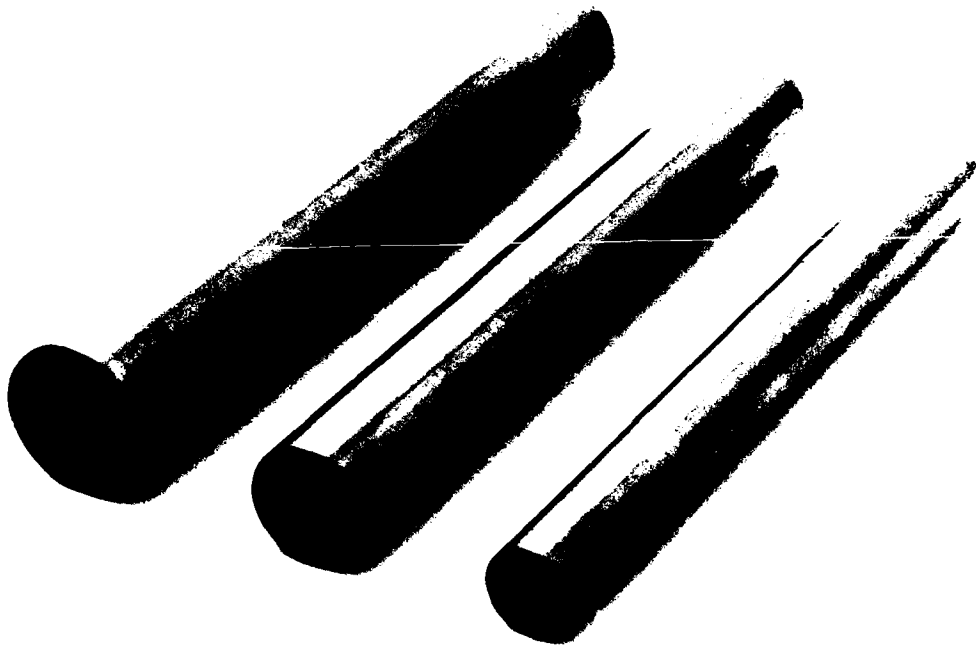
## SUMMARY

Laboratory and theoretical studies were made of the deformation of deep-based structures for a variety of reinforcement structures, rock types, and loading paths. Emphasis was on yielding structures, which allow plastic deformation of the rock immediately around the tunnel and take substantial advantage of rock strength. Tests were performed to study the influence of lateral confinement and specimen-to-tunnel diameter ratio on both tunnel and rock specimen response. After this demonstration of the efficacy of the laboratory method, further tests were performed to study deformation of tunnels in jointed rocks with various load-joint and tunnel-joint orientations. The influence on tunnel closure of repeat loading was studied both theoretically and experimentally.

### S.1 EFFECTS OF LATERAL CONFINEMENT AND SPECIMEN-TO-TUNNEL DIAMETER RATIO IN LABORATORY TESTING

We performed uniaxial strain loading experiments on 4-inch-diameter (0.1-m) specimens having three different tunnel sizes to determine the influence on tunnel closure of specimen-to-tunnel diameter ratio. Figure S.1 shows the tunnel reinforcing structures for the three tunnel sizes. We studied two rock simulants: a tuff simulant, designated SRI RMG 2C2, and a medium strength rock simulant, designated 16A.

The influence of the specimen-to-tunnel diameter ratio is shown in Figures S.2 and S.3, where the pressure required to produce specimen crown-invert tunnel closures is plotted as a function of the specimen-to-tunnel diameter ratio. Figure S.2 shows that for the tunnel sizes studied, closure does not depend on tunnel size in SRI RMG 2C2. However, Figure S.3 shows that for 16A rock simulant, greater pressure must be applied to specimens containing larger tunnels to obtain a specified crown-invert tunnel closure. We conclude that these two rock simulants



MP-5762-84

FIGURE S.1 LINERS FOR THE THREE DIFFERENT TUNNEL SIZES: 5/8 INCH,  
1/2 INCH, 3/8 INCH (15.9 mm, 12.7 mm, 9.5 mm)

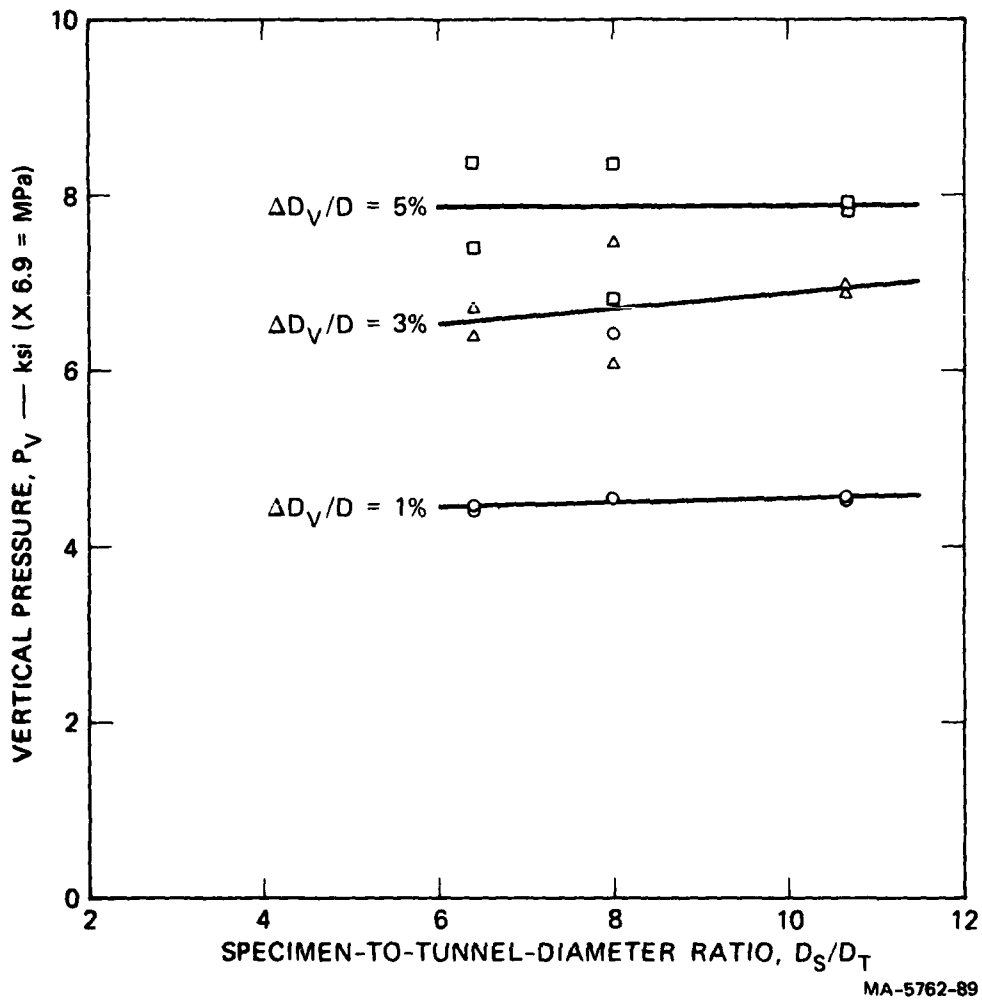
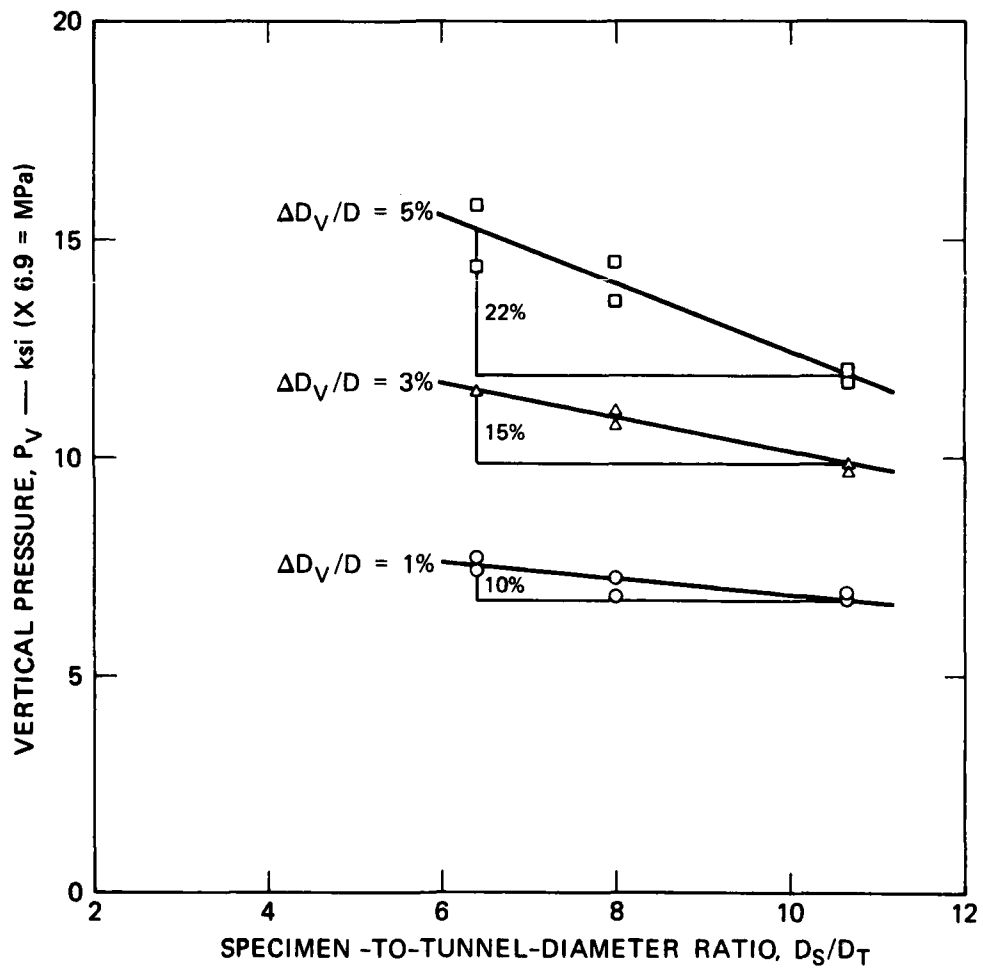


FIGURE S.2 VERTICAL PRESSURE TO PRODUCE SPECIFIED CROWN-INVERT TUNNEL CLOSURE VERSUS SPECIMEN-TO-TUNNEL DIAMETER RATIO — 2C2

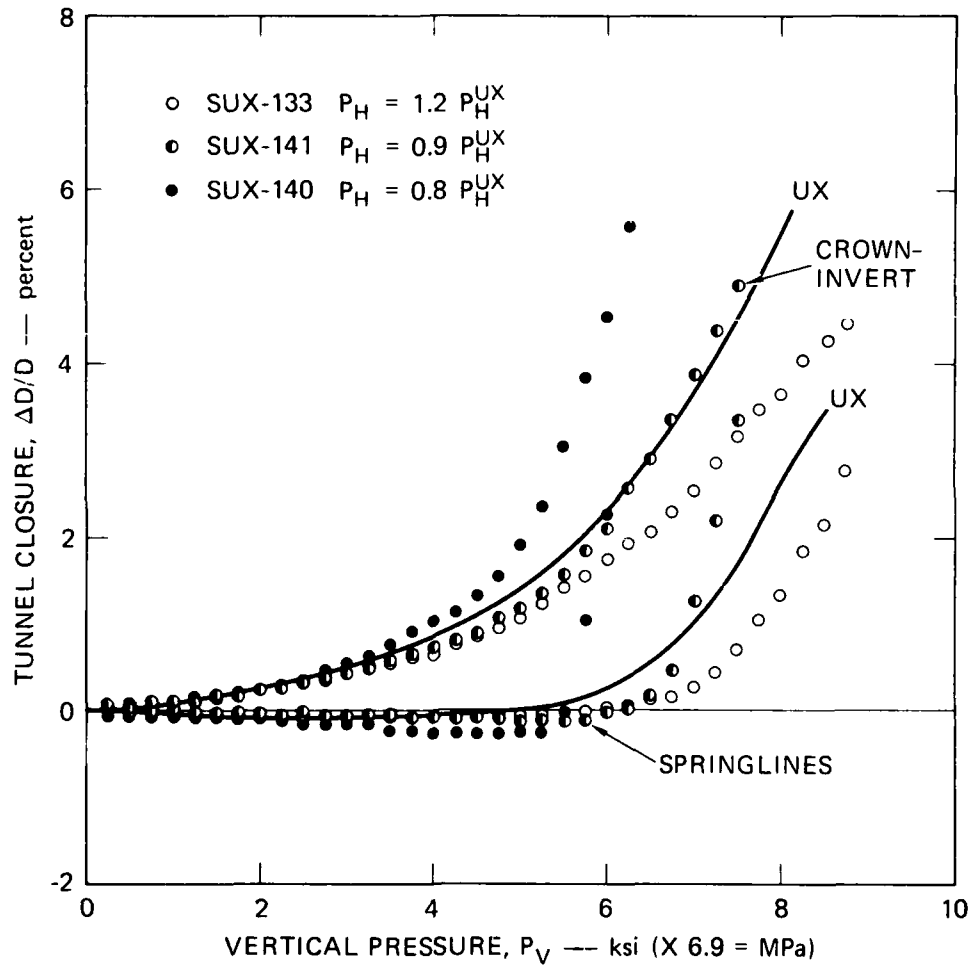


MA-5762-78A

FIGURE S.3 VERTICAL PRESSURE TO PRODUCE SPECIFIED CROWN-INVERT TUNNEL CLOSURE VERSUS SPECIMEN-TO-TUNNEL DIAMETER RATIO — 16A ROCK SIMULANT

respond differently because, in the stronger 16A rock simulant, a plastic zone that is localized around the tunnel grows outward toward the specimen boundary. Plastic zones around larger tunnels interact with the specimen boundary sooner than do those around smaller tunnels, and this produces the tunnel size effect. In SRI RMG 2C2, however, the entire specimen yields at low pressure, so that plastic deformation is not localized around the tunnel. Therefore, no tunnel size effect is observed for this material. This also emphasizes that such weak materials are inappropriate for deep basing and that laboratory testing should emphasize the higher friction materials modeled by the 6B and 16A simulants.

Specimens of SRI RMG 2C2 having the largest tunnel size were used to study the effect on tunnel closure of deviations in lateral confining pressure from that required to produce uniaxial strain. In two experiments the lateral confining pressure was reduced to 90% and 80% of the uniaxial strain lateral confining pressure, and in one experiment the lateral confining pressure was increased to 120% of the uniaxial strain lateral confining pressure. Figure S.4 plots tunnel closure as a function of vertical pressure for these experiments. A solid line that is fitted through closures obtained for uniaxial strain loading is also plotted. These results show that critical loads to produce a specified design crown-invert closure are approximately in proportion to the small deviations from the uniaxial strain lateral confining pressure. Springline closure, however, is especially sensitive to underconfinement. For the more underconfined test (SUX-140), springline closure increases very rapidly at the end of the test, and extrapolation of crown-invert and springline curves from this test shows that at only slightly greater pressure springline closure will dominate crown-invert closure. This trend is the same as that observed in some underconfined dynamic tests in which the tunnel closed completely along the springline diameter.



MA-5762-96

FIGURE S.4 TUNNEL CLOSURE AT CROWN-INVERT AND SPRINGLINE DIAMETERS  
 VERSUS VERTICAL PRESSURE FOR OVERCONFINED, UNDERCONFINED  
 AND UNIAXIAL STRAIN LOADING OF SRI RMG 2C2

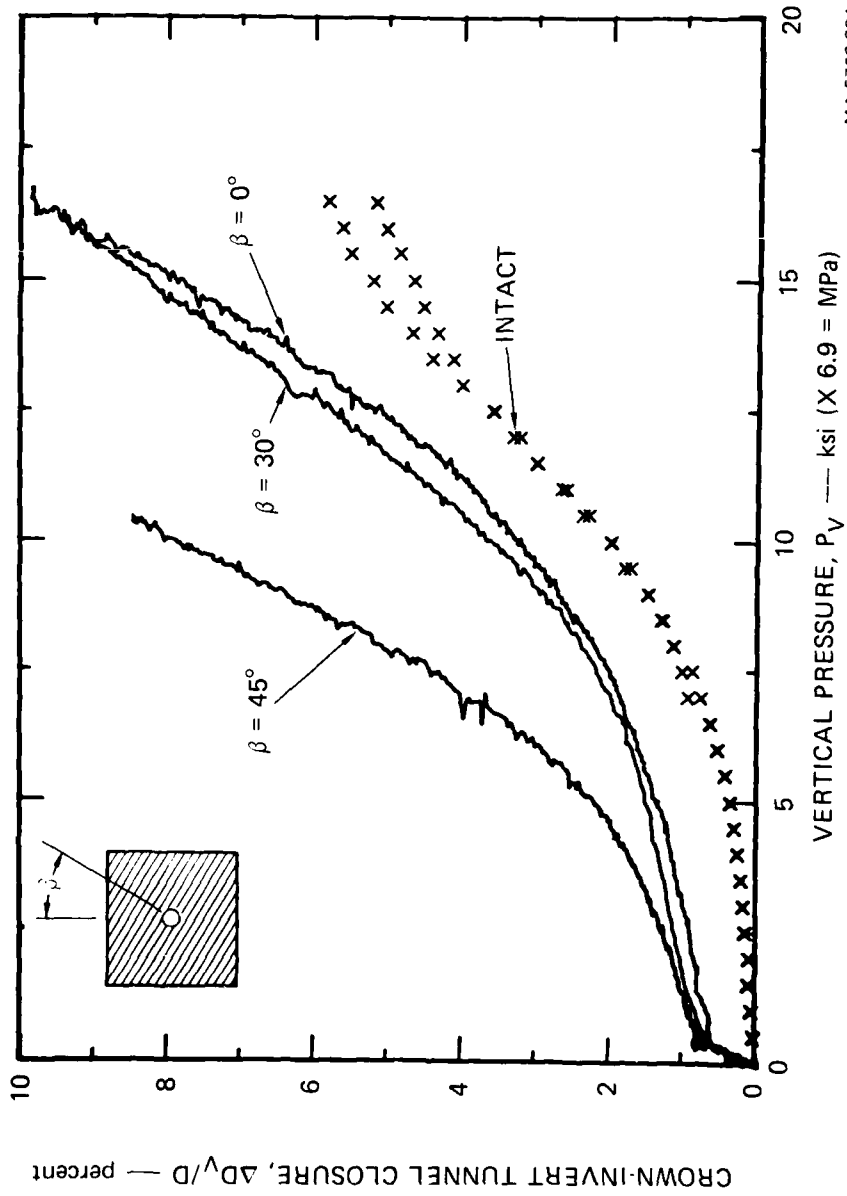
6061-T0 aluminum liner,  $a/h = 11.5$

## S.2 CYLINDRICAL STRUCTURES IN JOINTED ROCK

We performed static uniaxial strain loading experiments on 12-inch-diameter (0.3-m) specimens that contain a single set of parallel, equally spaced joints to determine the influence on tunnel deformation of joints and their orientation. For small load-joint orientation angles  $\beta$  (the angle between the vertical loading direction and the joint normal), the presence of joints and their orientation has little effect on tunnel deformation. For large  $\beta$ , however, the strength reduction can be large. These results are illustrated by plots of crown-invert tunnel closure versus vertical pressure, given in Figures S.5 and S.6 for a thick steel direct-contact structure and a polyurethane foam backpacked structure, respectively. For small load-joint orientation angles,  $\beta = 0^\circ$  and  $30^\circ$ , the primary difference between jointed and intact response is the jump in closure at low pressure in jointed specimens, due to the joint close-up. (This would not occur in the field, where the joints are filled and, also, in-situ stresses hold the joints closed.) For the largest joint orientation angle studied,  $\beta = 45^\circ$ , the reduction in strength is significant. For the backpacked structure, the pressure required to produce a crown-invert closure of 5% with  $\beta = 45^\circ$  is only 80% as great as that required to produce the same closure for  $\beta = 0$ . For the direct-contact structure, the critical pressure at 5% closure is only 60% of that for  $\beta = 0$ .

Results of repeat loading experiments show that the response of jointed specimens is the same as that of intact specimens: repeat loading does not produce a significant change in the specimen's load-bearing capacity, closures during unloading and reloading fall along a common line, and only a small additional closure is sustained during each cycle in load.

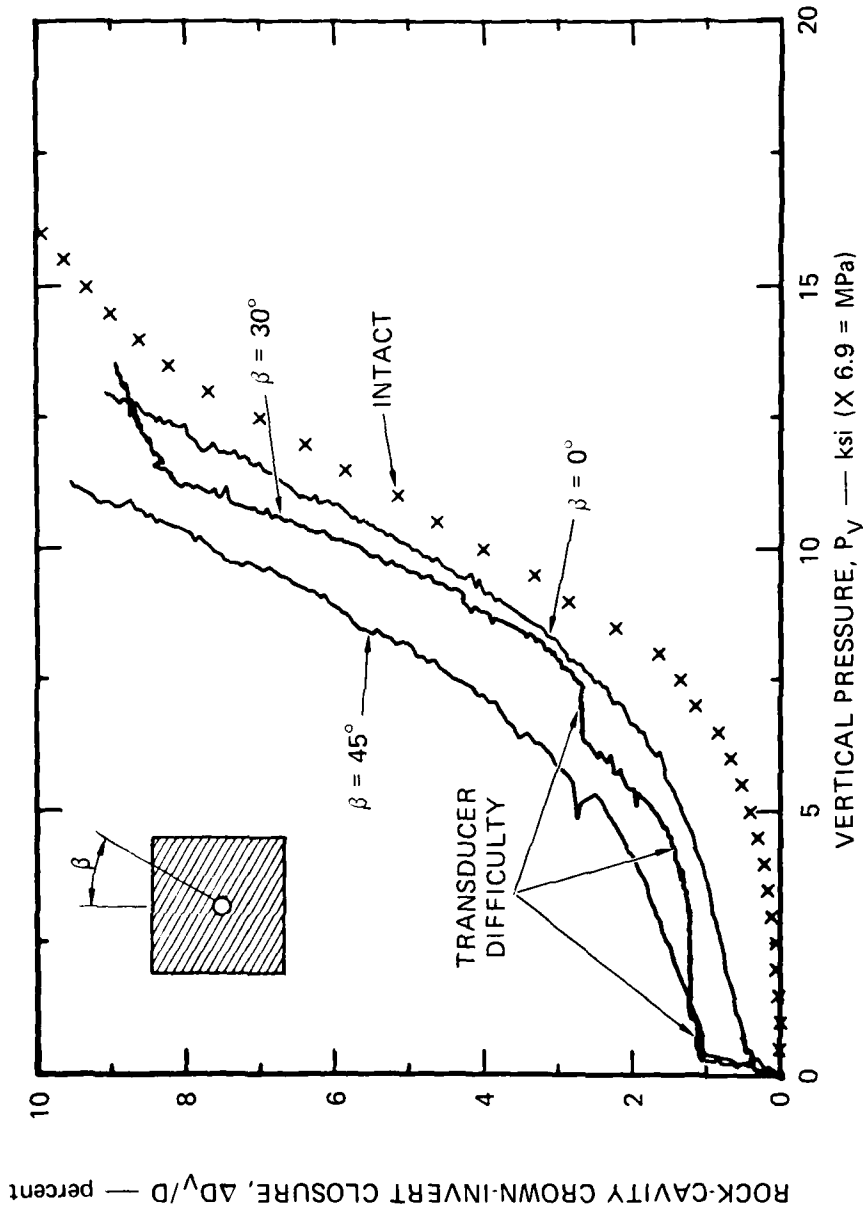
Smooth tunnel closure records and posttest specimen cross sections such as that shown in Figure S.7 indicate that block motion is not a deformation mechanism and, except for a small amount of tensile and shear cracking, deformation is due to elastic and plastic straining, plus localized slipping on the joints. *Therefore, tunnel closure in*



MA-5762-224

FIGURE S.5 CROWN-INVERT TUNNEL CLOSURE VERSUS PRESSURE FOR THREE LOAD-JOINT ORIENTATION ANGLES

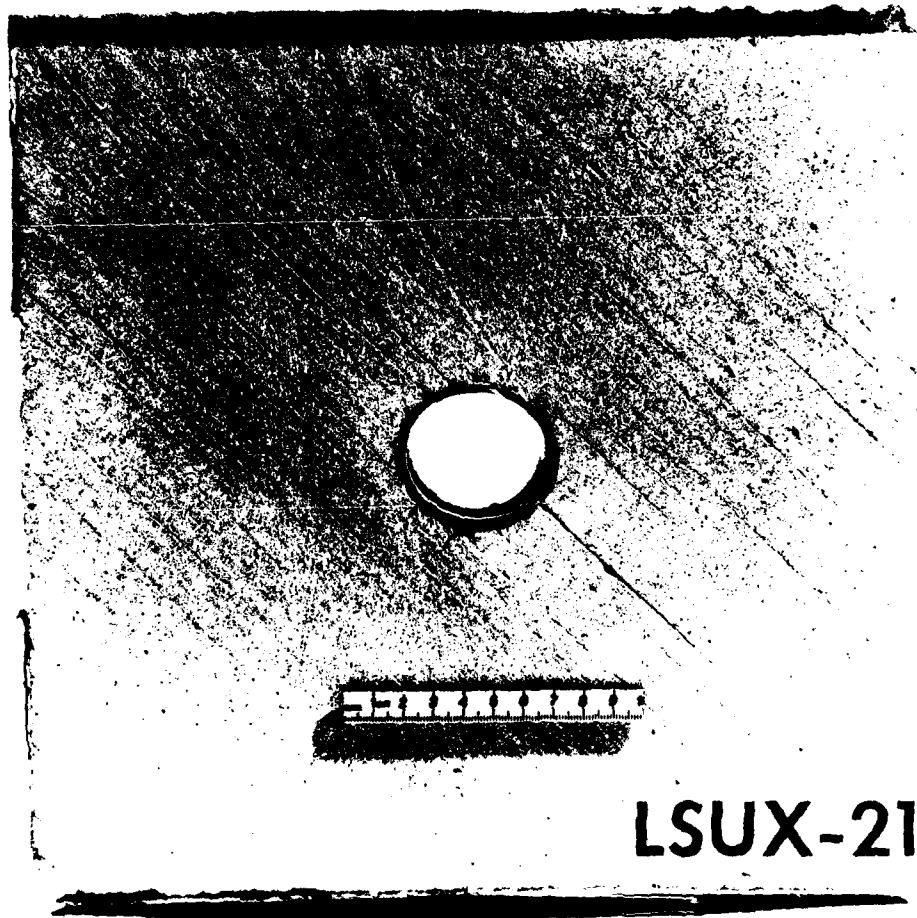
Data from intact specimens are plotted for comparison. Direct contact liner, 16A rock simulant,  $\gamma = 90^\circ$



MA-5762-226

FIGURE S.6 ROCK-CAVITY CROWN-INVERT CLOSURE VERSUS VERTICAL PRESSURE FOR THREE LOAD-JOINT ORIENTATION ANGLES

Data from an intact specimen is plotted for comparison. Backpacked liners, 16A rock simulant,  $\gamma = 90^\circ$



MP-5762-171

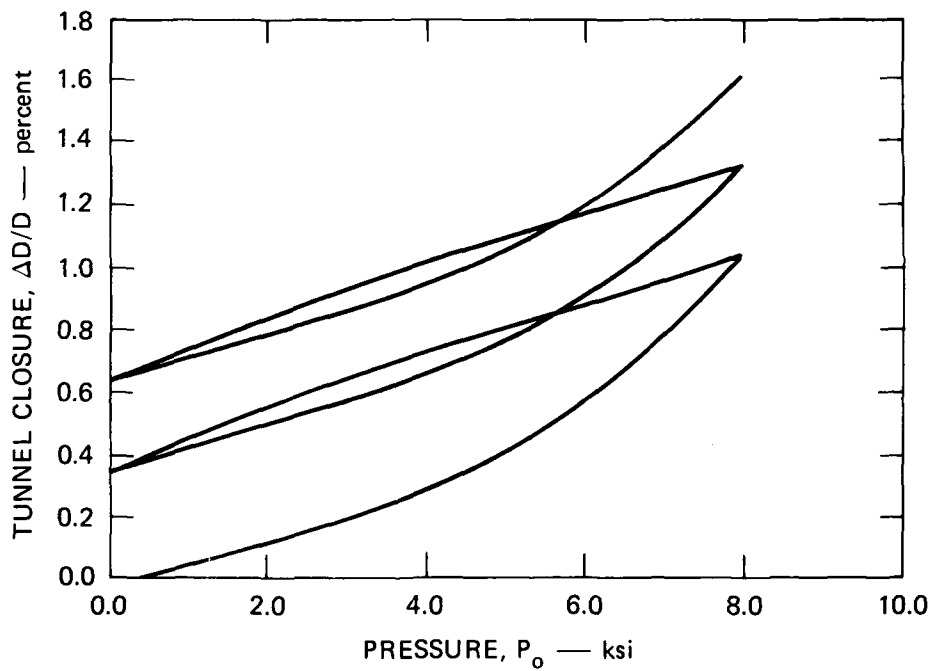
FIGURE S.7 SECTIONED SPECIMEN FROM TEST LSUX-21

*these experiments should be calculable using a homogeneous, transversely isotropic continuum to model the jointed rock response.* Data from material property tests performed at the Waterways Experiment Station (WES) have been used to determine parameters for an elastic, perfectly-plastic Mohr-Coulomb model that is transversely isotropic in both the elastic and plastic parts.

### S.3 REPEAT LOADING OF DEEP-BURIED STRUCTURES

We performed a theoretical study of the response to repeat loading of circular tunnels in rock. We solved analytically the problem of a circular tunnel having constant internal pressure subjected to far-field axisymmetric pressure for a single cycle in load. We used this analysis to study the influence on tunnel closure of internal pressure, applied pressure at which a cycle in load occurs, and rock strength parameters. We also used the stress and displacement fields determined in this analysis to verify a numerical solution to the problem. The numerical solution was obtained by use of the finite element code NONSAP. We then used NONSAP to calculate tunnel closure for two cycles in load under axisymmetric pressure, and then also for uniaxial strain loading. Results of the calculation for two cycles in load under axisymmetric pressure are shown in Figure S.8. The load is cycled twice at  $P_0 = 8$  ksi (55 MPa). The two cycles are very similar. Response to unloading is initially elastic, but before unloading is complete the rock yields and the tunnel opens faster with decreasing pressure. Reloading is initially elastic also, but before  $P_0 = 8$  ksi (55 MPa), yielding causes the tunnel to close faster with increasing pressure. Yielding during unloading and reloading causes the closure curve to form a narrow loop and also increases tunnel closure by a small amount.

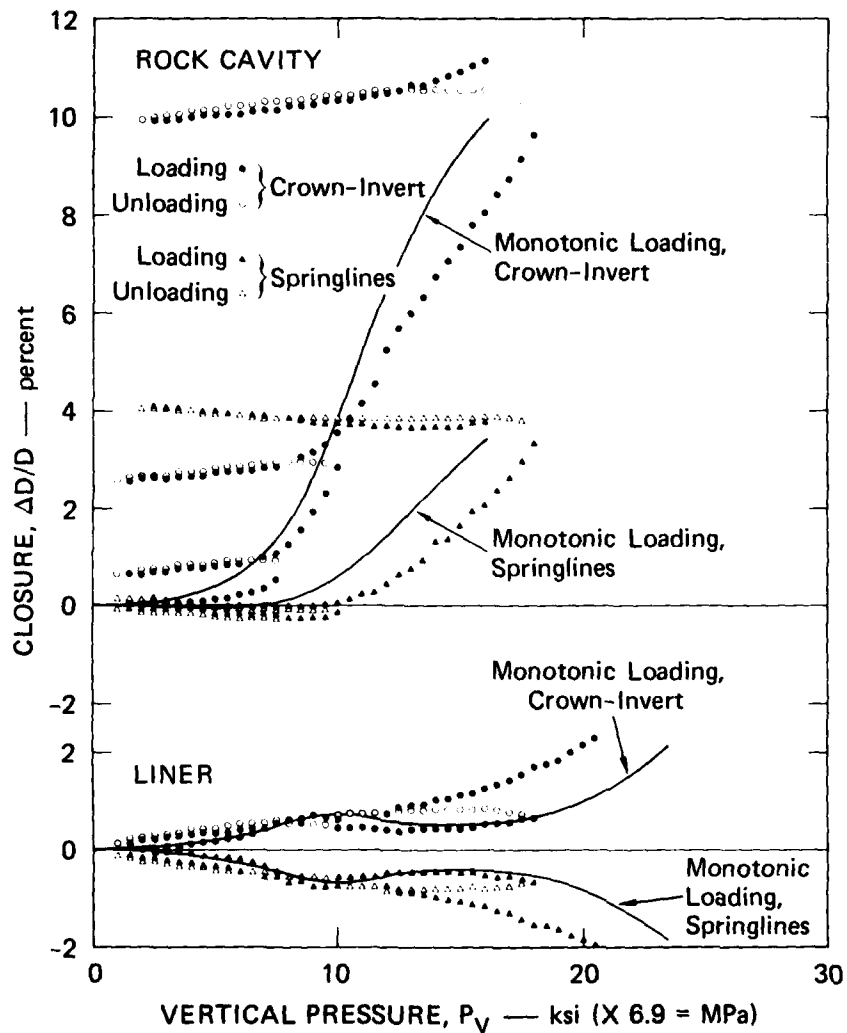
In addition to this theoretical study, we performed experiments with repeat loading of a backpacked structure in 16A rock simulant. Tunnel closure is plotted in Figure S.9 as a function of pressure. Monotonic closure curves are plotted as solid lines. Comparison of repeat and monotonic loading data shows that a rock opening reinforced with a backpacked structure responds similarly to a tunnel reinforced with a direct contact structure under repeat loading.



MA-5762-251

FIGURE S.8 FINITE ELEMENT RESULTS FOR TWO RELOADING CYCLES

$\bar{P}_o = 8$  ksi,  $\sigma_u = 4$  ksi,  $N_\phi = 3.39$ ,  $P_i = 500$  psi,  $E = 2.5 \times 10^6$  psi,  
 $\nu = 0.25$  (1 ksi = 6.9 MPa)



MA-5762-73A

FIGURE S.9 ROCK-CAVITY AND LINER CLOSURE FOR CYCLIC AND MONOTONIC UNIAXIAL STRAIN LOADING OF A BACKPACKED STRUCTURE IN SATURATED 16A ROCK SIMULANT

The results of this theoretical study, plus results of a wide variety of repeat loading experiments performed previously, show that yielding structure designs can withstand repeat loading and sustain only small additional closure of the tunnel. Thus, advantage can be taken of the large increase in load capacity of a yielding design above an elastic design (typically a factor of 3 or more) even for repeated attacks.

## PREFACE

This report describes a program performed for the Defense Nuclear Agency during the period September 1977 to August 1979 under Contract DNA 001-76-C-0385. The technical monitors were LTC Danny N. Burgess and LTC John C. Galloway.

The authors gratefully acknowledge the technical support at SRI of John Busma, Curt Benson, George Cartwright, Hugh Hanna, E. G. Eckert, W. B. Heckman, Mario Oyola and H. C. Rudnicki. All of the rock models made of 16A rock stimulant, including the intricate jointed rock models, were prepared by the staff of Richard Stowe of the U.S. Army Waterways Experiment Station, Vicksburg, Mississippi. Theoretical analysis of the effect of lateral specimen boundary conditions and tunnel size were performed by Martin Rosenblatt and Yasuo Marvin Ito of California Research and Technology, Woodland Hills, California. We gratefully acknowledge their permission to use some of their results prior to publication of their DNA report.

Conversion factors for U.S. customary  
to metric (SI) units of measurement

To Convert From	To	Multiply By
angstrom	meters (m)	1.000 000 X E -10
atmosphere (normal)	kilo pascal (kPa)	1.013 25 X E +2
bar	kilo pascal (kPa)	1.000 000 X E +2
barn	meter <sup>2</sup> (m <sup>2</sup> )	1.000 000 X E -28
British thermal unit (thermochemical)	joule (J)	1.054 350 X E +3
calorie (thermochemical)	joule (J)	4.184 000
cal (thermochemical)/cm <sup>2</sup>	mega joule/m <sup>2</sup> (MJ/m <sup>2</sup> )	4.184 000 X E -2
curie	*giga becquerel (GBq)	3.700 000 X E +1
degree (angle)	radian (rad)	1.745 329 X E -2
degree Fahrenheit	degree kelvin (K)	$t_K = (t_F + 459.67)/1.8$
electron volt	joule (J)	1.602 19 X E -19
erg	joule (J)	1.000 000 X E -7
erg/second	watt (W)	1.000 000 X E -7
foot	meter (m)	3.048 000 X E -1
foot-pound-force	joule (J)	1.355 818
gallon (U.S. liquid)	meter <sup>3</sup> (m <sup>3</sup> )	3.785 412 X E -3
inch	meter (m)	2.540 000 X E -2
jerk	joule (J)	1.000 000 X E +9
joule/kilogram (J/kg) (radiation dose absorbed)	Gray (Gy)	1.000 000
kilotons	terajoules	4.183
kip (1000 lbf)	newton (N)	4.448 222 X E +3
kip/inch <sup>2</sup> (ksi)	kilo pascal (kPa)	6.894 757 X E +3
ktap	newton-second/m <sup>2</sup> (N-s/m <sup>2</sup> )	1.000 000 X E +2
micron	meter (m)	1.000 000 X E -6
mil	meter (m)	2.540 000 X E -5
mile (international)	meter (m)	1.609 344 X E +3
ounce	kilogram (kg)	2.834 952 X E -2
pound-force (lbs avoirdupois)	newton (N)	4.448 222
pound-force inch	newton-meter (N·m)	1.129 848 X E -1
pound-force/inch	newton/meter (N/m)	1.751 268 X E +2
pound-force/foot <sup>2</sup>	kilo pascal (kPa)	4.788 026 X E -2
pound-force/inch <sup>2</sup> (psi)	kilo pascal (kPa)	6.894 757
pound-mass (lbm avoirdupois)	kilogram (kg)	4.535 924 X E -1
pound-mass-foot <sup>2</sup> (moment of inertia)	kilogram-meter <sup>2</sup> (kg·m <sup>2</sup> )	4.214 011 X E -2
pound-mass/foot <sup>3</sup>	kilogram/meter <sup>3</sup> (kg/m <sup>3</sup> )	1.601 846 X E +1
rad (radiation dose absorbed)	**Gray (Gy)	1.000 000 X E -2
roentgen	coulomb/kilogram (C/kg)	2.579 760 X E -4
shake	second (s)	1.000 000 X E -8
slug	kilogram (kg)	1.459 390 X E +1
torr (mm Hg, 0° C)	kilo pascal (kPa)	1.333 22 X E -1

\*The becquerel (Bq) is the SI unit of radioactivity; 1 Bq = 1 event/s.

\*\*The Gray (Gy) is the SI unit of absorbed radiation.

CONTENTS

SUMMARY . . . . .	1
PREFACE . . . . .	15
CONVERSION TABLE . . . . .	16
LIST OF ILLUSTRATIONS . . . . .	19
1. INTRODUCTION . . . . .	33
1.1 Background . . . . .	33
1.2 Approach and Scope of Investigation . . . . .	33
1.3 Report Organization . . . . .	35
2. EFFECTS OF LATERAL CONFINEMENT AND SPECIMEN-TO-TUNNEL DIAMETER RATIO IN LABORATORY TESTING . . . . .	36
2.1 Introduction . . . . .	36
2.2 Effect of Specimen-to-Tunnel Diameter Ratio . . . . .	36
2.2.1 Results for 16A Rock Simulant Models . . . . .	37
2.2.2 Results for SRI RMG 2C2 Rock Simulant Models . . . . .	39
2.2.3 Summary . . . . .	41
2.3 Effect of Lateral Confinement . . . . .	71
2.4 Conclusions . . . . .	80
3. CYLINDRICAL STRUCTURES IN JOINTED ROCK . . . . .	83
3.1 Introduction . . . . .	83
3.2 Influence of the Load-Joint Orientation Angle . . . . .	93
3.3 Influence of the Tunnel-Joint Orientation Angle . . . . .	102
3.4 Influence of Repeat Loading . . . . .	105
3.5 Influence of Structure Type . . . . .	114
3.6 Discussion . . . . .	122
3.7 Conclusions . . . . .	124

4.	REPEAT LOADING OF DEEP-BURIED STRUCTURES. . . . .	126
4.1	Introduction . . . . .	126
4.2	Analytical Solution. . . . .	127
4.2.1	Statement of Problem and Assumptions. . . . .	127
4.2.2	Features of Tunnel Response . . . . .	128
4.2.3	Method of Solution. . . . .	131
4.2.4	Solution. . . . .	133
4.2.5	Parameter Study . . . . .	143
4.3	Numerical Solution . . . . .	149
4.4	Test Specimens . . . . .	151
4.5	Experimental Results . . . . .	156
4.5.1	Isotropic Loading . . . . .	156
4.5.2	Uniaxial Strain Loading . . . . .	158
4.5.3	Uniaxial Strain Loading Followed by Isotropic Loading . . . . .	170
4.6	Comparison of Theory and Experiment. . . . .	170
4.7	Summary and Conclusions. . . . .	173
4.7.1	Analytical Solution . . . . .	173
4.7.2	Experimental Results. . . . .	174
	REFERENCES . . . . .	176
	APPENDIXES	
A	Data from Experiments on Jointed Rock. . . . .	179
B	Response to Cyclic Loading of Tunnels Reinforced with Backpacked Structures. . . . .	259

## ILLUSTRATIONS

### Figure

S.1	Liners for the three different tunnel sizes: 5/8 inch, 1/2 inch, 3/8 inch (15.9 mm, 12.7 mm, 9.5 mm) . . . . .	2
S.2	Vertical pressure to produce specified crown-invert tunnel closure versus specimen-to-tunnel diameter ratio--SRI RMG 2C2 . . . . .	3
S.3	Vertical pressure to produce specified crown-invert tunnel closure versus specimen-to-tunnel diameter ratio--16A rock simulant . . . . .	4
S.4	Tunnel closure at crown-invert and springline diameters versus vertical pressure for over-confined, underconfined and uniaxial strain loading of SRI RMG 2C2 . . . . .	6
S.5	Crown-invert tunnel closure versus pressure for three load-joint orientation angles . . . . .	8
S.6	Rock-cavity crown-invert closure versus pressure for three load-joint orientation angles . . . . .	9
S.7	Sectioned specimen from test LSUX-21 . . . . .	10
S.8	Finite element results for two reloading cycles . . . . .	12
S.9	Rock-cavity and liner closure for cyclic and monotonic uniaxial strain loading of a backpacked structure in saturated 16A rock simulant . . . . .	13
2.1	Liners for the three different tunnel sizes: 5/8 inch, 1/2 inch, 3/8 inch (15.9 mm, 12.7 mm, 9.5 mm) . . . . .	46
2.2	Location of specimen lateral strain gages . . . . .	47
2.3	Lateral pressure versus vertical pressure to maintain uniaxial strain in 16A rock simulant . . . . .	48
2.4	Tunnel closure at crown-invert and springline diameters versus vertical pressure for static uniaxial strain loading of 16A rock simulant [tunnel diameter = 5/8 inch (15.9 mm), $D_S/D_T = 6.4$ ] . . . . .	49

ILLUSTRATIONS (Continued)

Figure

2.5	Tunnel closure at crown-invert and springline diameters versus vertical pressure for static uniaxial strain loading of 16A rock simulant [tunnel diameter = 1/2 inch (12.7 mm), $D_S/D_T = 8.0$ ]	50
2.6	Tunnel closure at crown-inver and springline diameters versus vertical pressure for static uniaxial strain loading of 16A rock simulant [tunnel diameter = 3/8 inch (9.5 mm), $D_S/D_T = 10.57$ ]	51
2.7	Comparison of tunnel closure versus vertical pressure for three specimen-to-tunnel diameter ratios--16A rock simulant	52
2.8	Lateral strain versus vertical pressure	53
2.9	Specimen lateral strain at midheight versus vertical pressure [tunnel diameter = 5/8 inch (15.9 mm), $D_S/D_T = 6.4$ ]	54
2.10	Specimen lateral strain at midheight versus vertical pressure [tunnel diameter = 1/2 inch (12.7 mm), $D_S/D_T = 8.0$ ]	55
2.11	Specimen lateral strain at midheight versus vertical pressure [tunnel diameter = 3/8 inch (9.5 mm), $D_S/D_T = 10.67$ ]	56
2.12	Lateral pressure versus vertical pressure to maintain uniaxial strain in SRI RMG 2C2	57
2.13	Tunnel closure at crown-invert and springline diameters versus vertical pressure for static uniaxial strain loading of SRI RMG 2C2 [tunnel diameter = 5/8 inch (15.9 mm), $D_S/D_T = 6.4$ ]	58
2.14	Tunnel closure at crown-invert and springline diameters versus vertical pressure for static uniaxial strain loading of SRI RMG 2C2 [tunnel diameter = 1/2 inch (12.7 mm), $D_S/D_T = 8.0$ ]	59
2.15	Tunnel closure at crown-invert and springline diameters versus vertical pressure for static uniaxial strain loading of SRI RMG 2C2 [tunnel diameter = 3/8 inch (9.5 mm) $D_S/D_T = 10.67$ ]	60

ILLUSTRATIONS (Continued)

Figure

2.16	Comparison of tunnel closure versus vertical pressure for three specimen-to-tunnel diameter ratios--SRI RMG 2C2 . . . . .	61
2.17	Specimen lateral strain at midheight versus vertical pressure--SRI RMG 2C2 [tunnel diameter = 5/8 inch, $D_S/D_T = 6.4$ ] . . . . .	62
2.18	Specimen lateral strain at midheight versus vertical pressure--SRI RMG 2C2 [tunnel diameter = 1/2 inch (12.7 mm), $D_S/D_T = 8.0$ ] . . . . .	63
2.19	Specimen lateral strain at midheight versus vertical pressure--SRI RMG 2C2 [tunnel diameter = 3/8 inch (9.5 mm), $D_S/D_T = 10.67$ ] . . . . .	64
2.20	Vertical pressure to produce specified crown-invert tunnel closure versus specimen-to-tunnel diameter ratio--16A rock simulant . . . . .	65
2.21	Vertical pressure to produce specified crown-invert tunnel closure versus specimen-to-tunnel diameter ratio--SRI RMG 2C2 . . . . .	66
2.22	Vertical pressure to produce specified crown-invert tunnel closure versus specimen-to-tunnel diameter ratio--HUSKY ACE rock-matching grout . . . . .	67
2.23	Posttest cross sections showing distribution of pores in HUSKY ACE rock-matching grout . . . . .	68
2.24	Mean and standard deviation of specimen lateral strain in 16A rock simulant at midheight and 0.625 inch (15.9 mm) above midheight . . . . .	69
2.25	Mean and standard deviation of specimen lateral strain in SRI RMG 2C2 at midheight and 0.625 inch (15.9 mm) above midheight . . . . .	70
2.26	Load paths used to study effect of confining pressure on tunnel closure in saturated SRI RMG 2C2 . . . . .	72

ILLUSTRATIONS (Continued)

Figure

2.27	Tunnel closure at crown-invert and springline diameters versus vertical pressure for overconfined, underconfined and uniaxial strain loading of SRI RMG 2C2 . . . . .	73
2.28	Comparison of experimental and theoretical crown-invert tunnel closure in SRI RMG 2C2 for underconfined, overconfined and uniaxial strain loading . . . . .	75
2.29	Specimen lateral strain at midheight versus vertical pressure for overconfined, underconfined, and uniaxial strain loading of SRI 2C2 . . . . .	77
2.30	Load paths used to study effect of confining pressure on tunnel closure in dry SRI RMG 2C2 . . . . .	79
2.31	Tunnel closure at crown-invert and springline diameters versus vertical pressure for several loading paths in dry SRI RMG 2C2 . . . . .	81
3.1	Load path for tests on jointed specimens--16A rock simulant	84
3.2	Schematic showing joint orientation . . . . .	87
3.3	Engineering sketches for all joint angles tested . . . . .	88
3.4	Stress-strain curve for uniaxial strain loading of 13.1 lb/ft <sup>3</sup> (210 kg/m <sup>3</sup> ) polyurethane foam . . . . .	89
3.5	Sectioned specimen from test LSUX-20 . . . . .	90
3.6	Sectioned specimen from test LSUX-21 . . . . .	91
3.7	Sectioned specimen from test LSUX-24 . . . . .	92
3.8	Crown-invert tunnel closure versus vertical pressure for three load-joint orientation angles . . . . .	94
3.9	Springline tunnel closure versus vertical pressure for two load-joint orientation . . . . .	95
3.10	Rock-cavity crown-invert closure versus vertical pressure for three load-joint orientation angles . . . . .	97

ILLUSTRATIONS (Continued)

Figure

3.11	Rock-cavity springline closure versus vertical pressure for three load-joint orientation angles . . . . .	98
3.12	Tunnel liner closure versus pressure for three load-joint orientation angles . . . . .	101
3.13	Crown-invert tunnel closure versus vertical pressure for three tunnel-joint orientation angles . . . . .	103
3.14	Springline tunnel closure versus vertical pressure for two tunnel-joint orientation angles . . . . .	104
3.15	Load path for repeat loading test in which unloading was underconfined . . . . .	106
3.16	Crown-invert tunnel closure versus vertical pressure for repeat and monotonic loading ( $\beta = 0^\circ$ ) . . . . .	107
3.17	Springline tunnel closure versus vertical pressure for repeat and monotonic loading ( $\beta = 0^\circ$ ) . . . . .	108
3.18	Crown-invert tunnel closure versus vertical pressure for repeat and monotonic loading ( $\beta = 45^\circ$ ) . . . . .	109
3.19	Springline tunnel closure versus vertical pressure for repeat and monotonic loading ( $\beta = 45^\circ$ ) . . . . .	110
3.20	Crown-invert tunnel closure versus vertical pressure for repeat and monotonic loading, with unloading part of cycle in load underconfined . . . . .	112
3.21	Springline tunnel closure versus vertical pressure for repeat and monotonic loading, with unloading part of cycle in load underconfined . . . . .	113
3.22	Crown-invert closure versus vertical pressure for backpacked and direct contact tunnel liners--intact 16A rock stimulant	115
3.23	Crown-invert closure versus vertical pressure for backpacked and direct contact tunnel liners--jointed 16A rock simulant ( $\beta = 0^\circ$ ) . . . . .	116

ILLUSTRATIONS (Continued)

Figure

3.24	Crown-invert closure versus vertical pressure for backpacked and direct contact tunnel liners--jointed 16A rock simulant ( $\beta = 30^\circ$ ) . . . . .	117
3.25	Crown-invert closure versus vertical pressure for backpacked and direct contact tunnel liner--jointed 16A rock simulant ( $\beta = 45^\circ$ ) . . . . .	118
3.26	Springline closure versus vertical pressure for backpacked and direct contact tunnel liners--intact 16A rock simulant . . . . .	119
3.27	Springline closure versus vertical pressure for backpacked and direct contact tunnel liners--jointed 16A rock simulant ( $\beta = 0^\circ$ ) . . . . .	120
3.28	Springline closure versus vertical pressure for backpacked and direct contact tunnel liners--jointed 16A rock simulant ( $\beta = 45^\circ$ ) . . . . .	121
4.1	Positions of current (shaded) and previous plastic zones during the four loading stages . . . . .	129
4.2	Effect of $\bar{P}_o$ on reload closure . . . . .	144
4.3	Effect of $P_i$ on reload closure with fixed load $P_o$ . . . . .	146
4.4	Effect of $P_i$ on reload closure with fixed design closure . . . . .	147
4.5	Effect of $\sigma_u$ and $N_\phi$ on reload closure fixed design closure . . . . .	148
4.6	Finite element results for two reloading cycles . . . . .	150
4.7	Twelve-inch diameter specimen of tuff simulant and a representative tunnel reinforcing structure . . . . .	152
4.8	Stress-strain curve for uniaxial strain loading of 13.2 lb/ft <sup>3</sup> (211 kg/m <sup>3</sup> ) polyurethane foam . . . . .	157
4.9	Tunnel closure for cyclic isotropic loading of 6B rock simulant . . . . .	159

ILLUSTRATIONS (Continued)

Figure

4.10	Tunnel closure for cyclic and monotonic isotropic loading of SRI RMG 2C2 rock simulant . . . . .	160
4.11	Crown-invert tunnel closure for cyclic and monotonic uniaxial strain loading of 6B rock simulant . . . . .	162
4.12	Crown-invert tunnel closure for cyclic and monotonic uniaxial strain loading of saturated SRI RMG 2C2 rock simulant . . . . .	163
4.13	Rock-cavity and liner closure for cyclic and monotonic uniaxial strain loading of a backpacked structure in saturated 16A rock simulant . . . . .	164
4.14	Posttest section views of jointed rock model with $\beta = 45^\circ$ .	167
4.15	Tunnel closure for cyclic and monotonic uniaxial strain loading of jointed 16A rock simulant--load joint orientation angle $\beta = 0^\circ$ . . . . .	168
4.16	Tunnel closure for cyclic and monotonic uniaxial strain loading of jointed 16A rock simulant--load-joint orientation angle $\beta = 45^\circ$ . . . . .	169
4.17	Crown-invert tunnel closure versus applied pressure for saturated SRI RMG 2C2 subjected to uniaxial strain loading following by isotropic loading . . . . .	171
A.1	Schematic showing joint orientation . . . . .	181
A.2	Sectioned specimen for test LSUX-13 . . . . .	183
A.3	Enlargement of tunnel region in LSUX-13 specimen . . . . .	184
A.4	Lateral confining pressure versus vertical pressure--test LSUX-13 . . . . .	185
A.5	Crown-invert tunnel closure versus vertical pressure--test LSUX-13 . . . . .	185
A.6	Springline tunnel closure versus vertical pressure--test LSUX-13 . . . . .	186

ILLUSTRATIONS (Continued)

Figure

A.7	Tunnel liner strain at crown versus vertical pressure--test LSUX/13 . . . . .	186
A.8	Tunnel liner strain at springline versus vertical pressure-- test LSUX-13 . . . . .	187
A.9	Sectioned specimen from test LSUX-14 . . . . .	189
A.10	Enlargement of tunnel region in LSUX-14 specimen . . . . .	190
A.11	Lateral confining pressure versus vertical pressure--test LSUX-14 . . . . .	191
A.12	Crown-invert tunnel closure versus vertical pressure--test LSUX-14 . . . . .	191
A.13	Springline tunnel closure versus vertical pressure--test LSUX-14 . . . . .	192
A.14	Tunnel liner strain at crown versus vertical pressure--test LSUX-14 . . . . .	192
A.15	Tunnel liner strain at left springline versus vertical pressure--test LSUX-14 . . . . .	193
A.16	Tunnel liner strain at right springline versus vertical pressure--test LSUX-14 . . . . .	193
A.17	Sectioned specimen from test LSUX-16 . . . . .	195
A.18	Enlargement of tunnel region in LSUX-16 specimen . . . . .	196
A.19	Lateral confining pressure versus vertical pressure--test LSUX-16 . . . . .	197
A.20	Crown-invert tunnel closure versus vertical pressure-- test LSUX-16 . . . . .	197
A.21	Springline tunnel closure versus vertical pressure--test LSUX-16 . . . . .	198

ILLUSTRATIONS (Continued)

Figure

A.22	Tunnel liner strain at crown versus vertical pressure--test LSUX-16 . . . . .	198
A.23	Tunnel liner strain at left springline versus vertical pressure--Test LSUX-16 . . . . .	199
A.24	Tunnel liner strain at right springline versus vertical pressure--test LSUX-16 . . . . .	199
A.25	Sectioned specimen from test LSUX-17 . . . . .	201
A.26	Enlargement of tunnel region in LSUX-17 specimen . . . . .	202
A.27	Lateral confining pressure versus vertical pressure--test LSUX-17 . . . . .	203
A.28	Crown-invert closure versus vertical pressure--test LSUX-17	203
A.29	Springline tunnel closure versus vertical pressure-test LSUX-17 . . . . .	204
A.30	Tunnel liner strain at crown versus vertical pressure--test LSUX-17 . . . . .	204
A.31	Tunnel liner strain at springline versus vertical pressure--test LSUX-17 . . . . .	205
A.32	Sectioned specimen from test LSUX-18 . . . . .	207
A.33	Enlargement of tunnel region in LSUX-18 specimen . . . . .	208
A.34	Lateral confining pressure versus vertical pressure--test LSUX-18 . . . . .	209
A.35	Crown-invert tunnel closure versus vertical pressure--test LSUX-18 . . . . .	209
A.36	Springline tunnel closure versus vertical pressure--test LSUX-18 . . . . .	210
A.37	Tunnel liner strain at crown versus vertical pressure--test LSUX-18 . . . . .	210

ILLUSTRATIONS (Continued)

Figure

A.38	Tunnel liner strain at invert versus vertical pressure--test LSUX-18 . . . . .	211
A.39	Tunnel liner strain at springline versus vertical pressure--test LSUX-18 . . . . .	211
A.40	Sectioned specimen from test LSUX-19 . . . . .	213
A.41	Enlargement of tunnel region in LSUX-19 specimen . . . . .	214
A.42	Lateral confining pressure versus vertical pressure--test LSUX-19 . . . . .	215
A.43	Rock-cavity crown-invert tunnel closure versus vertical pressure--test LSUX-19 . . . . .	215
A.44	Rock-cavity springline tunnel closure versus vertical pressure--test LSUX-19 . . . . .	216
A.45	Liner crown-invert closure versus vertical pressure--test LSUX-19 . . . . .	216
A.46	Liner springline tunnel closure versus vertical pressure--test LSUX-19 . . . . .	217
A.47	Tunnel liner strain at crown versus vertical pressure--test LSUX-19 . . . . .	217
A.48	Tunnel liner strain at invert versus vertical pressure--test LSUX-19 . . . . .	218
A.49	Tunnel liner strain at left springline versus vertical pressure--test LSUX-19 . . . . .	218
A.50	Tunnel liner strain at right springline versus vertical pressure--test LSUX-19 . . . . .	219
A.51	Sectioned specimen from test LSUX-20 . . . . .	221
A.52	Enlargement of tunnel region in LSUX-20 specimen . . . . .	222

ILLUSTRATIONS (Continued)

Figure

A.53	Lateral confining pressure versus vertical pressure . . .	223
A.54	Rock-cavity crown-invert tunnel closure versus vertical pressure--test LSUX-20 . . . . .	223
A.55	Rock-cavity springline tunnel closure versus vertical pressure--test LSUX-20 . . . . .	224
A.56	Liner crown-invert tunnel closure versus vertical pressure--test LSUX-20 . . . . .	224
A.57	Liner springline tunnel closure versus vertical pressure--test LSUX-20 . . . . .	225
A.58	Tunnel liner strain at crown versus vertical pressure--test LSUX-20 . . . . .	225
A.59	Tunnel liner strain at invert versus vertical pressure--test LSUX-20 . . . . .	226
A.60	Tunnel liner strain at left springline versus vertical pressure--test LSUX-20 . . . . .	226
A.61	Tunnel liner strain at right springline versus vertical pressure--test LSUX-20 . . . . .	227
A.62	Sectioned specimen from test LSUX-21 . . . . .	229
A.63	Enlargement of tunnel region in LSUX-21 specimen . . . . .	230
A.64	Lateral confining pressure versus vertical pressure--test LSUX-21 . . . . .	231
A.65	Crown-invert tunnel closure versus vertical pressure--test LSUX-21 . . . . .	231
A.66	Springline tunnel closure versus vertical pressure--test LSUX-21 . . . . .	232
A.67	Tunnel liner strain at invert versus vertical pressure--test LSUX-21 . . . . .	232

ILLUSTRATIONS (Continued)

Figure

A.68	Tunnel liner strain at springline versus vertical pressure-- test LSUX-21 . . . . .	233
A.69	Sectioned specimen from test LSUX-22 . . . . .	235
A.70	Enlargement of tunnel region in LSUX-22 specimen . . . . .	236
A.71	Lateral confining pressure versus vertical pressure--test LSUX-22 . . . . .	237
A.72	Crown-invert closure versus vertical pressure--test LSUX-22 .	237
A.73	Springline tunnel closure versus vertical pressure--test LSUX-22 . . . . .	238
A.74	Tunnel liner strain at left springline versus vertical pressure--test LSUX-22 . . . . .	238
A.75	Tunnel liner strain at right springline versus vertical pressure--test LSUX-22 . . . . .	239
A.76	Sectioned specimen from test LSUX-23 . . . . .	241
A.77	Enlargement of tunnel region in LSUX-23 specimen . . . . .	242
A.78	Lateral confining pressure versus vertical pressure--test LSUX-23 . . . . .	243
A.79	Crown-invert tunnel closure versus vertical pressure--test LSUX-23 . . . . .	243
A.80	Springline tunnel closure versus vertical pressure--test LSUX-23 . . . . .	244
A.81	Tunnel strain at crown versus vertical pressure--test LSUX-23	244
A.82	Tunnel liner strain at springline versus vertical pressure-- test LSUX-23 . . . . .	245
A.83	Sectioned specimen from test LSUX-24 . . . . .	247

ILLUSTRATIONS (Continued)

<u>Figure</u>	
A.84	Enlargement of tunnel region in LSUX-24 specimen . . . . . 248
A.85	Lateral confining pressure versus vertical pressure-- test LSUX-24 . . . . . 249
A.86	Crown-invert tunnel closure versus vertical pressure-- test LSUX-24 . . . . . 249
A.87	Tunnel liner strain at crown versus vertical pressure-- test LSUX-24 . . . . . 250
A.88	Tunnel liner strain at springline versus vertical pressure--test LSUX-24 . . . . . 250
A.89	Sectioned specimen from test LSUX-25 . . . . . 252
A.90	Enlargement of tunnel region in LSUX-25 specimen . . . . . 253
A.91	Lateral confining pressure versus vertical pressure-- test LSUX-25 . . . . . 254
A.92	Rock-cavity crown-invert tunnel closure versus vertical pressure--test LSUX-25 . . . . . 254
A.93	Rock-cavity springline tunnel closure versus vertical pressure--test LSUX-25 . . . . . 255
A.94	Liner crown-invert closure versus vertical pressure-- test LSUX-25 . . . . . 255
A.95	Liner springline tunnel closure versus vertical pressure--test LSUX-25 . . . . . 256
A.96	Tunnel liner strain at crown versus vertical pressure-- test LSUX-25 . . . . . 256
A.97	Tunnel liner strain at left springline versus vertical pressure--test LSUX-25 . . . . . 257
A.98	Tunnel liner strain at right springline versus vertical pressure--test LSUX-25 . . . . . 257

ILLUSTRATIONS (Concluded)

Figure

B.1	Backpacked structure and end-fittings . . . . .	264
B.2	Stress-strain curve for uniaxial strain loading of 13.2 lb/ft <sup>3</sup> (211 kg/m <sup>3</sup> ) polyurethane foam . . . . .	265
B.3	Rock-cavity and liner closure for static monotonic uniaxial strain loading of 16A a backpacked structure in rock simulant . . . . .	266
B.4	Rock-cavity and liner closure for cycles and monotonic uniaxial strain loading of a backpacked structure in 16A rock simulant . . . . .	267

## 1. INTRODUCTION

### 1.1 BACKGROUND

This report is the sixth in a series that describes DNA-funded deep-buried structure laboratory programs carried out at SRI International [1-5].\* These reports describe laboratory tests performed in direct support of specific experiments fielded in underground nuclear tests, as well as laboratory experiments performed to provide both qualitative and quantitative understanding of some fundamental aspects of reinforced rock-cavity deformation.

Laboratory testing of scale-model cavities provides an efficient means of quickly evaluating and developing proposed deep-based structural concepts, so that it is necessary to field only models of the most promising of these in the underground nuclear tests. Laboratory results also allow extrapolation of field results to other geological environments. Further, since in laboratory tests rock properties and specimen boundary conditions are known, results provide a check on the accuracy of material models and computer codes used to predict structural response in the field.

### 1.2 APPROACH AND SCOPE OF INVESTIGATION

This volume of the final report describes work performed under Contract No. DNA 001-76-C-0385 after April 1, 1978. Results obtained before that date are reported in Volume I [5]. Topics presented in Volume I are:

- (1) Tunnel response under dynamic versus static loading.
- (2) Borehole/cable interaction.

---

\* Numbers in brackets designate references at the end of the report.

- (3) Experimental procedures and initial experiments for cylindrical structures in jointed rock.
- (4) Theoretical analysis of elliptical structures.

In Volume II we present results of experimental and theoretical studies of:

- (1) The effects of lateral confinement and specimen-to-tunnel diameter ratio in laboratory testing.
- (2) The effects of joints on tunnel deformation.
- (3) The effect of repeat loading on tunnel closure.

The purpose of the first experimental study described in the present volume was to determine the ability of our laboratory tests to simulate loading of deep-buried structures in the field. Special attention was given to establishing whether a finite laboratory specimen can adequately model the essentially infinite geology in the field, and whether the confining pressure applied to the specimen lateral surface properly simulates a uniaxial strain loading in the field.

The second experimental study continued our investigation of the effect on tunnel deformation of a single set of parallel joints. We present results for direct contact and backpacked structures in rock masses with various joint orientations under both monotonic and cyclic loading.

A theoretical study of the effect of repeat loading on tunnel closure was performed to help understand laboratory results obtained for yielding structures under cyclic loading. Analytical expressions are given for the stress and displacement fields in the rock for repeat axisymmetric loading, and numerical results are given for both axisymmetric and asymmetric loading. Theoretical results are compared with experiments performed during the current program and our previous programs.

Experimental techniques are not described in this report. Testing machines and intact specimen preparation are described in references [2] and [3]. Jointed specimen preparation and handling techniques are described in Chapter 4 of Volume I.

### 1.2.2 REPORT ORGANIZATION

The next two chapters present results of our major current experimental studies. Chapter 2 gives results of the study of the influence on laboratory results of lateral confinement and the specimen-to-tunnel diameter ratio. Chapter 3 gives results of tests performed on jointed specimens. The final chapter, Chapter 4, describes our study of the effect of repeat loading on tunnel closure. Two appendixes conclude the report. Appendix A gives test records and photographs of specimen posttest cross sections for each of the twelve tests on jointed specimens. Appendix B describes four experiments that study the effect of repeat loading on the deformation of a backpacked tunnel liner in intact 16A rock simulant.

## 2. EFFECTS OF LATERAL CONFINEMENT AND SPECIMEN-TO-TUNNEL DIAMETER RATIO IN LABORATORY TESTING

### 2.1 INTRODUCTION

This chapter describes tests performed on 4-inch-diameter (0.1-m) specimens to study the influence of the specimen-to-tunnel diameter ratio and of lateral confinement in laboratory testing. The laboratory study was carried out in conjunction with a computational study performed by California Research and Technology (CRT). Both studies were motivated by discussions about tunnel closure measured in the laboratory under dynamic uniaxial strain loading [5]. Goals of these studies were:

- (1) To test agreement between measured tunnel closure and tunnel closure calculated by using the finite element code NONSAP with a simple constitutive model and an approximation of the three-dimensional uniaxial strain loading in the laboratory.
- (2) To determine the effect on tunnel deformation of the specimen-to-tunnel diameter ratio,  $D_S/D_T$ .
- (3) To determine the actual lateral boundary conditions applied in nominally uniaxial-strain-loading laboratory tests.
- (4) To determine the effect on tunnel closure of changes in lateral confinement.

The study of the effect of the specimen-to-tunnel diameter ratio addresses topics (1), (2), and (3), while the study of the effect of lateral confinement addresses topics (1) and (4). The CRT computational study investigated all four topics [6]. Some of their results are included in this report for comparison.

### 2.2 EFFECT OF SPECIMEN-TO-TUNNEL DIAMETER RATIO

Tests were performed to study the influence on tunnel closure of the ratio of specimen-to-tunnel diameter in both 16A rock simulant and SRI RMG 2C2. We performed static uniaxial strain loading tests on

4-inch-diameter (0.1-m) models that contained tunnels of three diameters: 5/8, 1/2, and 3/8 inch (15.9, 12.7, and 9.5 mm). These tunnel diameters gave specimen-to-tunnel diameter ratios  $D_S/D_T = 6.4, 8.0, \text{ and } 10.67$ . A 1015 steel monocoque cylinder having mean-radius-to-wall-thickness ratio  $a/h = 12.5$  reinforced each tunnel in the 16A specimens and a 6061-T0 aluminum monocoque cylinder having  $a/h = 11.5$  reinforced each tunnel in the SRI RMG 2C2 specimens. Figure 2.1 shows the three cylinder sizes.\*

We measured tunnel closure at the crown-invert and springline diameters, and rock specimen lateral strain at midheight and at 0.625 inch (15.9 mm) above the midheight. These strain gage locations are shown in Figure 2.2. The uniaxial strain condition was imposed by maintaining zero average strain at the two gages above the specimen midheight. Comparison of these strains with those from the two gages at the midheight showed any deviation from uniaxial strain due to bulging. Data from tests on 16A and 2C2 simulants are presented separately, and are then summarized and discussed in detail at the end of the section.

#### 2.2.1 Results for 16A Rock Simulant Models

We performed six tests on specimens of 16A rock simulant. Figure 2.3 plots lateral pressure to maintain uniaxial strain as a function of vertical pressure for all six tests. The lateral pressure is roughly the same in all tests. One exception is a test in which  $D_S/D_T = 8.0$ , where the lateral pressure is slightly higher between  $P_V = 5 \text{ ksi}$  and  $10 \text{ ksi}$  (34.5 MPa and 69 MPa) and produces minor deviations from the expected trend for the springline closure and the specimen lateral strain data.

Figures 2.4, 2.5, and 2.6 plot tunnel closure as a function of vertical pressure for each of the three values of specimen-to-tunnel diameter ratio. Each plot gives data from two repeat tests and shows

---

\* Illustrations in Section 2.2 are grouped at the end of the section.

that, for a given value of  $D_S/D_T$ , both the crown-invert and springline closures are repeatable. For comparison of closures of the three tunnels, curves fitted through the average of each data pair are plotted in Figure 2.7. Crown-invert closure of the three tunnels is positive for all pressures, as expected. However, for the two larger tunnel sizes, the rate of closure decreases for pressures greater than about 13 ksi (90 MPa). The expected trend, that the rate of crown-invert closure increases with increasing vertical pressure, is obtained with the smallest tunnel.

Figure 2.7 also shows that the pressure required to produce a specified crown-invert closure decreases slightly with decreasing tunnel size. For example, the pressure to produce a 3% crown-invert closure of a 5/8-inch-diameter (15.9 mm) tunnel is 11.5 ksi (79 MPa), while that for a 3/8-inch-diameter tunnel (9.5 mm) is only 9.7 ksi (67 MPa), about 15% less.

While the shapes of the crown-invert closure curves for the three tunnel sizes are similar, the shapes of the springline closure curves differ. For all three tunnel sizes springline closure is similar until the loading pressure reaches 10 ksi (69 MPa). At this point the springlines in the larger two tunnels begin to move inward, producing a positive closure for pressures greater than about 14 ksi (97 MPa). The springlines in the small tunnel continue to move outward to give a closure of -2% at the end of the test (when the crown-invert closure is about +6%). The mildly exaggerated springline motion in test SUX-124 (Figure 2.5) is probably due to the slightly higher lateral confining pressure in that test.

In addition to measuring tunnel closure in these experiments, we also measured specimen midheight lateral strain to determine if the presence of the tunnels causes the specimen to bulge. Figure 2.8 plots the strains recorded at all four gage stations for a single test, SUX-122 ( $D_S/D_T = 6.4$ ). Strain gages #1 and #2, mounted 0.625 inch (15.9 mm) above midheight, were used to maintain the uniaxial strain condition (zero average). Hence, their outputs are equal in magnitude

and opposite in sign. For pressures up to about 10 ksi (69 MPa), the magnitude of these strains is less than  $10 \times 10^{-6}$ . They then increase to about  $200 \times 10^{-6}$  near  $P_v = 15$  ksi (103 MPa), and then decrease slightly until the end of the test. Strain gages #3 and #4, at midheight, show that the specimen contracts about 0.2 mil (0.005 mm) early in the test, and then bulges slightly at higher pressures: strain at station #3 is about  $-100 \times 10^{-6}$ , and at station #4 it is about  $+200 \times 10^{-6}$ .

For simplicity in the remaining plots (Figures 2.9 to 2.11), only one curve is given for each test. This curve is the average of the two gages at the specimen midheight (the average of the other two gages is zero, by our test procedure). These curves show that the specimen does not bulge significantly, and actually that both positive strains (outward displacement) and negative strains (inward displacement) were measured. We conclude that tunnel size does not influence the rock specimen lateral strain. The fairly large strains shown in Figure 2.10 for SUX-124 ( $-600 \times 10^{-6} = -0.06\%$ ) are attributed to the slightly higher lateral confining pressure.

These data will be discussed more fully after presentation of data for SRI RMG 2C2.

### 2.2.2 Results for SRI RMG 2C2 Rock Simulant Models

We performed similar experiments with tunnels in six specimens of SRI RMG 2C2. In Figure 2.12, lateral pressure is plotted as a function of vertical pressure for these six uniaxial strain loading tests. The lateral pressure required to maintain uniaxial strain does not depend on tunnel size. In one test (SUX-132,  $D_S/D_T = 6.4$ ), however, the lateral pressure does increase more rapidly than in the other five tests when  $P_v$  is greater than about 5 ksi (34.5 MPa). We will see later (Figure 2.13) that the higher lateral pressure influences the tunnel closure only slightly.

The lateral pressure data indicate that the properties of the SRI RMG 2C2 are slightly different from those reported in Volume I for the previous grout pours.<sup>[5]</sup> Poisson's ratio is about 0.18, down from 0.23. The friction angle is about 5°, up from 2.5°. Also, the unconfined compressive strength, determined from separate unconfined compression tests, is 4350 psi (30 MPa), which is up from 3675 psi (25.3 MPa). These changes in constitutive parameters are relatively small. The increase in unconfined compressive strength is less than 20%, and although the friction angle is twice as large, the parameter  $N_\phi$ , which appears in the failure criterion, increases by only 10%. The 20% decrease in Poisson's ratio gives the same value, 0.18, as reported by Terra Tek<sup>[7]</sup>. These changes in constitutive parameters should be kept in mind if tunnel closure and specimen lateral strain data from the present tests are compared with data obtained previously.

In Figures 2.13, 2.14, and 2.15, tunnel closures at the crown-invert and springline diameters are plotted as functions of vertical pressure for two repeat tests of each of the three tunnel sizes. Scatter in results is small except for the  $D_S/D_T = 8.0$  crown-invert closures (Figure 2.14). For these two tests, there is a difference in pressure of approximately 1.75 ksi (12 MPa) at the same crown-invert closure. Springline closures, however, are nearly identical.

The influence of the higher lateral pressure in test SUX-132 is shown in Figure 2.13. As the load path moves toward the hydrostat (Figure 2.12), tunnel closure becomes more symmetric: the crown-invert and springline closures tend toward a single curve, as would be obtained for axisymmetric (isotropic) loading. However, for the range of pressures and closures studied, the spread in closure data above  $P_V = 6.5$  ksi (45 MPa) for  $D_S/D_T = 6.4$  is fairly small.

Figure 2.16 presents the summary plot of tunnel closure as a function of vertical pressure for all three tunnel sizes. The curves show that tunnel closure in SRI RMG 2C2 does not depend significantly on the specimen-to-tunnel diameter ratio,  $D_S/D_T$ . This result contrasts with that obtained for the 16A rock simulant, for which the pressure

required to produce a specified crown-invert closure decreases slightly with decreasing tunnel size. The change in behavior of springline closure for the smallest tunnel ( $D_S/D_T = 10.67$ ) is similar to that for the 16A rock simulant.

Figures 2.17, 2.18, and 2.19 plot specimen lateral strain at the midheight as a function of vertical pressure. The values plotted, as for the 16A rock specimens, are the average of two gages. They show a small deviation from uniaxial strain [which is imposed by maintaining zero average lateral strain, measured by the two gages at 0.625 inch (15.9 mm) above the midheight]. Generally, the specimen bulges slightly ( $\epsilon_L = 200 \times 10^{-6}$ ) near the end of the test. This strain corresponds to an 0.8-mil (0.02-mm) increase in the 4-inch (0.1-m) diameter. The largest diameter changes occur for  $D_S/D_T = 10.67$ , as shown in Figure 2.19. At the end of the test, midheight lateral strain is  $+500 \times 10^{-6}$  in test SUX-135 and  $-100 \times 10^{-6}$  in test SUX-134. However, this relatively large difference in midheight lateral strain has no discernible influence on tunnel closure. Figure 2.15 shows that both crown-invert and springline closures are nearly identical for both tests.

### 2.2.3 Summary

The results presented show that tunnel closure measured in the laboratory depends on the specimen-to-tunnel diameter ratio  $D_S/D_T$  in 16A rock simulant, but not in SRI RMG 2C2. Figures 2.20, 2.21, and 2.22 plot the vertical pressure required to produce crown-invert closures of 1%, 3%, and 5% as a function of the specimen-to-tunnel diameter ratio for 16A, 2C2, and HUSKY ACE rock-matching grout, respectively. The results for HUSKY ACE rock-matching grout were obtained previously [2] and are reported here for comparison. A straight line is fitted through the data for each value of crown-invert closure. These plots show that the finite specimen size in our tests introduces maximum errors in critical loads of only 10% to 20%.

A possible explanation for the difference in tunnel response for the tunnels of three different sizes in 16A rock simulant is interaction of the plastic zone with the specimen boundary. We assume that initially the plastic zones around the tunnels are similar but of different scales, which are determined by the tunnel size. As the plastic zone grows and the elastic-plastic boundary nears the specimen boundary, the interaction with the specimen boundary becomes more significant. The plastic zone around a larger tunnel will interact with the specimen boundary sooner than will the plastic zone around a smaller tunnel. If the effect of the interaction between the plastic zone and the specimen boundary were to produce a more symmetric load on the tunnel, then the results would be as observed: the springlines would move inward and the rate of closure at the crown-invert would be slowed.

By the same argument, we confirm that no size effect is observed for SRI RMG 2C2 because the entire specimen yields at fairly low pressure, so that there is no elastic-plastic boundary around the tunnel. However, this argument suggests that no size effect would be observed in the HUSKY ACE rock-matching grout specimens, because these also yield at low pressure. The observed tunnel size effect in HUSKY ACE rock-matching grout may be the result of a volume strain property that is much different from that of the other two materials. A notable difference emerged between the results of tests performed on HUSKY ACE rock-matching grout and those of the current tests on 16A rock simulant and SRI RMG 2C2: the volume of the HUSKY ACE specimens decreased by about 10%, whereas the volume of the 16A rock simulant and SRI RMG 2C2 specimens decreased by only about 1%. This suggests that, in addition to shearing, compaction was an important deformation mechanism in the HUSKY ACE specimens. Figure 2.23 shows posttest cross sections of the HUSKY ACE rock-matching grout specimens. Each specimen contains a distribution of large pores, comparable in size to the tunnel, so that the specimen material itself has a length scale. These pores compact under low pressure and contribute significantly to the deformation. It is therefore possible that the size effect observed in HUSKY ACE rock-matching grout may be a result of the deformation of the pores.

The caving in at the top and bottom of the specimens should also be noted. This did not occur on any of the rocks tested in the current program.

CRT performed calculations to study theoretically the influence of  $D_S/D_T$  in specimens of SRI RMG 2C2. Their numerical model used a simple constitutive model (Drucker-Prager yield with strain hardening and a variable angle of friction) and a generalized plane strain computational technique that seems to model adequately some of the three-dimensional characters of the laboratory experiments. Their results for the large tunnel,  $D_S/D_T = 6.4$ , show good agreement with our experiments, at both the crown-invert and springline diameters. However, their study gives conflicting results for the two different lateral boundary conditions they studied. The two theoretical lateral boundary conditions they used were: 1) a pressure boundary condition for which the lateral pressure on the boundary is the uniform pressure,  $P_\ell$ , needed to produce uniaxial strain in a tunnelless specimen, and 2) a displacement boundary condition for which the radial displacement on the lateral surface is zero. Neither of these conditions was imposed in our experiments. The experimental lateral boundary condition was a pressure boundary condition for which the lateral pressure on the boundary is the pressure,  $P_H^{UX}$ , that produces zero circumferential strain at 0.625 inches (15.9 mm) above the specimen midheight. For a specimen with  $D_S/D_T = 6.4$ , the resulting experimental uniaxial strain pressure,  $P_H^{UX}$ , is found to be related to the theoretical tunnelless pressure boundary condition by  $P_H^{UX} = 1.2 P_\ell$ .

In the numerical simulations, when the lateral boundary is subjected to the pressure that gives uniaxial strain in a tunnelless specimen, a significant dependence of tunnel closure on  $D_S/D_T$  is found. Less pressure is needed to produce a specified crown-invert closure of a large tunnel than to produce the same closure of a small tunnel. For the two tunnel sizes studied, a specimen containing the larger tunnel ( $D_S/D_T = 6.4$ ) requires about 25% less pressure to produce a 5% crown-invert closure than does a specimen containing the smaller tunnel ( $D_S/D_T = 18$ ).

If, however, the lateral boundary condition imposed in the numerical simulation is zero radial displacement with the tunnel present, then the theoretical influence of  $D_S/D_T$  on tunnel closure is negligible. This result agrees with the experimental results for SRI RMG 2C2. One would expect results obtained for this condition to agree more closely with the experiments, because the numerical procedure used by CRT predicts radial displacements for the pressure boundary condition that are much too large. This problem will be discussed in the following paragraphs, in which we summarize the midheight lateral strain measurements.

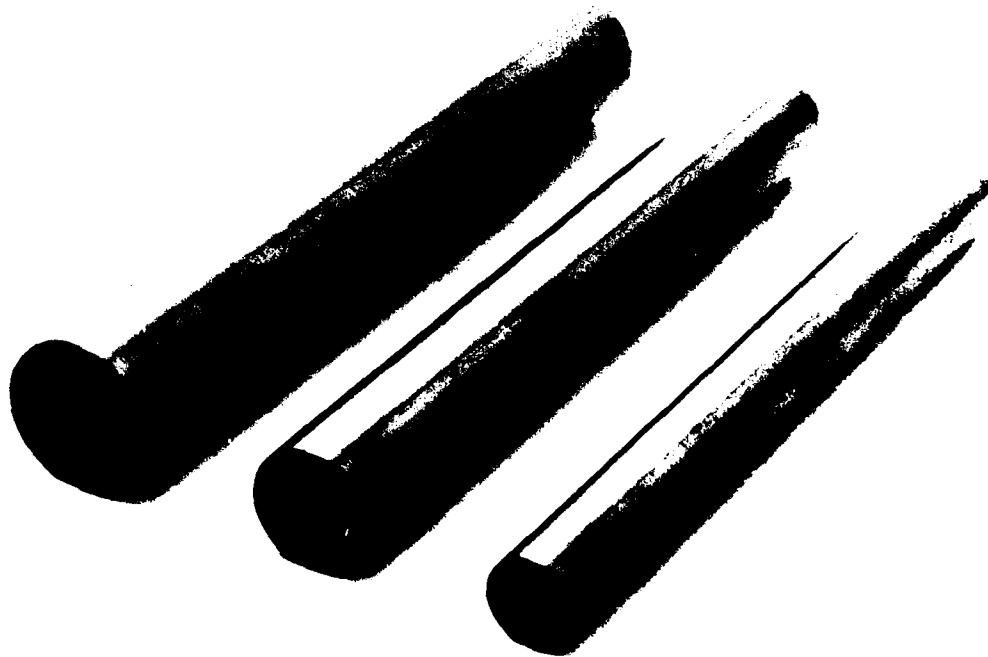
The plots of midheight lateral strain as a function of vertical pressure show no systematic variation: some specimens bulged while others moved inward. Since there is no apparent systematic variation of midheight lateral strain with vertical pressure for the six individual experiments, the average value for all 12 gages is a more representative measure of midheight lateral strain. Averaging the strains eliminates some of the random variations and yields a more tractable relationship between midheight lateral strain and vertical pressure.

Figure 2.24 (top) plots mean midheight lateral strain as a function of vertical pressure for 16A rock simulant. The error bars span one standard deviation above and one below the mean. The mean strain for 16A rock shows no systematic variation with vertical pressure: the specimen caves in at low pressure, bulges at moderate pressure, and then caves in again at high pressure. This variation is much smaller than the standard deviations of both the midheight lateral strain and the lateral strain at 0.625 inch (15.0 mm) above midheight [Figure 2.24 (bottom)]. These deviations, in turn, are small compared with strains necessary to influence tunnel response (shown in next section). We conclude that the lateral boundaries of the 16A rock specimens tend to remain straight and that small observed deviations are random perturbations in each test.

Figure 2.25 (top) plots mean midheight lateral strain as a function of vertical pressure for SRI RMG 2C2. The strain is always positive and small (the specimens bulge slightly) and increases fairly smoothly with increasing vertical pressure. At the end of the test, when the vertical pressure  $P_V = 7.5$  ksi (51.7 MPa), the midheight lateral strain is about  $+150 \times 10^{-6}$ , considerably smaller than the value of  $+800 \times 10^{-6}$  calculated by CRT. The calculated midheight lateral strain does not lie within three standard deviations of the mean, so the calculated strains are excessively large.

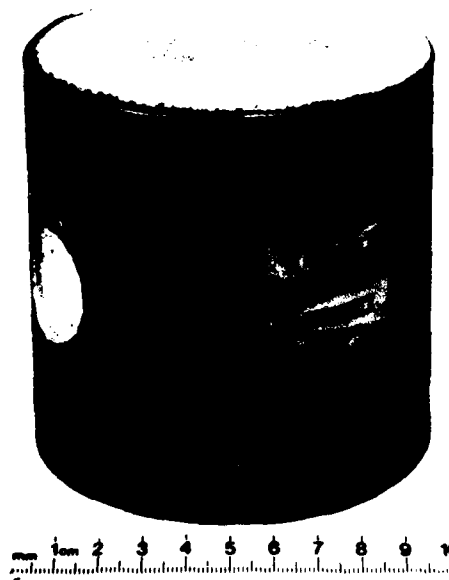
Finally, we plot in Figure 2.25 (bottom) both the mean and standard deviation of the SRI RMG 2C2 rock specimen lateral strain at 0.625 inch (15.9 mm) above midheight as a function of vertical pressure. The standard deviation is about as large as that for the midheight lateral strain data. Comparison of these two data sets suggests that the specimens do bulge, but only slightly. The increase in midheight diameter at the end of the test is only 0.6 mils (0.016 mm).

We believe that it is reasonable to assume that both theory and experiment are correct, and that these differences in experimental and theoretical boundary strains result from hoop stresses in the cylindrical test specimens of the experiment that are not present in the two-dimensional meshes in the theory. This assumption leads to the conclusion that the cylindrical test geometry tends to keep the specimen boundaries more nearly in a uniaxial strain condition than would be obtained in a "two-dimensional" test specimen shaped like a long loaf of bread, with the tunnel along the length. Thus we also conclude that the cylindrical test geometry results in a good approximation of plane deformation around the tunnel, as assumed in the theory and for long tunnels in the field.



MP-5762-84

FIGURE 2.1 LINERS FOR THE THREE DIFFERENT TUNNEL SIZES: 5/8 INCH,  
1/2 INCH, 3/8 INCH (15.9 mm, 12.7 mm, 9.5 mm)



MP-5762-252

FIGURE 2.2 LOCATION OF SPECIMEN LATERAL STRAIN GAGES  
Two gages mounted on opposite side at similar stations.

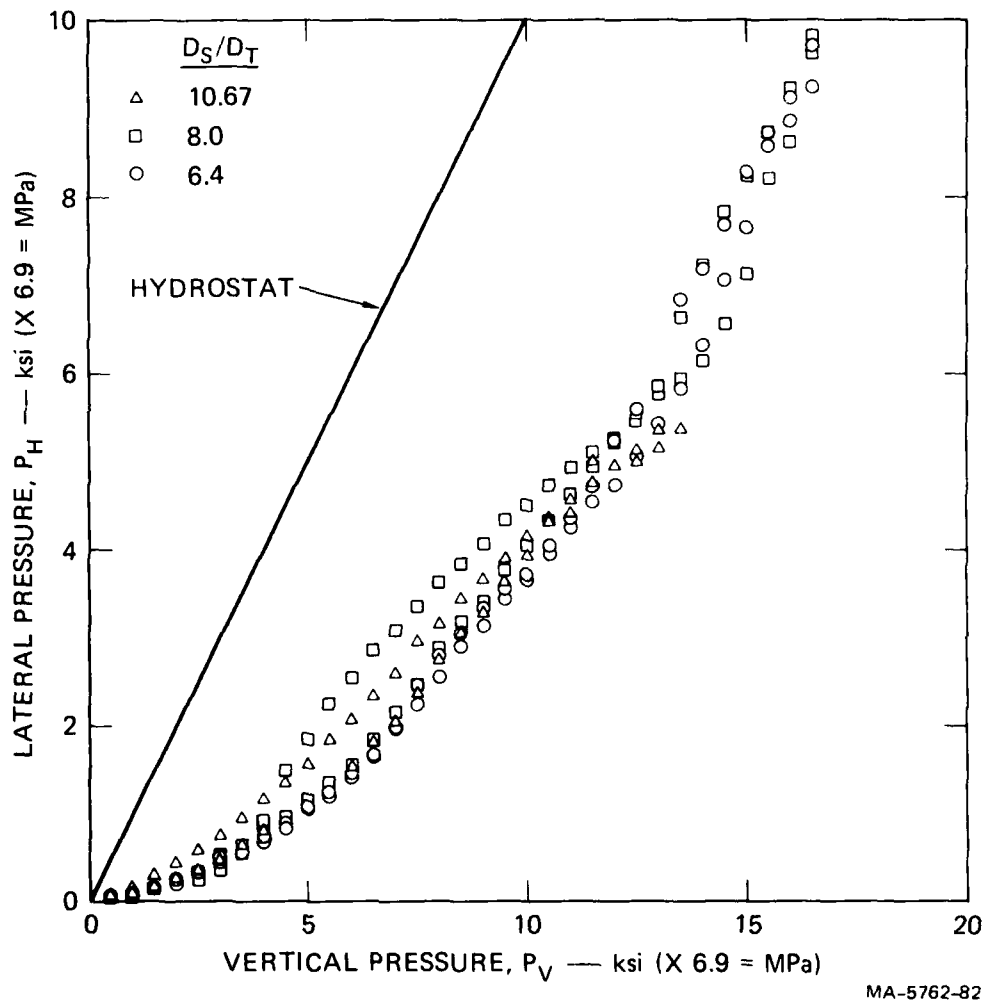
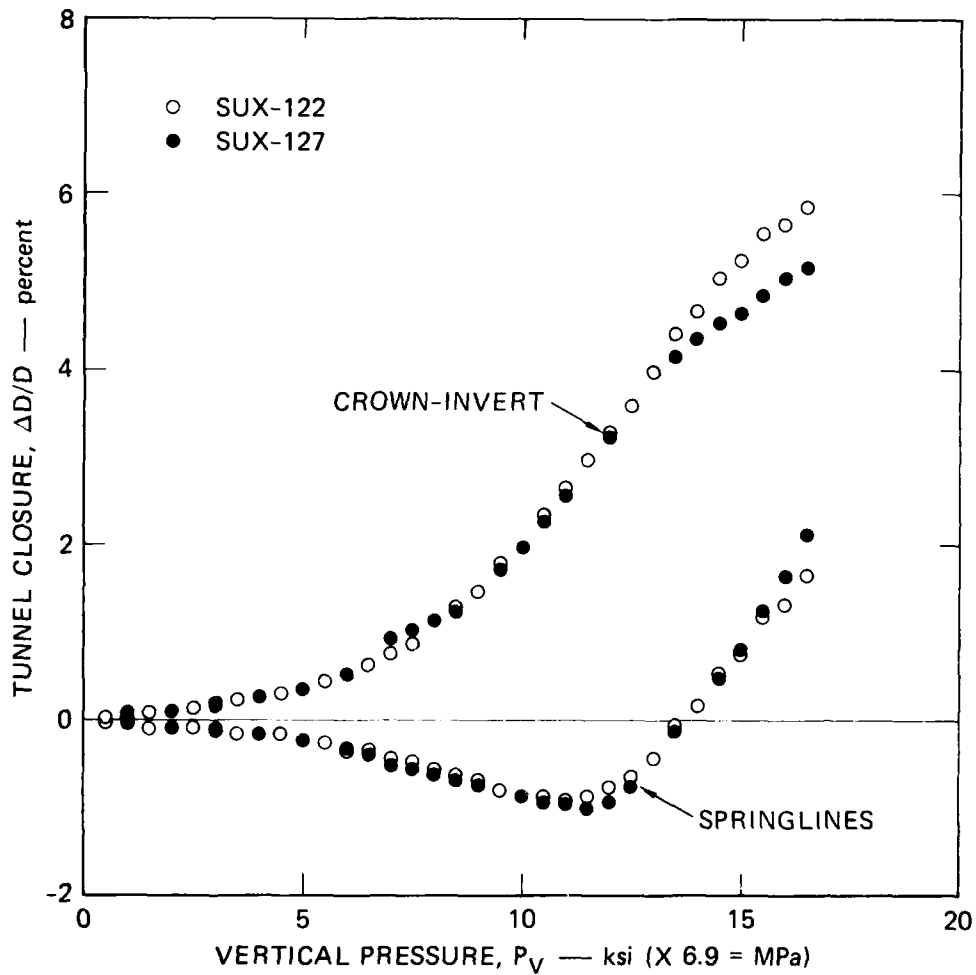


FIGURE 2.3 LATERAL PRESSURE VERSUS VERTICAL PRESSURE TO MAINTAIN UNIAXIAL STRAIN IN 16A ROCK SIMULANT



MA-5762-74

FIGURE 2.4 TUNNEL CLOSURE AT CROWN-INVERT AND SPRINGLINE DIAMETERS VERSUS VERTICAL PRESSURE FOR STATIC UNIAXIAL STRAIN LOADING OF 16A ROCK SIMULANT

Tunnel diameter = 5/8 inch (15.9 mm),  $D_S/D_T = 6.4$ , 1015 steel liner,  $a/h = 12.5$

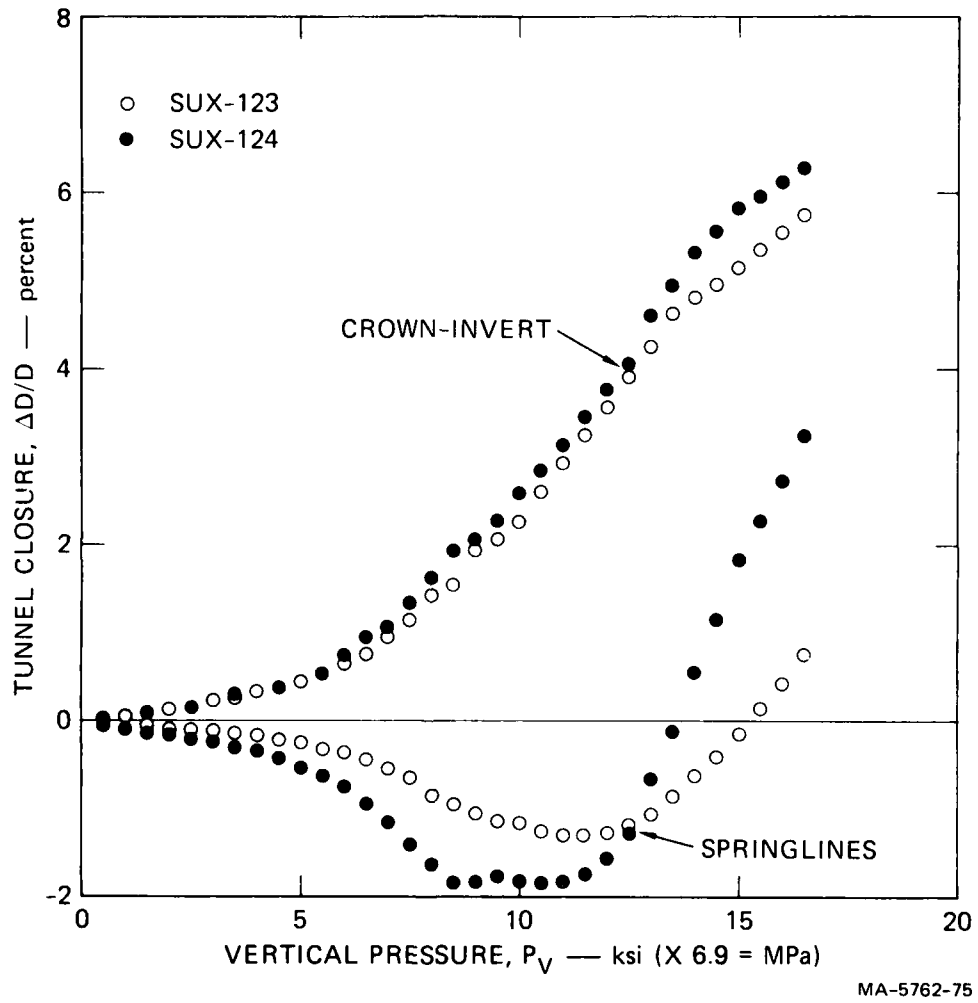


FIGURE 2.5 TUNNEL CLOSURE AT CROWN-INVERT AND SPRINGLINE DIAMETERS VERSUS VERTICAL PRESSURE FOR STATIC UNIAXIAL STRAIN LOADING OF 16A ROCK SIMULANT

Tunnel diameter = 1/2 inch (12.7 mm),  $D_S/D_T = 8.0$ , 1015 steel liner,  $a/h = 12.5$

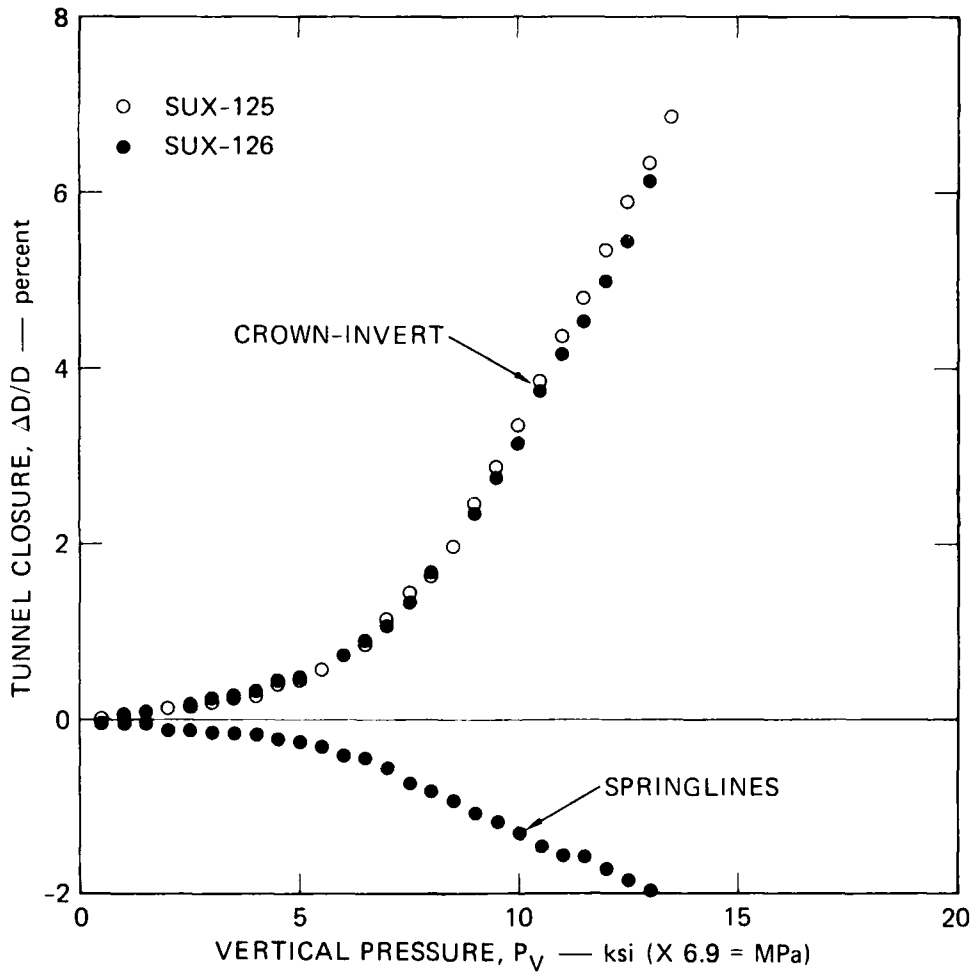
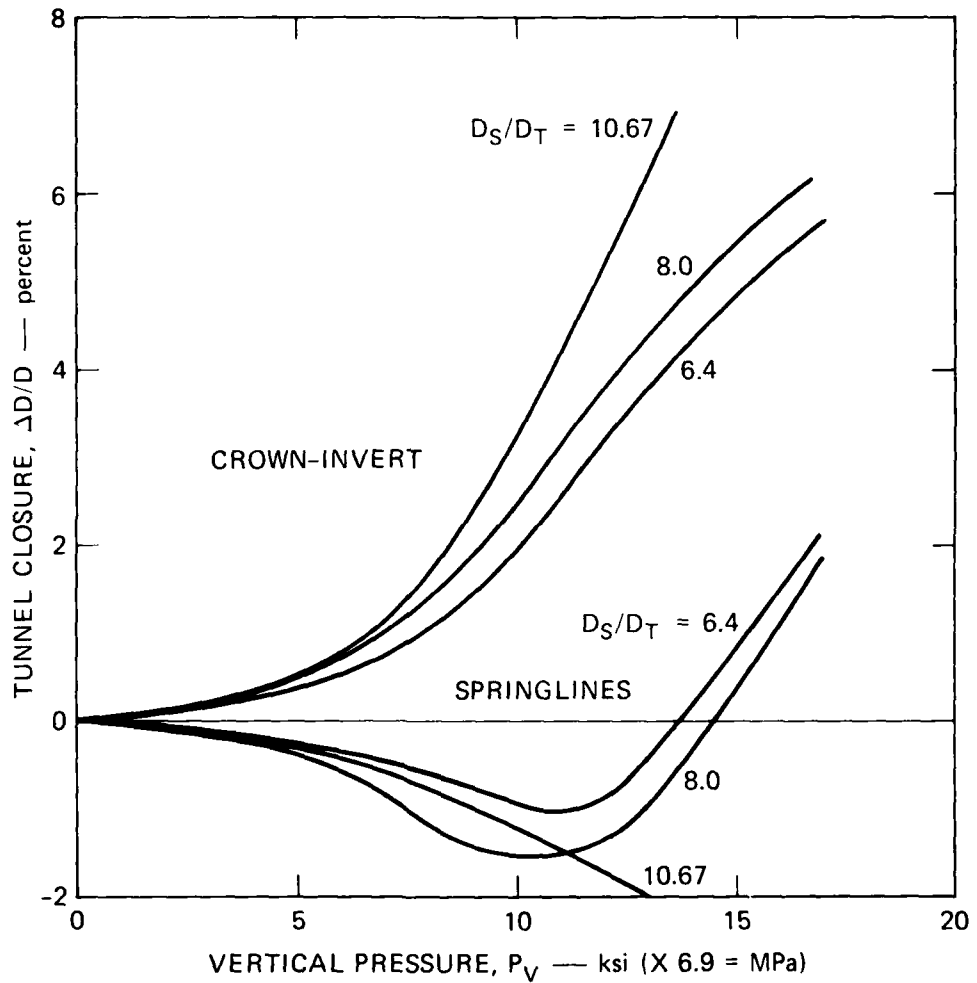


FIGURE 2.6 TUNNEL CLOSURE AT CROWN-INVERT AND SPRINGLINE DIAMETERS VERSUS VERTICAL PRESSURE FOR STATIC UNIAXIAL STRAIN LOADING OF 16A ROCK SIMULANT

Tunnel diameter = 3/8 inch (9.5 mm),  $D_S/D_T$ , 1015 steel liner,  $a/h = 12.5$



MA-5762-77

FIGURE 2.7 COMPARISON OF TUNNEL CLOSURE VERSUS VERTICAL PRESSURE FOR THREE SPECIMEN-TO-TUNNEL DIAMETER RATIOS — 16A ROCK SIMULANT

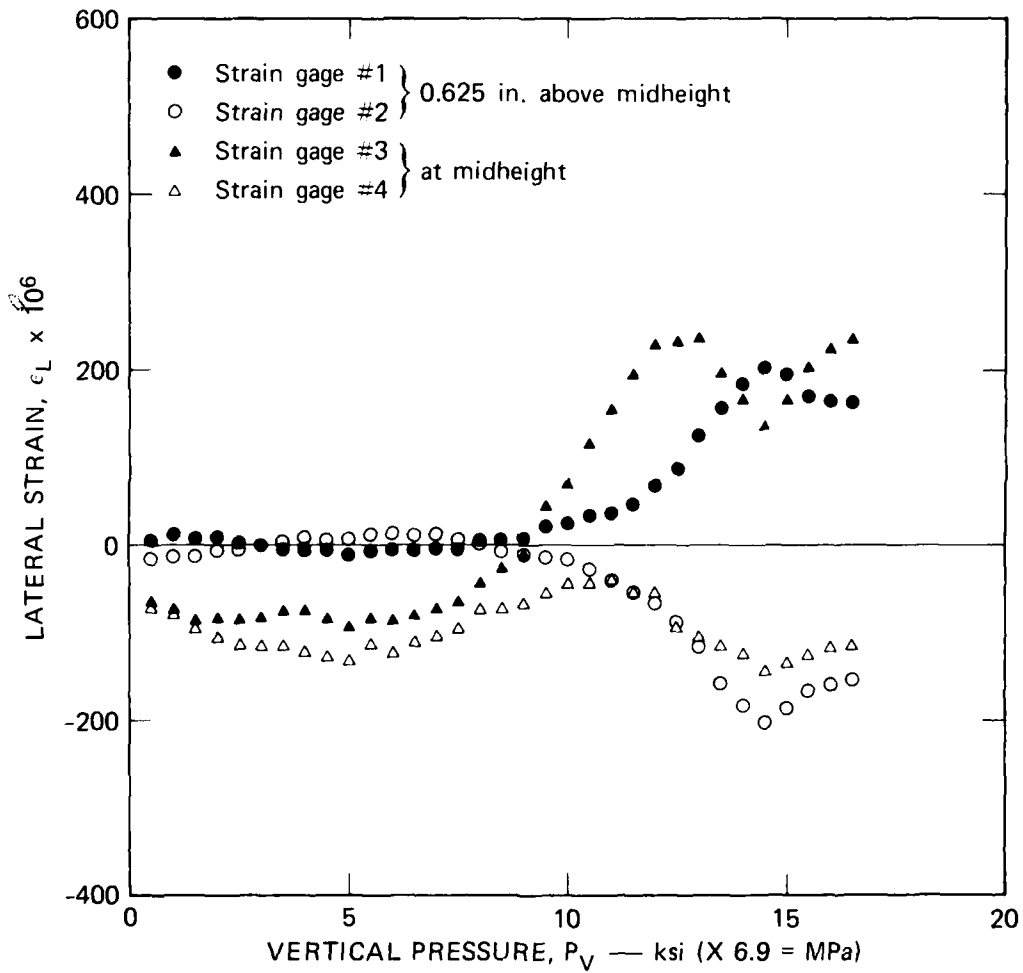


FIGURE 2.8 LATERAL STRAIN VERSUS VERTICAL PRESSURE  
 Output from all four strain gages in SUX-122, 16A rock simulant

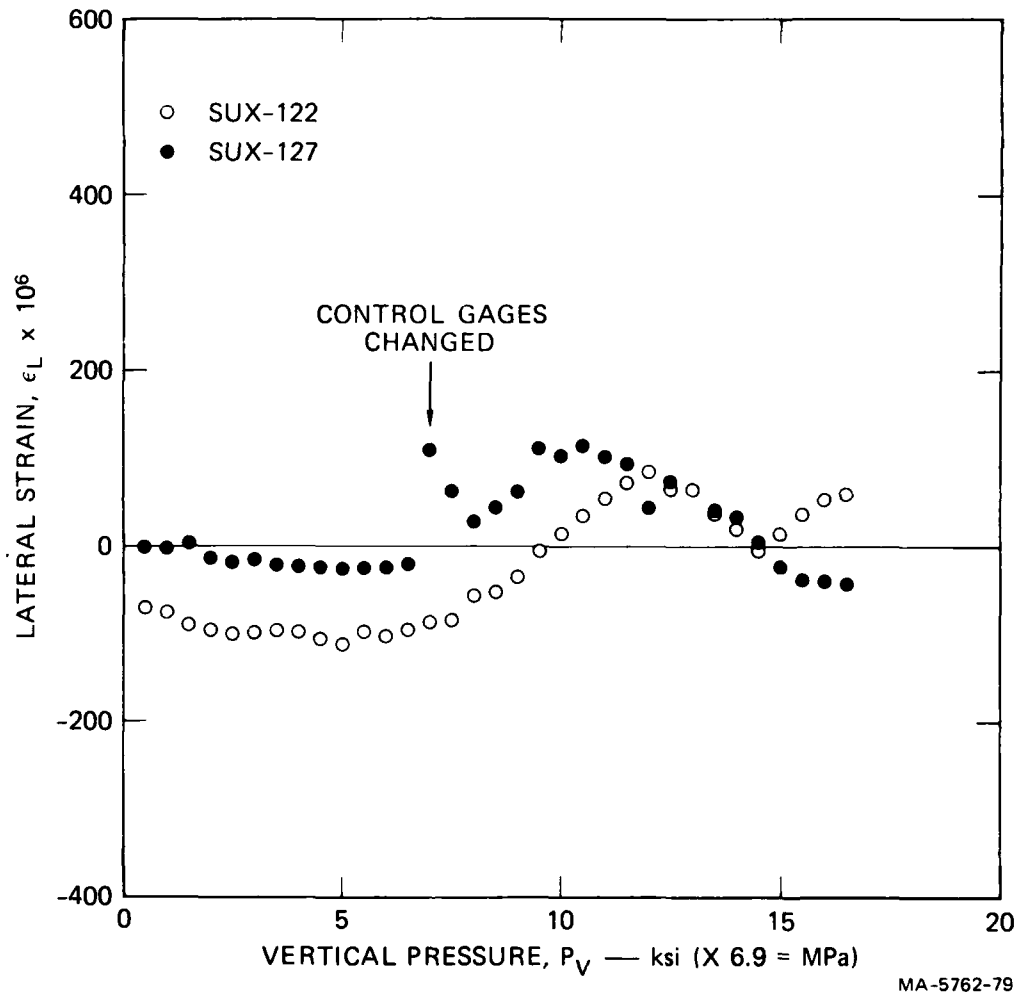
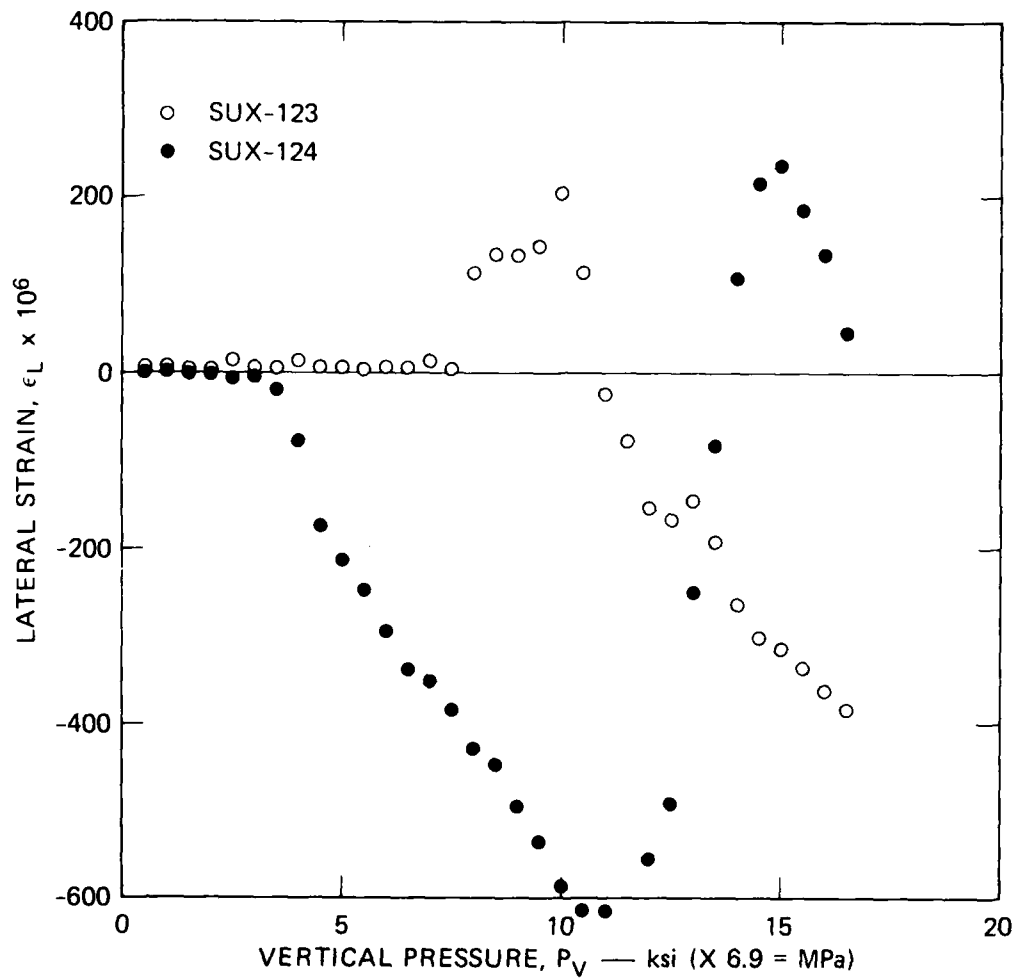


FIGURE 2.9 SPECIMEN LATERAL STRAIN AT MIDHEIGHT VERSUS VERTICAL PRESSURE

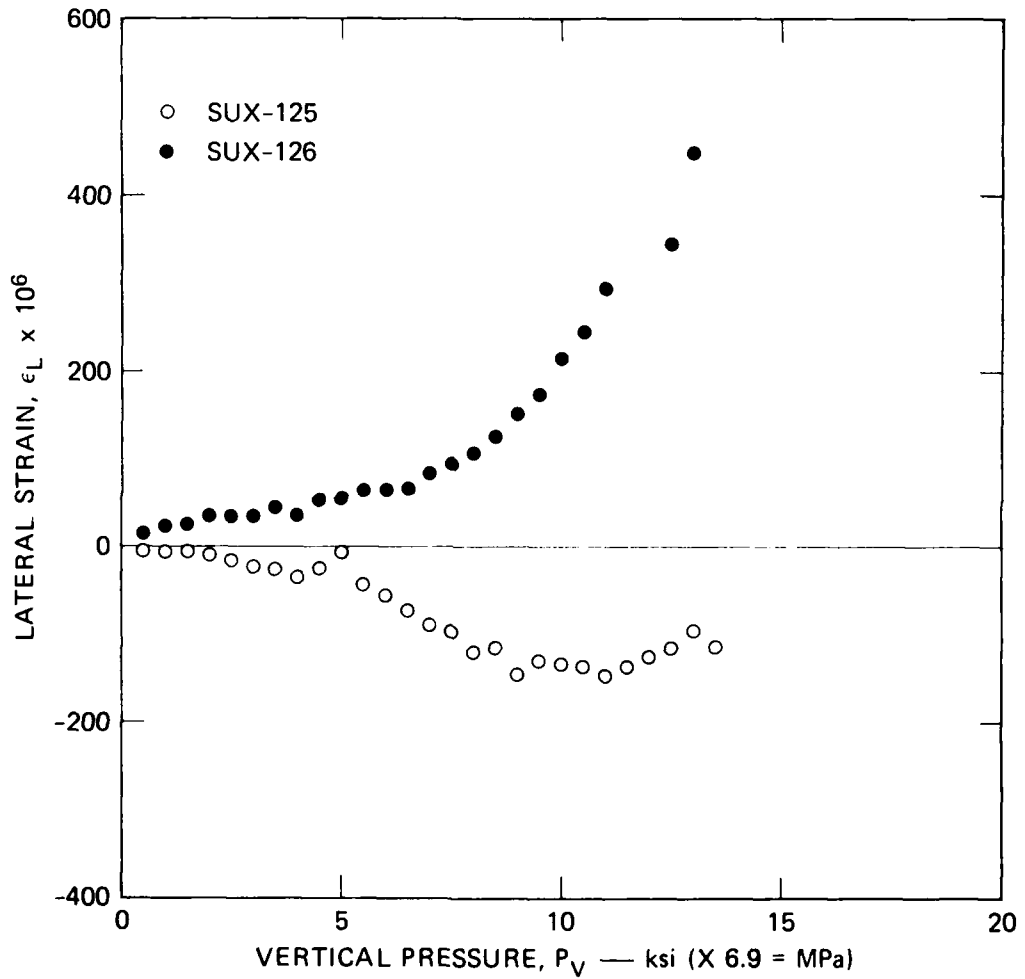
Tunnel diameter = 5/8 inch (15.9 mm),  $D_S/D_T = 6.4$ , 16A rock simulant. In SUX-127, the uniaxial strain condition was imposed at the midheight gages for pressures greater than 7 ksi (48 MPa). Lateral strain data plotted for  $P_V \geq 7$  ksi (48 MPa) are the averages of gages at 0.625 inch (15.9 mm) above midheight.



MA-5762-80

FIGURE 2.10 SPECIMEN LATERAL STRAIN AT MIDHEIGHT VERSUS VERTICAL PRESSURE

Tunnel diameter = 1/2 inch (12.7 mm),  $D_S/D_T = 8.01$ , 16A rock simulant



MA-5762-81

FIGURE 2.11 SPECIMEN LATERAL STRAIN AT MIDHEIGHT VERSUS VERTICAL PRESSURE  
Tunnel diameter = 3/8 inch (9.5 mm),  $D_S/D_T = 10.67$ , 16A rock simulant

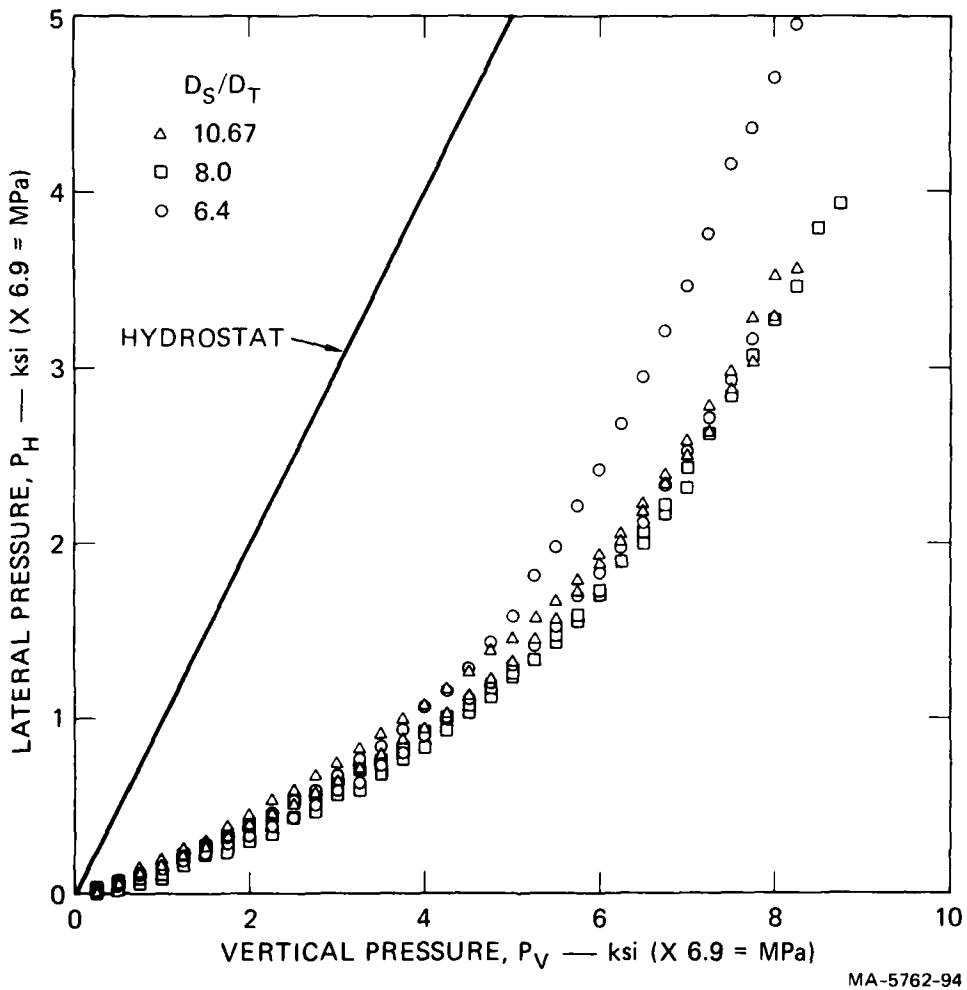


FIGURE 2.12 LATERAL PRESSURE VERSUS VERTICAL PRESSURE TO MAINTAIN UNIAXIAL STRAIN IN SRI RMG 2C2

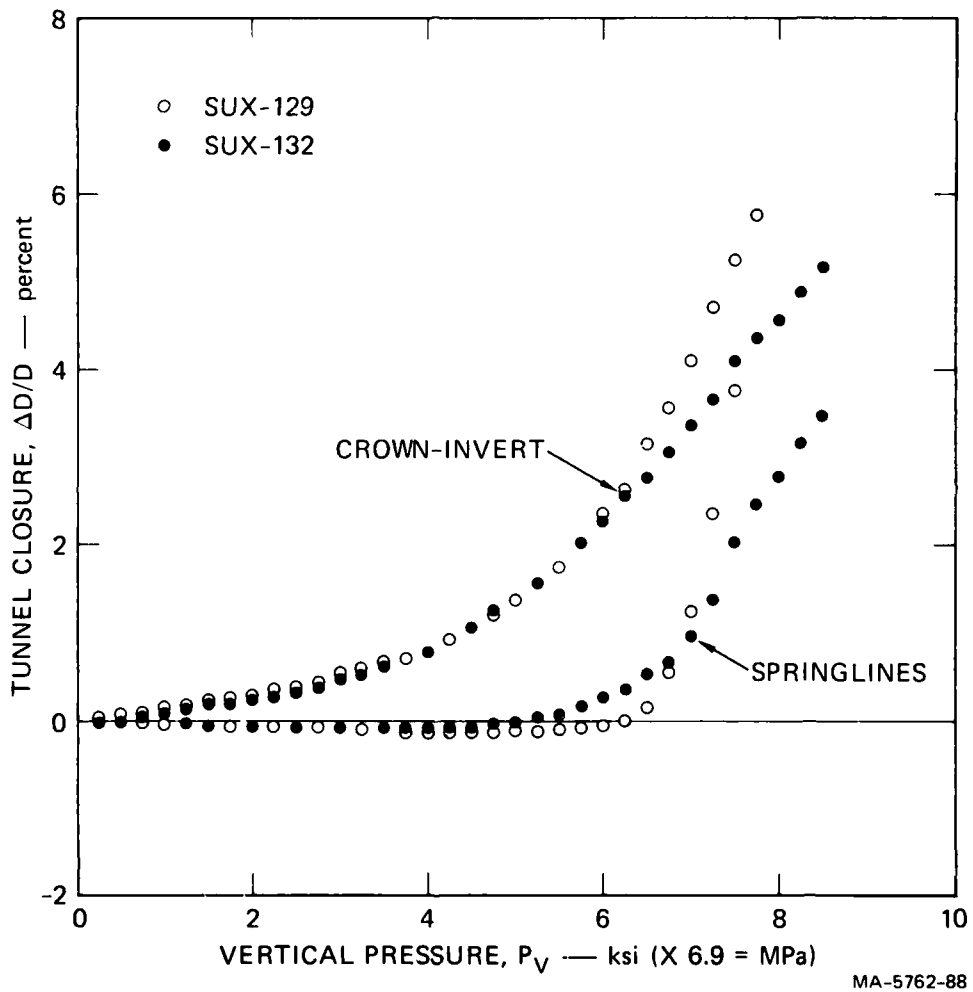


FIGURE 2.13 TUNNEL CLOSURE AT CROWN-INVERT AND SPRINGLINE DIAMETERS VERSUS VERTICAL PRESSURE FOR STATIC UNIAXIAL STRAIN LOADING OF SRI RMG 2C2

Tunnel diameter = 5/8 inch (15.9 mm),  $D_S/D_T = 6.4$ , 6061-T0 aluminum liner,  $a/h = 11.5$

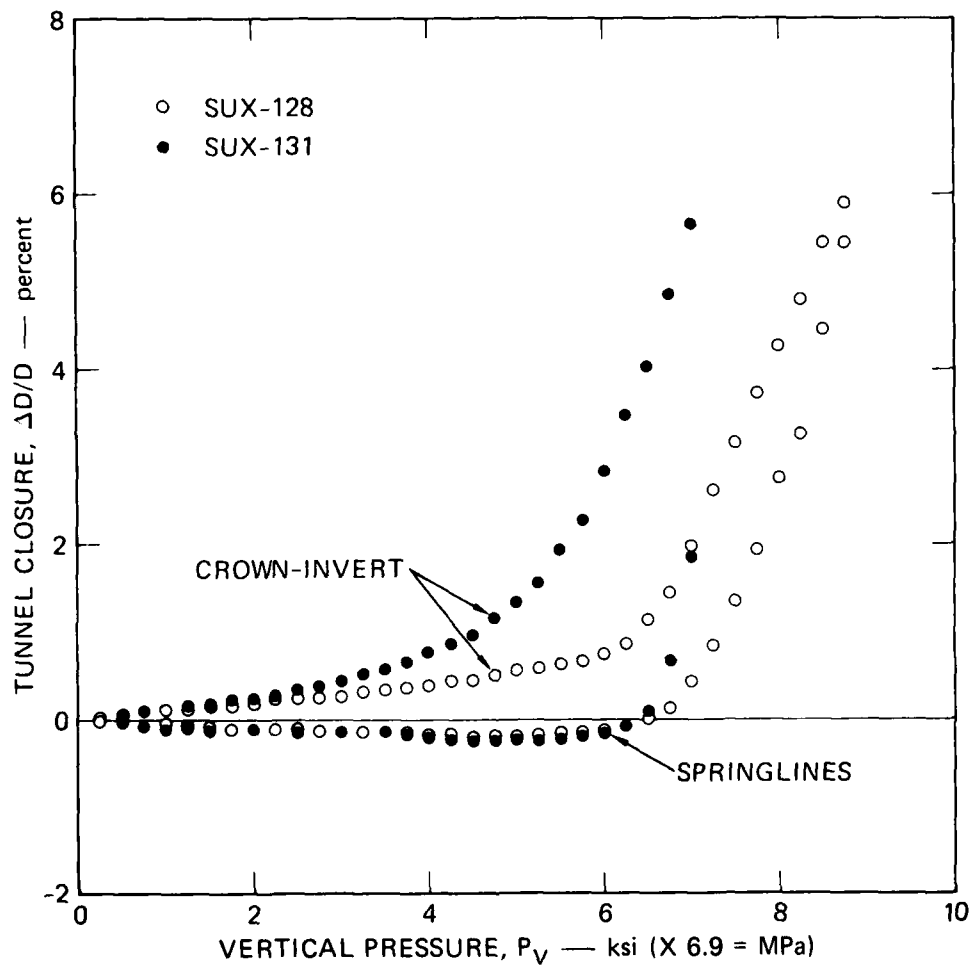
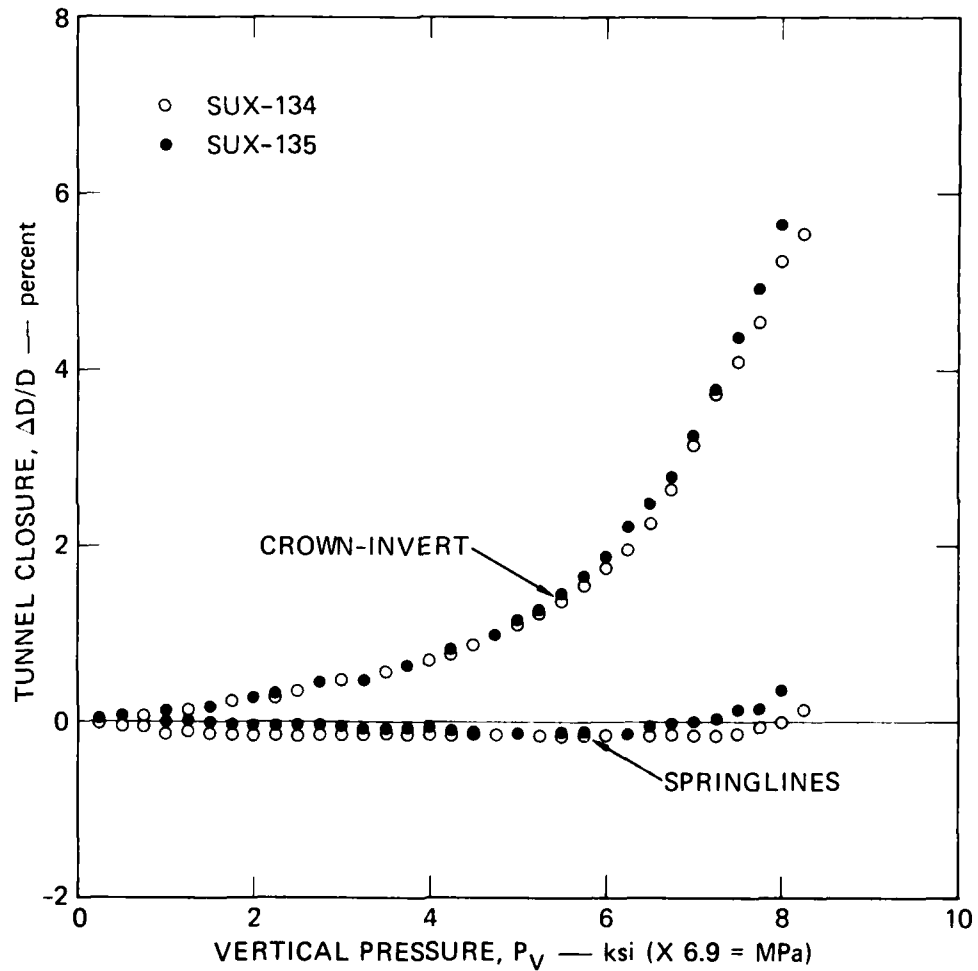


FIGURE 2.14 TUNNEL CLOSURE AT CROWN-INVERT AND SPRINGLINE DIAMETERS VERSUS VERTICAL PRESSURE FOR STATIC UNIAXIAL STRAIN LOADING OF SRI RMG 2C2

Tunnel diameter = 1/2 inch (12.7 mm),  $D_S/D_T = 8.0$ , 6061-T0 aluminum liner,  $a/h = 11.5$



MA-5762-86

FIGURE 2.15 TUNNEL CLOSURE AT CROWN-INVERT AND SPRINGLINE DIAMETERS VERSUS VERTICAL PRESSURE FOR STATIC UNIAXIAL STRAIN LOADING OF SRI RMG 2C2

Tunnel diameter = 3/8 inch (9.5 mm),  $D_S/D_T = 10.67$ , 6061-T0 aluminum liner,  $a/h = 11.5$

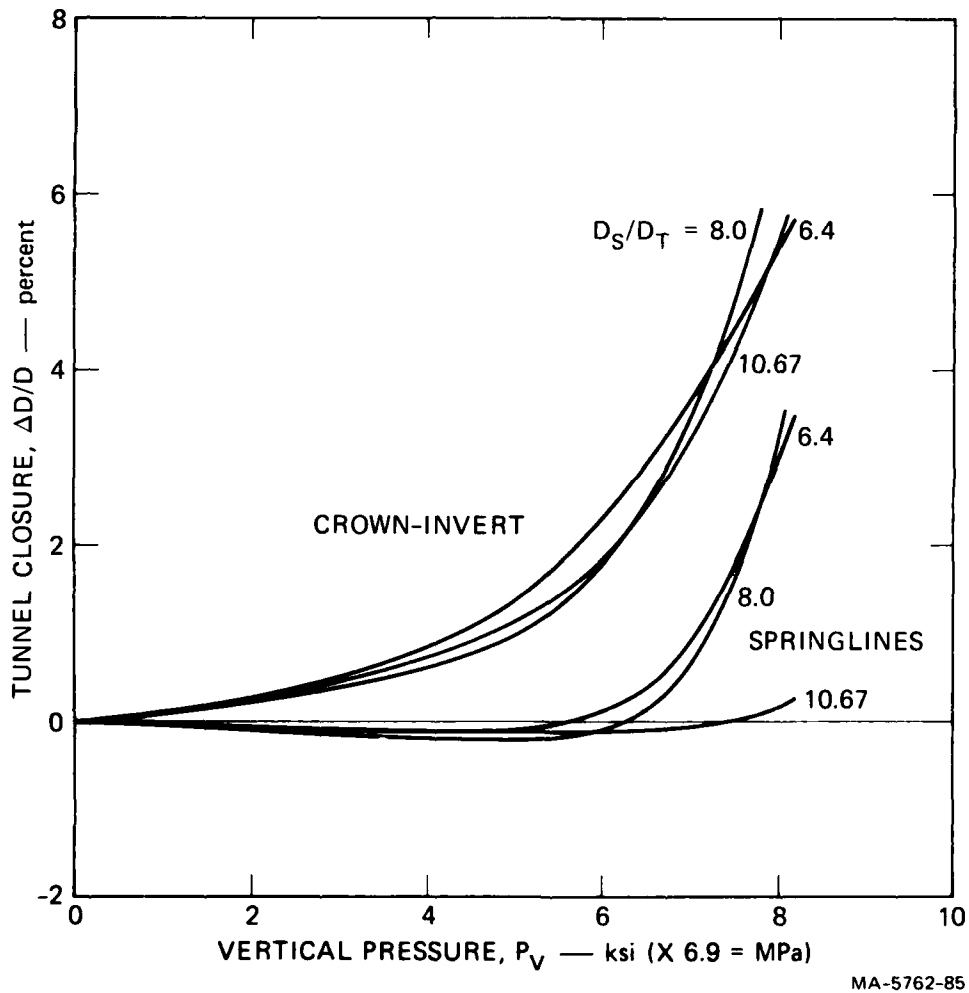


FIGURE 2.16 COMPARISON OF TUNNEL CLOSURE VERSUS VERTICAL PRESSURE FOR THREE SPECIMEN-TO-TUNNEL DIAMETER RATIOS — SRI RMG 2C2

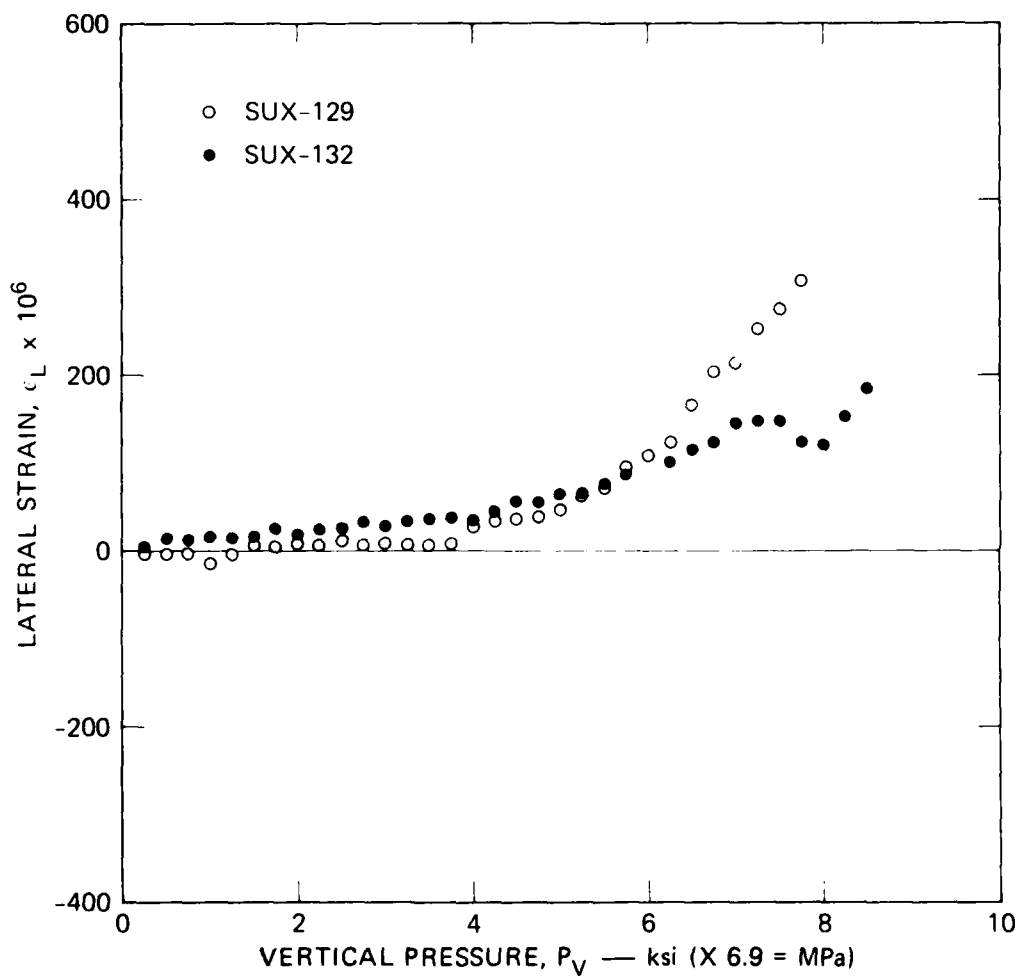


FIGURE 2.17 SPECIMEN LATERAL STRAIN AT MIDHEIGHT VERSUS VERTICAL PRESSURE  
Tunnel diameter = 5/8 inch (15.9 mm),  $D_S/D_T = 6.4$ , SRI RMG 2C2

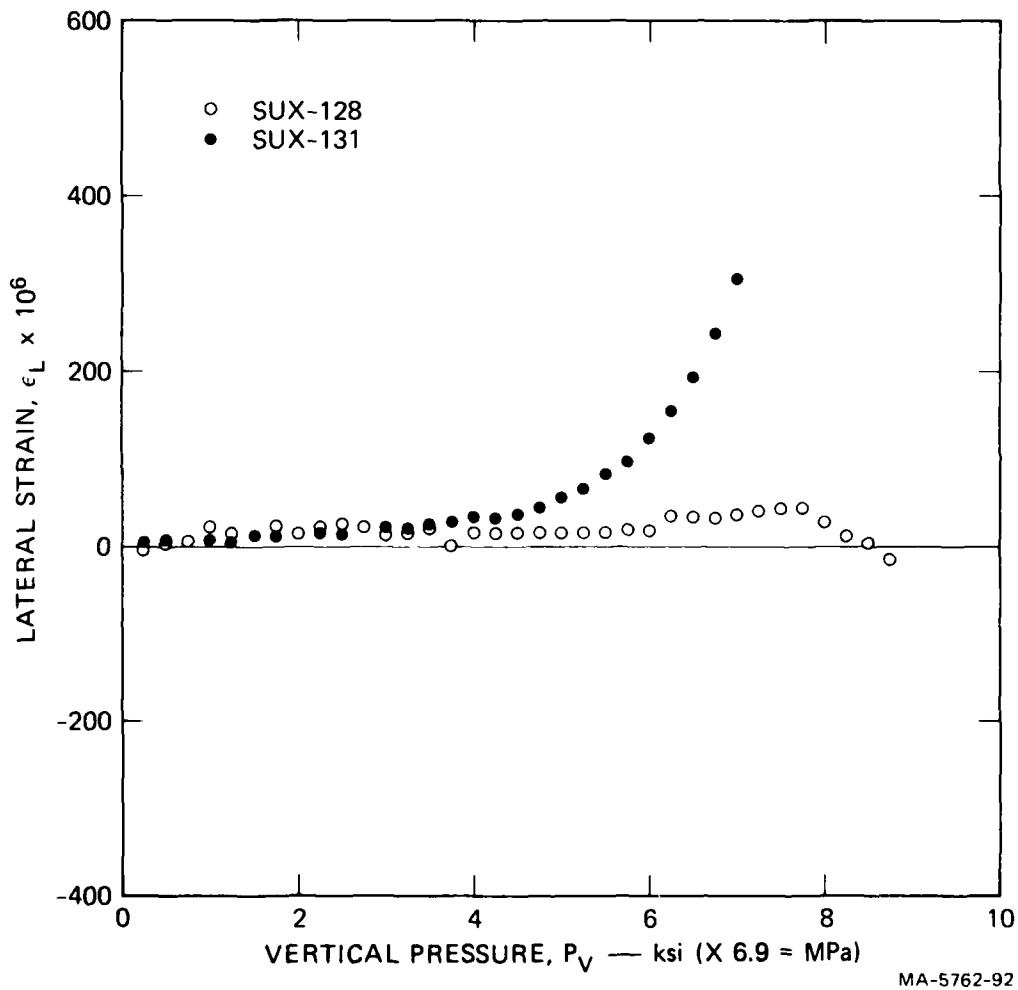


FIGURE 2.18 SPECIMEN LATERAL STRAIN AT MIDHEIGHT VERSUS VERTICAL PRESSURE  
 Tunnel diameter = 1/2 inch (12.7 mm),  $D_S/D_T = 8.0$ , SRI RMG 2C2

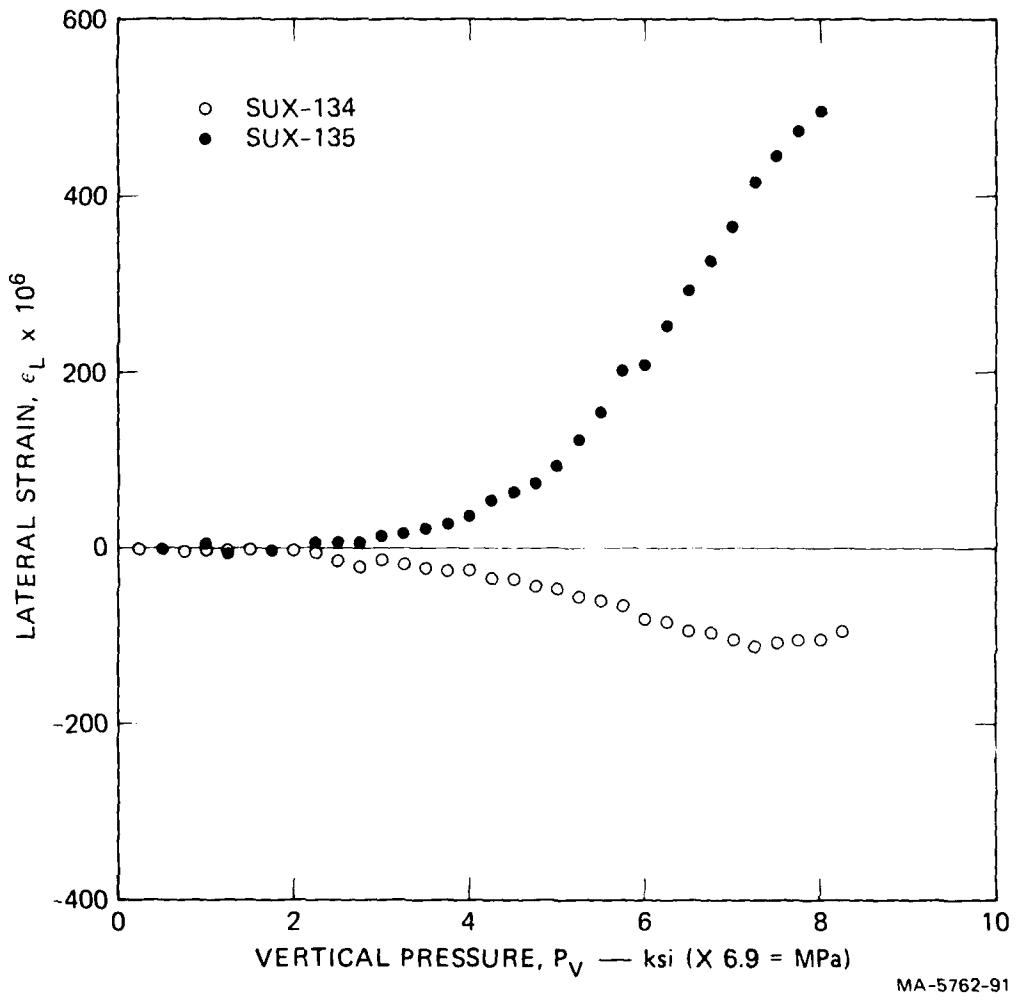
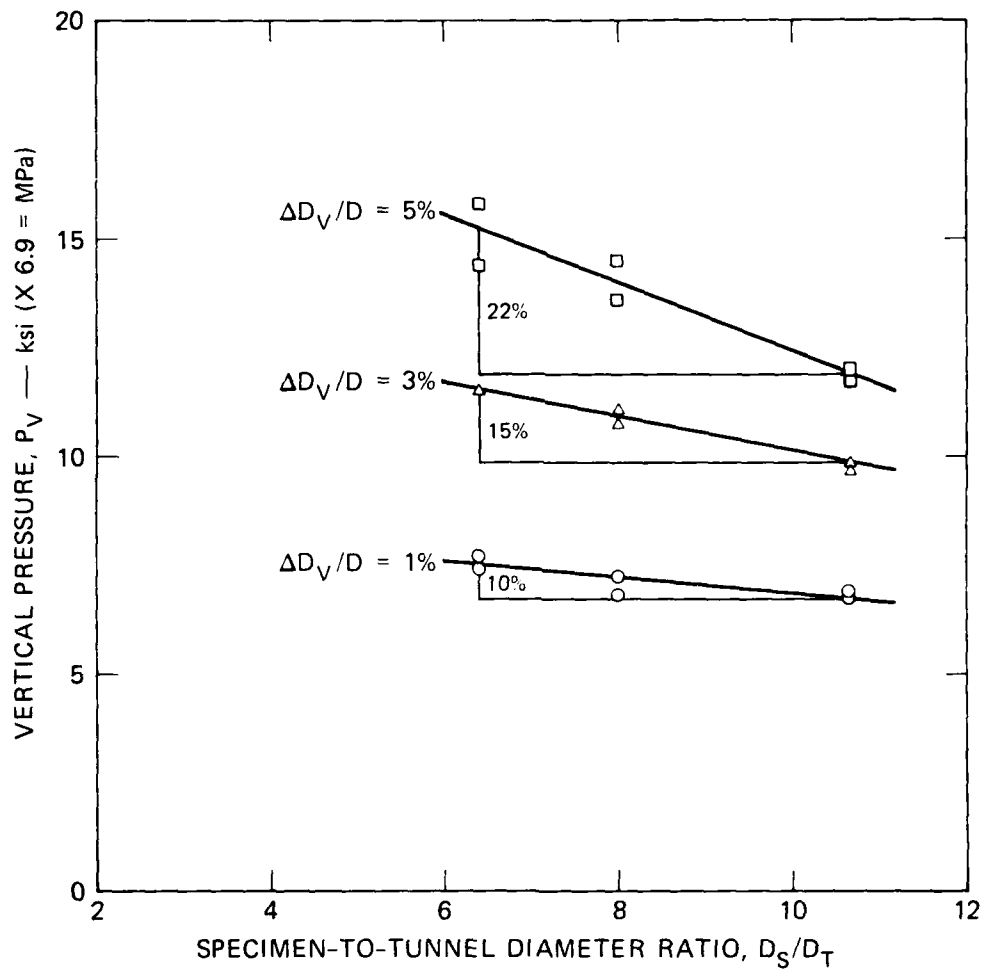
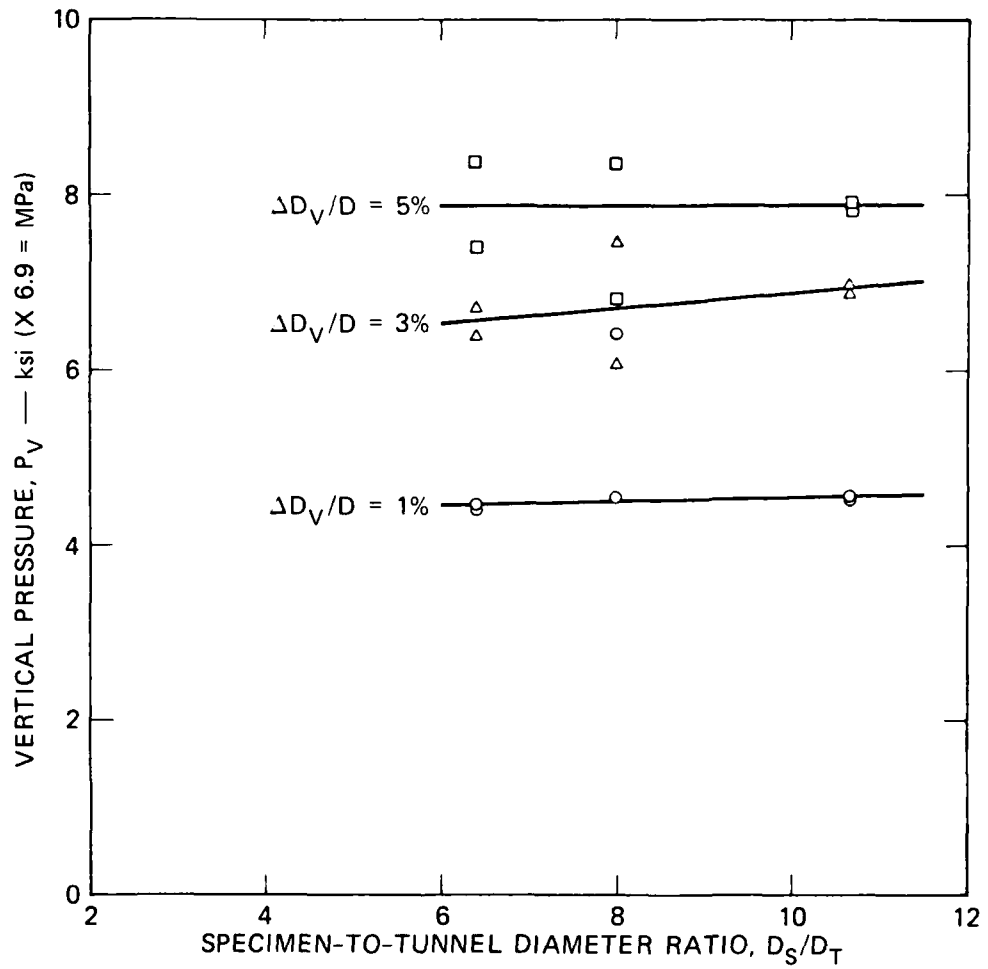


FIGURE 2.19 SPECIMEN LATERAL STRAIN AT MIDHEIGHT VERSUS VERTICAL PRESSURE  
 Tunnel diameter = 3/8 inch (9.5 mm),  $D_S/D_T = 10.67$ , SRI RMG 2C2



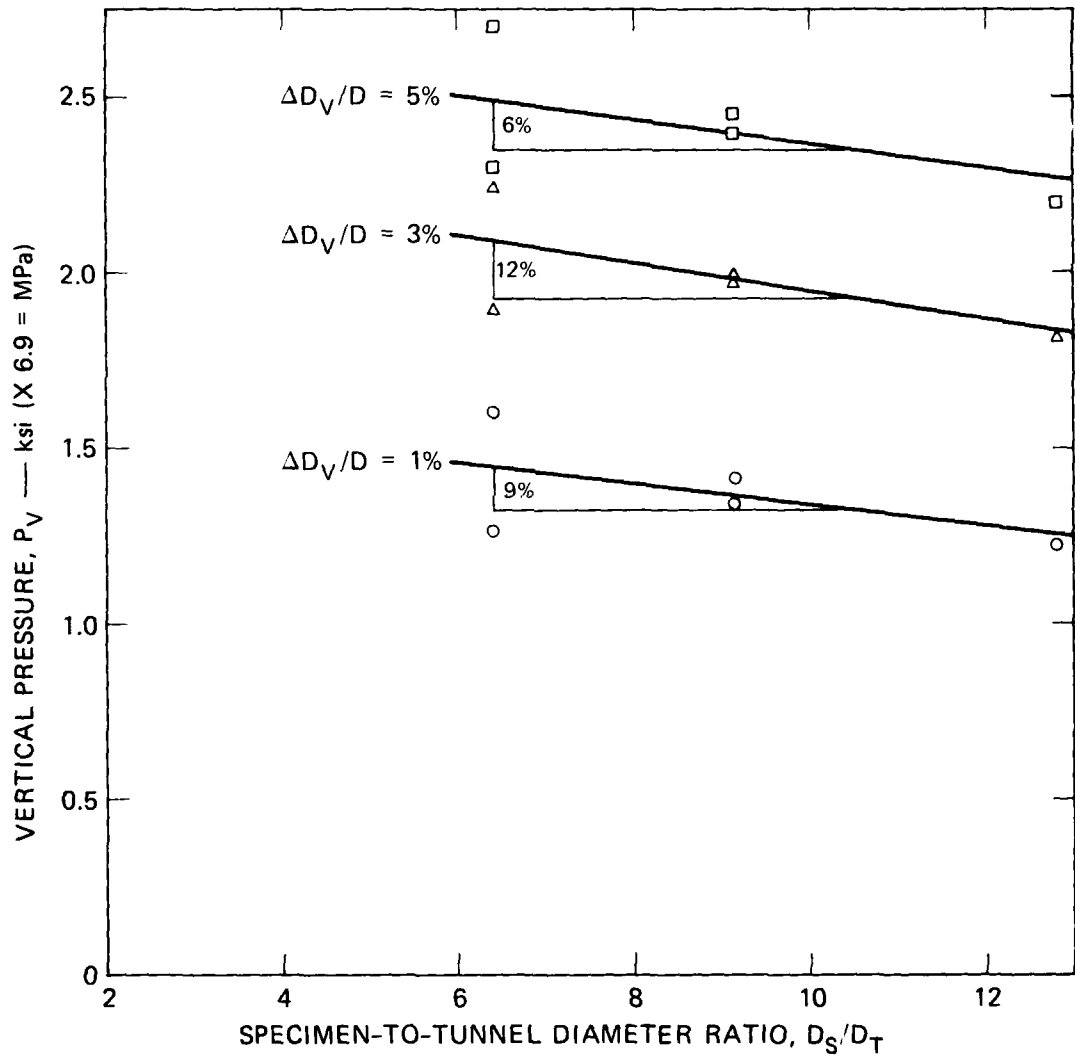
MA-5762-78A

FIGURE 2.20 VERTICAL PRESSURE TO PRODUCE SPECIFIED CROWN-INVERT TUNNEL CLOSURE VERSUS SPECIMEN-TO-TUNNEL DIAMETER RATIO — 16A ROCK SIMULANT



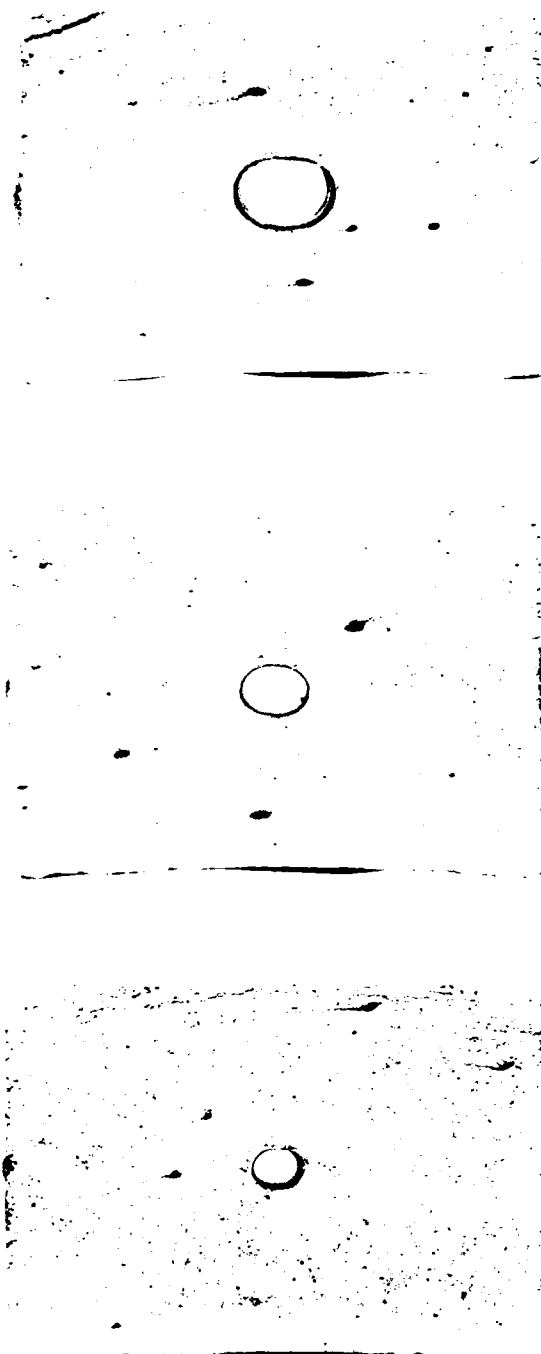
MA-5762-89

FIGURE 2.21 VERTICAL PRESSURE TO PRODUCE SPECIFIED CROWN-INVERT TUNNEL CLOSURE VERSUS SPECIMEN-TO-TUNNEL DIAMETER RATIO — 2C2

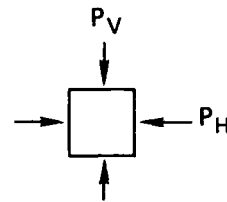


MA-5762-90

FIGURE 2.22 VERTICAL PRESSURE TO PRODUCE SPECIFIED CROWN-INVERT TUNNEL CLOSURE VERSUS SPECIMEN-TO-TUNNEL DIAMETER RATIO  
HUSKY ACE rock-matching grout



- (a)  $D = 5/8''$  (15.9 mm) (SUX-45)  
 $P_{VMAX} = 4250$  psi (29.3 MPa)  
 $P_{HMAX} = 1880$  psi (13.0 MPa)  
 $\Delta D_V/D = 21\%$   
 $\Delta D_H/D = -14\%$



- (b)  $D = 7/16''$  (11.1 mm) (SUX-46)  
 $P_{VMAX} = 4000$  psi (27.6 MPa)  
 $P_{HMAX} = 1690$  psi (11.7 MPa)  
 $\Delta D_V/D = 21\%$   
 $\Delta D_H/D = -12\%$

- (c)  $D = 5/16''$  (7.9 mm) (SUX-4z)  
 $P_{VMAX} = 3500$  psi (24.1 MPa)  
 $P_{HMAX} = 1420$  psi (9.8 MPa)  
 $\Delta D_V/D = 16\%$   
 $\Delta D_H/D = -12\%$

MP-3743-88

FIGURE 2.23 POSTTEST CROSS SECTIONS SHOWING DISTRIBUTION OF PORES IN HUSKY ACE ROCK-MATCHING GROUT

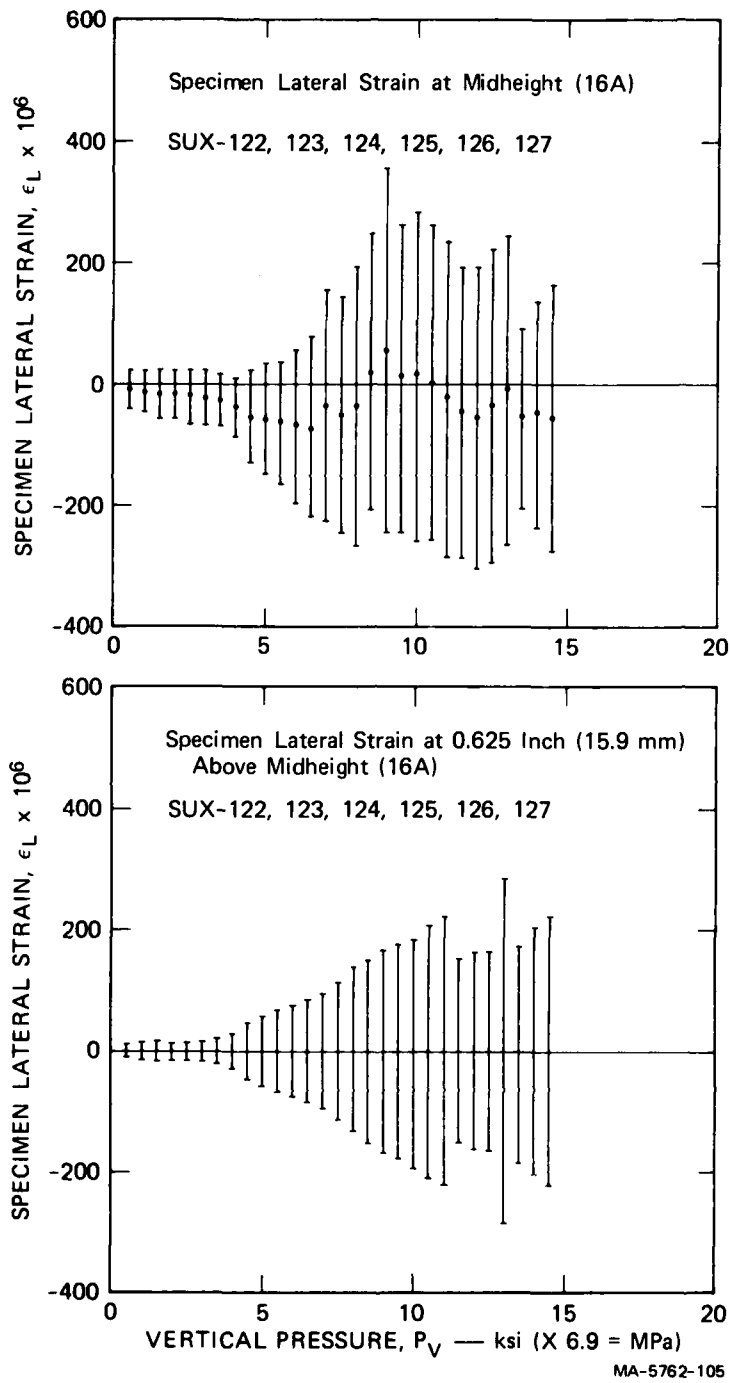


FIGURE 2.24 MEAN AND STANDARD DEVIATION OF SPECIMEN LATERAL STRAIN IN 16A ROCK SIMULANT AT MIDHEIGHT AND 0.625 INCH (15.9 mm) ABOVE MIDHEIGHT

Six tests, two gages at midheight and two gages above midheight per test

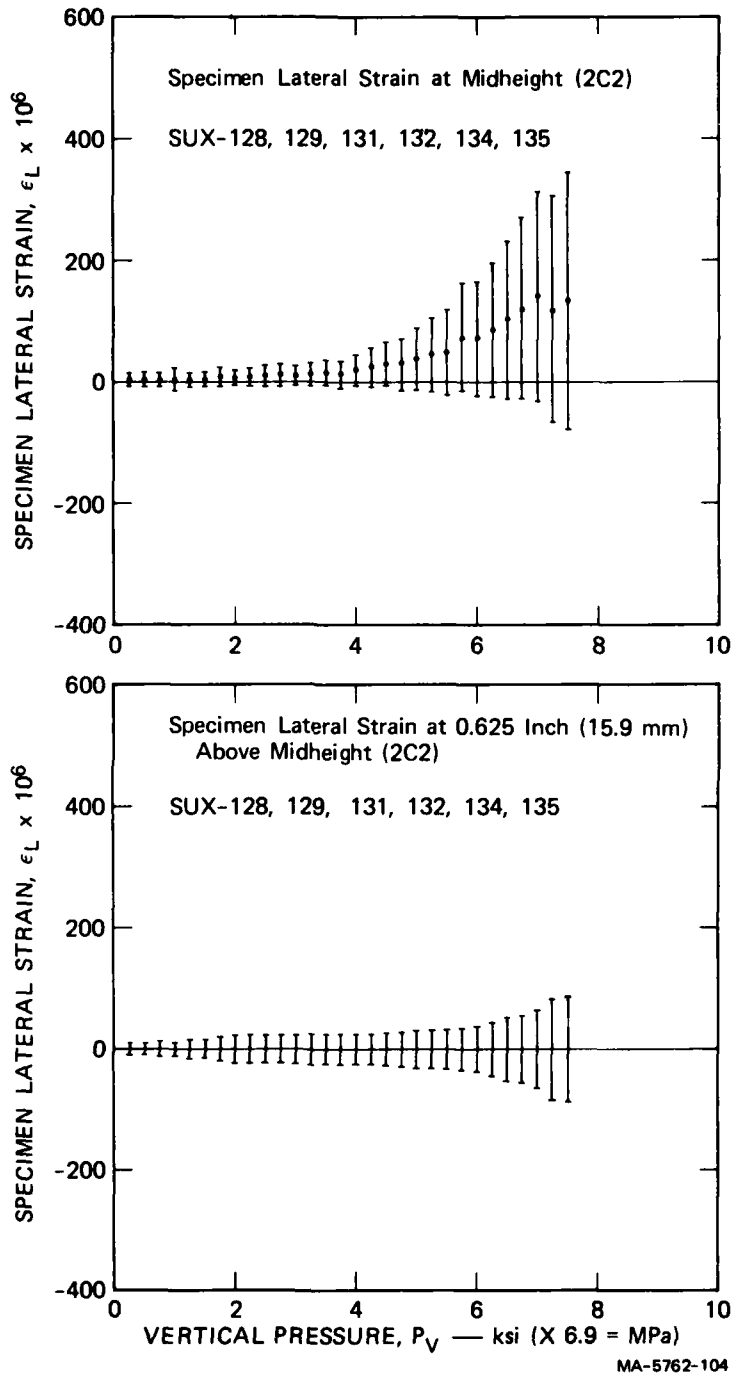


FIGURE 2.25 MEAN AND STANDARD DEVIATION OF SPECIMEN LATERAL STRAIN IN SRI RMG 2C2 AT MIDHEIGHT AND 0.625 INCH (15.9 mm) ABOVE MIDHEIGHT

Six tests, two gages at midheight and two gages above midheight per test

### 2.3 EFFECT OF LATERAL CONFINEMENT

In this section we present results of six tests performed on 4-inch-diameter (0.1-m) specimens of SRI RMG 2C2 that study the influence of lateral confinement on tunnel closure and specimen lateral strain. Three specimens were fully water-saturated and three were dry. They all contained 5/8-inch-diameter (15.9 mm) tunnels ( $D_S/D_T = 6.4$ ), which were reinforced by 6061-T0 aluminum monocoque cylinders having  $a/h = 11.5$ . We present test results for saturated specimens first.

Figure 2.26 shows the uniaxial strain load path and three other load paths that deviate from the uniaxial strain load path by fixed percentages. Along the uniaxial strain load path, the lateral pressure  $P_H$  equals  $P_H^{UX}$ , the lateral pressure required to maintain uniaxial strain as shown in Figure 2.12 (excepting the single load path that is higher than the other five). To study the influence of confinement, we followed three different load paths that deviated from uniaxial strain. Along one path the specimen was overconfined with  $P_H = 1.2 P_H^{UX}$ . Along the other two paths the specimen was underconfined with  $P_H = 0.9 P_H^{UX}$  and  $P_H = 0.8 P_H^{UX}$ .

In Figure 2.27, tunnel closure at the crown-invert and springlines is plotted as a function of vertical pressure for the three load paths. For comparison, lines fitted through the uniaxial strain closure data plotted in Figure 2.13 are also drawn. For all three tests, both the crown-invert and springline closures lie initially on the uniaxial strain closure curve. In the overconfined tests ( $P_H = 1.2 P_H^{UX}$ , test SUX-133), the closures lie below the uniaxial strain closure curves. In the first underconfined test ( $P_H = 0.9 P_H^{UX}$ , test SUX-141), the closures are nearly the same as the uniaxial strain closures throughout the entire test. In the second underconfined test ( $P_H = 0.8 P_H^{UX}$ , SUX-140), the crown-invert closure data lie above the uniaxial strain crown-invert closure curve. Springline closure in this test is slightly more negative at first, but then becomes considerably more positive than the uniaxial strain springline closure.

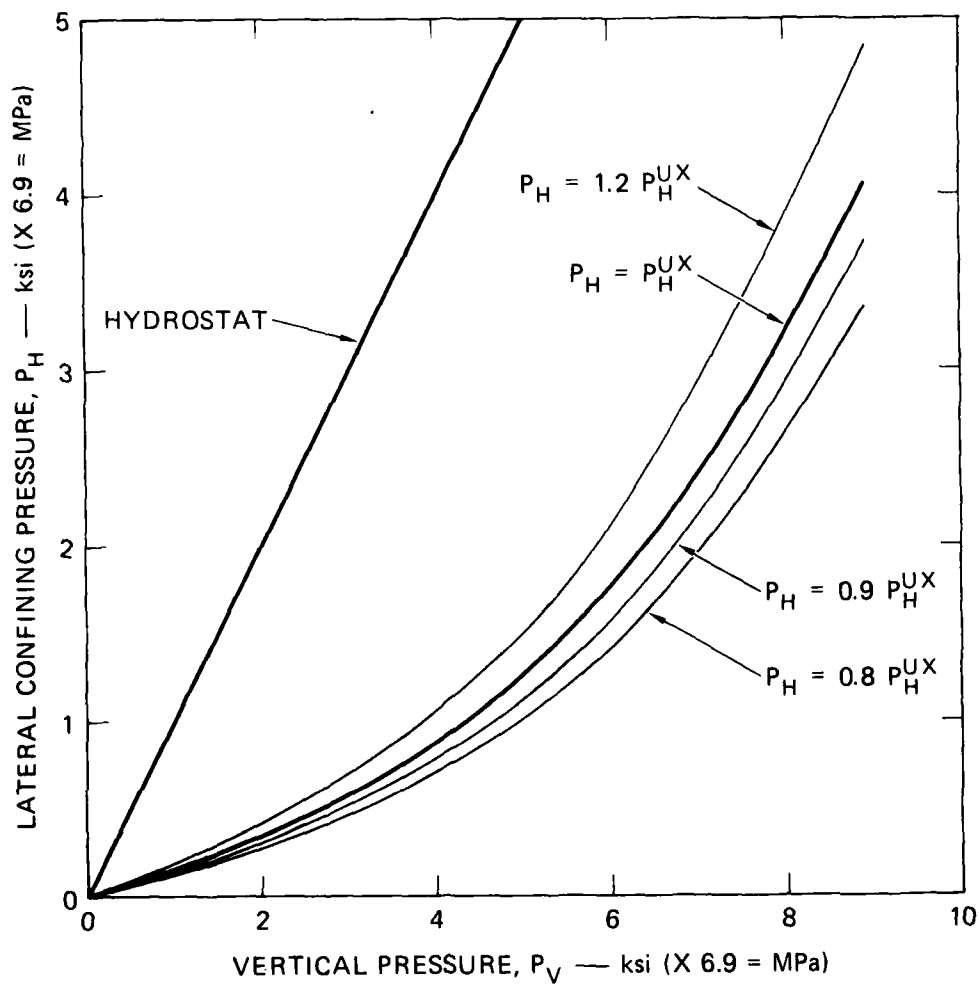


FIGURE 2.26 LOAD PATHS USED TO STUDY EFFECT OF CONFINING PRESSURE ON TUNNEL CLOSURE IN SATURATED SRI RMG 2C2

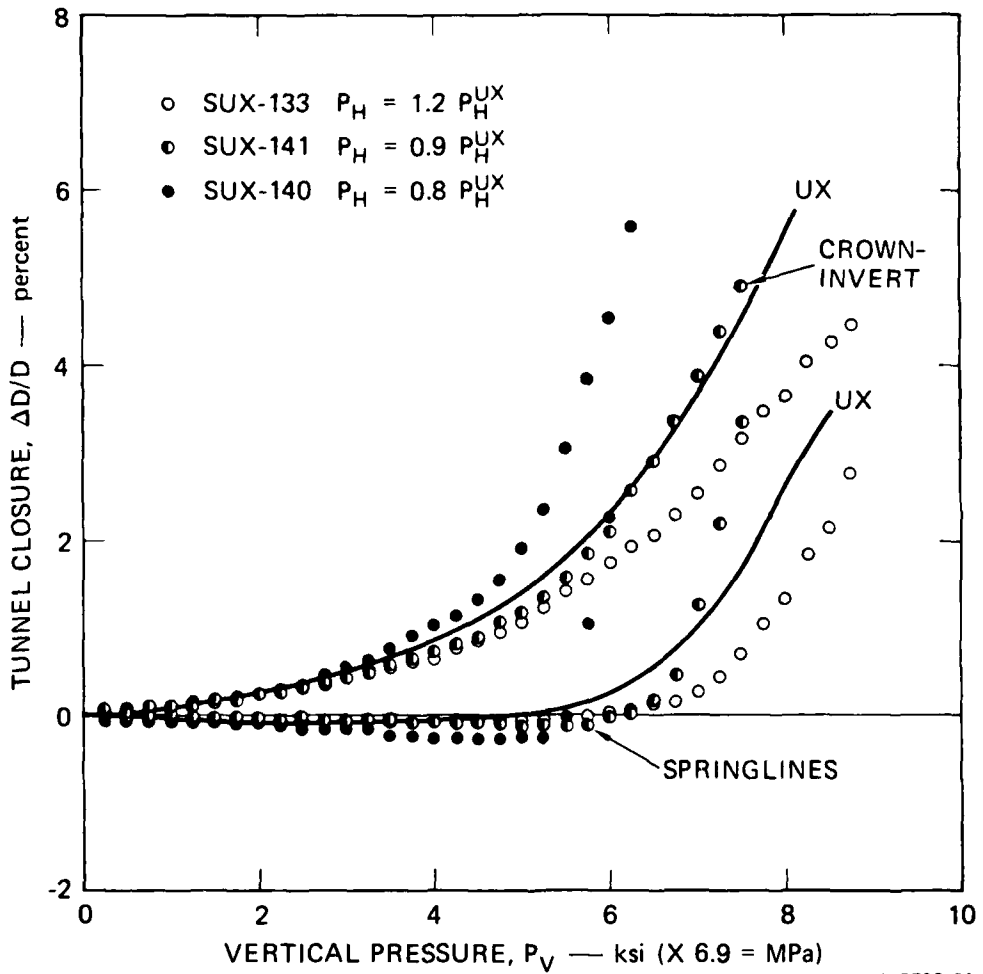


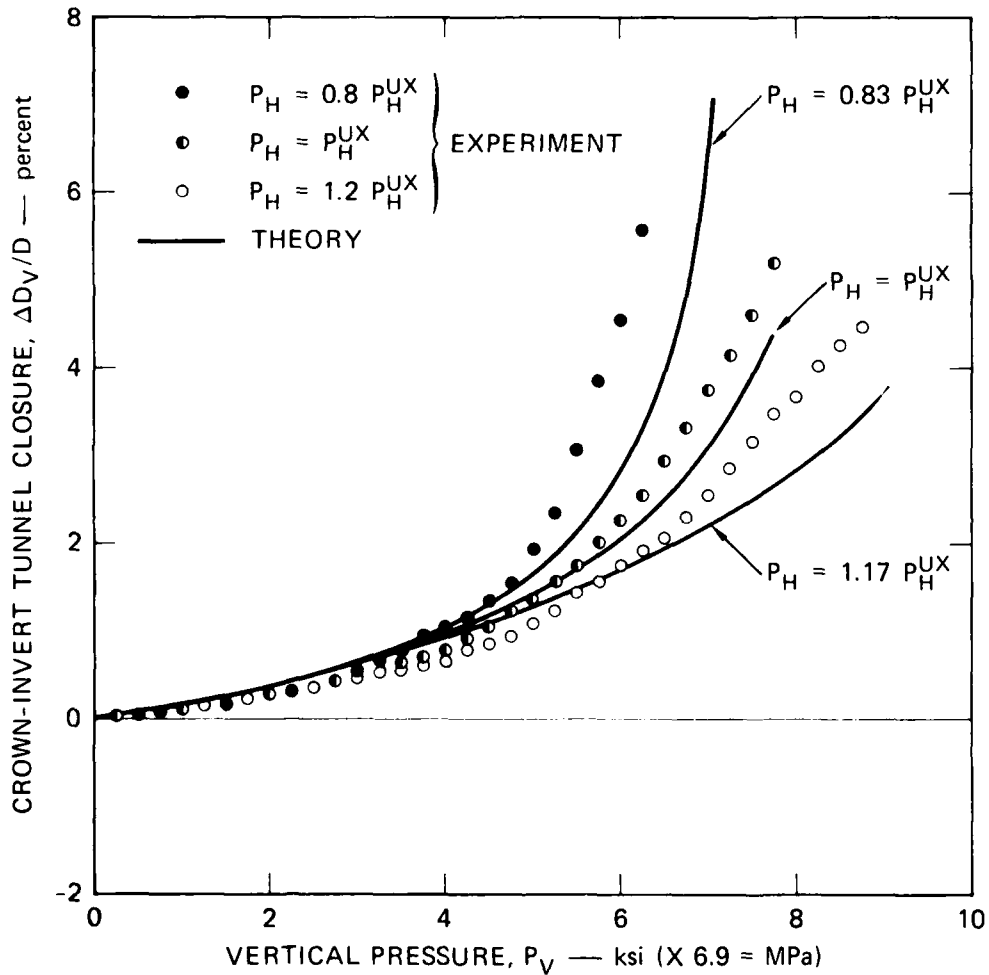
FIGURE 2.27 TUNNEL CLOSURE AT CROWN-INVERT AND SPRINGLINE DIAMETERS VERSUS VERTICAL PRESSURE FOR OVERCONFINED, UNDERCONFINED AND UNIAXIAL STRAIN LOADING OF SRI RMG 2C2  
 6061-T0 aluminum liner,  $a/h = 11.5$

The crown-invert closures clearly show the expected trend: data from overconfined tests give lower bounds on closure for uniaxial strain, while data from underconfined tests give upper bounds on closure for uniaxial strain tests. These data also show that for crown-invert closures up to about 5%, a 20% deviation from the lateral pressure required to maintain uniaxial strain gives an error of less than 20% in the vertical pressure needed to produce a specified crown-invert closure.

Springline closures in the most underconfined test are always more extreme than the uniaxial strain springline closures: if springline closure is negative, the underconfined closure is more negative than the uniaxial; if closure is positive, the underconfined closure is more positive than the uniaxial. In the overconfined test, the springline closure is less than that in a uniaxial strain test. However, with more severe overconfinement, say, isotropic loading, the springline closure will be greater than that in a uniaxial strain test. Therefore, it is difficult to infer uniaxial strain springline closures from the results of tests in which the specimen is overconfined.

Tunnel closure data from test SUX-140 in Figure 2.27 show a trend observed in underconfined dynamic tests: at the end of the test, both crown-invert and springline closures are increasing rapidly, but the rate of closure at the springlines is greater. This indicates that at higher loading (and larger closures) the springline closure would be larger than the crown-invert closure. In underconfined dynamic tests that result in complete tunnel closure, the tunnel closes along the springline diameter and not along the crown-invert diameter, as might be expected.

Figure 2.28 compares experimental and theoretical (CRT calculations) crown-invert tunnel closures for overconfined, underconfined, and uniaxial strain loading. In the overconfined experiment the lateral confining pressure,  $P_H$ , was 20% greater than the lateral pressure  $P_H^{UX}$  (i.e.,  $P_H = 1.2 P_H^{UX}$ ). In the underconfined test,  $P_H$  was 20% less than  $P_H^{UX}$  (i.e.,  $P_H = 0.8 P_H^{UX}$ ). The numerical data are from calculations in



MA-5762-103

FIGURE 2.28 COMPARISON OF EXPERIMENTAL AND THEORETICAL CROWN-INVERT TUNNEL CLOSURE IN SRI RMG 2C2 FOR UNDERCONFINED, OVERCONFINED AND UNIAXIAL STRAIN LOADING

6061-T0 aluminum liner,  $a/h = 11.5$ .  $P_H^{UX}$  is the lateral pressure required to maintain uniaxial strain.

which the corresponding lateral pressure changes were 17%:  $P_H = 1.17 P_H^{UX}$  and  $P_H = 0.83 P_H^{UX}$ . The numerical predictions agree quite well with the experimental trend of closure variation with confinement condition. The calculations differ from the experimental data only in that they consistently predict slightly greater pressure required to provide given closures than those observed in the experiments. These theoretical results were obtained before CRT saw the experimental results and show remarkable ability to predict the effect of changing confinement, an important parameter in analyzing a range of deep-base loading threats.

In Figure 2.29, specimen lateral strain at the midheight is plotted as a function of vertical pressure for the overconfined and underconfined tests. Also drawn is a line fitted through the midheight lateral strain data shown in Figure 2.17 for uniaxial strain loading. The lateral strain is negative and fairly small for test SUX-133, the overconfined test. The strain magnitude is small because the specimen free-field response is elastic and therefore fairly stiff. For both underconfined tests, the lateral strain is positive and fairly large. In test SUX-141, in which  $P_H = 0.9 P_H^{UX}$ , the strain at the end of the test is roughly  $650 \times 10^{-6}$ , about three times larger than in a uniaxial strain test. Even though the lateral pressure deviation from that required for uniaxial strain is only -10%, the lateral strain magnitude is much larger than in test SUX-133 because the specimen has yielded in the free field. In test SUX-140, in which  $P_H = 0.8 P_H^{UX}$ , the lateral strain at the end of the test is over  $1700 \times 10^{-6}$ , about ten times larger than in the uniaxial strain loading tests. This strain corresponds to a specimen-diameter change of about 7 mils (0.17 mm).

These results show that, even when the midheight lateral strain is about three times as large as that measured in uniaxial strain loading, the tunnel closure is not changed (see Figure 2.27). In fact, when the midheight lateral strain is large, say,  $1200 \times 10^{-6}$ , the pressure needed to produce a 5% crown-invert closure is only about 20% lower than when the midheight lateral strain is ten times smaller (uniaxial strain loading). However, when the specimen is overconfined, midheight lateral strain is small for the same 20% deviation from uniaxial strain confining

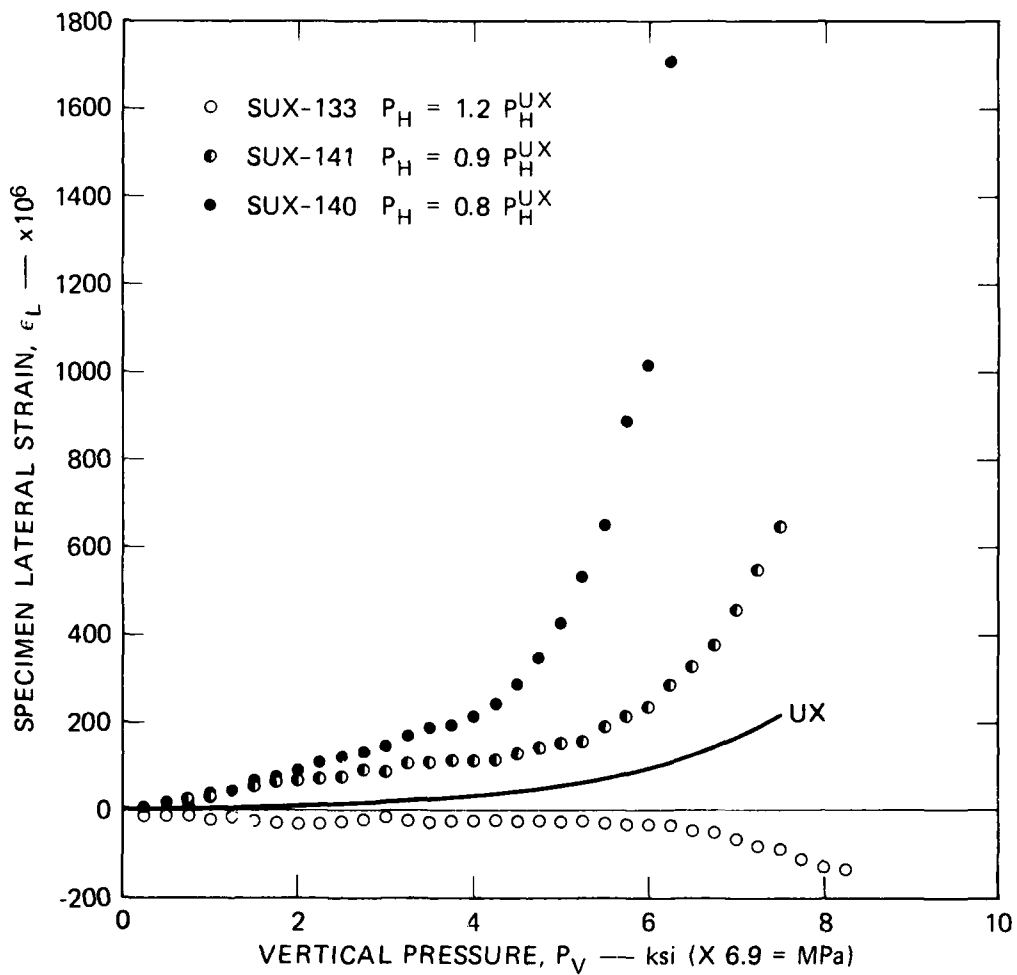


FIGURE 2.29 SPECIMEN LATERAL STRAIN AT MIDHEIGHT VERSUS VERTICAL PRESSURE FOR OVERCONFINED, UNDERCONFINED AND UNIAXIAL STRAIN LOADING OF SRI RMG 2C2

pressure. Also, by comparing the midheight lateral strains in Figure 2.29 with those in Figures 2.17-2.19, we see that the axial variation of lateral strain in a uniaxial strain test is very small and has a negligible effect on tunnel closure.

These results help us to interpret tunnel closures measured in our dynamic tests. In dynamic uniaxial strain loading tests we do not know the uniaxial strain load path, and hence the specimens can be either overconfined or underconfined. We do, however, measure specimen lateral strain. By comparing the strains measured in the dynamic tests with those obtained in the static overconfined and underconfined tests (Figure 2.29), we can make more accurate estimates of the pressure required to produce a specified crown-invert tunnel closure under truly uniaxial strain dynamic loading. For example, if in a dynamic uniaxial strain loading test we measure a peak specimen lateral strain of  $+0.1\%$   $= 1000 \times 10^{-6}$ , then by using the bounds established from these three static tests, we predict a 20% greater pressure to produce the same closure under truly uniaxial strain dynamic loading.

Agreement of measured and calculated lateral strain is not as good as the agreement for tunnel closure. Calculated specimen midheight lateral strains for underconfined, overconfined, and uniaxial strain loading do show the same trends and relative magnitudes as the corresponding measured lateral strains. However, the calculated lateral strains are about five times larger than the measured strains. As stated previously, we believe that the predicted strains are too large because hoop strains (and hence, hoop stresses) that result from radial displacements are present in the experiments but not accounted for in the calculations.

The three tests studying the influence of lateral confinement on tunnel closure in dry SRI RMG 2C2 were not as systematic as those studying saturated specimens. Because the copper jackets on which the strain gages were mounted did not fit the specimen snugly, the uniaxial strain load path was not well defined. The load paths followed in these tests are shown in Figure 2.30. Each path corresponds to zero average

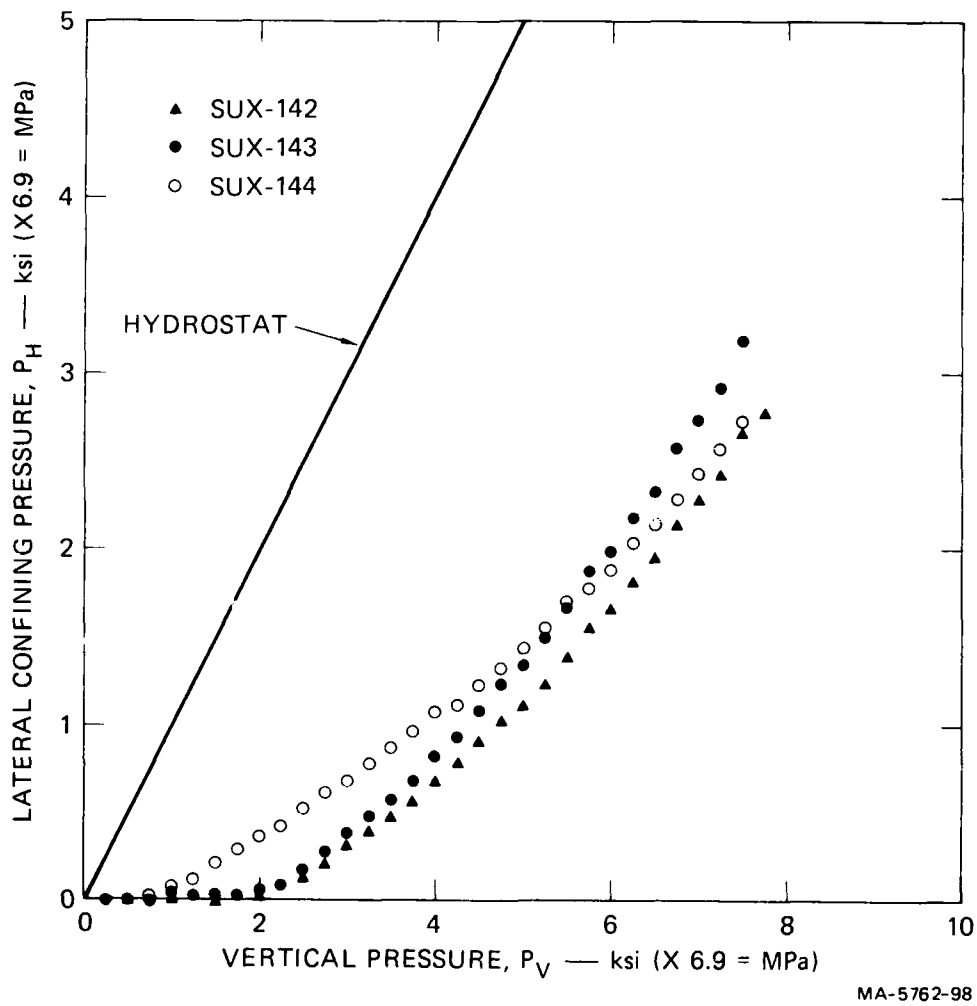


FIGURE 2.30 LOAD PATHS USED TO STUDY EFFECT OF CONFINING PRESSURE ON TUNNEL CLOSURE IN DRY SRI RMG 2C2

lateral strain, but since at low pressure the copper jacket was not firmly seated on the specimen, very little pressure was required to produce the uniaxial strain condition. Figure 2.31 plots the tunnel closure as a function of vertical pressure for the three tests. Closures at the crown-invert are about the same in all three tests. Springline closures do vary, but with no obvious trend.

#### 2.4 CONCLUSIONS

The results of these studies allow us to draw four major conclusions regarding the ability of laboratory tests to simulate field response and the capability to predict theoretically the tunnel closures measured in our laboratory test:

- (1) Specimen-to-tunnel diameter ratio influences laboratory results when plastic deformation is localized around the tunnel (no free-field yielding) or when the specimen material has an inherent size scale. Results show that our standard specimen geometry,  $D_S/D_T = 6.4$ , introduces maximum errors in critical load of between 10% and 20%.
- (2) The SRI uniaxial strain loading laboratory tests adequately simulate uniaxial strain loading in the field: the specimen boundaries are far enough from the tunnel so that the lateral boundary of the specimen remains nearly straight. Thus, with a hydraulic confining pressure we accurately simulate a uniaxial strain condition. Measured deviations in lateral strain from one axial location to another are very small compared to those that cause significant changes in the measured tunnel closure.
- (3) Small changes in the uniaxial strain confining pressure (less than 10%) have a negligible effect on tunnel closure. Larger changes (up to 20%) produce changes in critical loads of less than 20%. Specimen lateral strains that correspond to these deviations in lateral confining pressure can be used to narrow the band between the experimentally determined upper and lower bounds on tunnel closure under dynamic uniaxial strain loading in the laboratory. Results of this study can be extended to field tests, where loading may deviate from uniaxial strain because of spherical or cylindrical divergence of the loading wave or because of diffraction of the loading wave by inhomogeneities such as faults, large inclusions, or nearby strata.

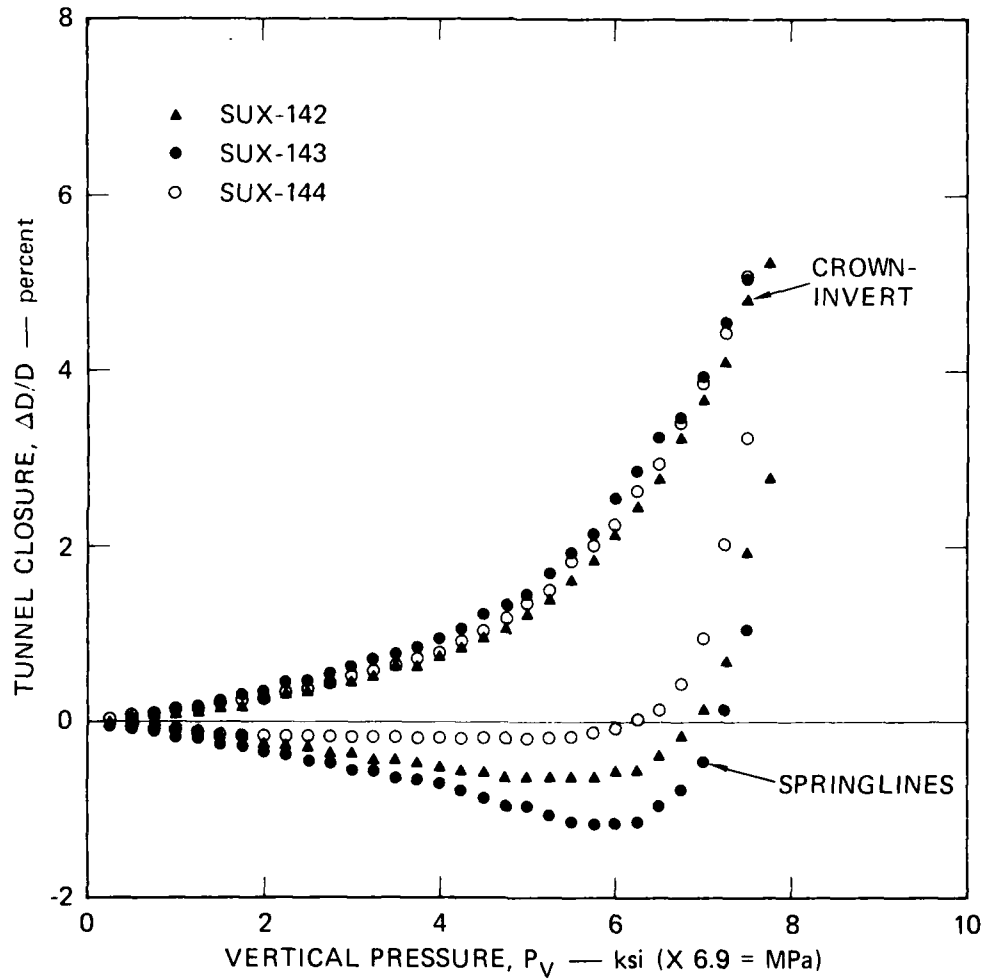


FIGURE 2.31 TUNNEL CLOSURE AT CROWN-INVERT AND SPRINGLINE DIAMETERS  
 VERSUS VERTICAL PRESSURE FOR SEVERAL LOADING PATHS IN DRY  
 SRI RMG 2C2  
 6061-T0 aluminum liner,  $a/h = 11.5$

- (4) A simple constitutive model and a two-dimensional calculation can be used to predict accurately the tunnel closures measured in the laboratory under uniaxial strain loading, near-uniaxial strain loading, and isotropic loading. The computational technique cannot, however, predict the measured specimen lateral strains, because it neglects the resistance to lateral deformation of hoop stresses the accompany the lateral deformation.

### 3. CYLINDRICAL STRUCTURES IN JOINTED ROCK

#### 3.1 INTRODUCTION

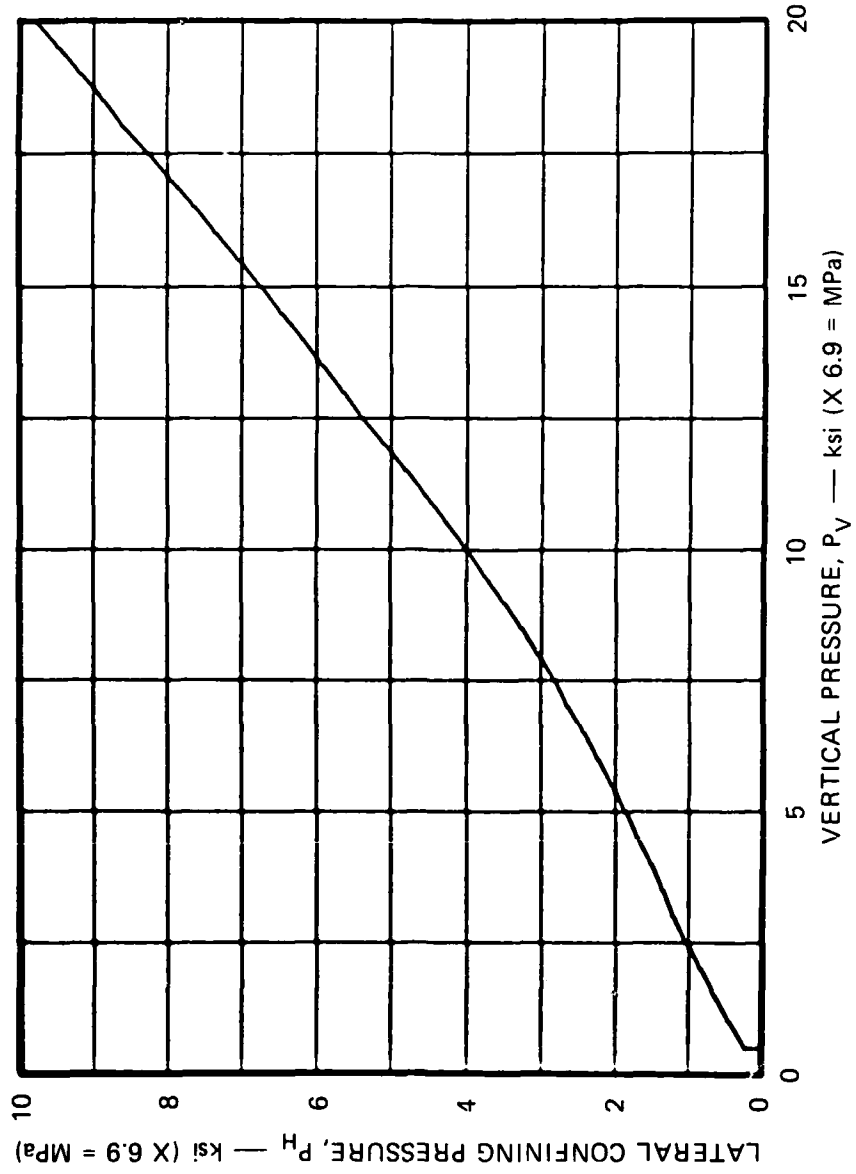
This chapter describes laboratory tests performed on 12-inch-diameter (0.3-m) jointed specimens to investigate the influence on tunnel deformation of a single set of equally spaced parallel joints.\* Initial progress in this study is given in Volume I [5], where we describe specimen preparation and tunnel liner instrumentation, and give results from the first two tests. Those test results are also included in this chapter. Appendix A of the present report gives test records and photographs of posttest specimen cross sections for all of jointed rock experiments. Tunnel liner strain records are also presented in Appendix A.

We performed twelve tests on jointed specimens of 16A rock simulant to study the influence on tunnel deformation of joint orientation, tunnel orientation, tunnel reinforcing structure type, and repeat loading. The loading in all twelve experiments was static and in ten experiments followed a common load path, the path that produces uniaxial strain loading for joints perpendicular to the specimen axis. Figure 3.1 shows the load path that we imposed.

The test matrix for the ten common load path experiments is given in Table 3.1. We studied the influence of joint orientation with both direct contact structures and backpacked structures, designated in the table by STEEL and FOAM, respectively. The effect of repeat loading was studied for two joint orientations. The difference in response of tunnels reinforced with direct contact and backpacked structures was investigated for three joint orientations. Finally, three tests studied the influence of tunnel orientation on tunnel deformation. Only ten

---

\*The specimens for this study were supplied by R. L. Stowe of the U.S. Army Waterways Experiment Station, Vicksburg, Mississippi.



MA-5762-223

FIGURE 3.1 LOAD PATH FOR TESTS ON JOINTED SPECIMENS --- 16A ROCK SIMULANT

TABLE 3.1 JOINTED MODEL TEST MATRIX

Test Number: LSUX-	13	24	14	17	21	20	19	25	22	23
Loading Type	Mono	Mono	Mono	Repeat	Repeat	Mono	Mono	Mono	Mono	Mono
Load-Joint Orientation $\beta$ (DEG)	0	30	45	0	45	0	30	45	30	30
Tunnel-Joint Orientation $\gamma$ (DEG)	90	90	90	90	90	90	90	90	60	69.3
Reinforcement Type	Steel	Steel	Steel	Steel	Steel	Foam	Foam	Foam	Steel	Steel
Response Comparisons:										
Joint Orientation										
Repeat vs. Mono										
Steel vs. Foam										
Tunnel Orientation										

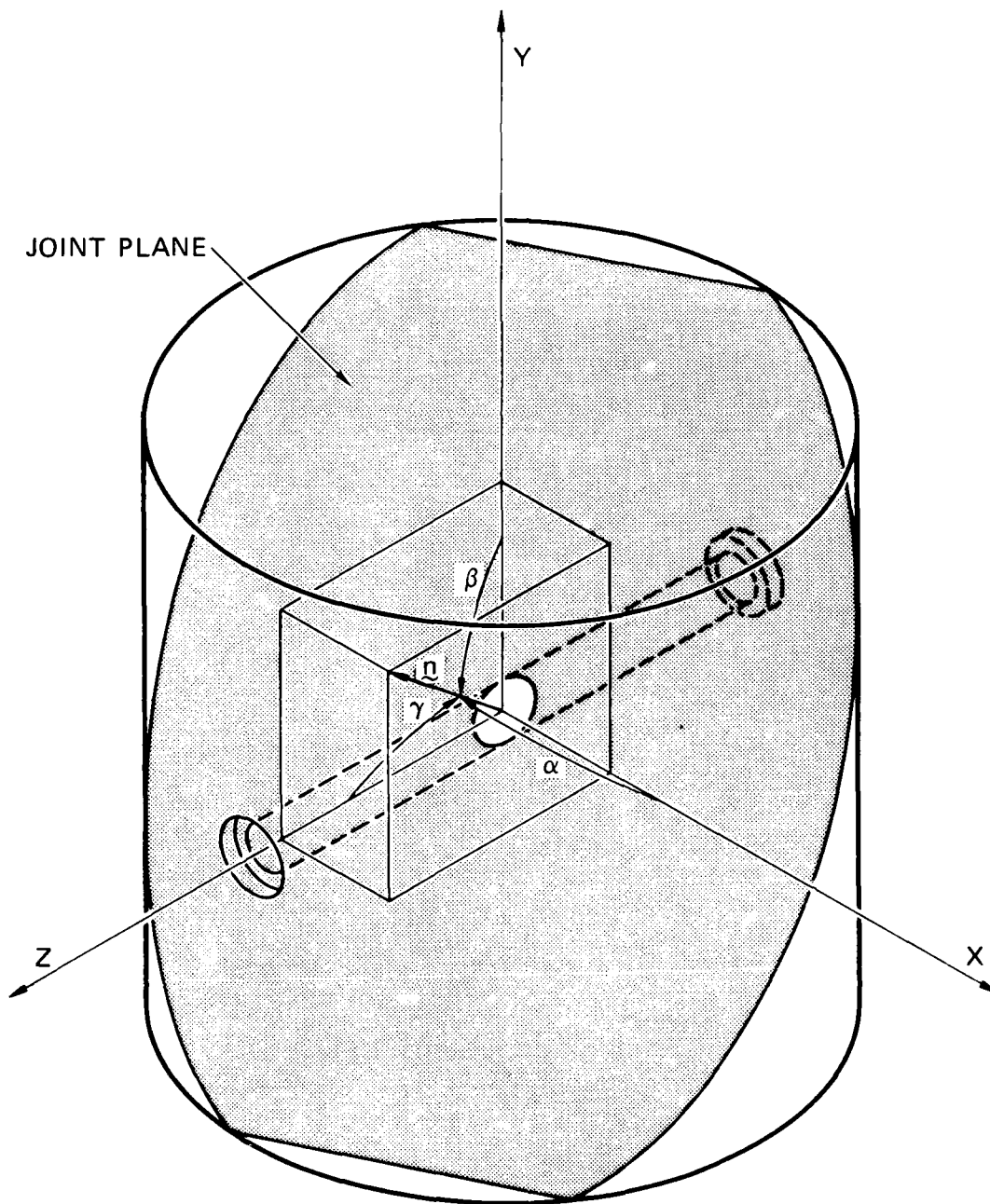
tests are listed in the test matrix because the specimens in two tests, LSUX-16 and LSUX-18, were loaded along a different path and the results are therefore not comparable.

The sketch in Figure 3.2 defines the angles used to specify joint orientation. The load-joint orientation angle  $\beta$  is the angle between the vertical loading direction (the specimen axis) and the direction of the joint normal. The tunnel-joint orientation angle  $\gamma$  is the angle between the tunnel axis and the joint normal. The specimen geometry is given uniquely by the specification of these two angles, the tunnel diameter and the joint spacing. In all twelve tests the tunnel diameter is 2 inches (50 mm) and the joint spacing is 1/3 inch (8-1/2 mm), so that the ratio of tunnel diameter to joint spacing is 6.

The engineering sketches in Figure 3.3 show the orientations studied. Figure 3.3(a) shows the three load-joint orientation angles studied and Figure 3.3(b) shows the three tunnel-joint orientation angles tested.

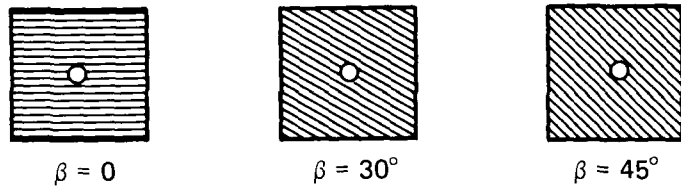
The two structures that reinforce the tunnels in these experiments are a direct contact 1015 steel monocoque cylinder having mean-radius-to-wall-thickness ratio  $a/h = 12.5$ , and a similar monocoque cylinder backpacked with polyurethane foam whose outer-radius-to-wall thickness ratio is  $R/H = 4.3$ . The crush strength (at 20% strain) of the polyurethane foam is  $\sigma_{20} = 550$  psi (3.8 MPa). The complete strain-strain curve for the foam is given in Figure 3.4.

An important result, common to all twelve experiments, is that there is no evidence of block motion. The closure curves presented for jointed specimens in the following sections are as smooth as those presented for intact specimens. Furthermore, examination of the photographs of specimen posttest cross sections in Appendix A shows that the tunnel wall is still smooth. Figures 3.5 to 3.7 show good examples of this for LSUX-20, LSUX-21, and LSUX-24. Other posttest cross sections do not show this as clearly because of small chips lost during sectioning or severe damage to the whole model while removing it from the test machine.

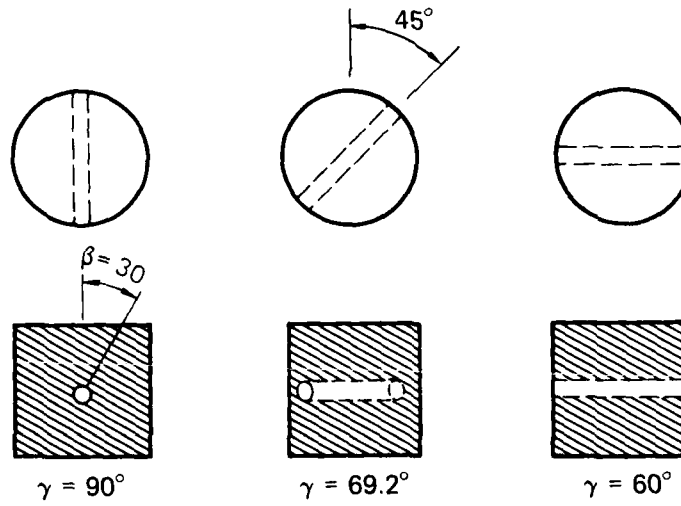


MA-5762-22A

FIGURE 3.2 SCHEMATIC SHOWING JOINT ORIENTATION  
 $\underline{n}$  is normal to the joint plane



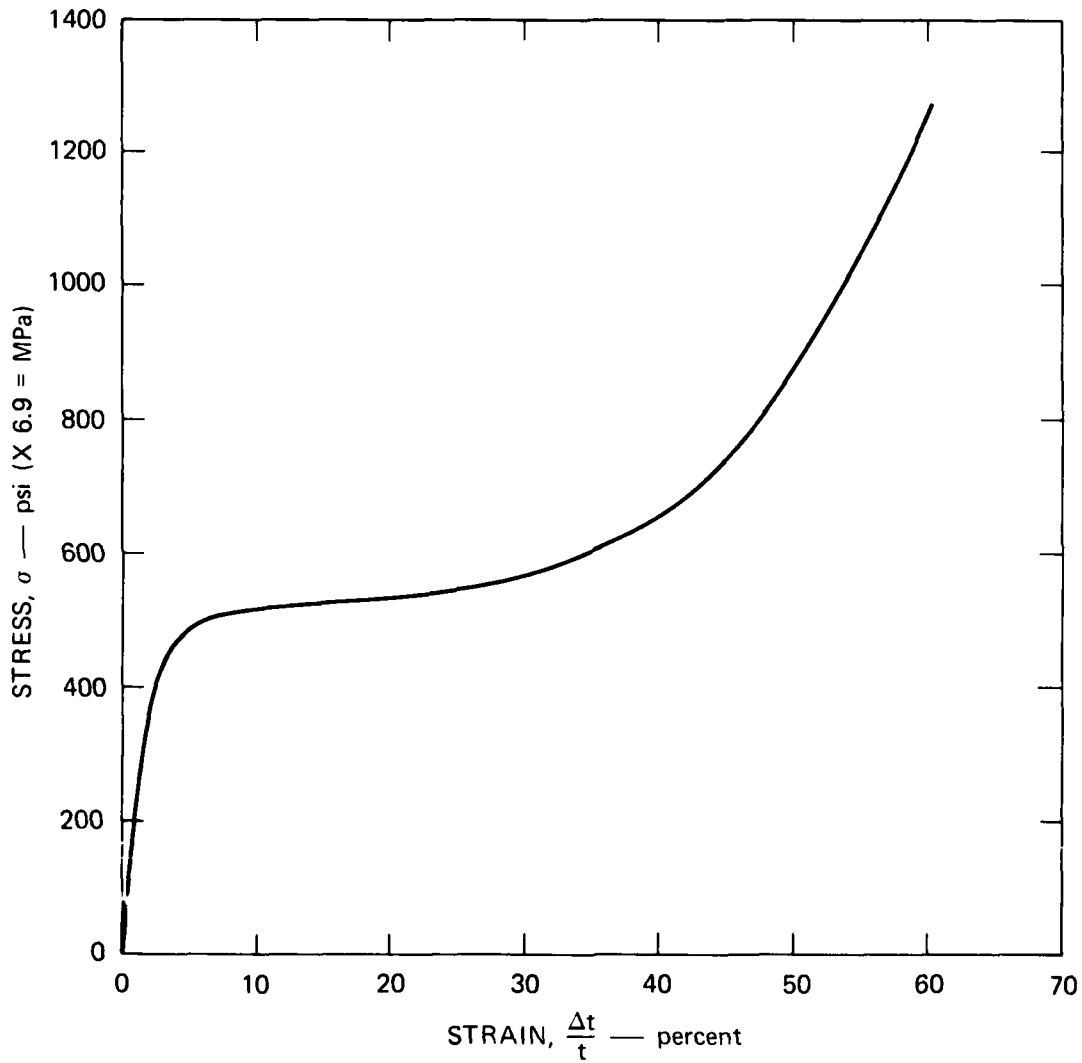
(a)  $\beta$  orientations for  $\gamma = 90^\circ$  (tunnel axis and joint planes perpendicular to paper)



(b)  $\gamma$  orientations for  $\beta = 30^\circ$  (joint planes perpendicular to paper)

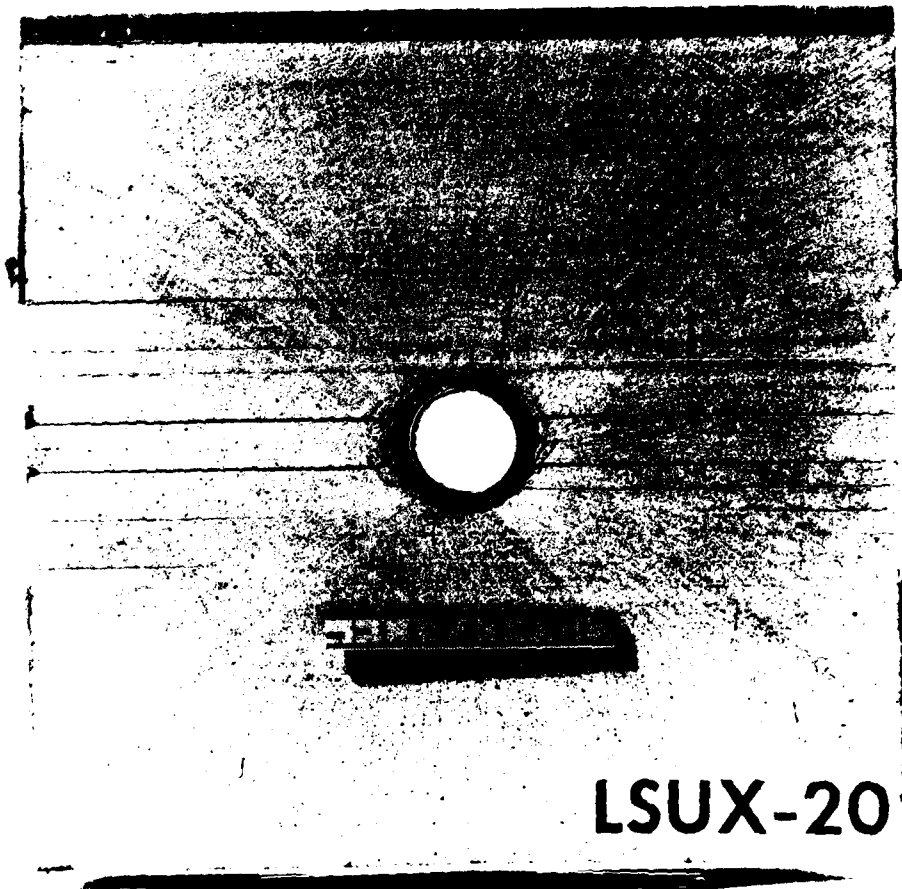
MA-5762-245

FIGURE 3.3 ENGINEERING SKETCHES FOR ALL JOINT ANGLES TESTED



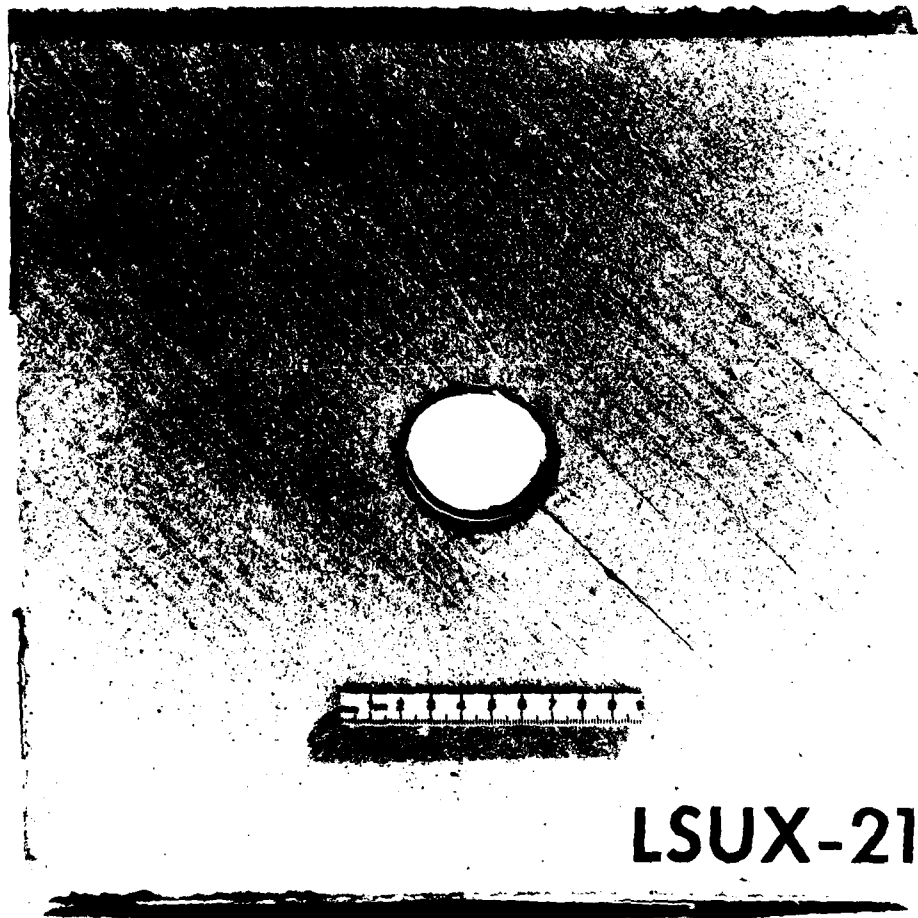
MA-5762-106

FIGURE 3.4 STRESS-STRAIN CURVE FOR UNIAXIAL STRAIN LOADING OF 13.1 lb/ft<sup>3</sup> (210 kg/m<sup>3</sup>) POLYURETHANE FOAM  $\dot{\epsilon} \approx 3.3 \times 10^{-2} \text{ s}^{-1}$



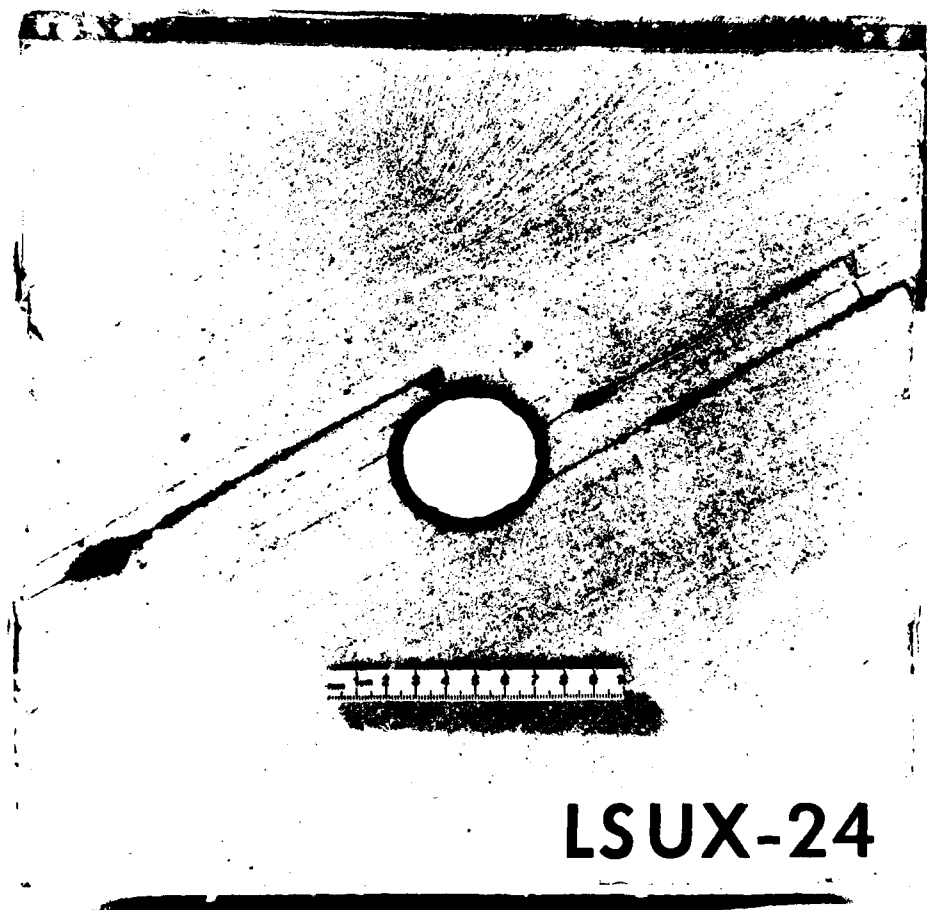
MP-5762-160

FIGURE 3.5 SECTIONED SPECIMEN FROM TEST LSUX-20



MP-5762-171

FIGURE 3.6 SECTIONED SPECIMEN FROM TEST LSUX-21



MP-5762-192

FIGURE 3.7 SECTIONED SPECIMEN FROM TEST LSUX-24

AD-A088 912

SRI INTERNATIONAL MENLO PARK CA  
THEORETICAL AND EXPERIMENTAL STUDY OF DEEP-BASED STRUCTURES IN --  
SEP 79 P E SENSENY, H E LINDBERG

F/G 1 /13  
TC(U)

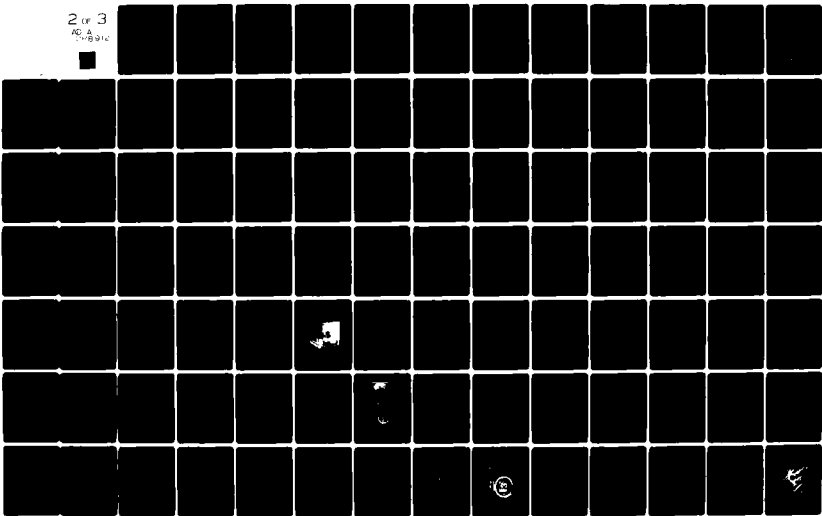
DNA001-76-C-0385

UNCLASSIFIED

DNA-5208F

NL

2 of 3  
AD-A088 912



35

### 3.2 INFLUENCE OF THE LOAD-JOINT ORIENTATION ANGLE

Six experiments studied the influence on tunnel deformation of the load-joint orientation angle  $\beta$ . Specimens having three different orientations were tested:  $\beta = 0^\circ$ ,  $30^\circ$ , and  $45^\circ$ . Two tests were performed at each orientation, one with a direct contact tunnel reinforcement structure and the other with a backpacked structure. The tunnel-joint orientation angle was  $\gamma = 90^\circ$  in all six specimens, i.e., the joint planes were parallel to the tunnel axis and tilted at various angles from the loading direction.

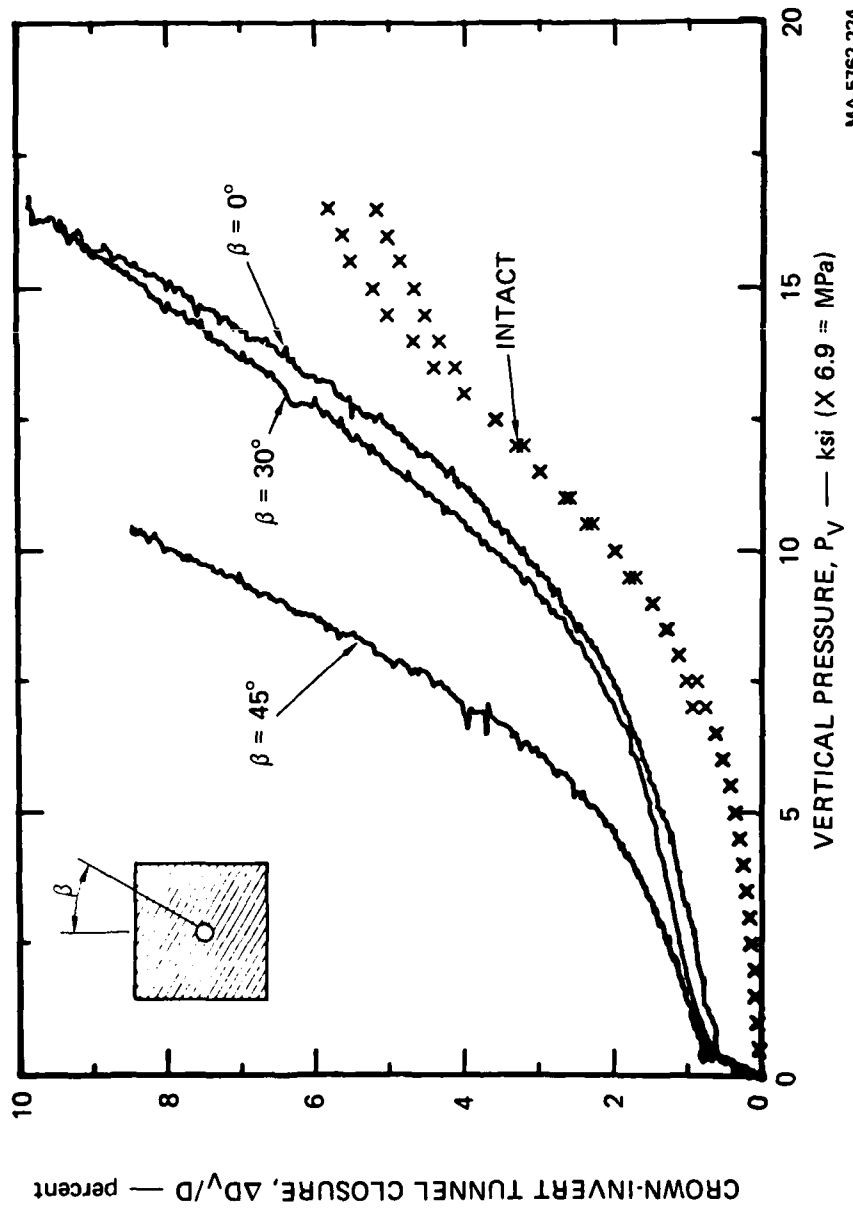
Figures 3.8 and 3.9 plot crown-invert and springline closures, respectively, as functions of vertical pressure for tests on specimens containing direct contact liners. The figures also plot the corresponding closures from two uniaxial strain loading tests performed on intact 4-inch-diameter (0.1-m) specimens of 16A rock simulant whose tunnels were reinforced with similar direct contact liners.\*

The closure curves for the jointed specimens have a distinct feature not present for the intact specimen: during initial loading, there is a jump in closure with only a small increase in pressure. This occurs because the joints are very compliant initially, when the plates on either side of a joint touch at only a relatively few points. As the loading begins and more points come into contact, the joints close and stiffen. The plots show that when the load reaches 500 psi (3.5 MPa), the jointed specimens are about as stiff as the intact specimens and the tunnel closes much more slowly. This response is not expected in the field because the in-situ stresses are large enough so that the joints are closed from the outset. Also, natural joints are generally filled with material.

Figure 3.8 shows that the crown-invert closure curves for the jointed specimens having  $\beta = 0^\circ$  and  $30^\circ$  are nearly parallel to the crown-invert closure curve for the intact specimens at pressures below

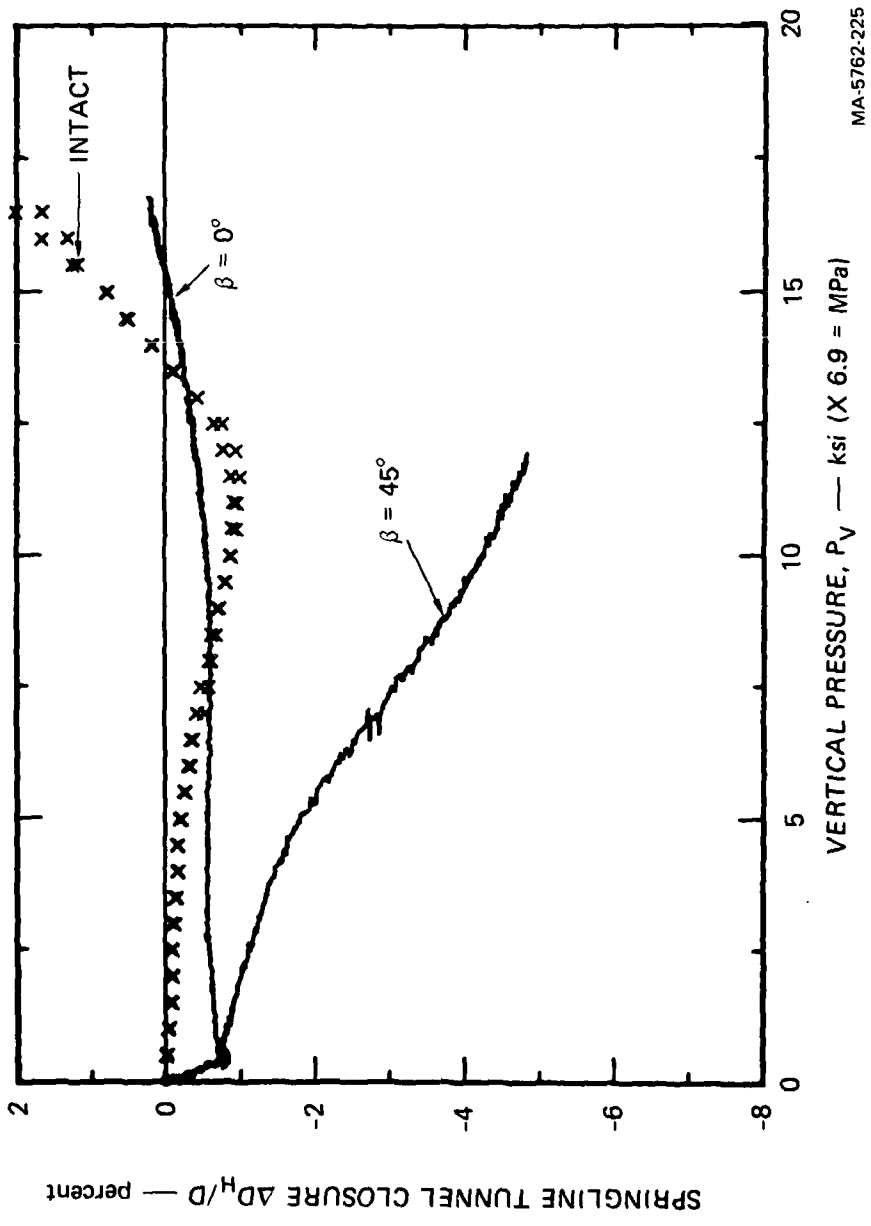
---

\* These data are taken from Figure 2.3.



MA-5762-224

FIGURE 3.8 CROWN-INVERT TUNNEL CLOSURE VERSUS PRESSURE FOR THREE LOAD-JOINT ORIENTATION ANGLES  
 Data from intact specimens are plotted for comparison. Direct contact liner, 16A rock simulatant,  $\gamma = 90^\circ$



MA-5762-225

FIGURE 3.9 SPRINGLINE TUNNEL CLOSURE VERSUS VERTICAL PRESSURE FOR TWO LOAD-JOINT ORIENTATION ANGLES

Data from intact specimens are plotted for comparison. Direct contact liner, 16A rock simulant,  $\gamma = 90^\circ$

12.5 ksi (85 MPa). For these joint orientations, the effect of joints on crown-invert closure is to shift the curve upwards initially by the amount that corresponds to the effective gap in the joints.

Thus, we conclude that the influence on crown-invert closure of the load-joint orientation angle is very small for small angles,  $\beta \leq 30^\circ$ . However, for larger angles, the influence of  $\beta$  can be significant. For example, the vertical pressure required to produce a crown-invert closure of 5% for  $\beta = 45^\circ$  is only 60% as large as that required to produce the same closure for  $\beta = 0^\circ$ .

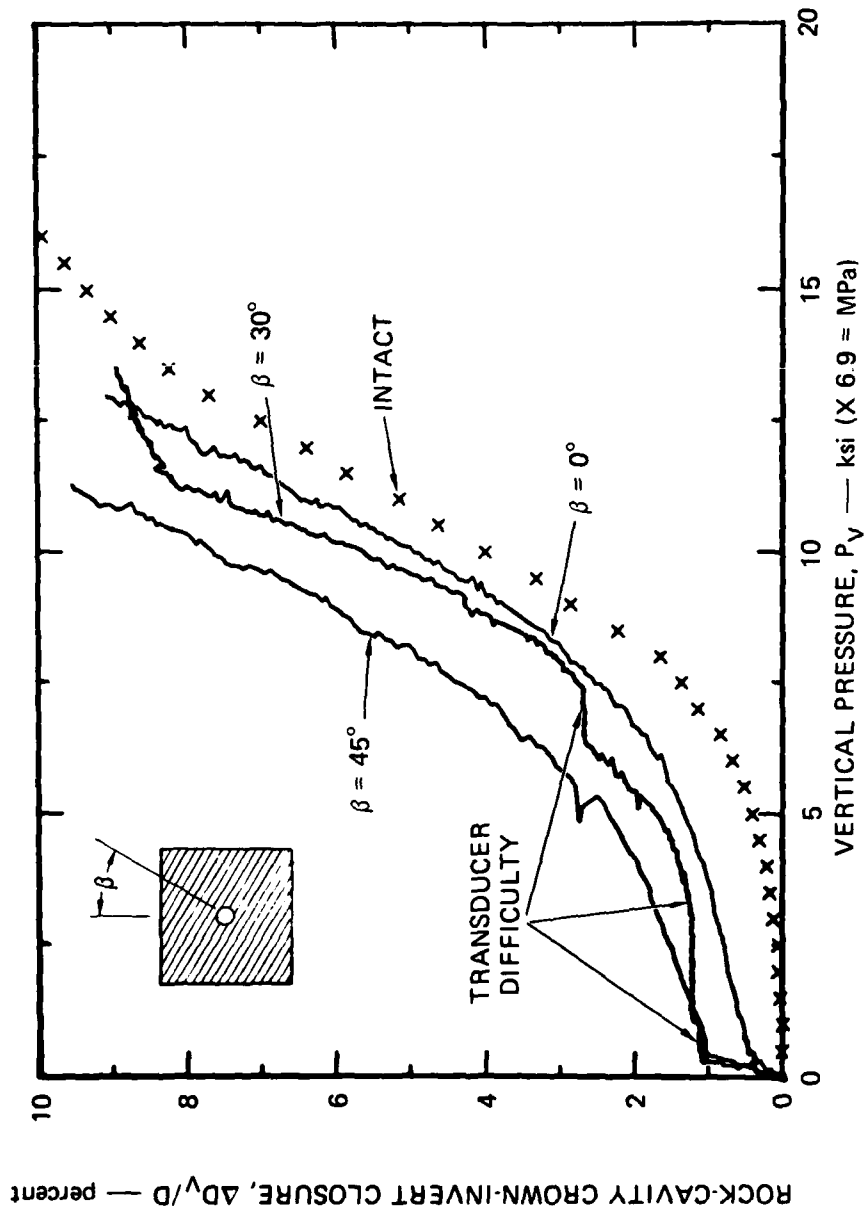
The springline closures plotted in Figure 3.9 show that both positive and negative closures are obtained for the intact specimens. For the  $\beta = 0^\circ$ , jointed specimen, the springline closures are qualitatively the same: negative at low pressure and positive at higher pressure. However, the motion of the springlines in the intact specimens is more pronounced: the outward motion peaks rather sharply at just over 10 ksi (70 MPa) and then the inward motion occurs at a much more rapid rate than for the jointed specimen with  $\beta = 0^\circ$ .

Although only negative springline closure was measured for  $\beta = 45^\circ$ , the shape of the closure curve is more like that obtained for intact specimens. The curve is concave downward at low pressures, then concave upward at higher pressures. However, the amplitude is much greater than that for intact specimens; the peak negative closure is between 5% and 6% for  $\beta = 45^\circ$ , but it is only about 1% for the intact specimens. No record of springline closure was obtained from the test in which  $\beta = 30^\circ$ .

Figures 3.10 and 3.11 plot rock-cavity crown-invert and springline closures for intact and jointed specimens whose tunnels are reinforced with backpacked structures.\* The plot of crown-invert closure in Figure 3.10 shows the same trend as that found for direct contact structures in Figure 3.8: closures in specimens for which  $\beta = 0^\circ$  and  $30^\circ$  are nearly identical and are not significantly larger than those in

---

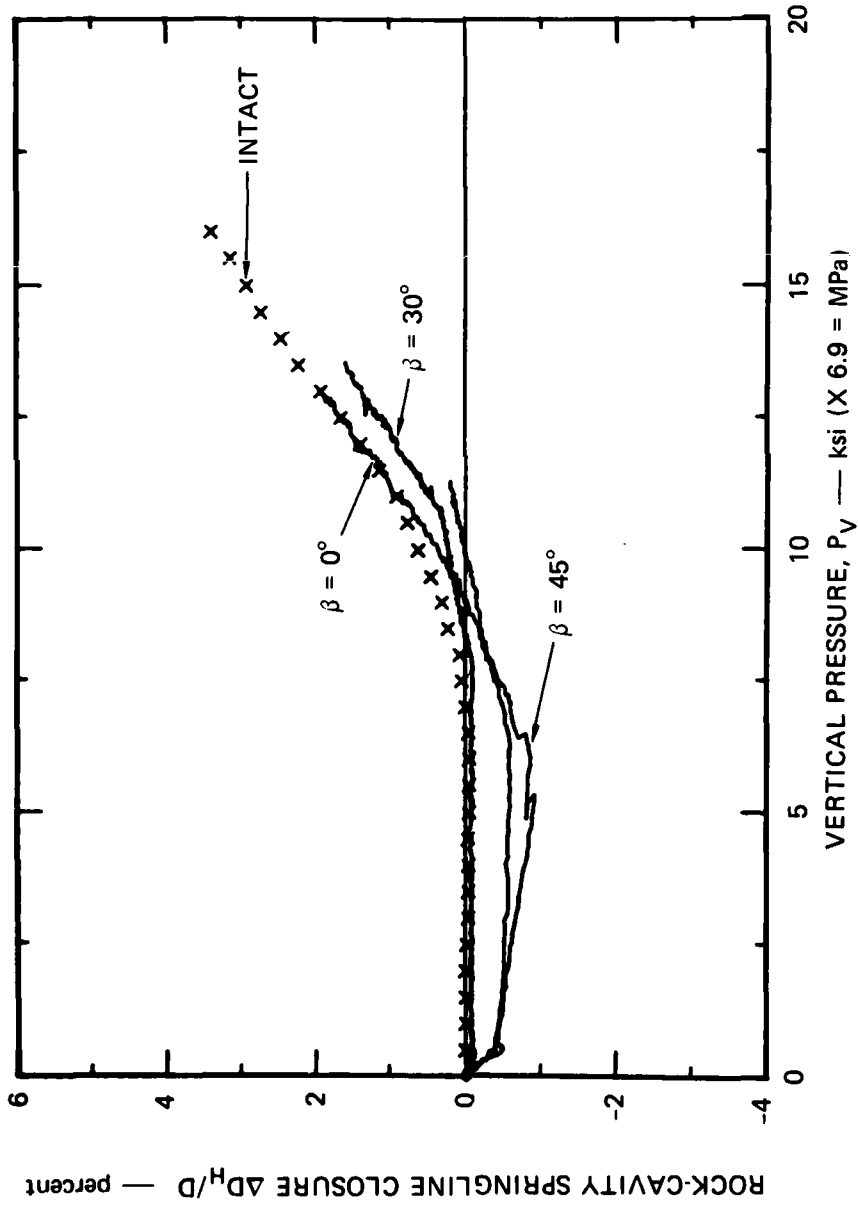
\*The intact data are taken from Figure B.3 in Appendix B.



MA-5762-226

FIGURE 3.10 ROCK-CAVITY CROWN-INVERT CLOSURE VERSUS VERTICAL PRESSURE FOR THREE LOAD-JOINT ORIENTATION ANGLES

Data from an intact specimen is plotted for comparison. Backpacked liners. 16A rock simulant,  $\gamma = 90^\circ$



MA-5762-227

FIGURE 3.11 ROCK-CAVITY SPRINGLINE CLOSURE VERSUS VERTICAL PRESSURE FOR THREE LOAD-JOINT ORIENTATION ANGLES

Data from an intact specimen are plotted for comparison. Backpackered liners, 16A rock simulant,  $\gamma = 90^\circ$

intact specimens (except for the initial jump while the joints close). However, for a larger load-joint orientation  $\beta = 45^\circ$ , the closure curve is shifted to the left (smaller loads for given closures). The pressure required to produce a 5% closure for  $\beta = 45^\circ$  is 80% of that required to produce the same closure for  $\beta = 0^\circ$ . This decrease in strength between  $\beta = 0^\circ$  and  $\beta = 45^\circ$  for backpacked structures is not as large as is the corresponding decrease (60%) for direct contact structures.

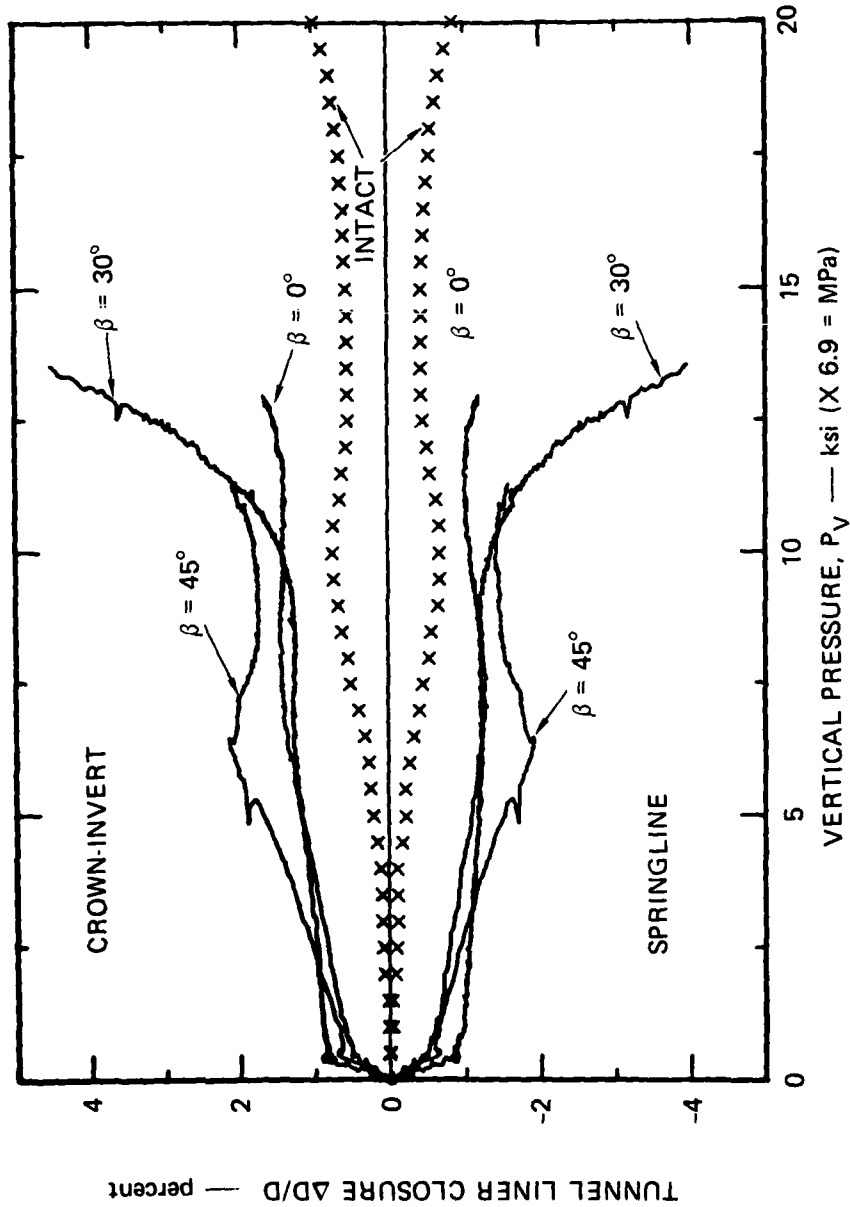
The rock-cavity crown-invert closure curve plotted in Figure 3.10 for  $\beta = 30^\circ$  has three horizontal plateaus, two near 1.2% and the third at 2.8%. These are caused by transducer difficulty associated with the tight fit between the tunnel and the reinforcing structure. When the structure was pressed into the tunnel, the interference between the tunnel and the structure caused the polyurethane foam to crush up and shear slightly. The shearing caused misalignment of the closure transducer and hence the subsequent intermittent closure indications: the transducer froze in the structure and recorded no increase in closure as the pressure increased, then the transducer slipped and recorded a fairly rapidly increasing closure with increasing pressure. The sequence repeated several times until late in the test, when the large crush of the foam eliminated the effect of the shearing misalignment and the closure record increased smoothly.

Figure 3.11 plots rock-cavity springline closure measured in the same four tests. Here the difference between the response of jointed and intact specimens is small. The primary difference is that for two jointed specimens, the initial closing of the joints produces about 0.5% outward motion of the springlines. However, subsequent springline motion is identical to that measured in intact specimens: constant, slightly negative closure to about  $P_v = 7.5$  ksi (50 MPa), then moderately increasing positive closure to the end of the test. No initial outward motion of springlines was measured for  $\beta = 30^\circ$  because of the deformation of the structure when it was pushed into the tunnel.

Figure 3.12 plots tunnel liner closure for the tests with backpacked structures. The liner deformation is qualitatively the same for all four specimens. Crown-invert closure is always positive, springline closure is always negative, and the magnitudes of the closures are nearly equal: the liner deforms from a circular cross section into an elliptical cross section of nearly equal area. The primary difference between jointed and intact response is that the relatively large rock-cavity deformation accompanying initial closing of the joints eliminates the part of the response prior to constant stress crushing of the backpacking; i.e., the part of the curve obtained for the intact specimen for  $P_v < 10$  ksi (70 MPa).

The results of tests for which  $\beta = 30^\circ$  and  $45^\circ$  are complicated by experimental difficulties. In the test for which  $\beta = 30^\circ$ , the reinforcing structure deformed slightly as it was pushed into the tunnel. This caused some crushing of the backpacking prior to the test. Therefore, the liner response plotted in Figure 3.12 appears to indicate premature lockup of the backpacking beginning at  $P_v = 10$  ksi (70 MPa). In the test for which  $\beta = 45^\circ$ , one of the small holes through the foam backpacking that provided access to the liner closure transducer mounts was inadvertently filled with epoxy, creating a thin epoxy column between the steel liner and the tunnel wall, so that the steel liner was not completely isolated from the rock-cavity deformation. In spite of these difficulties, the liner closure records from all four tests show that backpacking effectively isolates the liner from the rock-cavity deformation.

These six tests show that for specimens having small load-joint orientation angles,  $\beta = 0^\circ$  and  $30^\circ$ , tunnel closures are about the same as for intact specimens; the major difference is the fairly large closures measured at low pressure that are attributed to closing of the joints. However, the strength of specimens having a larger load-joint orientation angle,  $\beta = 45^\circ$ , can be reduced appreciably. For example, if the tunnel is reinforced with a backpacked structure, the pressure required to produce a 5% crown-invert closure of the tunnel for  $\beta = 45^\circ$  is only 80% of that required to produce the same closure for  $\beta = 0^\circ$ ; if the tunnel is reinforced with a direct-contact liner, the required pressure is only 60% as great as for  $\beta = 0^\circ$ .



MA-5762-228

FIGURE 3.12 TUNNEL LINER CLOSURE VERSUS VERTICAL PRESSURE FOR THREE LOAD-JOINT ORIENTATION ANGLES

Data from an intact specimen are plotted for comparison. Back-packed liners, 16A rock simulant,  $\gamma = 90^\circ$

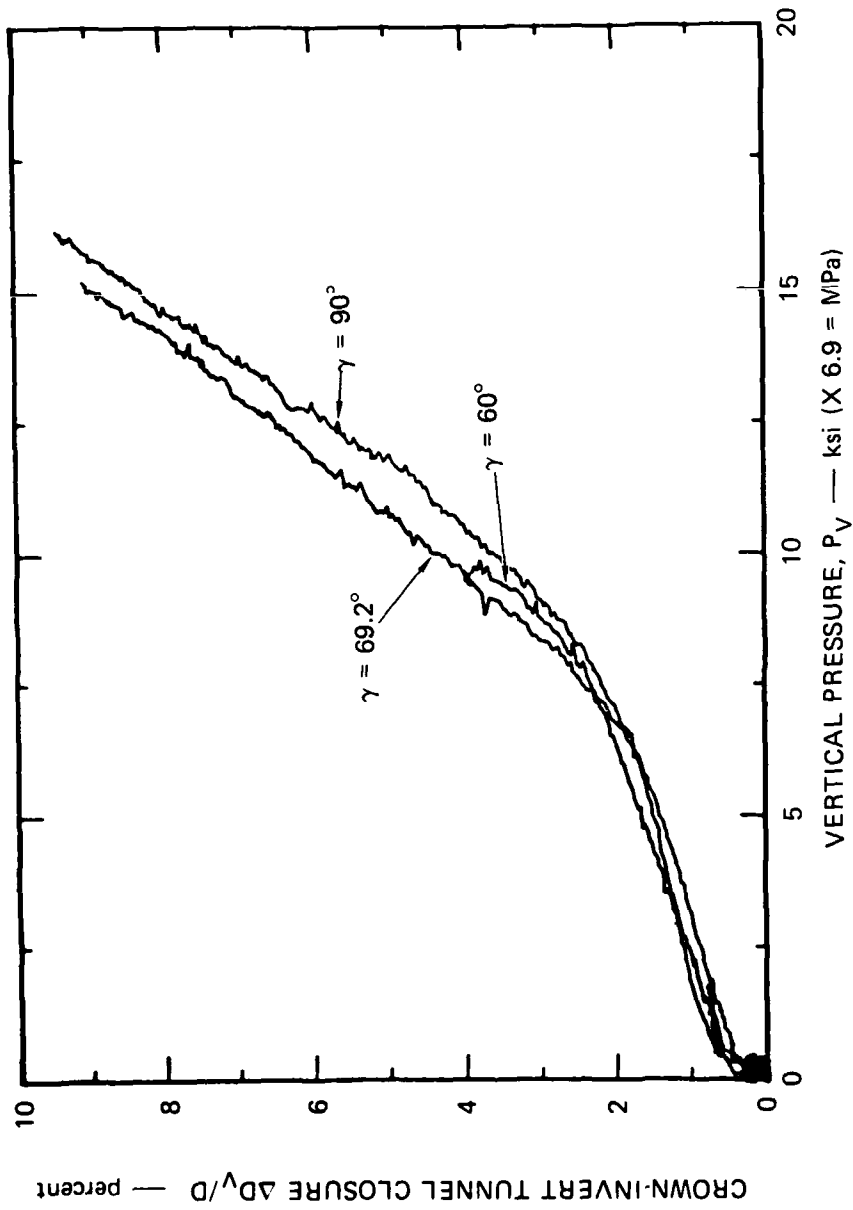
Test results for backpacked structures show that tunnel liner closure is not influenced by the load-joint orientation angle as long as the backpacking does not lock up. The pressure at which the backpacking begins to lock up, however, does depend on the load-joint orientation angle. The pressure at which the backpacking locks up is greater than 15 ksi (100 MPa) in the three tests performed (allowing for the initial crush when the backpacking deformed in one test), so the backpacking effectively limits the liner deformation for jointed as well as intact rocks.

### 3.3 INFLUENCE OF THE TUNNEL-JOINT ORIENTATION ANGLE

We performed three tests to study the influence on tunnel deformation of the tunnel-joint orientation angle  $\gamma$ . The load-joint orientation angle was  $\beta = 30^\circ$  and the tunnel reinforcing structure was a direct contact liner in all three tests. The three tunnel-joint orientation angles tested are  $\gamma = 60^\circ$ ,  $69.2^\circ$  and  $90^\circ$  (see Figure 3.3b). The orientation with  $\gamma = 90^\circ$  is the one tested to study the influence of the load-joint orientation angle  $\beta$ .

Figure 3.13 plots the crown-invert tunnel closures from these tests as functions of the vertical pressure. The three closure curves differ very little. This result could be anticipated, since the study of the load-joint orientation showed that for  $\beta \leq 30^\circ$  the presence of joints does not significantly influence specimen strength. Perhaps if the load-joint orientation angle had been larger, the measured crown-invert tunnel closure would have depended on the tunnel-joint orientation angle  $\gamma$ .

Springline tunnel closure is plotted in Figure 3.14 for  $\gamma = 60^\circ$  and  $69.2^\circ$ . No springline tunnel closure record was obtained for  $\gamma = 90^\circ$ . This plot shows that springline closure does depend on the tunnel-joint orientation angle  $\gamma$ . When  $P_v = 10$  ksi (70 MPa) the outward springline motion for  $\gamma = 69.2^\circ$  is twice as large as for  $\gamma = 60^\circ$ : the deformed shaped of the tunnel is more elliptical for the larger  $\gamma$ .



MA-5762-229

FIGURE 3.13 CROWN-INVERT TUNNEL CLOSURE VERSUS VERTICAL PRESSURE FOR THREE TUNNEL-JOINT ORIENTATION ANGLES  
Direct contact liner, 16A rock simuliant,  $\beta = 30^\circ$

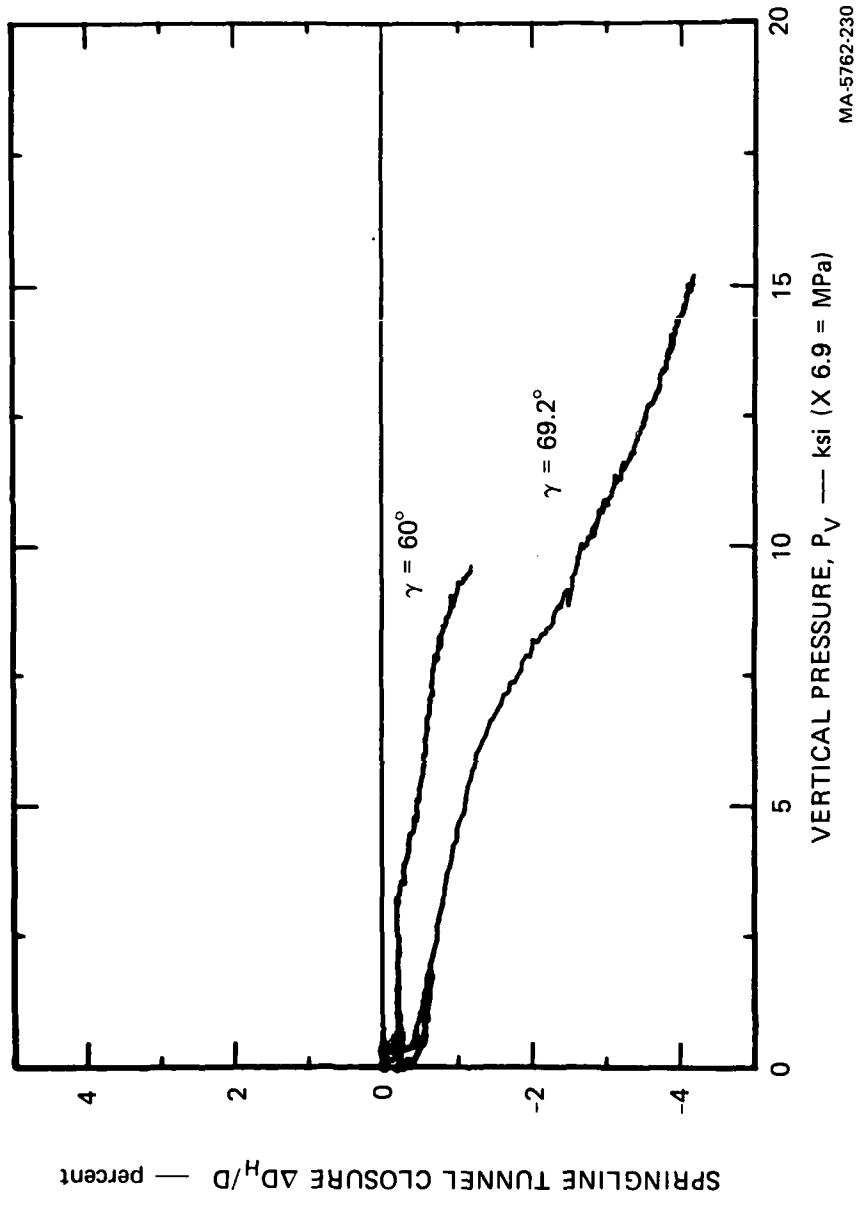


FIGURE 3.14 SPRINGLINE TUNNEL CLOSURE VERSUS VERTICAL PRESSURE FOR TWO TUNNEL-JOINT ORIENTATION ANGLES  
Direct contact liner, 16A rock simulant,  $\beta = 30^\circ$

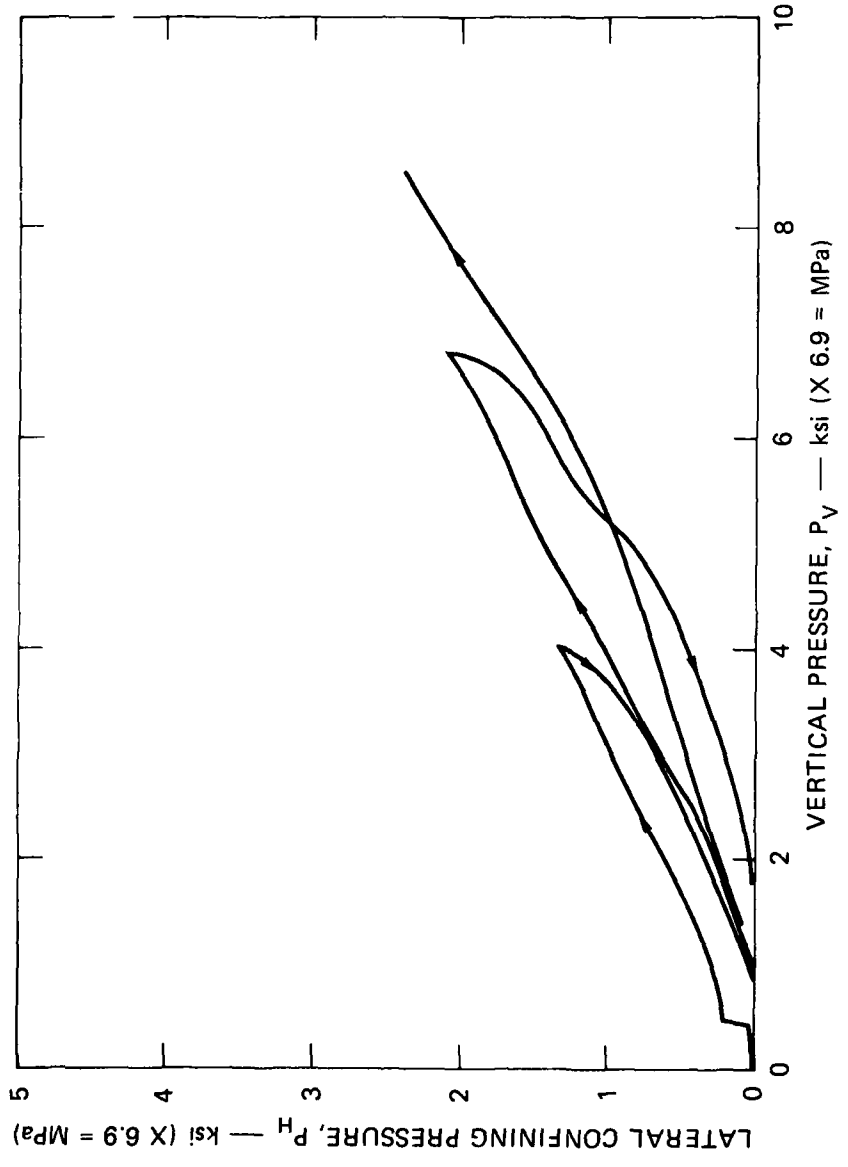
### 3.4 INFLUENCE OF REPEAT LOADING

Three tests were performed to study the influence on tunnel deformation of repeat loading, one with load-joint orientation angle  $\beta = 0^\circ$  and two with  $\beta = 45^\circ$ . In all three tests the tunnel-joint orientation angle was  $\gamma = 90^\circ$  and the tunnels were reinforced with direct contact liners. The specimens were unloaded and reloaded at crown-invert closures  $\Delta D_V/D = 2\%$ ,  $3\%$ ,  $5\%$  and  $8\%$ .

In two tests, one at each orientation, loading and unloading followed our standard specified load path (Figure 3.1). In the third test ( $\beta = 45^\circ$ ), however, loading followed the specified load path but unloading did not. This occurred because the microprocessor controlling the vertical and lateral confining pressures was not properly programmed and therefore caused the lateral confining pressure to drop rapidly during unloading. Figure 3.15, plotting the load-unload paths for this test, shows that during unloading the specimen was severely underconfined. This had a marked effect on tunnel response, as discussed later.

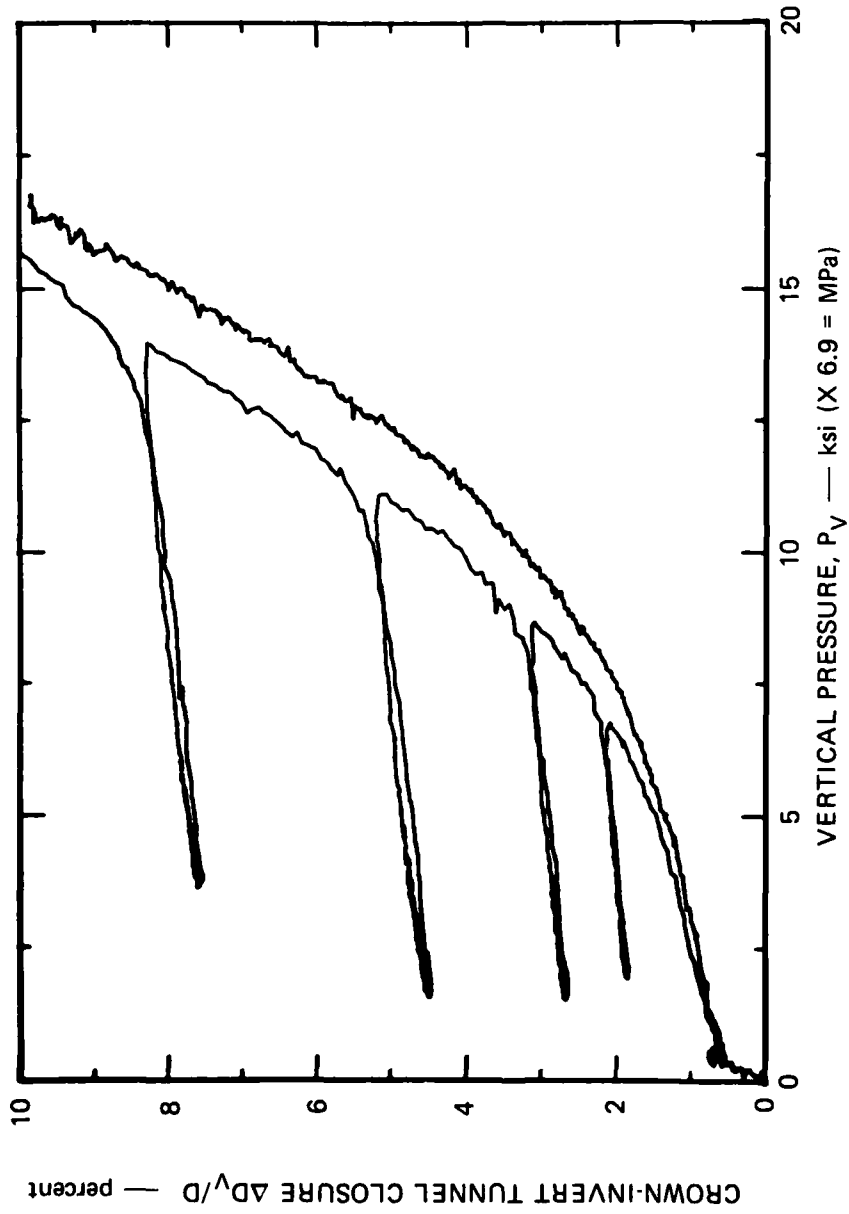
Crown-invert and springline closures are plotted as functions of vertical pressure for  $\beta = 0$  in Figures 3.16 and 3.17, along with the corresponding closure curves for monotonic loading of a similar specimen. Comparison of the two curves in Figure 3.16 shows that repeat loading does not significantly influence the crown-invert closure curve. This result is identical to that obtained for intact specimens (see Chapter 4). Comparison of the two curves in Figure 3.17 shows a significant difference in springline closure between these two tests. However, this difference is not attributable to the influence of repeat loading, because a significant difference in springline closures occurs before the first cycle in load. The large difference is probably due to a difference in experimental conditions.

Figures 3.18 and 3.19 plot similar crown-invert and springline closure curves for  $\beta = 45^\circ$  under our standard loading path. These results are also consistent with those obtained previously for intact specimens. Comparison of crown-invert closures for monotonic and repeat loading again shows that repeat loading does not significantly influence



MA-5762-231

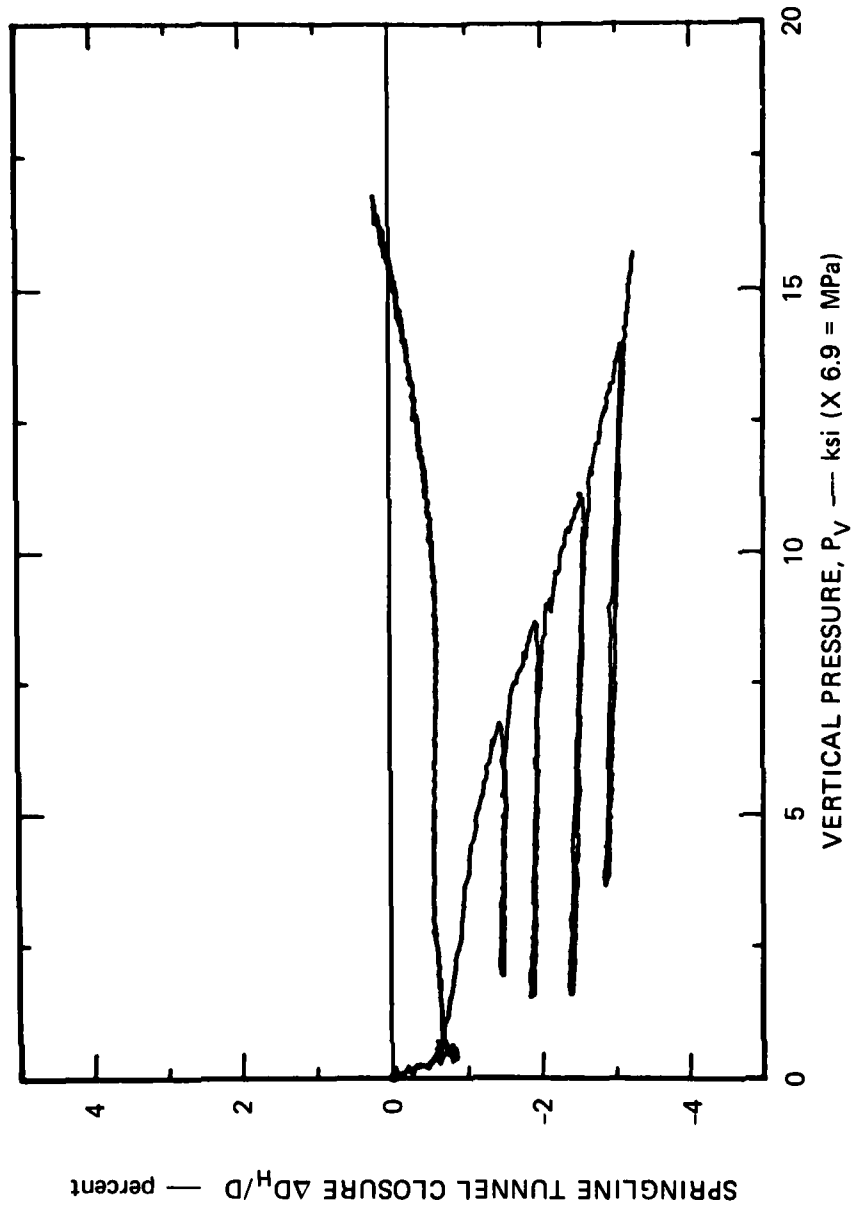
FIGURE 3.15 LOAD PATH FOR REPEAT LOADING TEST IN WHICH UNLOADING WAS UNDERCONFINED



MA-5762-232

FIGURE 3.16 CROWN-INVERT TUNNEL CLOSURE VERSUS VERTICAL PRESSURE FOR REPEAT AND MONOTONIC LOADING

Direct contact liner, 16A rock simulant,  $\beta = 90^\circ$



MA-5762-233

FIGURE 3.17 SPRINGLINE TUNNEL CLOSURE VERSUS VERTICAL PRESSURE FOR REPEAT AND MONOTONIC LOADING

Direct contact liner, 16A rock simulant,  $\beta = 0^\circ$ ,  $\gamma = 90^\circ$

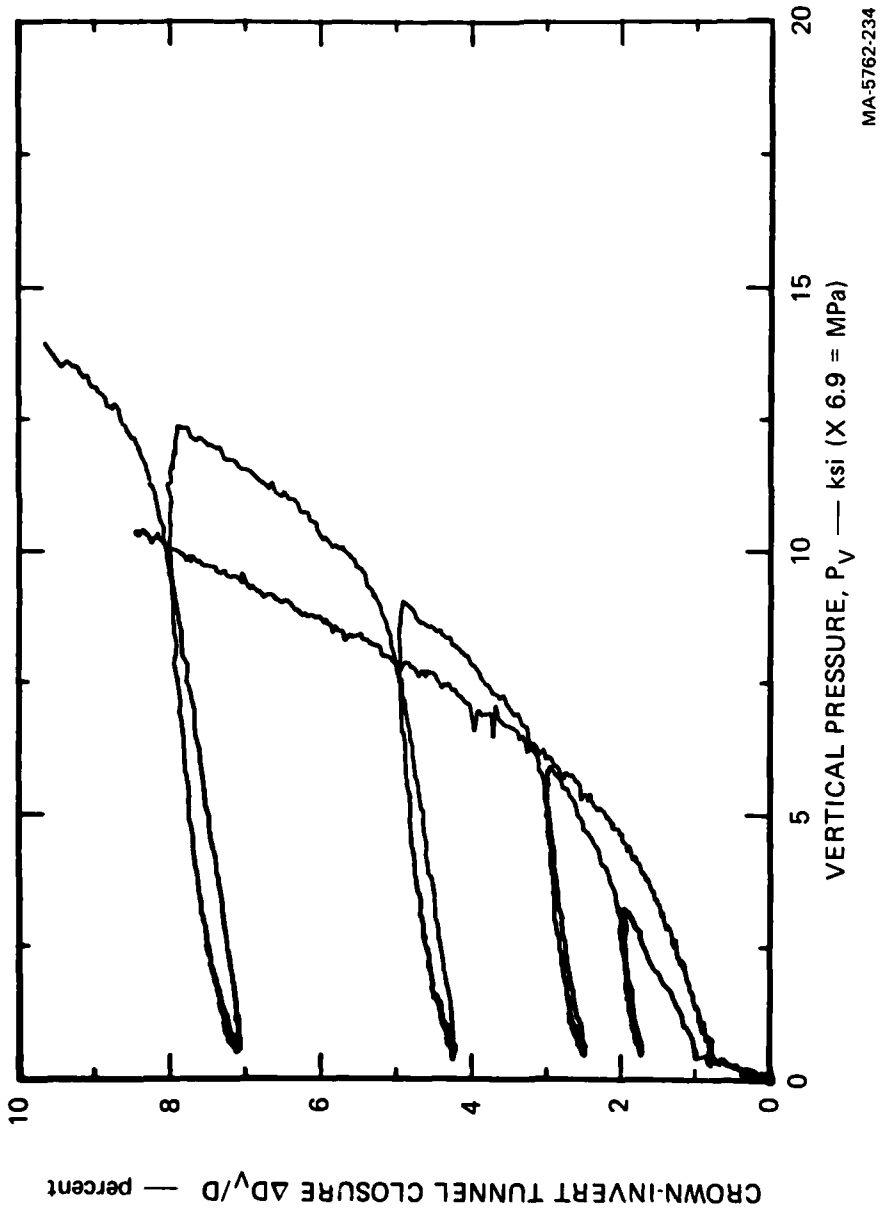


FIGURE 3.18 CROWN-INVERT TUNNEL CLOSURE VERSUS VERTICAL PRESSURE FOR REPEAT AND MONOTONIC LOADING  
 Direct contact liner, 16A rock simulant,  $\beta = 45^\circ$ ,  $\gamma = 90^\circ$  ( $\pi/4$  and  $\pi/2$  rad)

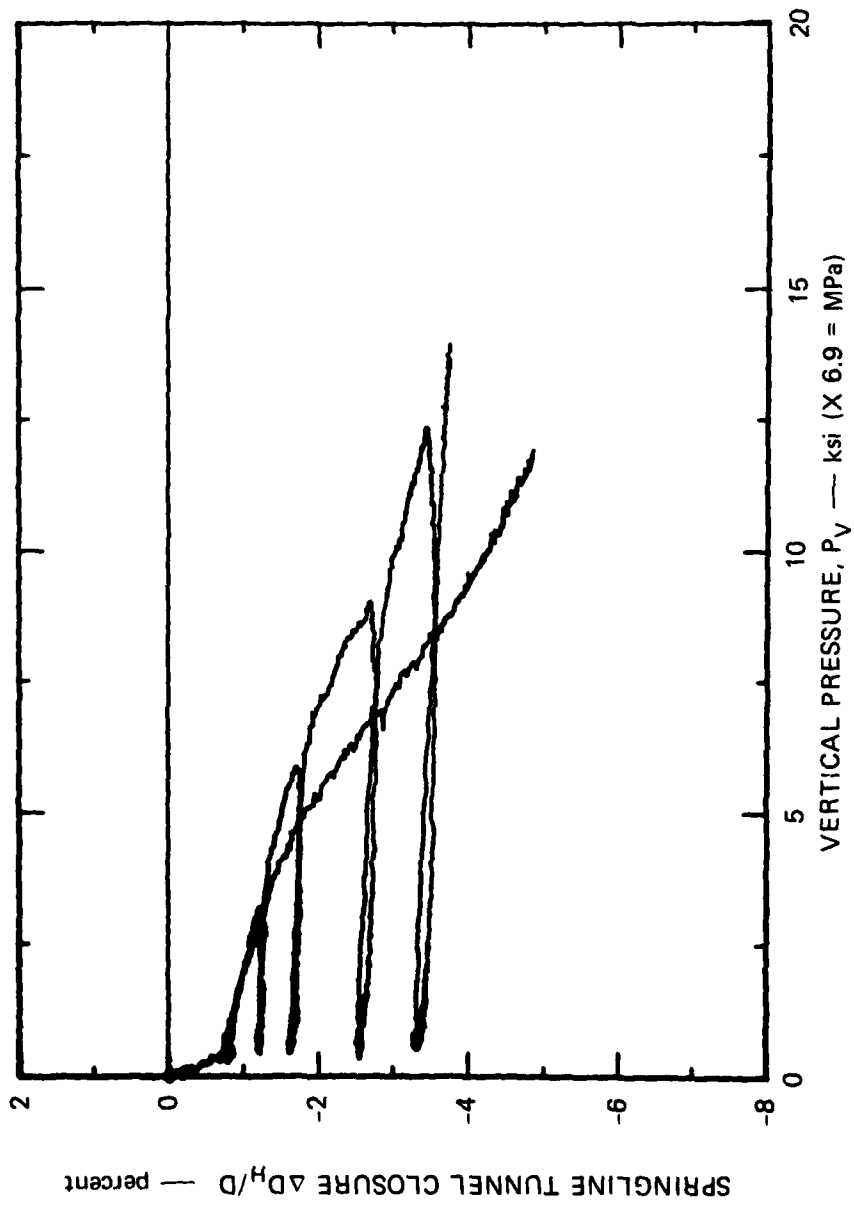
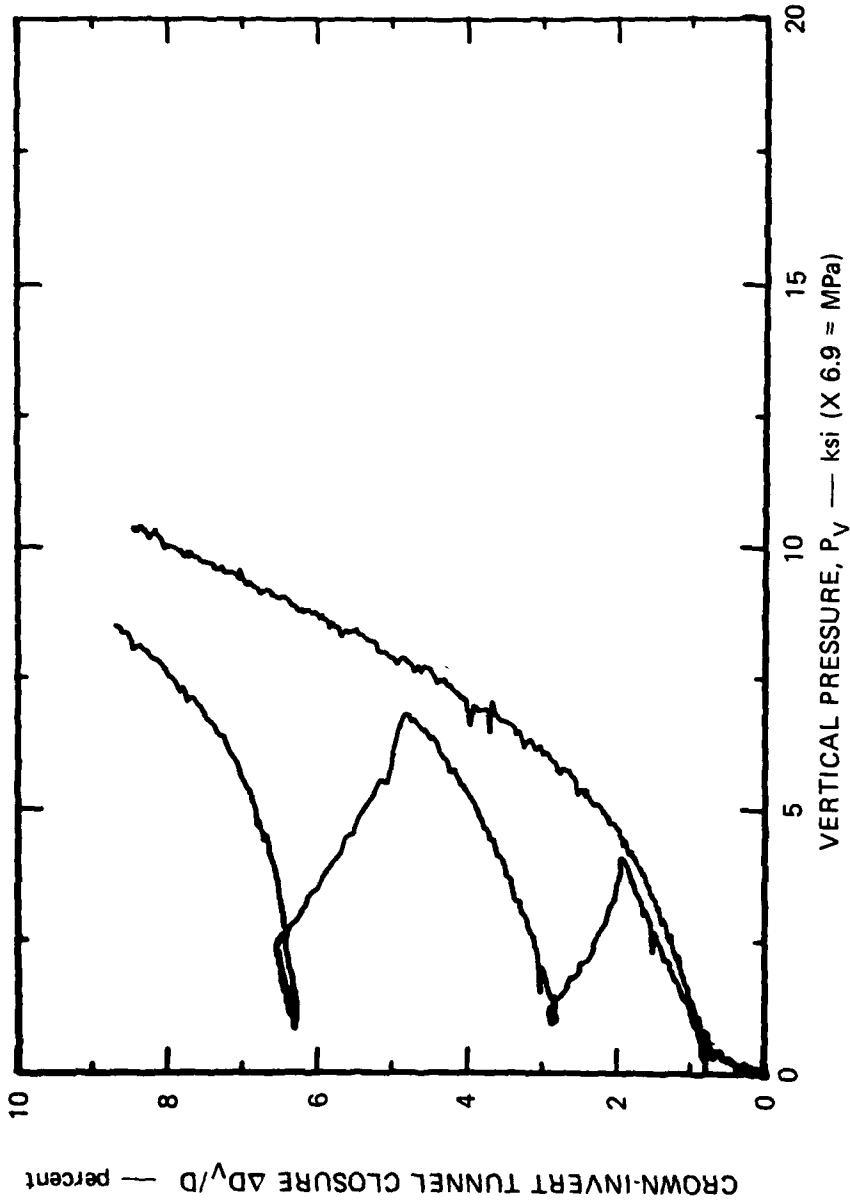


FIGURE 3.19 SPRINGLINE TUNNEL CLOSURE VERSUS VERTICAL PRESSURE FOR REPEAT AND MONOTONIC LOADING  
Direct contact liner, 16A rock simulatant,  $\beta = 45^\circ$ ,  $\gamma = 90^\circ$

the closure curve. In these tests, the specimen subjected to repeat loading happened to be stronger than the specimen loaded monotonically. The similarity in springline closure for monotonic and repeat loading is shown in Figure 3.19. The two loading curves are identical up to the first cycle in load. Then the outward springline motion increases more rapidly in the specimen that is loaded monotonically, consistent with the observation that this specimen was weaker.

Crown-invert and springline closures are plotted in Figures 3.20 and 3.21 as functions of vertical pressure for the third repeat loading test, in which the unloading portion of the cycle in load was underconfined (Figure 3.15). Corresponding closure curves for monotonic loading are plotted for comparison. These plots show that during unloading the magnitudes of both crown-invert and springline closures increase as the vertical pressure is reduced. This occurs because the lateral confining pressure decreases so rapidly that the specimen strength decreases faster than the reduction in vertical pressure. Near the end of unloading the magnitude of the closures does decrease, because the lateral confining pressure remains constant (nearly zero), so that the specimen strength does not decrease further.

These results, although obtained from a test on a jointed specimen, are not unique to tunnel deformation in jointed rock. They show that unless the specimen is suitably confined during unloading, tunnel closures sustained after peak load can be nearly as large as those reached at peak load. The results point out the importance of knowing the stress and strain paths in the field as the blast wave passes. For example, the confinement during the loading phase may be great enough so that the structure survives the peak load, but because of spherical divergence during the unloading phase the confinement drops rapidly and the structure could fail.



MA-5762-236

FIGURE 3.20 CROWN-INVERT TUNNEL CLOSURE VERSUS VERTICAL PRESSURE FOR REPEAT AND MONOTONIC LOADING WITH UNLOADING PART OF CYCLE IN LOAD UNDERCONFINED

Direct contact liner, 16A rock simulant,  $\beta = 45^\circ$ ,  $\gamma = 90^\circ$

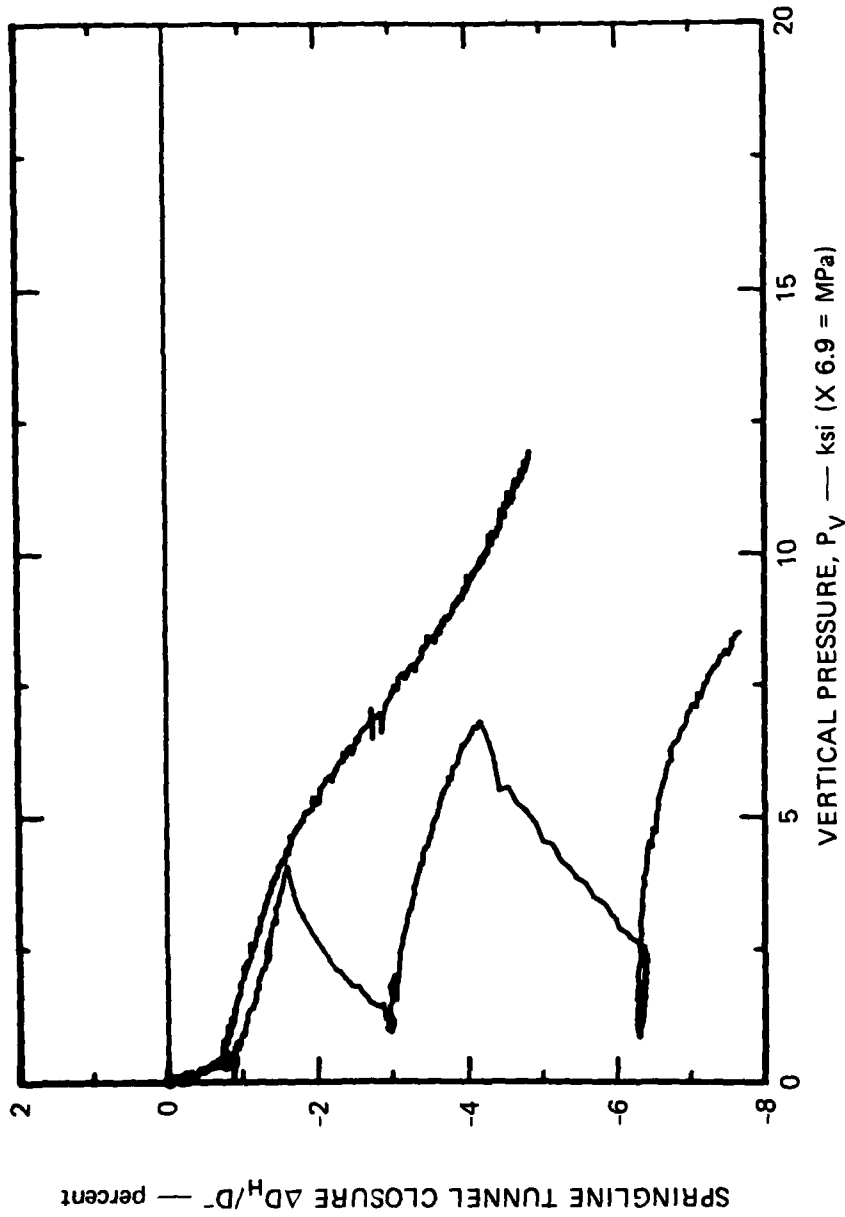


FIGURE 3.21 SPRINGLINE TUNNEL CLOSURE VERSUS VERTICAL PRESSURE FOR REPEAT AND MONOTONIC LOADING WITH UNLOADING PART OF CYCLE IN LOAD UNDERCONFINED

Direct contact liner, 16A rock simulant,  $\beta = 45^\circ$ ,  $\gamma = 90^\circ$

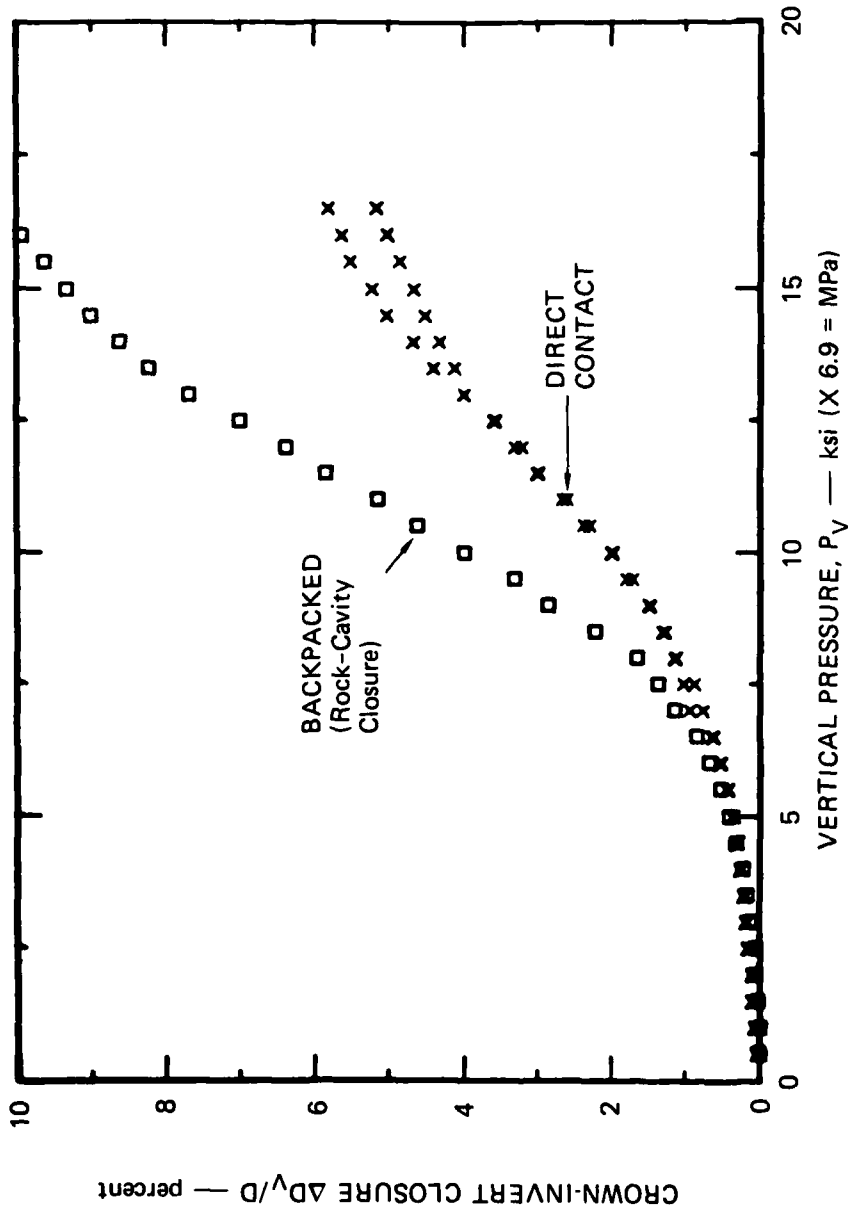
### 3.5 INFLUENCE OF STRUCTURE TYPE

We studied the influence on tunnel deformation of reinforcing structure type by testing specimens containing direct contact and backpacked structures. Tests were performed on intact and jointed specimens having three load-joint orientation angles,  $\beta = 0^\circ$ ,  $30^\circ$ , and  $45^\circ$ , all with a tunnel-joint orientation angle of  $\gamma = 90^\circ$ . Comparisons are made for rock-cavity closures because the liner closures for the backpacked structures are isolated from the rock cavity by the backpacking and are, of course, very small.

Figures 3.22 to 3.25 plot direct contact and backpacked structure crown-invert closure curves for intact and jointed specimens. The first three plots show qualitatively the same response: at low pressure the closure is the same for both structures. As the pressure increases, the closure curve for the backpacked structure becomes steeper than that for the direct contact structure. However, the fourth plot (Figure 3.25), for a load-joint orientation angle  $\beta = 45^\circ$ , shows that the two closure curves are coincident over the entire range of pressure. This is not expected, because the direct contact liner is stiffer than the polyurethane foam backpacking, and consequently the expected trend is that found in the first three plots, a steeper curve for the backpacked structure.

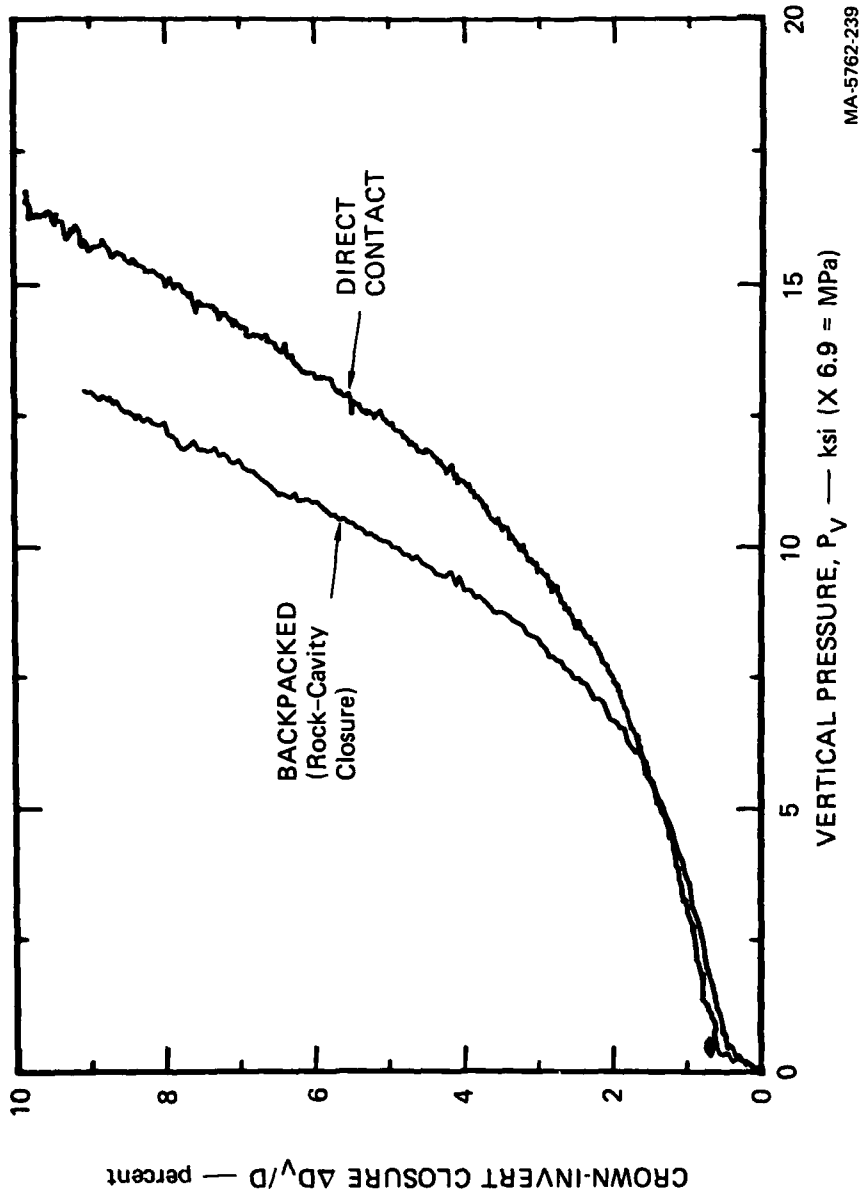
Figures 3.26 to 3.28 plot direct contact and backpacked structure springline closure curves for intact and jointed specimens. The plots show that springline closures for backpacked structures are more positive (less negative) than those for direct contact structures. (No springline closure record was obtained for the direct contact structure with  $\beta = 30^\circ$ .)

An important result shown by the closure plots for jointed specimens is that even though the backpacked structure exerts a pressure of only 500 psi (3.8 MPa) on the tunnel wall, there is no indication of block motion in the rock-cavity closure records. Furthermore, the polyurethane foam backpacking is easily penetrated and hence gives ample opportunity for block motion if this were a dominant response feature. Also, the



MA-5762-238

FIGURE 3.22 CROWN-INVERT CLOSURE VERSUS VERTICAL PRESSURE FOR BACKPACKED AND DIRECT CONTACT TUNNEL LINERS — INTACT 16A ROCK SIMULANT



MA-5762-239

FIGURE 3.23 CROWN-INVERT CLOSURE VERSUS VERTICAL PRESSURE FOR BACKPACKED AND DIRECT CONTACT TUNNEL LINERS — JOINTED 16A ROCK SIMULANT  
 $\beta = 0^\circ, \gamma = 90^\circ$

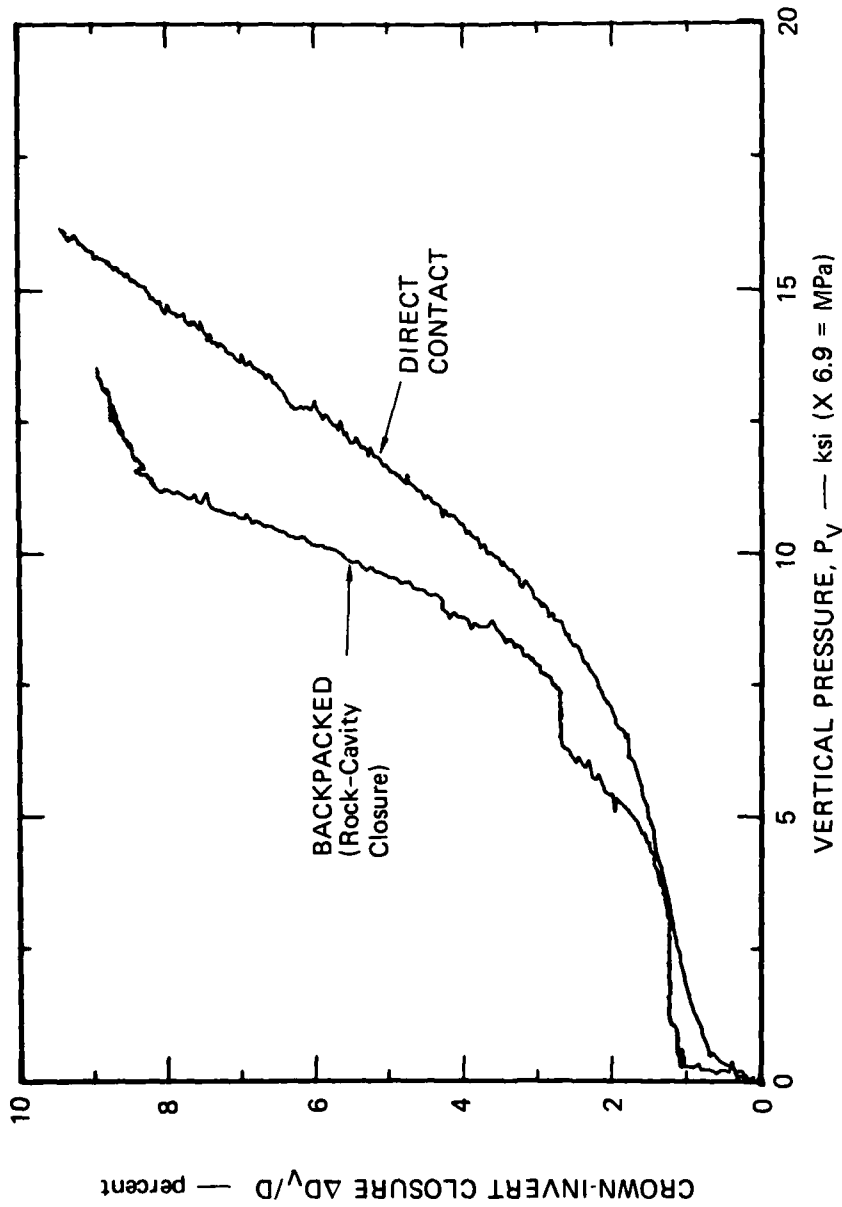
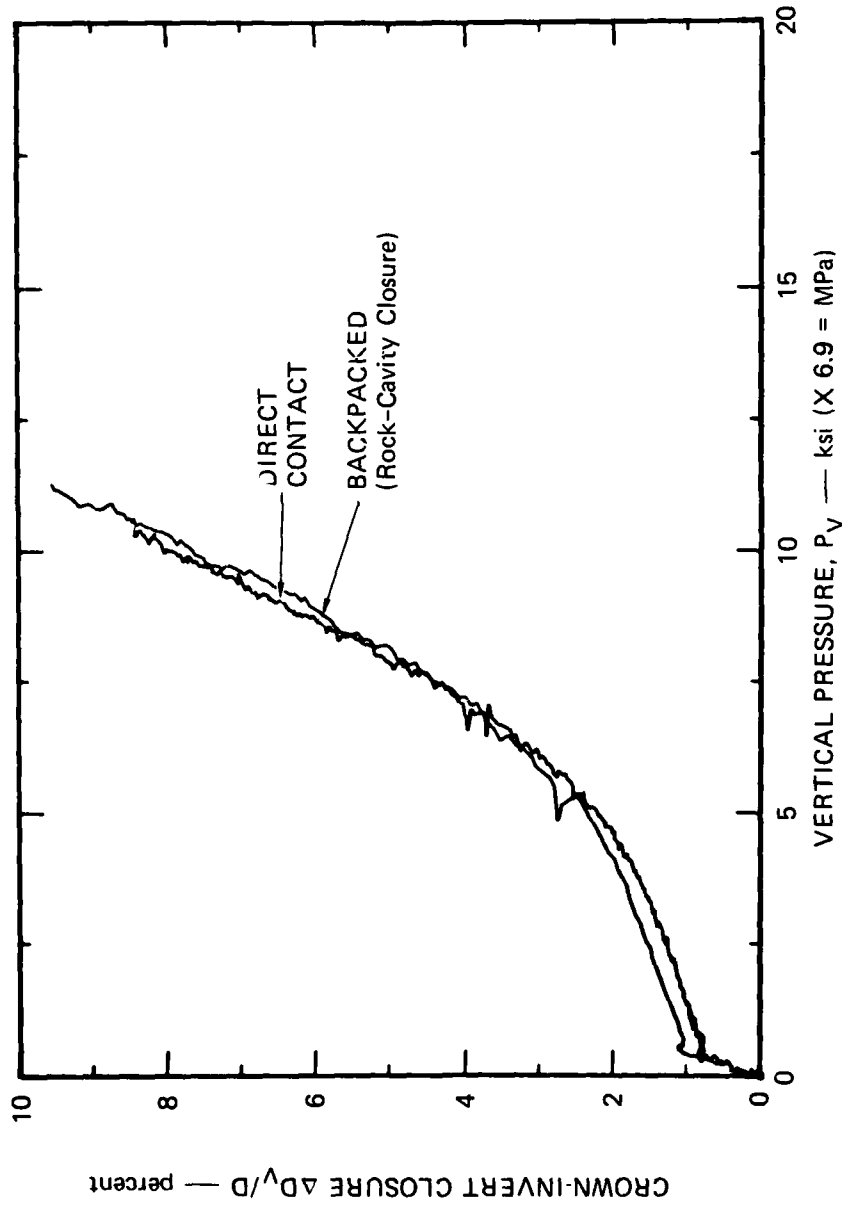
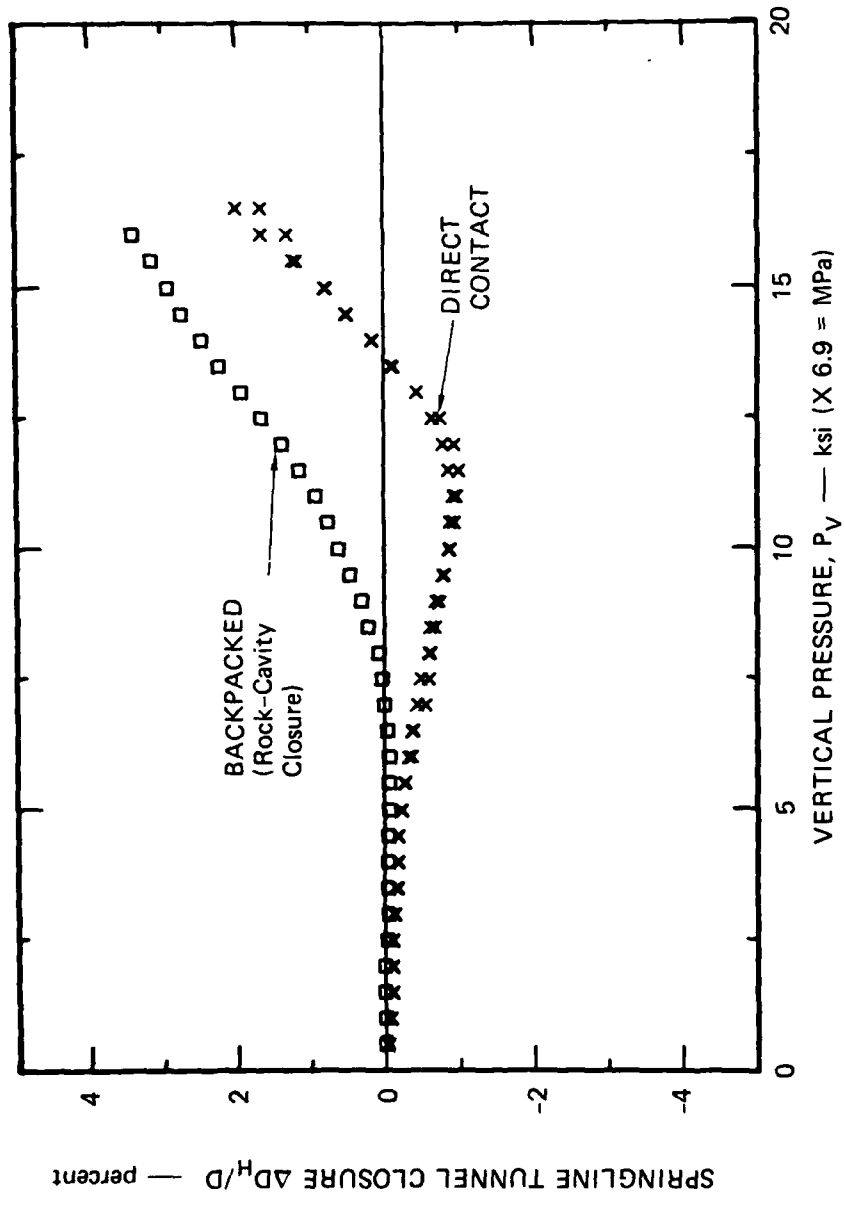


FIGURE 3.24 CROWN-INVERT CLOSURE VERSUS VERTICAL PRESSURE FOR BACKPACKED AND DIRECT CONTACT TUNNEL LINERS — JOINTED 16A ROCK SIMULANT  
 $\beta = 30^\circ, \gamma = 90^\circ$



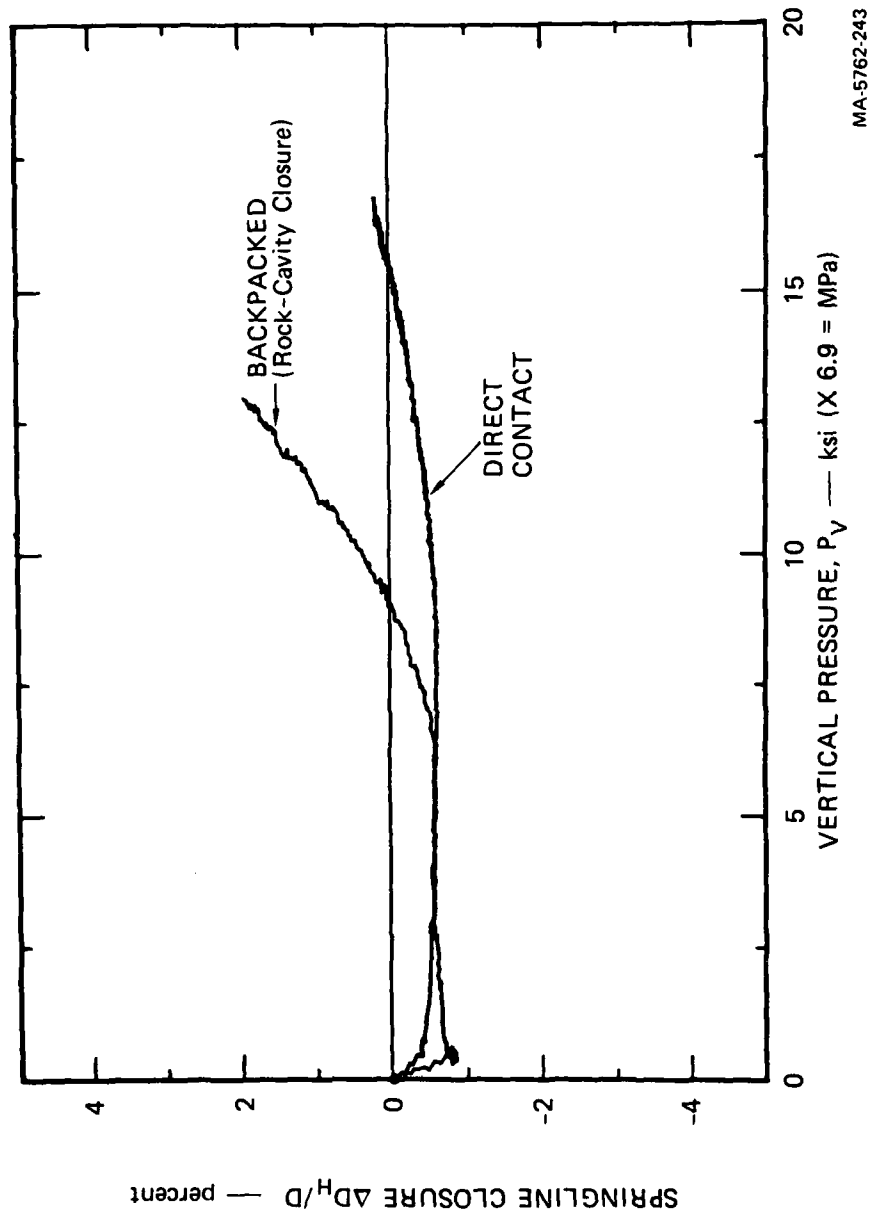
MA-5762-241

FIGURE 3.25 CROWN-INVERT CLOSURE VERSUS VERTICAL PRESSURE FOR BACKPACKED AND DIRECT CONTACT TUNNEL LINERS — JOINTED 16A ROCK SIMULANT  $\beta = 45^\circ, \gamma = 90^\circ$



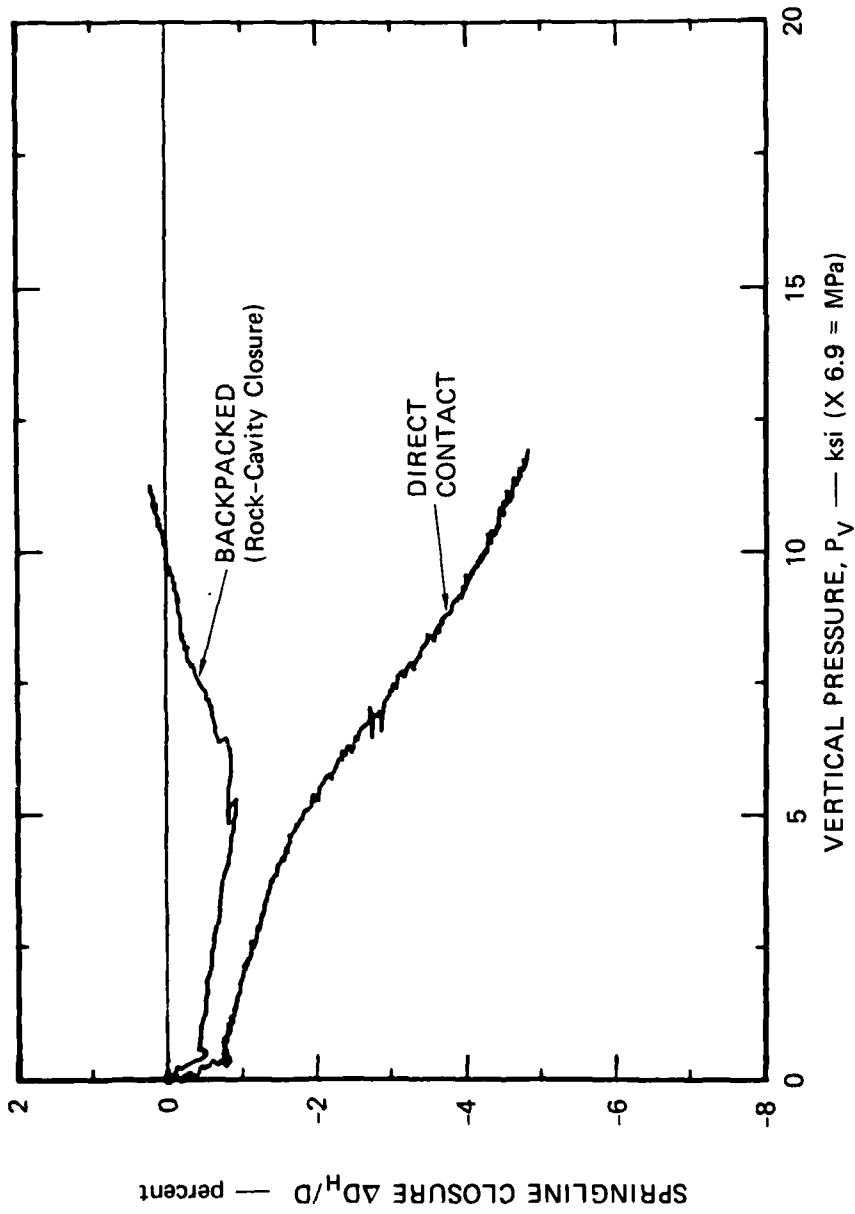
MA-5762-242

FIGURE 3.26 SPRINGLINE CLOSURE VERSUS VERTICAL PRESSURE FOR BACKPACKED AND DIRECT CONTACT TUNNEL LINERS — INTACT 16A ROCK SIMULANT



MA-5762-243

FIGURE 3.27 SPRINGLINE CLOSURE VERSUS VERTICAL PRESSURE FOR BACKPACKED AND DIRECT CONTACT TUNNEL LINERS — JOINTED 16A ROCK SIMULANT  $\beta = 0^\circ, \gamma = 90^\circ$



MA-5762-244

FIGURE 3.28 SPRINGLINE CLOSURE VERSUS VERTICAL PRESSURE FOR BACKPACKED AND DIRECT CONTACT TUNNEL LINERS — JOINTED 16A ROCK SIMULANT  
 $\beta = 45^\circ, \gamma = 90^\circ$

fluid boundary around the rock in the testing machine is 20 mm thick and would allow block motion. Hence we conclude that block motion is not prevented by the tunnel reinforcing structure or testing method, but rather by the frictional strength of the joints.

### 3.6 DISCUSSION

The tunnel deformation records show that, for the joint orientations and the tunnel-diameter-to-joint-spacing ratio tested, block motion does not contribute to tunnel deformation under static loading. Closure increases smoothly with pressure except during initial joint close-up. Also, examination of the posttest specimen cross sections given in Appendix A shows that the tunnel wall is still smooth (good examples are shown in Figures 3.5 to 3.7).

These results suggest that tunnel deformation in these experiments can be predicted theoretically by modelling the rock specimen as a homogeneous, transversely isotropic continuum. This approach ignores the finite spacing between the joints, and is exact only for infinite tunnel-diameter-to-joint-spacing ratio  $D/J$ . However, the test results indicate that  $D/J = 6$  is large enough to justify this simplifying assumption.

We used data provided by R. L. Stowe at WES<sup>[8]</sup> to evaluate the parameters in an elastic, perfectly plastic Mohr-Coulomb model. When the joints lie in a coordinate plane there are five independent nonzero components of the fourth-order tensor  $S_{ijkl}$  used in the constitutive relation that relates the elastic strain  $\epsilon_{ij}^e$  and the stress tensor  $\sigma_{kl}$ :

$$\epsilon_{ij}^e = S_{ijkl} \sigma_{kl}$$

When the  $x_2, x_3$  plane is the plane of isotropy (the joint normal points in the  $x_1$  direction), values for the elastic constants are

$$S_{1111} = 8.495 \times 10^{-7} \text{ psi}^{-1} = 1.230 \times 10^{-10} \text{ Pa}^{-1}$$

$$S_{1122} = -1.380 \times 10^{-7} \text{ psi}^{-1} = -2.000 \times 10^{-11} \text{ Pa}^{-1}$$

$$S_{2222} = 6.770 \times 10^{-7} \text{ psi}^{-1} = 9.820 \times 10^{-11} \text{ Pa}^{-1}$$

$$S_{2233} = -1.555 \times 10^{-7} \text{ psi}^{-1} = -2.255 \times 10^{-11} \text{ Pa}^{-1}$$

$$S_{1212} = 3.705 \times 10^{-6} \text{ psi}^{-1} = 5.370 \times 10^{-10} \text{ Pa}^{-1}$$

The remaining nonzero components can be determined by the relations

$$S_{2323} = 1/2 (S_{2222} - S_{2233}) \quad (\text{material symmetry})$$

$$S_{ijkl} = S_{jikl} \quad (\text{symmetry of elastic strain tensor})$$

$$S_{ijkl} = S_{ijlk} \quad (\text{symmetry of stress tensor})$$

$$S_{ijkl} = S_{klij} \quad (\text{existence of elastic potential})$$

WES data show that the friction angle  $\phi$  for a joint is the same as for intact material,  $\phi = 29^\circ$ . The cohesion  $c$  depends on direction: along the joint  $c = 0$ , but across the joint  $c = 1100 \text{ psi}$  (716 MPa), the value for intact 16A rock simulant.

Calculations have not been performed using this constitutive model because of time and money constraints. However, this approach should be investigated because it provides a theoretical tool that is a direct extension of the assumption of isotropy used to analyze data from intact specimens. Furthermore, in large scale field applications the tunnel-diameter-to-joint-spacing ratio will be much larger than that in these

laboratory tests, so that assumptions of homogeneity (smearing out the joints) are even more appropriate.

### 3.7 CONCLUSIONS

The results of twelve laboratory experiments to study the influence on tunnel deformation of joints and their orientation show:

- The load required to produce a specified crown-invert closure in jointed specimens is less than that required to produce the same closure in intact specimens. This decrease in load-bearing capacity depends on joint orientation; for small load-joint orientation angles,  $\beta \leq 30^\circ$ , the reduction in the vertical pressure required to produce a 5% crown-invert closure is less than 20%. However, for a larger load-joint orientation angle,  $\beta = 45^\circ$ , the reduction in pressure can be as great as 45%.
- For the load-joint orientation angle tested ( $\beta = 30^\circ$ ), changes in the tunnel-joint orientation angle  $\gamma$  do not influence crown-invert closure. However, greater outward springline motion was measured for larger tunnel-joint orientation angles.
- The response to repeat loading of tunnels in jointed specimens is qualitatively the same as that observed for tunnels in intact specimens: the load-bearing capacity of the specimen is not significantly influenced by repeat loading, closures during unloading and reloading lie long the same line, and a small increase in closure is sustained during each cycle in load.
- Backpacking effectively isolates the liner from rock-cavity deformation for all joint orientations tested. Even though rock-cavity closures depend on joint orientation, liner closures were nearly the same in all tests. This demonstrates again that liner deformation is determined primarily by the backpacking crush strength for loads and rock-cavity closures in the design range (before backpacking lock up).
- Test records and specimen posttest cross sections indicate that block motion is not a deformation mechanism. Some cracking perpendicular to the joints occurred near the tunnel; however, plasticity and local slipping on the joints appear to be the primary deformation mechanisms. This suggests that the specimen can be modelled as a homogeneous, transversely isotropic continuum. Parameters for an elastic, perfectly plastic Mohr-Coulomb model are given here from material property tests performed at WES.

Another important conclusion is not limited to jointed rock: if the specimen is underconfined during unloading, tunnel closure can increase beyond peak load closure.

## 4. REPEAT LOADING OF DEEP-BURIED STRUCTURES

### 4.1 INTRODUCTION

In this chapter we present results of both theoretical and experimental studies of repeat loading of deep-buried structures. The studies were undertaken because of the importance of understanding the response of deep-buried structures to repeat loading in the plastic range. Some scenarios for a deep-buried facility have repeat attacks by tens or more large bursts. Therefore, a primary factor to consider in choosing between several design concepts (for example, elastic versus yielding structures) is that the structure should be capable of withstanding repeated loading at levels below the single attack failure load without reaching the failure closure.

Our theoretical study uses both analytical and numerical solutions to provide understanding of the deformation of deep-buried structures under repeat loading. The analytical solution is similar to the analytical solution for monotonic loading of deep-buried structures. It is limited to axisymmetric loading, is valid over a limited but most useful range of constitutive parameters, and is restricted to a simple approximation of the reinforcing structure. The analytical solution provides insight into the influence on tunnel deformation of structure strength, design closure, and rock strength (cohesion and friction angle).

Our numerical solutions are obtained through the finite element method. Use of this numerical technique eliminates the restrictions on loading types, constitutive parameters, and reinforcing structure behavior. It allows us to treat uniaxial strain loading, complicated constitutive behavior, and the closure-dependent internal pressure supplied by real structures.

Our experimental study uses laboratory data taken from tests on a number of different rock-matching grouts, structure types, and loading

types. Most of these data were obtained in previous programs, and are simply repeated here. Exceptions are the results from tests on jointed rocks presented in the preceding chapter and the results from tests on backpacked structures presented in Appendix B.

The following section describes our analytical solution and gives several curves that show theoretically the influence on tunnel closure of structure strength, design closure, and rock strength. The third section describes our numerical technique and gives results that show the importance of accurately modeling reinforcing structures. Section 4.4 describes the test specimens. Section 4.5 presents experimental tunnel closure curves and the next section compares them with theoretical closure curves. Finally, we present our conclusions to date and make recommendations for future study, as well as for deep-buried structure design.

## 4.2 ANALYTICAL SOLUTION

### 4.2.1 Statement of Problem and Assumptions

The problem solved is that of a long circular tunnel of radius  $a$  in an infinite elastic-plastic medium that is subjected to repeated axisymmetric pressure at infinity. Plane strain deformation with yielding independent of  $\sigma_z$  is assumed. Constitutive parameters that meet this yielding constraint are given in reference [9]. The medium is isotropic, linear elastic, and perfectly plastic. The Mohr-Coulomb yield criterion is used with the associated flow rule for the plastic strain rates. Use of associated flow and consequent dilation gives conservative results (more tunnel closure) compared with nonassociated flow and zero dilatency [10]. Results with the associated flow theory also agree more closely with laboratory experiments [11].

With these assumptions, constitutive behavior of the medium is completely described by the elastic parameters  $\mu$  and  $\nu$  (shear modulus and Poisson's ratio) and the plastic strength parameters  $\sigma_u$  and  $N_\phi$  [unconfined compressive strength and pressure sensitivity coefficient

$N_\phi = (1+\sin\phi)/(1-\sin\phi)$ , where  $\phi$  is the angle of internal friction]. The tunnel reinforcement is represented as a constant pressure  $P_i$  within the tunnel. The magnitude of this pressure is small enough to cause no yielding before the pressure at infinity,  $P_o$ , is applied. This constraint is expressed in terms of constitutive parameters by the inequality  $P_i \leq \sigma_u/(N+1)$ .

The solution is developed in cylindrical coordinates  $r, \theta, z$ , with  $r$  being radius,  $\theta$  the angular coordinate, and  $z$  the coordinate along the tunnel axis. In the expressions for the radial and circumferential normal stresses,  $\sigma_{rr}$  and  $\sigma_{\theta\theta}$ , compression is taken as positive. In the expressions for the radial displacement,  $u_r$ , inward displacement (toward the center of the tunnel) is taken as positive. Tunnel closure  $\Delta D/D$  is simply  $u_r/r$  evaluated at  $r = a$ .

#### 4.2.2 Features of Tunnel Response

The problem can be divided into four loading stages:

- (1) Initial loading to some arbitrary pressure  $P_o = \bar{P}_o$
- (2) Unloading to  $P_o = 0$
- (3) Reloading to  $P_o = \bar{P}_o$
- (4) Loading Beyond  $\bar{P}_o$ .

Response in these four stages can be summarized with the aid of Figure 4.1. For initial loading, the material response is elastic at low pressure  $P_o$ . When  $P_o$  exceeds a certain value, the material yields at the tunnel and the yielded zone grows outward, Figure 4.1(a). The position of the elastic-plastic interface is denoted by  $R$ . Yielding takes place on the face of the yield surface for which the circumferential normal stress  $\sigma_{\theta\theta}$  is larger than the radial normal stress  $\sigma_{rr}$ . Loading is stopped when  $P_o = \bar{P}_o$  and the elastic-plastic interface is at the position  $r = \bar{R}$ .

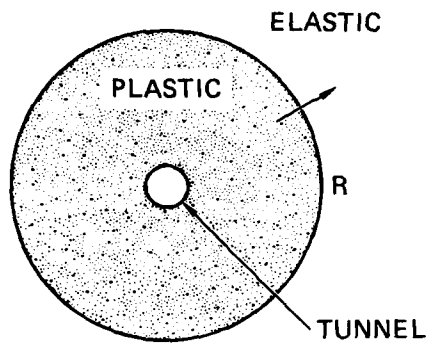
Because of the localized yielding ( $a \leq r \leq R$ ) in the first loading stage, the unloaded state at the end of stage two will have a residual stress field. If yielding is not too extensive, the material response to unloading will be entirely elastic. The residual stresses for this



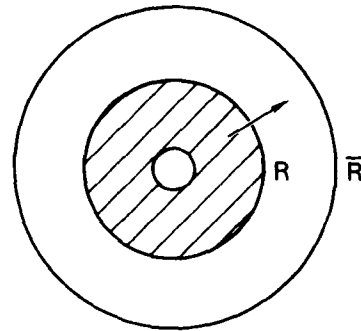
Yield by  $\sigma_{\theta\theta} = N_{\theta}\sigma_{rr} + \sigma_u$



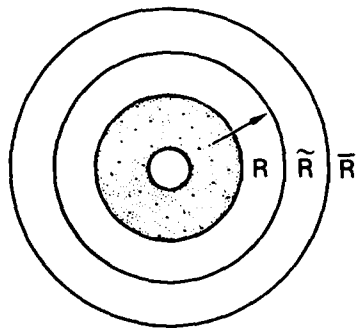
Yield by  $\sigma_{rr} = N_{\theta}\sigma_{\theta\theta} + \sigma_u$



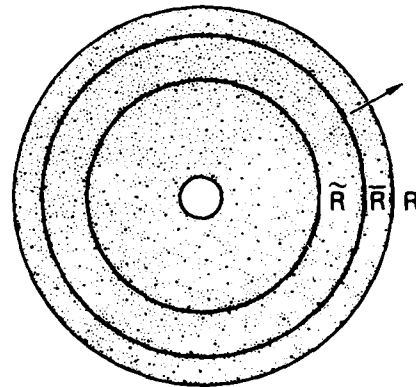
(a) INITIAL LOADING



(b) UNLOADING



(c) RELOADING,  $P_0 < \bar{P}_0$   
(for  $\bar{P}_0 > P_0^*$ )



(d) OVERLOADING,  $P_0 > \bar{P}_0$   
(for  $\bar{P}_0 > P_0^*$ )

MA-5762-110

FIGURE 4.1 POSITIONS OF CURRENT (SHADED) AND PREVIOUS PLASTIC ZONES DURING THE FOUR LOADING STAGES

case are found by simply adding to the elastic-plastic stress fields existing at load  $P_o = \bar{P}_o$  the stresses from the elastic solution to the problem with  $P_o = -P_o$ ,  $P_i = 0$ . However, if yielding is more extensive during loading, then before unloading is complete the stresses given by the addition of the elastic unloading stress fields will reach the yield surface, in this case on the face for which  $\sigma_{\theta\theta}$  is less than  $\sigma_{rr}$ . As unloading continues, a second elastic-plastic interface moves out from the tunnel, Figure 4.1(b). This is the new active interface and its position is again denoted by  $R$ . Although all material inside  $\bar{R}$  has yielded during the initial loading of stage one,  $R$  denotes the position of the active elastic-plastic interface: the interface between material that is currently responding elastically and that which is currently at yield. At the end of stage two (unloading),  $P_o = 0$  and the elastic-plastic interface that was active during unloading has reached a position inside  $\bar{R}$  given by  $r = \check{R}$ .

If the material response to unloading is entirely elastic, then its response to reloading to  $P_o = \bar{P}_o$  (stage three) will also be entirely elastic. When  $P_o = \bar{P}_o$ , all material inside  $\bar{R}$  is brought to incipient yield simultaneously. Response to loading beyond  $\bar{P}_o$  (stage four) in this case is simply a continuation of the elastic-plastic response to initial loading.

If the material yields during unloading, however, it will yield during reloading (stage three) before reaching  $P_o = \bar{P}_o$ . Yielding again begins at the tunnel, and the yielded zone grows as  $P_o$  increases. The stress state at yield has returned to the face of the yield surface that was activated during initial loading, the one for which  $\sigma_{\theta\theta}$  is greater than  $\sigma_{rr}$ . For  $P_o$  less than  $\bar{P}_o$ , the position of the active elastic-plastic interface  $R$  lies inside  $\check{R}$ , Figure 4.1(c). When  $P_o = \bar{P}_o$ , the entire annulus between  $\check{R}$  and  $\bar{R}$  is simultaneously at incipient yield, and for  $P_o$  greater than  $\bar{P}_o$  (stage four), the elastic-plastic interface  $R$  moves outward from  $\bar{R}$  through material that has not yielded previously, Figure 4.1(d).

#### 4.2.3 Method of Solution

For each of these four loading stages the method of solution is similar to that described previously [11]. The basic equations for axisymmetric elastic-plastic response are:

Equilibrium: 
$$\frac{\partial \sigma_{rr}}{\partial r} + \frac{\sigma_{rr} - \sigma_{\theta\theta}}{r} = 0$$

Strain displacement: 
$$\epsilon_{rr} = \frac{\partial u_r}{\partial r}, \quad \epsilon_{\theta\theta} = \frac{u_r}{r}$$

Compatibility: 
$$\frac{\partial \epsilon_{\theta\theta}}{\partial r} + \frac{\epsilon_{\theta\theta} - \epsilon_{rr}}{r} = 0$$

Hooke's law  
(elastic strain)

$$\epsilon_{rr} = \frac{1}{2\mu} \left[ (1-\nu)\sigma_{rr} - \nu\sigma_{\theta\theta} \right]$$

$$\epsilon_{\theta\theta} = \frac{1}{2\mu} \left[ (1-\nu)\sigma_{\theta\theta} - \nu\sigma_{rr} \right]$$

Mohr-Coulomb yield: 
$$\sigma_{\theta\theta} - N_\phi \sigma_{rr} - \sigma_u = 0 \quad \text{or} \quad \sigma_{rr} - N_\phi \sigma_{\theta\theta} - \sigma_u = 0$$

For brevity, we write only the final solutions for each loading stage. The intermediate equations are lengthy but are found by straightforward application of the basic equations above. The key observation for the solution is that, in spite of the several plastic regions in Figure 4.1, the current elastic-plastic configuration for all four loading stages is simply an infinite elastic zone surrounding a circular region that is entirely plastic, from  $r = a$  to the active plastic radius  $R$ . This situation is emphasized by the shading in Figure 4.1. Thus, the stress and displacement fields in the elastic region are always given by adding to the residual fields the elastic solution given below for a region with  $\sigma_{rr} = P_0$  at infinity and  $\sigma_{rr} = P_R$  at  $r = R$ .

Stresses in the current plastic zone are found by substituting from the appropriate yield condition into the equilibrium equation. This results in a linear ordinary differential equation of first order for  $\sigma_{rr}$ , with boundary condition  $\sigma_{rr} = P_i$  at  $r = a$ . This equation is easily integrated to give  $\sigma_{rr}$ . The expression for  $\sigma_{\theta\theta}$  is found by substituting the expression for  $\sigma_{rr}$  back into the appropriate yield condition.

The pressure  $P_R$  acting across the elastic-plastic interface is determined by requiring continuity of  $\sigma_{rr}$  at the elastic-plastic interface. The position of the elastic-plastic interface  $R$  is then found by requiring the stresses in the elastic region to satisfy the yield condition at the elastic-plastic interface.

The stresses, the position of the elastic-plastic interface, and the radial displacement in the elastic region are now determined. To complete the solution, we determine the radial displacement in the yielded zone.

The strain displacement relation  $\epsilon_{\theta\theta} = u_r/r$  is used to determine the radial displacement in the yielded zone. In this zone  $\epsilon_{\theta\theta}$  has both elastic and plastic components,  $\epsilon_{\theta\theta}^e$  and  $\epsilon_{\theta\theta}^p$ . The elastic component  $\epsilon_{\theta\theta}^e$  is written in terms of the stresses already determined by using Hooke's law. The plastic component  $\epsilon_{\theta\theta}^p$  is found by first using the flow rule to give the relationship between the plastic strain rates,  $\dot{\epsilon}_{\theta\theta}^p$  and  $\dot{\epsilon}_{rr}^p$ , and by then integrating this relationship and imposing the appropriate initial condition for plastic strain to determine  $\epsilon_{rr}^p$  in terms of  $\epsilon_{\theta\theta}^p$ . The resulting expressions for  $\epsilon_{rr}^p$ ,  $\epsilon_{\theta\theta}^p$ , and  $\epsilon_{rr}^e$  are then substituted into the compatibility equation to obtain a linear ordinary differential equation of first order for  $\epsilon_{\theta\theta}^p$ . The solution of this equation is chosen so that  $\epsilon_{\theta\theta}^p$ , and therefore  $u_r$ , is continuous across the active elastic-plastic interface.

Other steps in the solution, specific to each loading stage, are described below, as the complete solution is developed.

#### 4.2.4 Solution

Initial Loading to  $P_o = \bar{P}_o$ . At low pressure the response of the medium is entirely elastic. The stress and displacement fields are given by [12]:

$$\sigma_{rr} = P_o - \frac{a^2}{r^2} (P_o - P_i) \quad (1a)$$

$$\sigma_{\theta\theta} = P_o + \frac{a^2}{r^2} (P_o - P_i) \quad (1b)$$

$$\frac{u_r}{r} = \frac{1}{2\mu} \left[ P_o (1 - 2\nu) + \frac{a^2}{r^2} (P_o - P_i) \right] \quad (1c)$$

The medium yields at the tunnel when the pressure reaches the value given by

$$P_o = \frac{1}{2} \left[ (N_\phi + 1) P_i + \sigma_u \right] \quad (2)$$

As the pressure increases further, yielding spreads outward from the tunnel as shown in Figure 4.1(a). The yielded region is an annulus defined by  $a \leq r \leq R$ , where  $R$  is the elastic-plastic interface given by

$$R = a \left[ \frac{2}{N_\phi + 1} \left( P_o + \frac{\sigma_u}{N_\phi - 1} \right) / \left( P_i + \frac{\sigma_u}{N_\phi - 1} \right) \right]^{\frac{1}{N_\phi - 1}} \quad (3)$$

Inside the yielded region, the stresses satisfy the Mohr-Coulomb yield criterion

$$\sigma_{\theta\theta} - N_\phi \sigma_{rr} - \sigma_u = 0 \quad (4)$$

The stress and displacement fields in the yielded zone ( $a \leq r \leq R$ ) are given by

$$\sigma_{rr} = \left( P_i + \frac{\sigma_u}{N_\phi - 1} \right) \left( \frac{r}{a} \right)^{N_\phi - 1} - \frac{\sigma_u}{N_\phi - 1} \quad (5a)$$

$$\sigma_{\theta\theta} = N_\phi \left( P_i + \frac{\sigma_u}{N_\phi - 1} \right) \left( \frac{r}{a} \right)^{N_\phi - 1} - \frac{\sigma_u}{N_\phi - 1} \quad (5b)$$

$$\begin{aligned} \frac{u_r}{r} = \frac{1-\nu}{2\mu} \left( P_i + \frac{\sigma_u}{N_\phi - 1} \right) \left( \frac{r}{a} \right)^{N_\phi - 1} & \left\{ N_\phi - \frac{\nu}{1-\nu} + \frac{N_\phi^2 - 1}{2N_\phi} \left[ \left( \frac{R}{r} \right)^{2N_\phi} - 1 \right] \right\} \\ & - \frac{1-2\nu}{2\mu} \frac{\sigma_u}{N_\phi - 1} \end{aligned} \quad (5c)$$

In the elastic zone ( $R \leq r \leq \infty$ ), they are given by

$$\sigma_{rr} = P_o - \frac{R^2}{r^2} \left[ \frac{(N_\phi - 1)P_o + \sigma_u}{N_\phi + 1} \right] \quad (6a)$$

$$\sigma_{\theta\theta} = P_o + \frac{R^2}{r^2} \left[ \frac{(N_\phi - 1)P_o + \sigma_u}{N_\phi + 1} \right] \quad (6b)$$

$$\frac{u_r}{r} = \frac{1}{2\mu} \left\{ (1-2\nu)P_o + \frac{R^2}{r^2} \left[ \frac{(N_\phi - 1)P_o + \sigma_u}{N_\phi + 1} \right] \right\} \quad (6c)$$

The elastic fields (Eqs. 6) are similar to those for no yielding (Eqs. 1) except that the tunnel radius  $a$  is replaced by the elastic-plastic interface radius  $R$ , and the pressure in the tunnel is replaced by the pressure acting across the elastic-plastic interface.

The formulas for the yielded zone ( $a \leq r \leq R$ ) show that, once yielded, the stresses do not change as  $P_o$  increases; that is, as the plastic radius  $R$  moves out, it leaves behind a fixed stress field that does not change as  $P_o$  increases. The effect of the increased  $P_o$  is to increase both  $R$  and the radial displacement.

These expressions are identical to those reported in [11], in which the equations for radial displacement were used to predict tunnel closure for monotonic loading laboratory experiments.

Loading is stopped at some arbitrary pressure  $P_o = \bar{P}_o$ . The values of the elastic-plastic radius, the displacement, and the stresses at the end of loading are also denoted by the bar:

$$\text{at } P_o = \bar{P}_o; \quad R = \bar{R}, \quad \frac{u_r}{r} = \frac{\bar{u}_r}{r}, \quad \sigma_{rr} = \bar{\sigma}_{rr}, \quad \text{and} \quad \sigma_{\theta\theta} = \bar{\sigma}_{\theta\theta} .$$

Unloading to  $P_o = 0$ . Initially, the response is elastic as the pressure is reduced. The stress and displacement fields are obtained by adding to the barred fields (those at the end of the loading stage) the stresses and displacement that result from the elastic solution of the problem with  $P_i = 0$  and  $P_o = -\lambda \bar{P}_o$ . The total pressure in the tunnel is  $P_i$ , and at infinity is  $(1-\lambda)\bar{P}_o$ . The parameter  $\lambda$  is introduced to normalize the unloading:  $\lambda = 0$  gives no unloading,  $\lambda = 1$  gives complete unloading.

If  $P_o$  is small enough, the entire unloading is elastic. Specifically, if

$$\bar{P}_o \leq \frac{N_\phi^2 - 1}{2N_\phi} \left( P_i + \frac{\sigma_u}{N_\phi - 1} \right) \equiv P_o^* \quad (7)$$

the unloading is elastic and the stress and displacement fields everywhere are given by

$$\sigma_{rr} = \bar{\sigma}_{rr} - \lambda \bar{P}_o \left[ 1 - \frac{a^2}{r^2} \right] \quad (8a)$$

$$\sigma_{\theta\theta} = \bar{\sigma}_{\theta\theta} - \lambda \bar{P}_o \left[ 1 + \frac{a^2}{r^2} \right] \quad (8b)$$

$$\frac{u_r}{r} = \frac{\bar{u}_r}{r} - \frac{1}{2\mu} \left[ (1-2\nu) + \frac{a^2}{r^2} \right] \lambda \bar{P}_o \quad (8c)$$

For  $P_o$  larger than the value given in Eq. (7), unloading is elastic for

$$\lambda \leq \frac{1}{\bar{P}_o} \left[ \frac{N_\phi^2 - 1}{2N_\phi} \left( P_i + \frac{\sigma_u}{N_\phi - 1} \right) \right] \equiv \lambda_y \quad (9)$$

In this range the displacement and stresses are the same as for completely elastic unloading [Eqs. (8)]. The expression for  $\lambda_y$ , the value of the unloading parameter at incipient yield, shows that  $\lambda_y$  decreases as  $\bar{P}_o$  increases;  $\lambda_y$  is inversely proportional to  $\bar{P}_o$ , so the product  $\lambda_y \bar{P}_o$  is constant, independent of  $P_o$ . But this product, of course, is the reduction in pressure from  $\bar{P}_o$  to bring the medium to incipient yield at the tunnel, which is therefore independent of  $\bar{P}_o$ .

As unloading continues (as  $\lambda$  increases,  $\lambda > \lambda_y$ ), yielding begins around the tunnel and spreads outward from the tunnel as shown in Figure 4.1(b). In contrast to yielding during loading [Eq. (4)], the unloading yield occurs at stress states on the face of the Mohr-Coulomb yield surface that is defined by

$$\sigma_r - N_\phi \sigma_{\theta\theta} - \sigma_u = 0 \quad (10)$$

The position of the active elastic-plastic interface  $R$  is given by the solution of the implicit equation

$$\left( P_i + \frac{\sigma_u}{N_\phi - 1} \right) \left[ \left( \frac{a}{R} \right)^{\frac{N_\phi - 1}{N_\phi}} - N_\phi \left( \frac{R}{a} \right)^{N_\phi - 1} \right] + \frac{2N_\phi}{N_\phi + 1} \lambda \bar{P}_o = 0 \quad (11)$$

The stress and displacement fields in the yielded zone ( $a \leq r \leq R$ ) are given by

$$\sigma_{rr} = \left( P_i + \frac{\sigma_u}{N_\phi - 1} \right) \left( \frac{a}{r} \right)^{\frac{N_\phi - 1}{N_\phi}} - \frac{\sigma_u}{N_\phi - 1} \quad (12a)$$

$$\sigma_{\theta\theta} = \frac{1}{N_\phi} \left( P_i + \frac{\sigma_u}{N_\phi - 1} \right) \left( \frac{a}{r} \right)^{\frac{N_\phi - 1}{N_\phi}} - \frac{\sigma_u}{N_\phi - 1} \quad (12b)$$

$$\begin{aligned} & \frac{u_r}{r} = \frac{1 - \nu}{2\mu} \frac{N_\phi^2 - 1}{2N_\phi} \left( P_i + \frac{\sigma_u}{N_\phi - 1} \right) \times \\ & \times \left[ \left( \frac{r}{a} \right)^{N_\phi - 1} \left[ \left( \frac{\bar{R}}{r} \right)^{2N_\phi} + \frac{N_\phi^2 - 1}{N_\phi^2 + 1} \right] + \left( \frac{a}{r} \right)^{\frac{N_\phi - 1}{N_\phi}} \left[ 1 + \frac{2}{N_\phi^2 - 1} \left( 1 - \frac{\nu}{1 - \nu} N_\phi \right) \right] \right. \\ & \left. - \left( \frac{R}{r} \right)^{\frac{N_\phi + 1}{N_\phi}} \left[ \frac{2N_\phi^2}{N_\phi^2 + 1} \left( \frac{R}{a} \right)^{N_\phi - 1} + \left( \frac{a}{R} \right)^{\frac{N_\phi - 1}{N_\phi}} \right] \right] - \frac{1 - 2\nu}{2\mu} \frac{\sigma_u}{N_\phi - 1} \quad (12c) \end{aligned}$$

In the elastic zone ( $R \leq r \leq \infty$ ), they are given by

$$\sigma_{rr} = \bar{\sigma}_{rr} - \lambda \bar{P}_o + \frac{R^2}{r^2} (\lambda \bar{P}_o - P_R) \quad (13a)$$

$$\sigma_{\theta\theta} = \bar{\sigma}_{\theta\theta} - \lambda \bar{P}_o - \frac{R^2}{r^2} (\lambda \bar{P}_o - P_R) \quad (13b)$$

$$\frac{u_r}{r} = \frac{\bar{u}_r}{r} - \frac{1}{2\mu} \left[ \lambda \bar{P}_o (1 - 2\nu) + \frac{R^2}{r^2} (\lambda \bar{P}_o - P_R) \right] \quad (13c)$$

where

$$P_R = \left( P_i + \frac{\sigma_u}{N_\phi - 1} \right) \left[ \left( \frac{a}{R} \right)^{\frac{N_\phi - 1}{N_\phi}} - \left( \frac{R}{a} \right)^{N_\phi - 1} \right] \quad (13d)$$

By using the restriction on the internal pressure given earlier,  $P_i \leq \sigma_u / (N_\phi + 1)$ , we can show that the position of the elastic-plastic interface during unloading lies inside the position of that interface at the end of the initial loading phase; i.e.,  $R < \bar{R}$  for all  $\lambda$ .

When unloading is complete,  $\lambda = 1$ , the elastic-plastic radius is denoted by  $\bar{R}$  and the values of the stress and displacement fields are denoted by  $\tilde{\sigma}_{rr}$ ,  $\tilde{\sigma}_{\theta\theta}$ , and  $\tilde{u}_r/r$ .

Reloading to  $\bar{P}_o$ . Initially, the response to reloading is elastic. If there is no yielding during unloading ( $\bar{P}_o \leq P_o^*$ ) reloading is entirely elastic. The stress and displacement fields are given for all  $r \leq a$  by

$$\sigma_{rr} = \tilde{\sigma}_{rr} + P_o \left( 1 - \frac{a^2}{r^2} \right) \quad (14a)$$

$$\sigma_{\theta\theta} = \tilde{\sigma}_{\theta\theta} + P_o \left( 1 + \frac{a^2}{r^2} \right) \quad (14b)$$

$$\frac{u_r}{r} = \frac{\tilde{u}_r}{r} + \frac{1}{2\mu} \left[ 1 - 2\nu + \frac{a^2}{r^2} \right] P_o \quad (14c)$$

When the reloading reaches  $P_o = P_o$ , yield is incipient everywhere in the zone that yielded during initial loading ( $a < r \leq R$ ).

If there is yielding during unloading ( $\bar{P}_o \geq P_o^*$ ), the rock will yield during reloading before the pressure reaches  $P_o$ . During the initial elastic response, the stress and displacement fields are given by the same expressions found for totally elastic reloading [Eqs. (14)]. When the reloading pressure reaches a value given by

$$P_o = \frac{1}{2} \left[ (N_\phi + 1) P_i + \sigma_u \right] \quad (15)$$

the rock yields at the tunnel.

Notice that this pressure is independent of  $\bar{P}_0$ . The stress state at this yield lies on the same face of the yield surface that was active during initial loading, the face defined by

$$\sigma_{\theta\theta} - N_\phi \sigma_{rr} - \sigma_u = 0 \quad (16)$$

The position R of the active elastic-plastic interface, Figure 4.1(c), is determined by solving

$$\left( P_i + \frac{\sigma_u}{N_\phi - 1} \right) \left[ \left( \frac{a}{R} \right)^{\frac{N_\phi - 1}{N_\phi}} - N_\phi \left( \frac{R}{a} \right)^{N_\phi - 1} \right] + \frac{2N_\phi}{N_\phi + 1} P_o = 0 \quad (17)$$

If we compare this equation with Eq. (11), we find that for  $P_o < \bar{P}_0$ ,  $R < \hat{R}$ .

The stress and displacement fields in the yielded zone ( $a \leq r \leq R$ ) are given by

$$\sigma_{rr} = \left( P_i + \frac{\sigma_u}{N_\phi - 1} \right) \left( \frac{r}{a} \right)^{N_\phi - 1} - \frac{\sigma_u}{N_\phi - 1} \quad (18a)$$

$$\sigma_{\theta\theta} = N_\phi \left( P_i + \frac{\sigma_u}{N_\phi - 1} \right) \left( \frac{r}{a} \right)^{N_\phi - 1} - \frac{\sigma_u}{N_\phi - 1} \quad (18b)$$

$$\begin{aligned}
& \frac{u_r}{r} = \frac{1-\nu}{2\mu} \frac{(N_\phi^2-1)}{2N_\phi} \left( P_i + \frac{\sigma_u}{N_\phi-1} \right) \times \\
& \times \left\{ \left[ \frac{2N_\phi}{N_\phi^2-1} \left[ N_\phi - \frac{\nu}{1-\nu} \right] + \left[ \left( \frac{\bar{R}}{r} \right)^{2N_\phi} + \left( \frac{R}{r} \right)^{2N_\phi} - \frac{2}{N_\phi^2+1} \right] \right] \left( \frac{r}{a} \right)^{N_\phi-1} \right. \\
& \left. + \left[ \frac{N_\phi^2-1}{N_\phi^2+1} + \frac{2}{N_\phi^2+1} \left( \frac{R}{r} \right)^{\frac{N_\phi^2+1}{N_\phi}} \right] \left[ \left( \frac{a}{r} \right)^{\frac{N_\phi-1}{N_\phi}} - \left( \frac{\tilde{R}}{r} \right)^{\frac{N_\phi+1}{N_\phi}} \right] \times \right. \\
& \left. \times \left[ \left( \frac{a}{\tilde{R}} \right)^{\frac{N_\phi-1}{N_\phi}} + \frac{2N_\phi^2}{N_\phi^2+1} \left( \frac{\tilde{R}}{a} \right)^{N_\phi-1} \right] \right] - \frac{1-2\nu}{2\mu} \frac{\sigma_u}{N_\phi-1}
\end{aligned} \tag{18c}$$

In the elastic zone ( $R \leq r \leq \infty$ ), they are given by

$$\sigma_{rr} = \tilde{\sigma}_{rr} + P_o - \frac{R^2}{r^2} \left\{ P_o - \left( P_i + \frac{\sigma_u}{N_\phi-1} \right) \left[ \left( \frac{R}{a} \right)^{N_\phi-1} - \left( \frac{a}{R} \right)^{\frac{N_\phi-1}{N_\phi}} \right] \right\} \tag{19a}$$

$$\sigma_{\theta\theta} = \tilde{\sigma}_{\theta\theta} + P_o + \frac{R^2}{r^2} \left\{ P_o - \left( P_i + \frac{\sigma_u}{N_\phi-1} \right) \left[ \left( \frac{R}{a} \right)^{N_\phi-1} - \left( \frac{a}{R} \right)^{\frac{N_\phi-1}{N_\phi}} \right] \right\} \tag{19b}$$

$$\frac{u_r}{r} = \frac{\tilde{u}_r}{r} + \frac{1}{2\mu} \left[ P_o(1-2\nu) + \frac{R^2}{r^2} \left\{ P_o - \left( P_i + \frac{\sigma_u}{N_\phi-1} \right) \left[ \left( \frac{R}{a} \right)^{N_\phi-1} - \left( \frac{a}{R} \right)^{\frac{N_\phi-1}{N_\phi}} \right] \right\} \right] \tag{19c}$$

When  $P_o = \bar{P}_o$ , the annulus that yielded during initial loading but not during unloading, i.e., the region defined by  $R \leq r \leq \bar{R}$ , is at incipient yield throughout the entire region. This is the generalization of the reloading yield onset described previously for  $\bar{P}_o < P_o^*$ . For

brevity, Figures 4.1(c) and 4.1(d) are drawn only for this more general situation, i.e., only for  $P_o < P_o^*$ .

The additional closure sustained during the cycle in load,  $\Delta(\Delta D/D)$ , can be determined by finding the difference between the displacement fields  $u_r/r$  at the beginning and the end of the cycle (both at  $P_o = \bar{P}_o$ ) and evaluating this difference at the tunnel wall,  $r = a$ . For a cycle in which unloading and reloading are entirely elastic

$$\Delta\left(\frac{\Delta D}{D}\right) = 0 \quad (20)$$

However, if yielding occurs during the cycle, then

$$\Delta\left(\frac{\Delta D}{D}\right) = \frac{1-\nu}{2\mu} \frac{N_\phi^2-1}{2N_\phi} \left(P_i + \frac{\sigma_u}{N_\phi-1}\right) \left[ \left(\frac{\tilde{R}}{a}\right)^{2N_\phi} - \left(\frac{\tilde{R}}{a}\right)^{\frac{2}{N_\phi}} - 2 \frac{N_\phi^2-1}{N_\phi^2+1} \left[ \left(\frac{\tilde{R}}{a}\right)^{\frac{N_\phi^2+1}{N_\phi}} - 1 \right] \right] \quad (21)$$

Loading Beyond  $\bar{P}_o$ . As the load increases beyond  $\bar{P}_o$ , the active elastic-plastic interface moves outward from  $\bar{R}$  as shown in Figure 4.1(d). Its position is given by

$$R = a \left[ \frac{2}{N_\phi+1} \left(P_o + \frac{\sigma_u}{N_\phi-1}\right) \right]^{1/N_\phi} \left[ P_i + \frac{\sigma_u}{N_\phi-1} \right]^{N_\phi-1} \quad (22)$$

This is the same expression as for initial loading [Eq. (3)].

The stress field is given by exactly the same expressions as for initial loading [Eqs. (5a,b); Eqs. (6a,b)]: cycling the load at  $\bar{P}_o$  does not affect the stresses for loading above  $\bar{P}_o$ , even if the material yields during unloading and reloading.

The displacement field, however, is unaffected by the cycle in load only if no yielding occurred during unloading and reloading. If yielding during unloading does occur, the displacement field in the zone

$a \leq r \leq \tilde{R}$  is different from that obtained for initial loading. The displacement field in this case, for the region that yielded during unloading, ( $a \leq r \leq \tilde{R}$ ), is given by

$$\begin{aligned} \frac{u_r}{r} = & \frac{1-\nu}{2\mu} \frac{N_\phi^2-1}{2N_\phi} \left( P_i + \frac{\sigma_u}{N_\phi-1} \right) \times \\ & \times \left\{ \left[ \left( \frac{R}{r} \right)^{2N_\phi} - \frac{N_\phi^2-1}{N_\phi^2+1} \left( \frac{\tilde{R}}{r} \right)^{2N_\phi} - \frac{2}{N_\phi^2+1} + \frac{2N_\phi}{N_\phi^2-1} \left( N_\phi - \frac{\nu}{1-\nu} \right) \right] \left( \frac{r}{a} \right)^{N_\phi-1} \right. \\ & + \frac{N_\phi^2-1}{N_\phi^2+1} \left[ 1 - \left( \frac{\tilde{R}}{r} \right)^{\frac{N_\phi^2+1}{N_\phi}} \right] \left( \frac{a}{r} \right)^{\frac{N_\phi-1}{N_\phi}} + \left[ \left( \frac{\tilde{R}}{r} \right)^{N_\phi+1} - \left( \frac{\tilde{R}}{r} \right)^{\frac{N_\phi+1}{N_\phi}} \right] \times \\ & \left. \times \left[ \left( \frac{a}{\tilde{R}} \right)^{\frac{N_\phi-1}{N_\phi}} + \frac{2N_\phi^2}{N_\phi^2+1} \left( \frac{\tilde{R}}{a} \right)^{N_\phi-1} \right] \right\} - \frac{1-2\nu}{2\mu} \frac{\sigma_u}{N_\phi-1} \end{aligned} \quad (23)$$

In the remaining yielded region ( $\tilde{R} \leq r \leq R$ ), the displacement field is given by

$$\frac{u_r}{r} = \frac{1-\nu}{2\mu} \left( P_i + \frac{\sigma_u}{N_\phi-1} \right) \left( \frac{r}{a} \right)^{N_\phi-1} \left\{ N_\phi - \frac{\nu}{1-\nu} + \frac{N_\phi^2-1}{2N_\phi} \left[ \left( \frac{R}{r} \right)^{2N_\phi} - 1 \right] \right\} - \frac{1-2\nu}{2\mu} \frac{\sigma_u}{N_\phi-1} \quad (24)$$

In the elastic region ( $R \leq r \leq \infty$ ), the displacement field is given by

$$\frac{u_r}{r} = \frac{1}{2\mu} \left\{ (1-2\nu)P_o + \frac{R^2}{r^2} \left[ \frac{(N_\phi-1)P_o + \sigma_u}{N_\phi+1} \right] \right\} \quad (25)$$

The tunnel-closure-versus-pressure curves for  $P_o$  greater than  $\bar{P}_o$  are the same as would be obtained under monotonic loading to these pressures, except that if yielding occurs during unloading, the curve is shifted along the tunnel closure axis by the additional closure  $\Delta(\Delta D/D)$  sustained during the cycle in load.

#### 4.2.5 Parameter Study

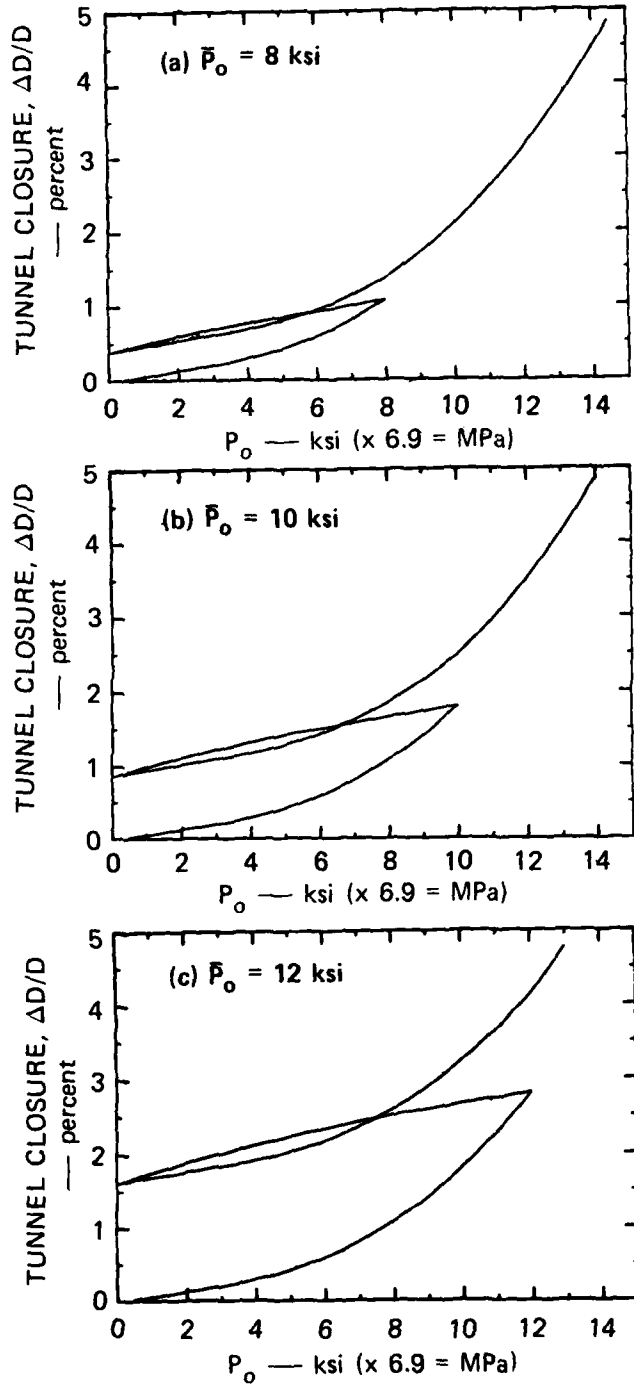
Results are now presented to illustrate how tunnel closure is influenced by the pressure at which the load is cycled,  $\bar{P}_o$ , the internal pressure  $P_i$  (reinforcement structure strength), and the material unconfined compressive strength  $\sigma_u$  and pressure sensitivity coefficient  $N_\phi$ . This is done by using the formulas for radial displacement given in the previous section to calculate tunnel closure as a function of pressure for a few examples.

Effect of  $\bar{P}_o$ . Three calculations were performed to study the effect of the pressure at which the load is cycled,  $\bar{P}_o$ . In these examples rock properties are: shear modulus  $\mu = 1 \times 10^6$  psi (6.9 GPa), Poisson's ratio  $\nu = 0.25$ , unconfined compressive strength  $\sigma_u = 4000$  psi (27.6 MPa), and pressure sensitivity coefficient  $N_\phi = 3$  ( $\phi = 30^\circ$ ). The tunnel reinforcement pressure is  $P_i = 500$  psi (3.5 MPa). Initial yield of the rock occurs at  $P_o = 3000$  psi (20.7 MPa) and yielding occurs during unloading for  $\bar{P}_o > 3333$  psi (23.0 MPa).

Figure 4.2 plots tunnel closure as a function of pressure for maximum pressures  $\bar{P}_o$  on first loading of 8, 10, and 12 ksi (55, 69, and 83 MPa). The three graphs all show the same trend. At low pressure the medium is elastic and closure depends linearly on pressure; the slope is determined by the two elastic constants. As the medium yields, the closure curves bend upward, becoming increasingly steeper as the plastic zone spreads from the tunnel.

Unloading from  $P_o$  is initially elastic at the same slope as in the low pressure part of the initial loading curve. When the medium yields, the closure decreases more rapidly as the load is removed, that is, the curves bend downward.

At the start of reloading, response is elastic, the closure curve is linear and again has the elastic slope. When the medium yields, the closure curve again bends upward. However, at any given pressure, the reloading curve is not as steep as the initial loading curve. For pressures above  $\bar{P}_o$ , the closure curve is the same as it is for monotonic loading, but shifted up by  $\Delta(\Delta D/D)$ , the closure change at  $P_o = \bar{P}_o$ .



MA-5762-247A

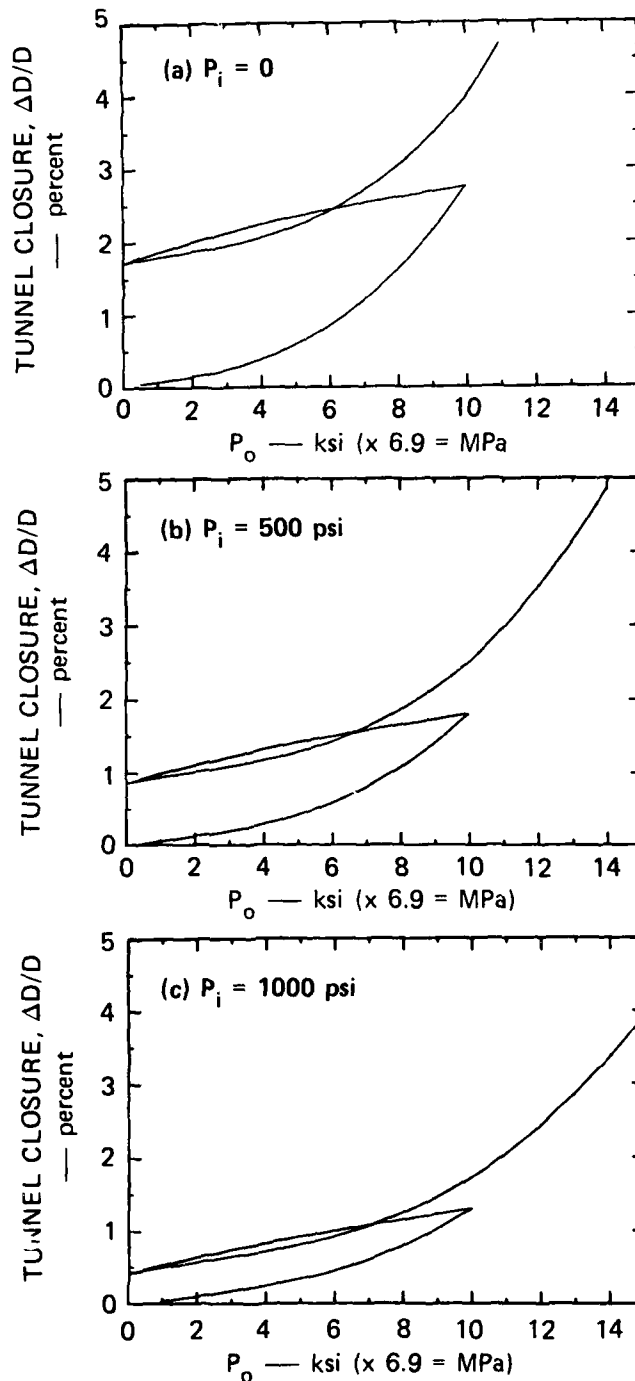
FIGURE 4.2 EFFECT OF  $\bar{P}_o$  ON RELOAD CLOSURE  
 $P_i = 0.5$  ksi,  $\sigma_u = 4$  ksi,  $N_\phi = 3$   
 (1 ksi = 6.9 MPa)

Comparison of the graphs shows that the larger the value of  $\bar{P}_o$ , the larger is the loop formed by the unloading and reloading parts of the closure curve. Also, the larger the value of  $\bar{P}_o$ , the greater the additional tunnel closure sustained during the cycle in load: at  $\bar{P}_o = 12$  ksi (83 MPa), the additional closure is more than 4-1/2 times as great as at  $\bar{P}_o = 8$  ksi (55 MPa).

Effect of  $P_i$ . For these examples the same material properties were used as in the study of the effect of  $\bar{P}_o$ . Tunnel closure curves were calculated for three different values of internal pressure:  $P_i = 0, 500, \text{ and } 1000$  psi (0, 3.5, and 6.89 MPa). The load was cycled at  $\bar{P}_o = 10$  ksi (68.9 MPa). Figure 4.3 gives the resulting plots of tunnel closure as a function of pressure. The plots show that the size of the unloading-reloading loops and the additional tunnel closure sustained during the cycle in load both decrease as the internal pressure increases.

However, if the load is cycled at a common tunnel closure (say  $\Delta D/D = 2\%$ ) rather than at a common pressure, then the width of the unload-reload loops and the magnitude of  $\Delta(\Delta D/D)$  does not change significantly as the internal pressure  $P_i$  changes. This result is shown in Figure 4.4, in which tunnel closure is plotted as a function of pressure out to closures of approximately 2% for the same three internal pressures as in Figure 4.3. This indicates that the additional closure sustained during a cycle in load in a particular material depends mainly on the design or working closure (the closure at the working load  $\bar{P}_o$ ).

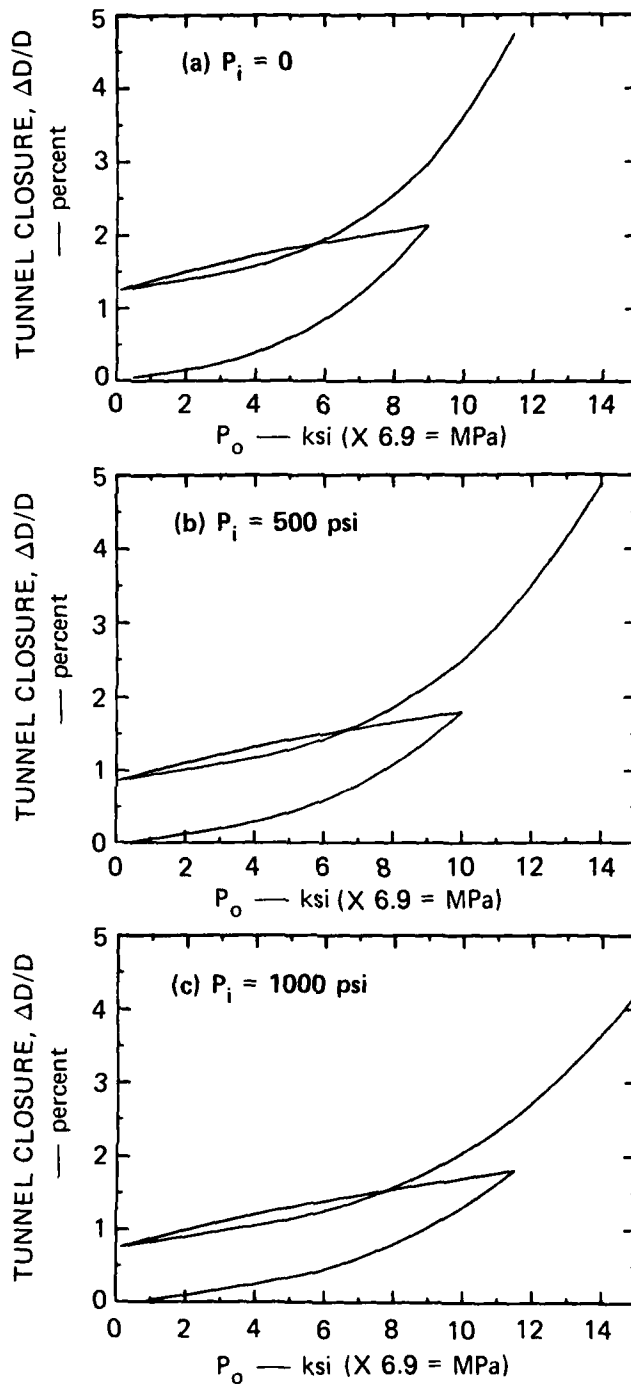
Effects of  $\sigma_u$  and  $N_\phi$ . To study how tunnel closure is influenced by the unconfined compressive strength and the pressure sensitivity coefficient, calculations were performed for two values of  $\sigma_u$  and two values of  $N_\phi$ . The elastic properties were the same as in the other parameter studies and the internal pressure was  $P_i = 0$ . Load was again cycled at a common value of tunnel closure, approximately 2%. Results are plotted in Figure 4.5. The effect of changes in the unconfined compressive strength  $\sigma_u$  can be seen by comparing Figures 4.5(a) and 4.5(b) to Figures 4.5(c) and 4.5(d). Figures 4.5(a) and 4.5(b) are plots of tunnel closure for  $N_\phi = 3$  ( $\phi = 30^\circ$ ), and  $\sigma_u = 2$  ksi and 4 ksi (13.8 and



MA-5762-246A

FIGURE 4.3 EFFECT OF  $P_i$  ON RELOAD CLOSURE WITH FIXED LOAD  $\bar{P}_o$

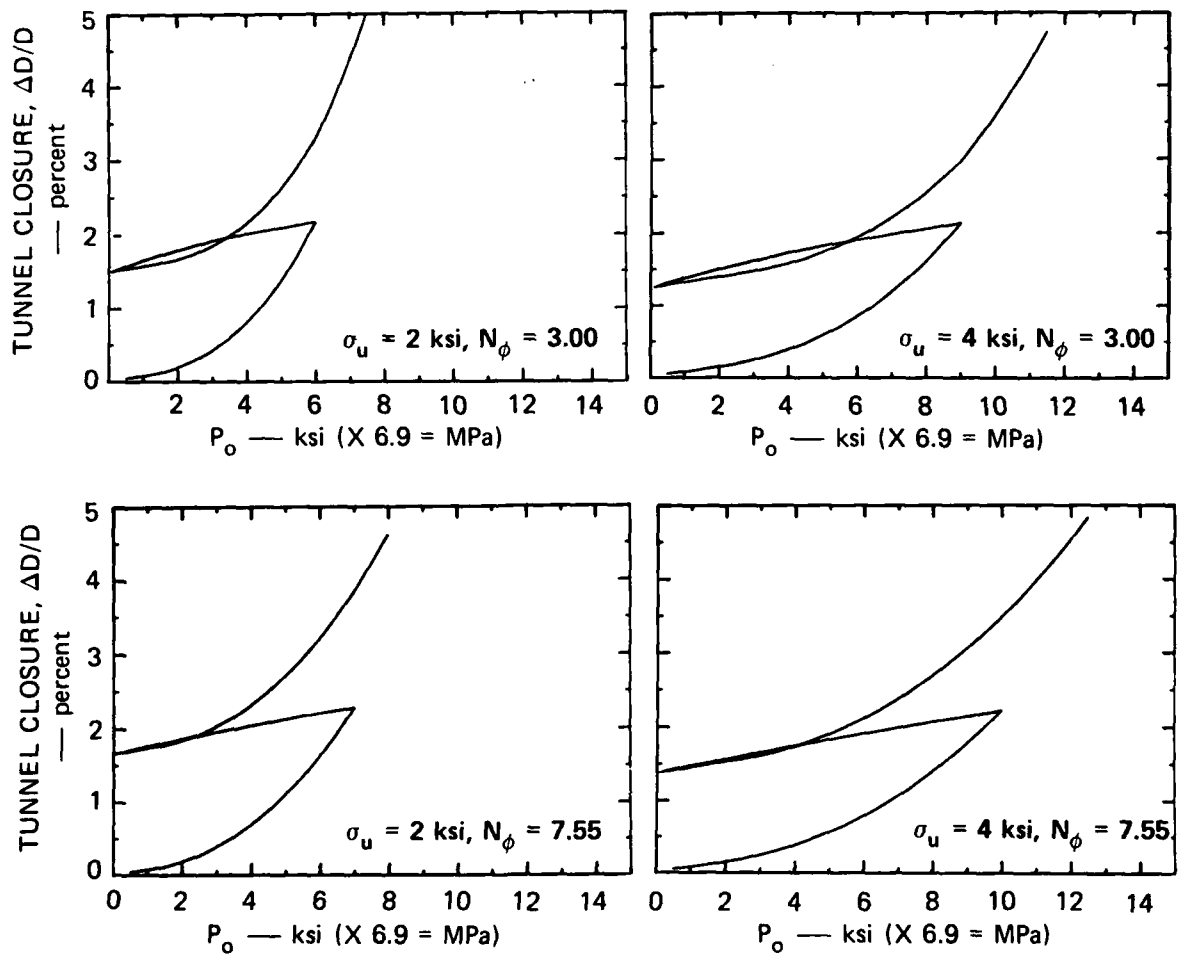
$\bar{P}_o = 10$  ksi,  $\sigma_u = 4$  ksi,  $N_\phi = 3$   
 (1 ksi = 6.9 MPa)



MA-5762-248A

FIGURE 4.4 EFFECT OF  $P_i$  ON RELOAD CLOSURE WITH FIXED DESIGN CLOSURE

( $\Delta D/D \approx 2\%$ ,  $\sigma_u = 4 \text{ ksi}$ ,  $N_\phi = 3$   
 (1 ksi = 6.9 MPa))



MA-5762-249A

FIGURE 4.5 EFFECT OF  $\sigma_u$  AND  $N_\phi$  ON RELOAD CLOSURE WITH FIXED DESIGN CLOSURE

$\Delta D/D \approx 2\%$ ,  $P_i = 0$  (1 ksi = 6.9 MPa)

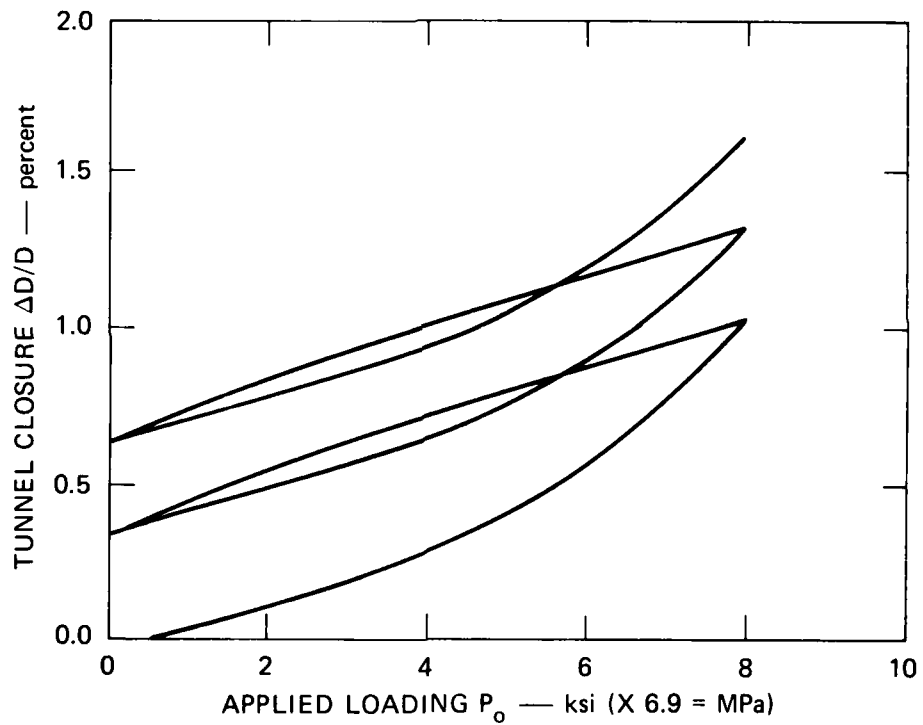
27.6 MPa), respectively. Figures 4.5(c) and 4.5(d) are plots of tunnel closure for  $N_\phi = 7.55$  ( $\phi = 50^\circ$ ) and the same unconfined compressive strengths. The effect of the increased unconfined compressive strength is to reduce the additional closure sustained during a cycle in load. For  $N_\phi = 3.00$ , the reduction is 36%, and for  $N_\phi = 7.55$ , it is 25%. The width of the loop formed by the unload-reload portion of the closure curve is not affected significantly.

The influence of the pressure sensitivity coefficient  $N_\phi$  can be determined by comparing closure curves corresponding to a common value of unconfined compressive strength; compare Figures 4.5(a) and 4.5(c) for  $\sigma_u = 2$  ksi (13.8 MPa) to Figures 4.5(b) and 4.5(d) for  $\sigma_u = 4$  ksi (27.6 MPa). Changes in  $N_\phi$  have large effects on the closure curve calculated for repeat loading. For large values of  $N_\phi$  the loop in the unload-reload portion of the curve disappears, but the additional tunnel closure sustained during the cycle in load increases:  $\Delta(\Delta D/D)$  is about 25% greater for  $N_\phi = 7.55$  than for  $N_\phi = 3$ .

#### 4.3 NUMERICAL SOLUTION

As a check on the lengthy algebra in the analytical solution, and to extend results to more complex tunnel problems, the finite element code NONSAP [13] was used to calculate response for several examples. These examples included the constant internal pressure, symmetric loading problem studied analytically; symmetric loading with a metal liner; and uniaxial strain loading side-on to the tunnel. In all but the first problem it was found that very small steps had to be taken during unloading. Thus, a parameter study would be very expensive. Work is continuing to make the unload computations more efficient for these problems. In the following paragraphs, results are given for two cycles of symmetric loading with a constant internal tunnel pressure.

Results of these computations are given in Figure 4.6. The parameters are the same as those for the analytical example in Figure 4.2, except that the friction angle is  $\phi = 33^\circ$  rather than  $\phi = 30^\circ$ . This change was made to avoid the numerical difficulty that occurs when the condition for yielding independent of  $\sigma_z$  is approached:  $\nu(N_\phi + 1) \leq 1$ , from reference [9]. Figures 4.2(a) and 4.6 show that the numerical theory



MA-5762-251

FIGURE 4.6 FINITE ELEMENT RESULTS FOR TWO RELOADING CYCLES  
Same material and loading parameters as in Figure 4.2(a).

accurately reproduces the analytical results given for the first re-loading cycle. The new result is the second cycle, which would require additional work for an analytical solution. The second cycle is identical with the first but shifted upward. This implies that the additional tunnel closure  $\Delta(\Delta D/D)$  sustained on the first reload cycle would be added cumulatively with each additional cycle to  $\bar{P}_0$ . Thus, after many reloading cycles to  $\bar{P}_0$ , the cumulative tunnel closure would eventually become unacceptably large.

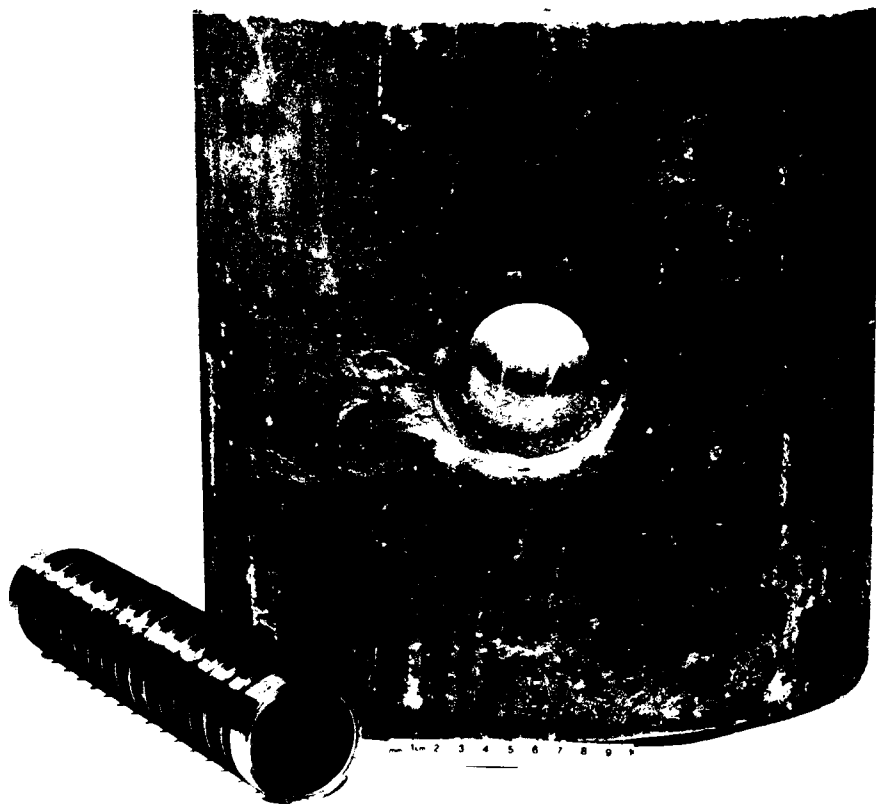
However, observe in Figure 4.2(c) that after a first loading to  $\bar{P}_0 = 12$  ksi (83 MPa), the reloading gives additional permanent closure only when  $P_0$  exceeds about 8 ksi (55 MPa). In contrast, Figure 4.2(a) shows that if the first loading is  $\bar{P}_0 = 8$  ksi (55 MPa), then reloading to 8 ksi (55 MPa) causes a substantial additional closure. This suggests that after an initial overload that produces permanent closure [Figure 4.2(c)], the loading range of essentially elastic response is increased markedly. It is possible that after loading to 12 ksi (83 MPa), cycle loading to 8 ksi (55 MPa) could be sustained indefinitely.

The experiments described in the next section show that the theory overestimates the additional closure  $\Delta(\Delta D/D)$  at any given  $\bar{P}_0$ , and that several cycles of loading can be sustained with little cumulative closure. Further experiments are required to determine whether cumulative closure remains small after many cycles at an initially plastic closure load. A more complete comparison of theory and experiment is given below.

#### 4.4 TEST SPECIMENS

Figure 4.7 shows the geometry of the specimens. They are right circular cylinders with circular tunnels drilled along a midheight diameter. The cylinder aspect ratio is unity. Two sizes are tested: a small 4-inch-diameter (0.1-m) cylinder with a 5/8-inch-diameter (15-mm) tunnel to study intact specimens, and a large 12-inch-diameter (0.3-m) cylinder with a 2-inch-diameter (50-mm) tunnel to study jointed specimens.

The specimens are made from three different rock simulants. Rock simulants are used because they have less specimen-to-specimen scatter



MP-4121-101

FIGURE 4.7 TWELVE-INCH (0.3 m) DIAMETER SPECIMEN OF TUFF SIMULANT AND A REPRESENTATIVE TUNNEL REINFORCING STRUCTURE

than real rocks, and because they allow the experimenter to select grain size as well as the various constitutive parameters. Two rock simulants, designated 6B and 16A, have strengths representative of medium strength rock. The third simulant, designated SRI RMG 2C2, has material properties similar to ash-fall tuff found at the Nevada Test Site. The recipes for these rock simulants are given in Table 4.1.

The rock simulant constitutive parameters are given in Table 4.2. The primary difference between the two medium-strength rock simulants and the ash-fall tuff simulant is the value of  $N_\phi$ , the pressure sensitivity coefficient, which is indicative of the very much lower angle of internal friction for ash-fall tuff. The major difference between the 6B and 16A rock simulants is not in their constitutive parameters but in the size of the largest sand particles used in the simulant. Both are made from commercial sand, but larger grains are present in the 6B formulation. All grains passing through a number 6 sieve are used in the 6B formulation, while only those passing through a number 16 sieve are used in the 16A formulation. All three rock simulants are used in the study of intact specimens, but only the 16A simulant is used in the study of jointed specimens. Intact specimens are either poured into cylindrical molds (SRI RMG 2C2) or cored from large blocks (6B and 16A). The cores or castings are centerless-ground to a 4-inch (0.1-m) diameter and then cut to a 4-inch (0.1-m) height. Jointed specimens are built by stacking 1/3-inch-thick (8.5-mm) elliptical plates of rock simulant at the desired inclination to the cylindrical axis. The elliptical plates are cut from larger cast plates by a high velocity water jet. Their size and shape depends on the angle between the joint plane normal and the cylindrical specimen axis. The larger specimen diameter is used for the jointed rock tests so that the plates can be thick compared with grain size, while they also have several joints intersecting the tunnel: the ratio of tunnel diameter to joint spacing is six.

Two fundamentally different types of structures reinforce the tunnels. The first, the direct contact liner, is used in most tests. This liner is a simple metal tube in direct contact with the tunnel wall. The tubes are either 1015 steel with radius-to-thickness ratio  $a/h = 12.5$  or

TABLE 4.1  
ROCK SIMULANT COMPOSITION  
(Percent by weight)

<u>Component</u>	<u>6B</u>	<u>16A</u>	<u>SRI RMG 2C2</u>
Portland cement, Type 1	10.25	18.61	31.14
Limestone sand	81.04	61.37	
Granite sand		6.62	
Monterey sand			20.86
Barite			19.89
Bentonite			2.73
CFR 2			0.076
Water	8.71	13.40	25.30
<i>Total</i>	100.00	100.00	100.00

TABLE 4.2

## ROCK SIMULANT CONSTITUTIVE PARAMETERS

Parameter	6B	16A	SRI RMG 2C2
Water saturation (%)	0	100	100
Shear modulus* $\mu$ ( $10^6$ psi) (GPa)	0.80→ 1.6 5.5 →11.0	1.25 8.6	0.47 3.2
Poisson's ratio, $\nu$	0.25	0.23	0.23
Compressive strength,* $\sigma_u$ (ksi) (MPa)	3.60 24.8	3.74 25.8	3.68 25.3
Friction angle* $\phi$ (deg.)	20→36	29.	2.5
Pressure coefficient, $N_\phi =$ ( $1+\sin\phi$ )/( $1-\sin\phi$ )	2.0→3.8	2.88	1.09

\* Modulus and friction decrease with increasing stress. Range given for 6B corresponds to stress range in tunnel tests, for later comparison with theory.

6061-T0 aluminum with  $a/h = 4$ . The second structure type, the backpacked liner, is a metal tube surrounded by a layer of crushable material that isolates the metal tube from the tunnel cavity. The backpacked liner in these tests is a 1015 steel liner with  $a/h = 12.5$ , surrounded by a layer of polyurethane foam having outer-radius-to-thickness ratio  $R/H = 4.3$ . Figure 4.8 plots a stress-strain curve for the polyurethane foam. It shows that crushing occurs at a fairly constant stress to over 30% strain. Therefore, large tunnel closure can be accommodated by the structure with only the small foam crush loads transmitted to the metal liner.

#### 4.5 EXPERIMENTAL RESULTS

This section presents the results of laboratory tests in which the loading was cycled at several pressure levels in a single test, and compares these results with those obtained from monotonic loading experiments on similar specimens. We also compare the tunnel closure curves of the experiments with those calculated using our finite element technique.

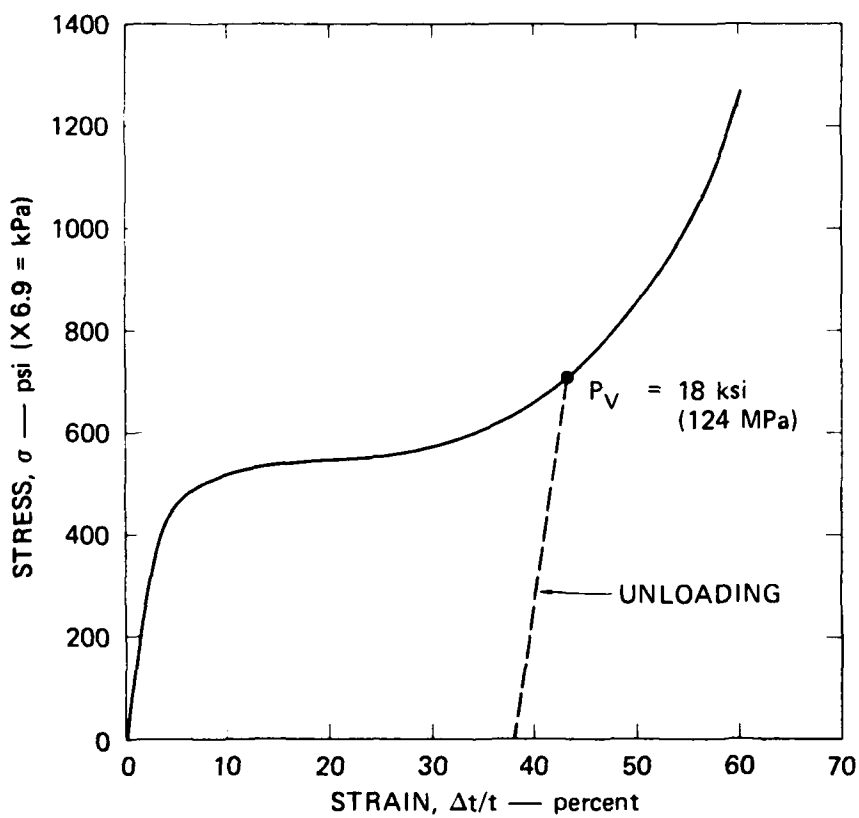
The experiments studied a number of parameters: three different rock-matching grouts, intact and jointed specimens, isotropic and uniaxial strain loading, and direct contact and backpacked structures. Details of these experiments are described elsewhere,<sup>\*</sup> and only the results are presented here.

##### 4.5.1 Isotropic Loading

Isotropic loading produces axisymmetric deformation of the tunnel, similar to that discussed analytically and numerically in the previous sections.

---

\* Tests on 6B rock simulant are described in Reference 2, pp. 99-101 and pp. 132-135, and tests on SRI RMG 2C2, in Reference 4, pp. 73-79. Tests on backpacked structures are described in Appendix B.



MA-5762-71B

FIGURE 4.8 STRESS-STRAIN CURVE FOR UNIAXIAL STRAIN LOADING OF 13.2 lb/ft<sup>2</sup> (211 kg/m<sup>3</sup>) POLYURETHANE FOAM  $\dot{\epsilon} = 3.3 \times 10^{-2} \text{ s}^{-1}$

Dry 6B Rock Simulant. The tunnel is reinforced with a thin 1015 steel liner. The load is cycled at  $\bar{P}_0 = 11.5$  ksi (twice) and at 17.5 ksi (79 and 121 MPa). Figure 4.9 plots the tunnel closure as a function of pressure. The unloading and reloading parts of each cycle lie along a single essentially horizontal straight line. The increased tunnel closure sustained during a cycle in load is small and about the same for all three loading cycles.

The theoretical curve in Figure 4.9 has the same features as the experimental curve, but falls below the experimental curve during the reload cycle. This is attributed, in part, to separation of the steel liner (which has little elastic recovery) from the rock cavity. This is discussed more fully in the next section.

Saturated SRI RMG 2C2 Rock Simulant. The tunnel in this specimen is reinforced with a thick 6061-T0 aluminum liner. The load is cycled at  $\bar{P}_0 = 5.5$  ksi (twice) and at 7 ksi (38 and 48 MPa). The tunnel closure curve, plotted in Figure 4.10, is similar to that given for dry 6B rock simulant. Within experimental accuracy, both unloading and reloading parts of the closure curve for each cycle fall on the same lines. The increased tunnel closure sustained during a cycle in load is small and is about the same for all three cycles. The tunnel closure curve for monotonic loading of a similar specimen is also plotted in the figure. Comparison of the monotonic and repeat loading curves shows that the load-carrying capacity of the tunnel is not significantly reduced by repeat loading.

#### 4.5.2 Uniaxial Strain Loading

Uniaxial strain loading produces asymmetric deformation of the tunnel. This simulates loading when a horizontal tunnel sustains a uniform vertical load  $P_v$  far from the tunnel. Results are presented only for crown-invert closure, except for the backpacked structure, for which springline closure is also presented. The crown-invert tunnel closure curves are qualitatively the same as the tunnel closure curves presented for isotropic loading.

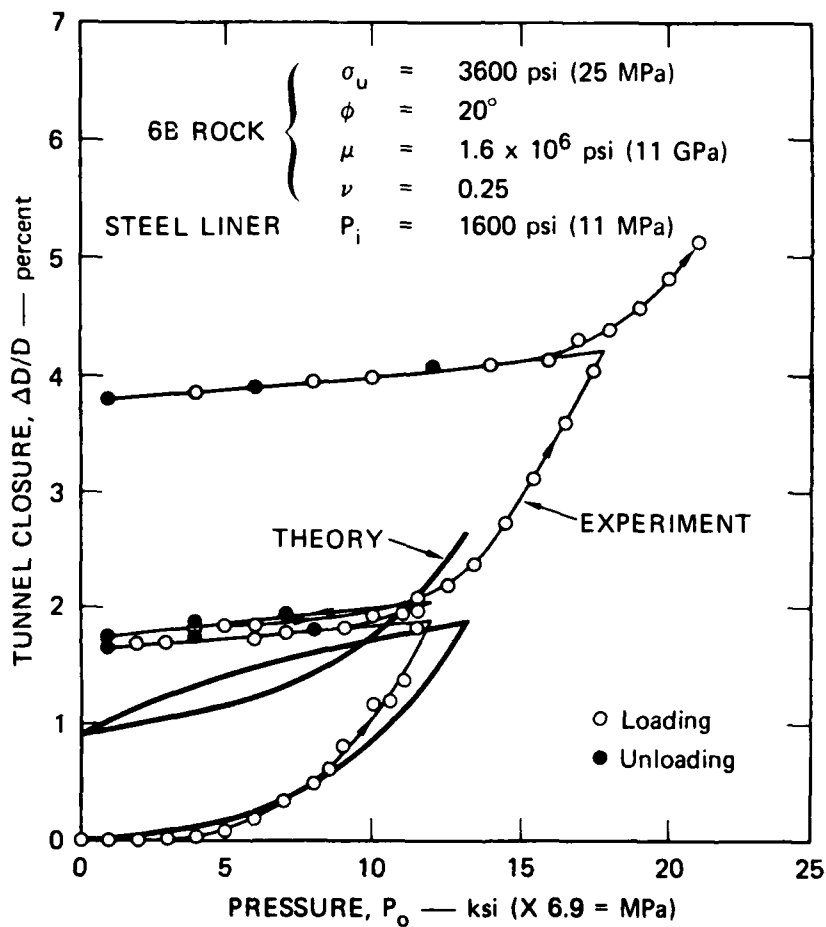


FIGURE 4.9 TUNNEL CLOSURE FOR CYCLIC ISOTROPIC LOADING OF 6B ROCK SIMULANT

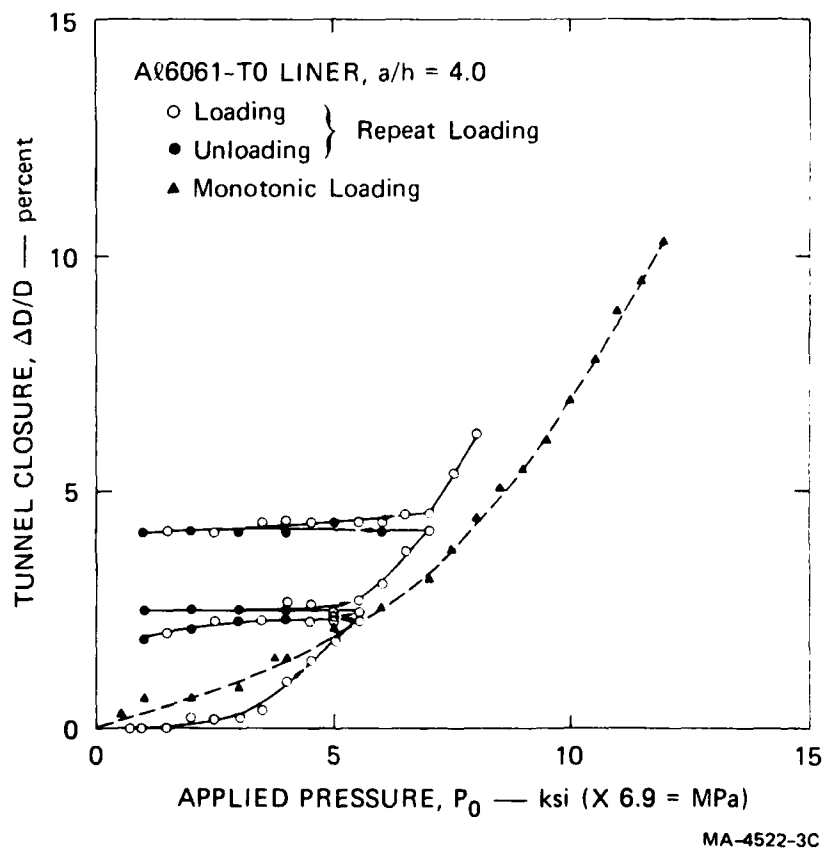


FIGURE 4.10 TUNNEL CLOSURE FOR CYCLIC AND MONOTONIC ISOTROPIC LOADING OF SRI RMG 2C2 ROCK SIMULANT

Dry 6B Rock Simulant. The tunnel in this specimen is reinforced with a thin steel liner similar to that used in the isotropic loading experiment on dry 6B rock simulant. The load was cycled at  $\bar{P}_V = 9.5$  ksi (twice) and 13 ksi (65.5 and 90 MPa). Figure 4.11 plots the crown-invert closure as a function of vertical pressure. There is a very large loop in the unloading and reloading portion of the closure curve during the first cycle in load  $\bar{P}_V = 9.5$  ksi (65.5 MPa). This is an anomalous result caused by poor control of the lateral confining pressure in this early test. This cycle in load gave no additional tunnel closure, i.e.  $\Delta(\Delta D/D) = 0$ . During the second cycle at this load, closure is more like that in the other experiments: the unload-reload portions of the closure curve form a small loop, and additional tunnel closure is sustained during the cycle in load. The unload-reload cycle at  $\bar{P}_V = 13$  ksi (90 MPa) produces an additional tunnel closure similar to that sustained during the second cycle at  $\bar{P}_V = 9.5$  ksi (65.5 MPa).

A tunnel closure curve for monotonic loading of a similar specimen is also plotted in Figure 4.11. Comparison of the two curves shows that repeat loading does not significantly affect the strength of the structure. The following paragraphs give similar comparisons of closure curves for repeat and monotonic loading of specimen pairs and also show that repeat loading does not significantly affect the strength of the tunnel.

Saturated SRI Rock Simulant. The tunnel reinforcing structure is an aluminum liner similar to the liner in the isotropic loading experiment on the same rock simulant. The load is cycled at  $\bar{P}_V = 4.5$  ksi (twice) and at 5.5 ksi (31 and 38 MPa). Cyclic and monotonic crown-invert tunnel closure curves for this simulant, given in Figure 4.12, are similar to those in Figure 4.11 for dry 6B simulant. (In Figure 4.12 there is no anomalous loop from poor load control.)

Saturated 16A Rock Simulant. The tunnel reinforcing structure is a polyurethane foam backpacked steel liner. The load is cycled at  $\bar{P}_V = 7.5, 10, \text{ and } 13$  ksi (52, 69, and 124 MPa). Figure 4.13 plots crown-invert and springline tunnel closure for both the rock cavity and

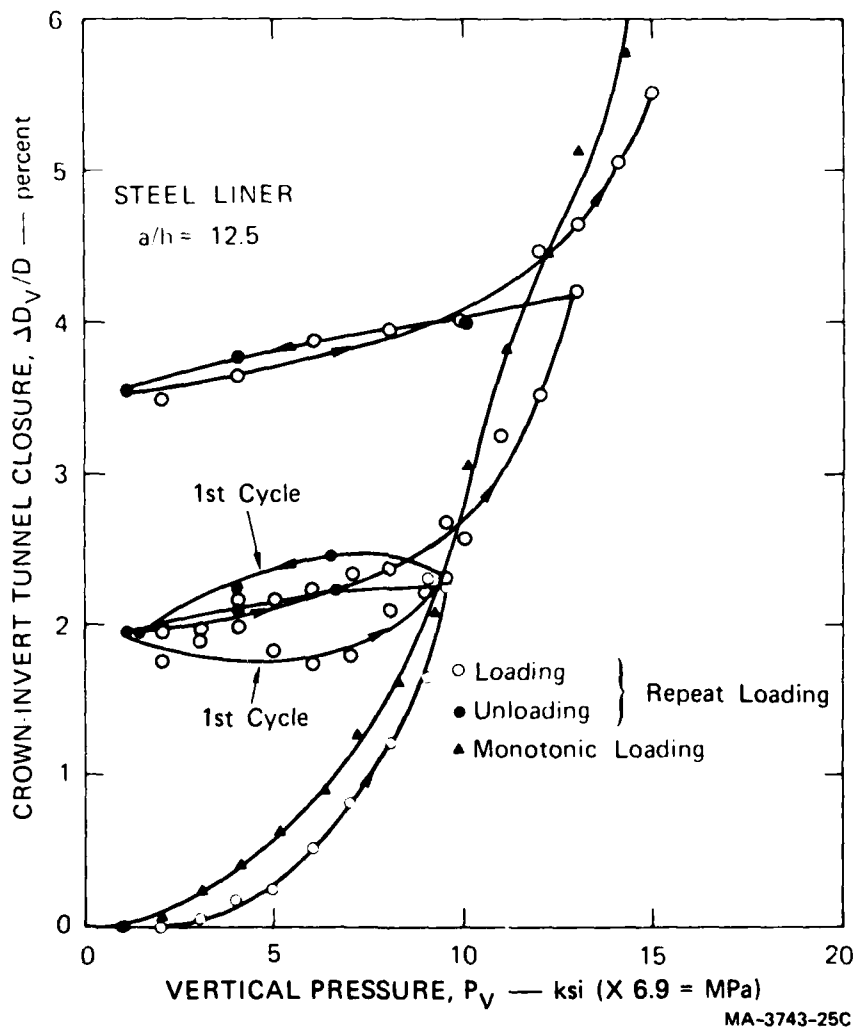


FIGURE 4.11 CROWN-INVERT TUNNEL CLOSURE FOR CYCLIC AND MONOTONIC UNIAXIAL STRAIN LOADING OF 6B ROCK SIMULANT

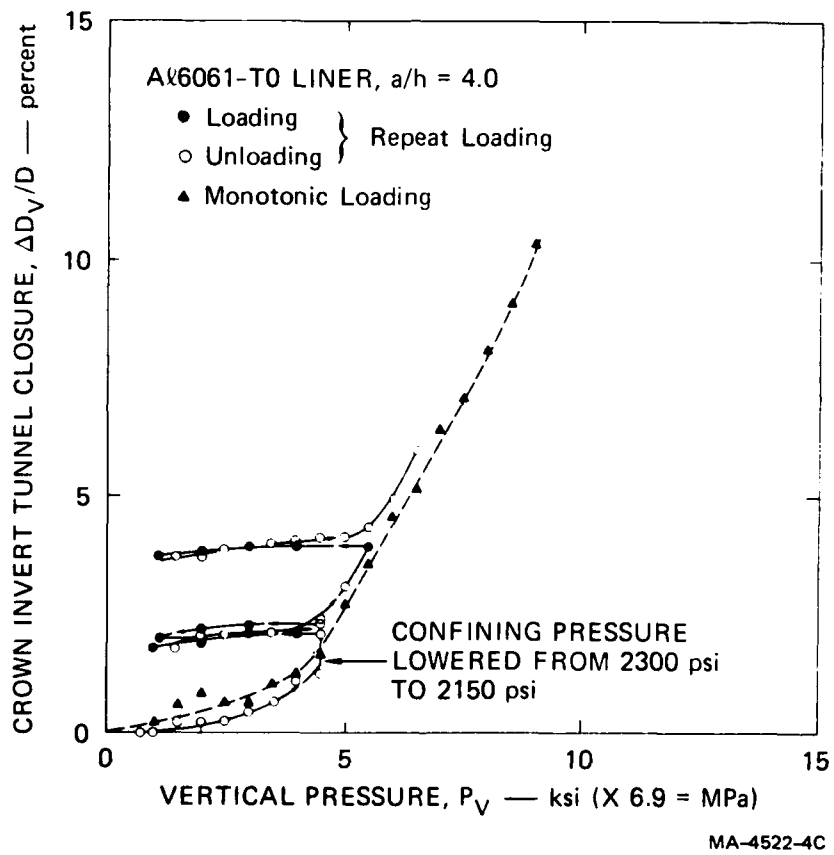
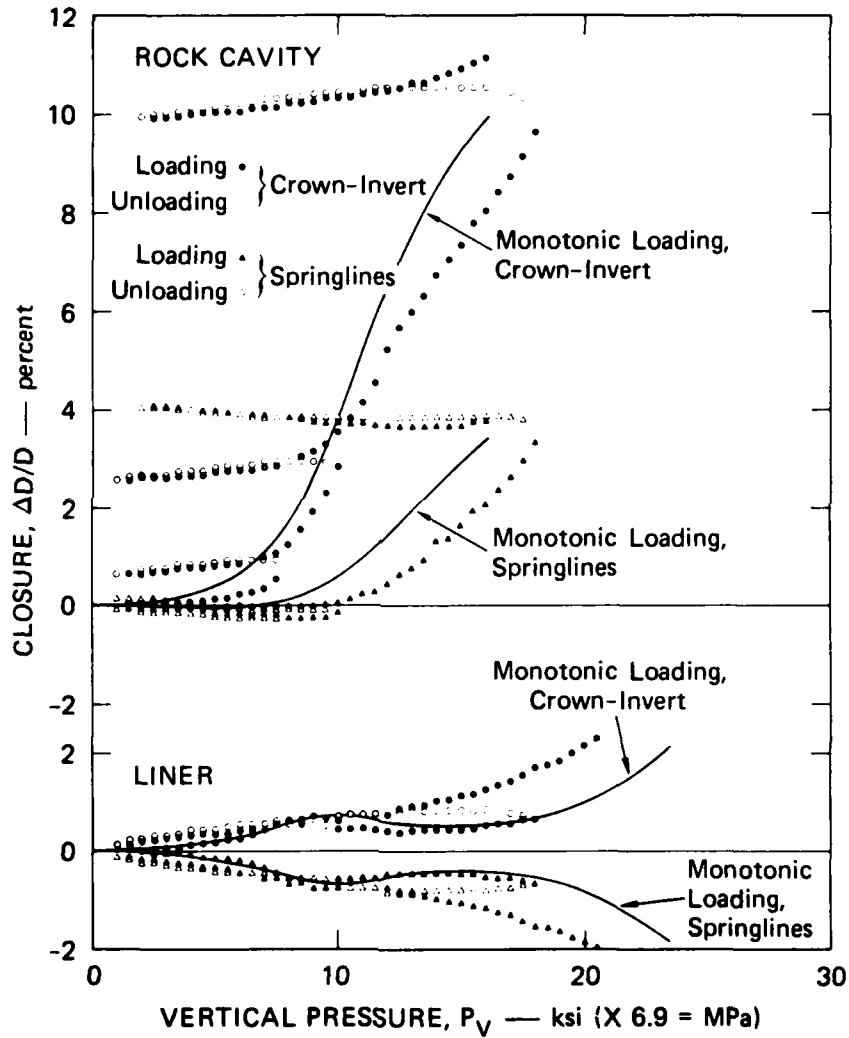


FIGURE 4.12 CROWN-INVERT TUNNEL CLOSURE FOR CYCLIC AND MONOTONIC UNIAXIAL STRAIN LOADING OF SATURATED SRI RMG 2C2 ROCK SIMULANT



MA-5762-73

FIGURE 4.13 ROCK-CAVITY AND LINER CLOSURE FOR CYCLIC AND MONOTONIC UNIAXIAL STRAIN LOADING OF A BACKPACKED STRUCTURE IN SATURATED 16A ROCK SIMULANT

the steel liner. The values of  $P_V$  were chosen by examining the liner closure curves for monotonic loading (plotted as solid lines). The first value,  $\bar{P}_V = 7.5$  ksi (52 MPa), is chosen so that liner closure is still increasing and the backpacking has not yet started to crush. The second value,  $\bar{P}_V = 10$  ksi (69 MPa), is chosen so that the backpacking at the crown and invert is crushing at constant stress but the backpacking at the springlines is not. The third value,  $P_V = 18$  ksi (124 MPa), is chosen so that the backpacking at the crown and invert is locking up, but at the springlines it is still crushing at constant stress.

The rock-cavity crown-invert closure curve is similar to the curves from the previous tests in which the reinforcing structure is a direct contact liner. The unload-reload portions of the closure curve form very small loops. Additional tunnel closure sustained during a cycle in load grows substantially with  $\bar{P}_V$ . Rock-cavity springline closure is not so simple. During a cycle in load it increases as the load decreases. This is expected when springline closure is negative, since the expected trend is that amplitude will decrease when the load is removed. However, when springline closure is positive ( $\bar{P}_V = 18$  ksi = 124 MPa), it increases as the load is removed. This indicates that relaxation of the oval mode deformation dominates relaxation of the hoop mode during unloading.

Closure of the steel liner shows that loops in the unload-reload cycle are very small. Additional tunnel closure during a cycle in load is zero until the last cycle, which is at an initial closure much larger than the few percent one would allow in practice.

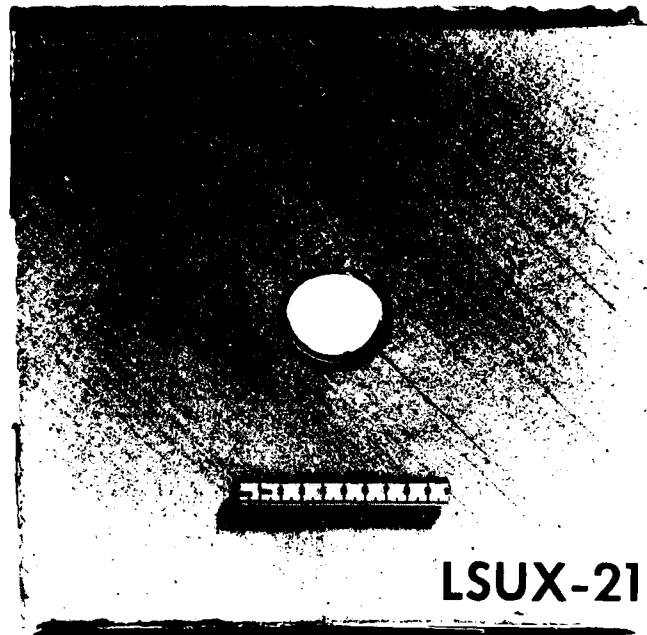
During the reload portion of this last cycle in load, the magnitude of the liner closure does not decrease at  $P_V = 10$  ksi (69 MPa), as it did for both monotonic loading and initial cyclic loading to 18 ksi (124 MPa), because loading to  $P_V = 18$  ksi (124 MPa) causes the backpacking to begin to lock up. This point is shown on the schematic stress-strain curve for the backpacking material given in Figure 4.8, where response to unloading is plotted as a dashed line. Reloading response also follows the dashed stress-strain path: stress increases monotonically with strain; there is no constant-stress crush as there is for monotonic

loading. Therefore, the load on the liner and, consequently, the amplitude of the liner closure, increase monotonically during reloading.

Jointed 16A Rock Simulant. Two experiments were performed to study the influence of joints and their orientation on tunnel closure under repeat loading. The rock specimens were assembled from plates to form a single set of equally spaced planar joints. The photographs in Figure 4.14 are overall and closeup views of a posttest section that shows tunnel deformation and joint orientation. In these experiments, the joint planes are parallel to the tunnel axis (perpendicular to the paper in the figure) and inclined at an angle  $\beta$  to the uniaxial strain loading direction (vertical in the figure). In the figure,  $\beta = 45^\circ$ . In the other test reported here,  $\beta = 0^\circ$  (joint planes would be horizontal in the figure).

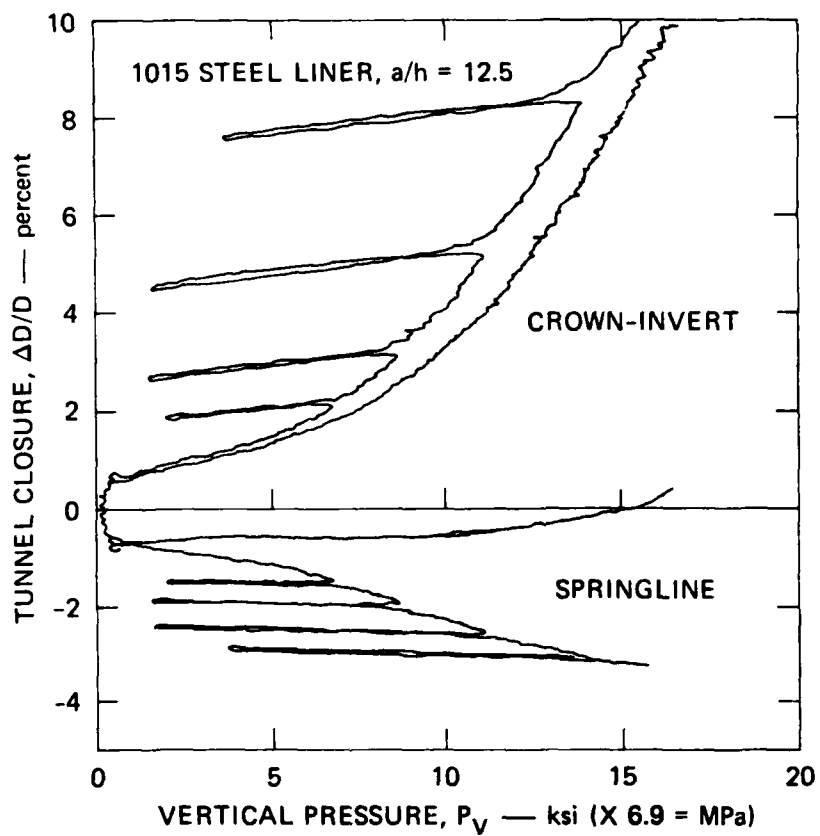
To allow direct comparison of the two tests, the load was cycled at common values of crown-invert tunnel closure, rather than at common values of  $\bar{P}_V$ . Values used were  $\Delta D_V/D = 2\%$ ,  $3\%$ ,  $5\%$ , and  $8\%$ . This eliminates the effect of inherent differences in strength between the two joint orientations. The load paths in these two experiments were the same: the path that produces uniaxial strain conditions in the specimen with  $\beta = 0$ . Because of the lack of specimen axial symmetry for a finite joint orientation, precise uniaxial strain conditions could not be achieved by the hydraulic fluid boundary pressure method for  $\beta = 45^\circ$ .

Figures 4.15 and 4.16 plot crown-invert tunnel closure as a function of vertical pressure for tests in which the load-joint orientation angles were  $\beta = 0^\circ$  and  $45^\circ$  ( $0$  and  $\pi/4$  rad), respectively. Closure curves for the two orientations are similar. They show an initial sharp rise in closure during initial close-up of the joints. The loops in the unload-reload portion of the curves and the additional closure sustained during a cycle in load both grow as  $\bar{P}_V$  increases. The values of  $\Delta(\Delta/D)$  and the loops in the closure curves are slightly larger for the specimen with the inclined joints ( $\beta = 45^\circ = \pi/4$  rad).



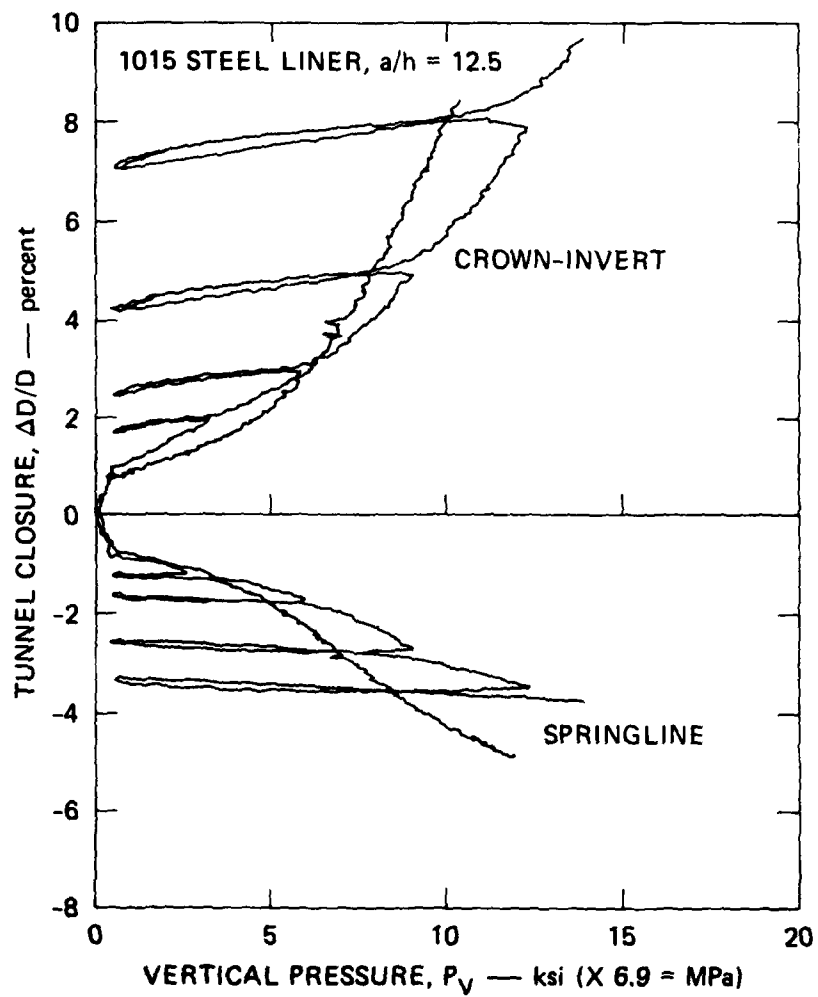
MP-5762-253

FIGURE 4.14 POSTTEST SECTION VIEWS OF JOINTED ROCK MODEL WITH  $\beta = 45^\circ$



MA-5762-208A

FIGURE 4.15 TUNNEL CLOSURE FOR CYCLIC AND MONOTONIC UNIAXIAL STRAIN LOADING OF JOINTED 16A ROCK SIMULANT — LOAD-JOINT ORIENTATION ANGLE  $\beta = 0^\circ$



MA-5762-209A

FIGURE 4.16 TUNNEL CLOSURE FOR CYCLIC AND MONOTONIC UNIAXIAL STRAIN LOADING OF JOINTED WES 16A ROCK SIMULANT — LOAD-JOINT ORIENTATION ANGLE  $\beta = 45^\circ$

#### 4.5.3 Uniaxial Strain Loading Followed by Isotropic Loading

This experiment studied the influence on tunnel closure measured during isotropic loading of previous asymmetric tunnel closure produced by uniaxial strain loading. We tested a saturated specimen of SRI RMG 2C2 whose tunnel is reinforced by a thick 6061-T0 aluminum liner similar to the reinforcing structures in the isotropic loading and uniaxial strain loading experiments in the same rock simulant. Figure 4.17 plots crown-invert tunnel closure as a function of pressure.

The specimen is loaded in uniaxial strain to  $\bar{P}_o = 7.5$  ksi (52 MPa), at which the crown-invert tunnel closure is about 5.5%. It is unloaded under uniaxial strain conditions to  $P_o = 0$ , at which the crown-invert closure is decreased slightly, to 5%. Reloading to  $\bar{P}_o$  is under isotropic loading, which produces a large loop in the closure curve. Crown-invert closure actually decreases initially, because the symmetric loading tends to push the tunnel from its elliptical shape back into its original circular shape. When  $P_o = \bar{P}_o$ , the reloading closure curve crosses the initial closure curve;  $\Delta(\Delta D/D)$  is negative.

As loading increases beyond  $P_o$ , the closure curve approaches that obtained for monotonic isotropic loading of a similar specimen: the influence of the initial asymmetric deformation fades as the isotropic load is increased beyond  $\bar{P}_o$ .

#### 4.6 COMPARISON OF THEORY AND EXPERIMENT

In Figure 4.9, the experimental closure curve for symmetric loading of dry 6B rock is accompanied by a corresponding theoretical curve for the first cycle of loading, calculated with the analysis given in Section 4.2. It reproduces the overall salience of the experimental curve but differs in the magnitude of detailed features. The initial loading curves for theory and experiment are reasonably close, considering the theoretical idealization of rock behavior by simple elastic, perfectly plastic deformation with a constant shear modulus  $\mu$  and constant friction angle  $\phi$ . The constant values used in the theory (see Figure 4.9) are intermediate values taken from WES triaxial compression test data

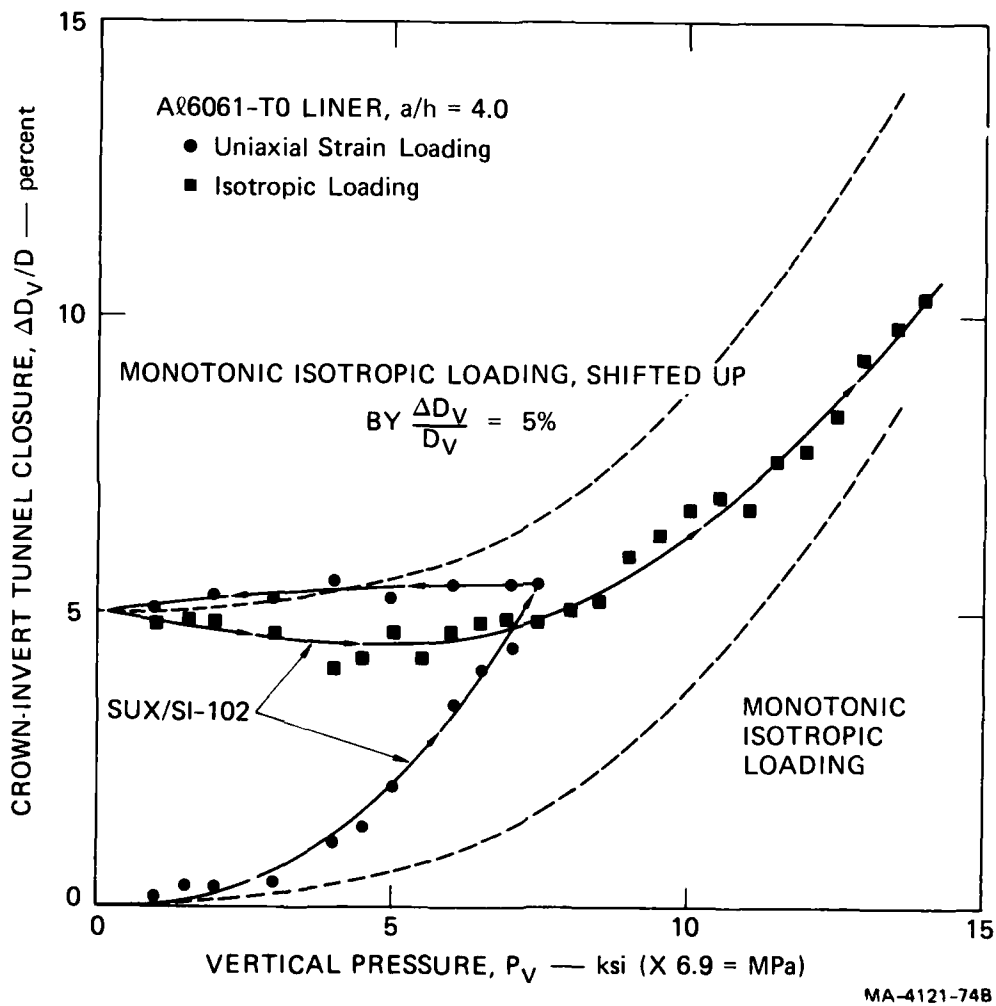


FIGURE 4.17 CROWN-INVERT TUNNEL CLOSURE VERSUS APPLIED PRESSURE FOR SATURATED SRI RMG 2C2 SUBJECTED TO UNIAXIAL STRAIN LOADING FOLLOWED BY ISOTROPIC LOADING

for the stress range in the calculations. The measured friction angle is about  $36^\circ$  at low stress and decreases to zero as the confinement stress approaches 10 ksi (69 MPa). The modulus chosen for the calculation is near the maximum low-stress value in order to properly reproduce unloading behavior. This tends to underestimate tunnel closure during loading, but this is compensated by using the  $20^\circ$  friction angle, the value at larger confining stress. To more accurately model the actual changing modulus and friction would require solution by numerical computation.

The theoretical unloading curve in Figure 4.9 slopes back more steeply than that of the experiment. This difference can be attributed to measurement in the experiment of the steel liner deformation, whereas in the theory only rock-cavity response is calculated. The elastic recovery capacity of the steel is less than 0.2%, and the steel is not bonded to the rock. The cavity probably opens more than the elastic recovery of the liner resulting in an unmeasured gap between the cavity and liner. In fact, the elastic recovery of the liner is of the same order as the measurement error so that, to experimental accuracy, the unload and reload lines are horizontal. (The same pattern can be seen in Figure 4.10.) Upon reloading, the rock cavity and liner eventually recontact and the liner again follows the rock cavity closure. Figures 4.9 and 4.10 show this by the abrupt slope change in the reload curves as  $P_o$  approaches  $\bar{P}_o$ . (Under uniaxial strain loading the liner is in flexure and can follow the rock-cavity deformation. Thus, the reload cycles in Figures 7, 8, 9, 11, and 12 have more nearly the same character as in the theory.)

However, separation of the liner from the rock does not explain the measurably smaller net added deformation in the unload-reload cycle of the experiment (Figure 4.9) as compared with the theory. The theory predicts a reload closure increment of  $\Delta(\Delta D/D) = 0.8\%$ , whereas the experimental increment is about 0.2%, near the measurement resolution of these early experiments. The larger theoretical reload closure increment is attributed in part to the simplified idealization of the

liner as a constant internal pressure  $P_i$ . Upon unloading in the experiment, the pressure exerted by the liner actually drops to zero, as discussed. Thus, in the theory, a larger closure tends to be retained than in the experiment. Upon reloading, this larger closure is maintained and results in a larger predicted reload closure increment. However, the more dominant reason for differences between theory and experiment is simply that the actual rock behavior is more complicated than given by the constant parameter elastic-plastic idealization.

#### 4.7 SUMMARY, CONCLUSIONS, AND RECOMMENDATIONS

##### 4.7.1 Analytical Solution

An analytic solution has been completed for cyclic elastic-plastic response of a circular tunnel in a Mohr-Coulomb medium subjected to a symmetric far-field loading  $P_o$  that cycles to a maximum load  $\bar{P}_o$ . It is found that for modest plastic deformation upon initial loading (for  $P_o \leq P_o^*$ ), unloading and reloading responses are entirely elastic. If the initial loading is higher ( $P_o > P_o^*$ ), the medium around the tunnel yields a second time (in the reverse direction) as the initial load is removed. When the load is reapplied, the medium around the tunnel yields a third time (in the original direction). The unload-reload cycle to the initial maximum load  $\bar{P}_o$  in this case results in a net increment  $\Delta(\Delta D/D)$  in tunnel closure. A numerical finite element solution extends the results to a second unload-reload cycle, and shows that the closure increment during the first loading cycle is permanent. Also, the second unload-reload cycle is identical with the first, but shifted by the amount of increment in the first cycle closure. Thus, cyclic closure increments are cumulative.

A parameter study shows that the cycle-load closure increment increases with increasing maximum load  $\bar{P}_o$ . With a fixed  $\bar{P}_o$ , increases in the tunnel reinforcement pressure  $P_i$  markedly reduce both the peak closure and the cycle-load closure increment. However, if the peak closure is taken as a fixed allowable design closure, so that the reinforcement strength  $P_i$  is increased appropriately with increases in design

load  $P_0$ , then the cycle-load closure increment also remains nearly fixed. Variations in the medium unconfined compressive strength  $\sigma_u$  and friction angle  $\phi$  show that, for a fixed design closure, the cycle-load closure increment decreases with increasing  $\sigma_u$  but increases with increasing  $\phi$ .

Comparisons of these theoretical results with experimental results show that the theory reproduces the salience of cyclic loading response. However, the theory is conservative in that it overestimates the cycle-load closure increments measured in the experiments. The theory also overestimates the accumulation of closure increments, as compared with experimental closures after several cycles. These differences are attributed to the theoretical oversimplification of rock behavior by a fixed Mohr-Coulomb yield surface approximation. Further experimental work is needed to better characterize constitutive behavior under cyclic loading. Further theoretical work might include calculation of tunnel response with other constitutive assumptions to determine sensitivity to theoretical modelling.

The present theory adds to the understanding of tunnel response in the elastic-plastic range and hence adds confidence in the ability of tunnels to safely carry loads in this range. Since these loads can be two to three times higher than for purely elastic response, increased understanding is of practical importance.

#### 4.7.2 Experimental Results

Repeat loading experiments have been performed well into the plastic range of tunnel medium response in a variety of simulant media containing both direct contact and backpacked tunnel reinforcement structures. The experimental results show that little further plastic tunnel closure occurs until the reload exceeds the initial maximum load. Only upon further increase in load do the load-closure curves resume the more rapid plastic closure rates of the initial loading curves. The load can be cycled several times at several intermediate peak loads with only modest increases in closure (modest decreases in strength) over that for a simple monotonic loading to the same maximum load. This is found

to be true even for jointed rock masses, more typical of those in rock tunnelling application. The load distribution can be either symmetric or asymmetric--the main requirement for avoiding cumulative closures comparable to the initial closure appears to be that the load-unload paths do not differ widely.

These laboratory results suggest that tunnels to carry large service loads can be designed to take advantage of the substantial increase in strength afforded by allowing plastic deformation of the rock or soil medium around the tunnel. A strong but crushable backpacking layer between the cavity opening and reinforcement liner can isolate the liner from the few percent cavity closure on initial loading. Subsequent loading produces little or no further crush of the backpacking. Field tests are needed to confirm whether these laboratory observations accurately model reload behavior of tunnels in real soil and rock masses.

## REFERENCES

1. T. C. Kennedy, J. V. Zaccor, and H. E. Lindberg, "Laboratory Investigation of Response of Deep-Based Structures," DNA 3601F, Final Report, SRI Project 3044, SRI International, Menlo Park, California (October 1975).
2. T. C. Kennedy and H. E. Lindberg, "Laboratory Investigation of Rock Cavity Reinforcement," DNA 4023F, Final Report, SRI Project 3743, SRI International, Menlo Park, California (April 1976).
3. P. E. Senseny and H. E. Lindberg, "Theoretical and Laboratory Study of Deep-Based Structures, Vol. 1: "Triaxial Machine for Static and Dynamic Testing of 12-inch-Diameter Rocks," DNA 4425F, Final Report, SRI Project 4121, SRI International, Menlo Park, California (July 1977).
4. P. E. Senseny and H. E. Lindberg, "Theoretical and Laboratory Study of Deep-Based Structures, Vol. 2: "Model Tests and Analysis of Mighty Epic Structures," DNA 4425F, Final Report, SRI Project 4121, SRI International, Menlo Park, California (December 1977).
5. P. E. Senseny and H. E. Lindberg, "Laboratory Study of Deep-Based Structures in Support of Diablo Hawk," DNA 0000Z, Final Report, Vol. 1, SRI Project 5762, SRI International, Menlo Park, California (February 1978).
6. Y. M. Ito, R. H. England, T. E. Woverton, and R. B. Nelson, "Analysis of Small-Scale Laboratory Experiments of Deep-Based Structures," CRT Report 32-10-1, California Research and Technology, Woodland Hills, California (November 1978).
7. "Material Properties in Support of the Nevada Test Site Nuclear Test Program," Vol. 1, DNA 3870F-1, Terra Tek, Inc., Salt Lake City, Utah (October 1975).
8. Private communication from R. L. Stowe, U.S. Army Waterways Experiment Station (February 1979).
9. A. I. Florence and L. E. Schwer, "Axisymmetric Compression of a Mohr-Coulomb Medium Around a Circular Hole," *International Journal for Numerical and Analytical Methods in Geomechanics*, Vol. 2, pp. 367-379 (1978).

10. T. C. Kennedy and H. E. Lindberg, "Tunnel Closure for Nonlinear Mohr-Coulomb Functions," *Journal of the Engineering Mechanics Division*, ASCE, Vol. 104, No. EM6, Proc. Paper 14245, pp. 1313-1326 (December 1978).
11. T. C. Kennedy and H. E. Lindberg, "Model Tests for Plastic Response of Lined Tunnels," *Journal of the Engineering Mechanics Division*, ASCE, Vol. 104, No. EM2, Proc. Paper 13692, pp. 399-420 (April 1978).
12. I. S. Sokolnikoff, *Mathematical Theory of Elasticity*, McGraw Hill Book Co., New York, N.Y. (1956).
13. K. J. Bathe, R. K. Ozdermir, and E. L. Wilson, "Static and Dynamic Geometric and Material Nonlinear Analysis," University of California Report UCSECM74-4, Berkeley, California (1974).

## Appendix A

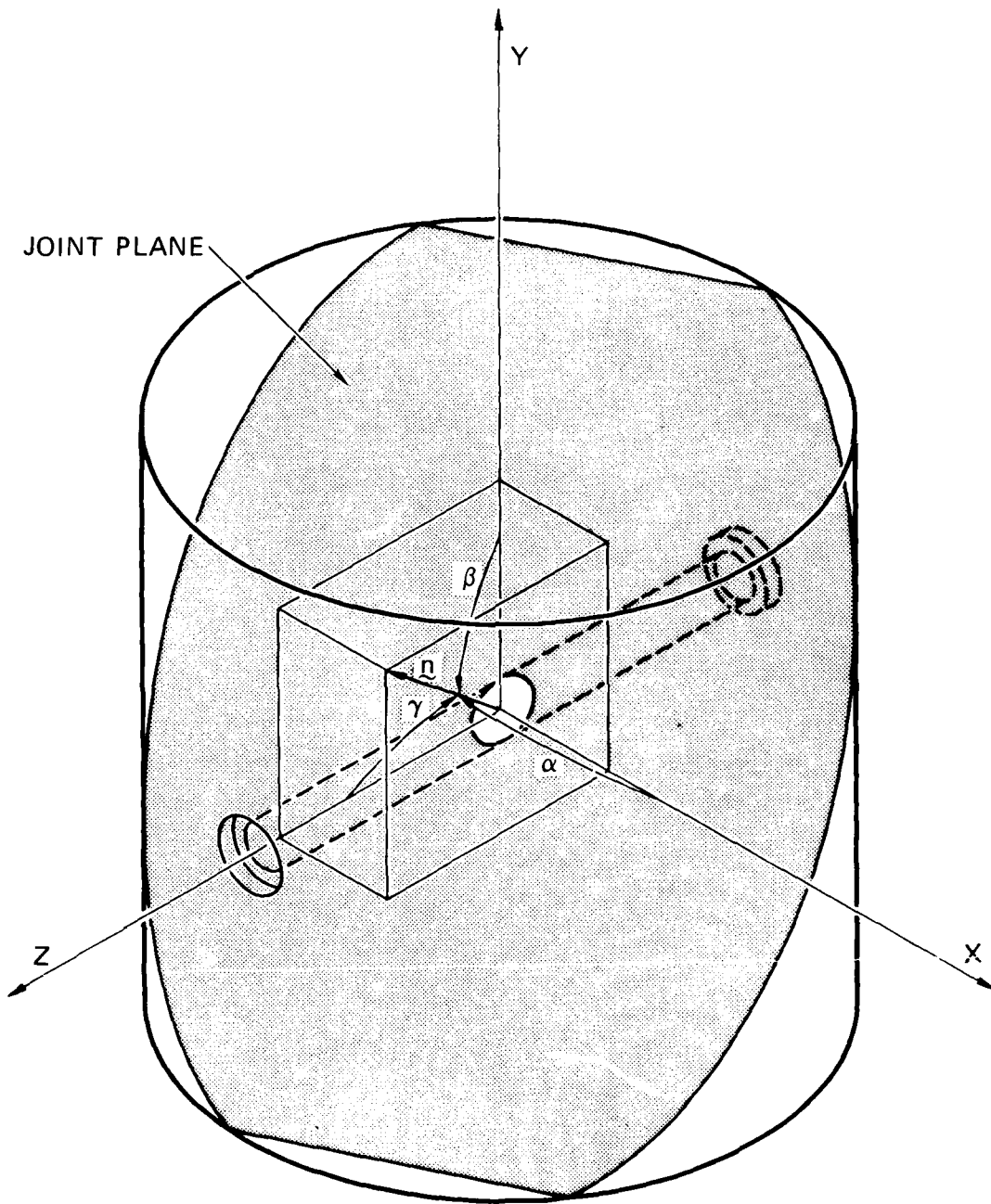
### DATA FROM EXPERIMENTS ON JOINTED ROCK

This appendix consists of test records from twelve experiments performed on 12-inch-diameter (0.3-m) jointed specimens of 16A rock simulant. These tests study the influence on tunnel deformation of the presence of a single set of parallel joints and their orientation, of tunnel reinforcing structure type, and of cyclic loading. Most specimens were tested statically along a common load path. Figure A.1 shows how joint orientation is specified, and Table A.1 gives the test matrix.

The data for each test include a brief description of the test, photographs of a posttest specimen cross section, and gage outputs plotted as functions of the vertical pressure.

TABLE A.1 JOINTED MODEL TEST MATRIX

Test Number: LSUX-	13	24	14	17	21	20	19	25	22	23
Loading Type	Mono	Mono	Mono	Repeat	Repeat	Mono	Mono	Mono	Mono	Mono
Load-Joint Orientation $\beta$ (DEG)	0	30	45	0	45	0	30	45	30	30
Tunnel-Joint Orientation $\gamma$ (DEG)	90	90	90	90	90	90	90	90	60	69.3
Reinforcement Type	Steel	Steel	Steel	Steel	Steel	Foam	Foam	Foam	Steel	Steel
Response Comparisons:										
Joint Orientation										
Repeat vs. Mono										
Steel vs. Foam										
Tunnel Orientation										



MA-5762-22A

FIGURE A.1 SCHEMATIC SHOWING JOINT ORIENTATION  
 $n$  is normal to the joint plane.

LSUX-13

LOAD-JOINT ORIENTATION ANGLE  $\beta$ :  $0^\circ$

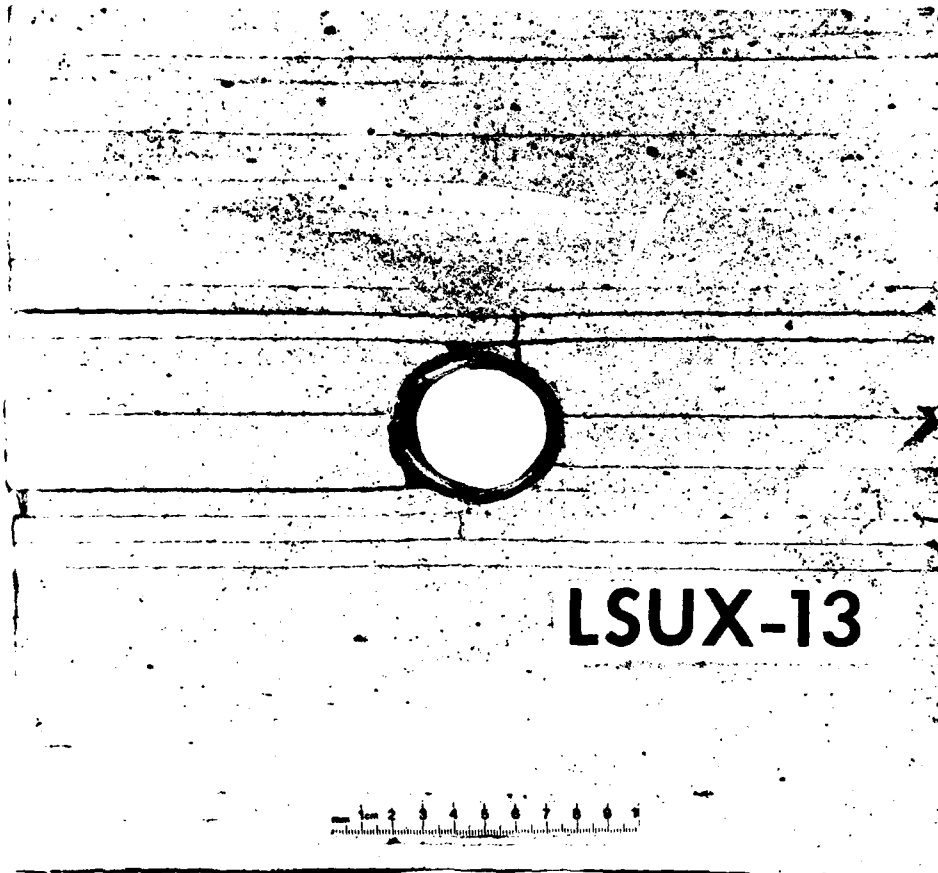
TUNNEL-JOINT ORIENTATION ANGLE  $\gamma$ :  $90^\circ$

STRUCTURE: Direct contact 1015 steel liner,  $a/h = 12.5$

LOADING: Monotonic

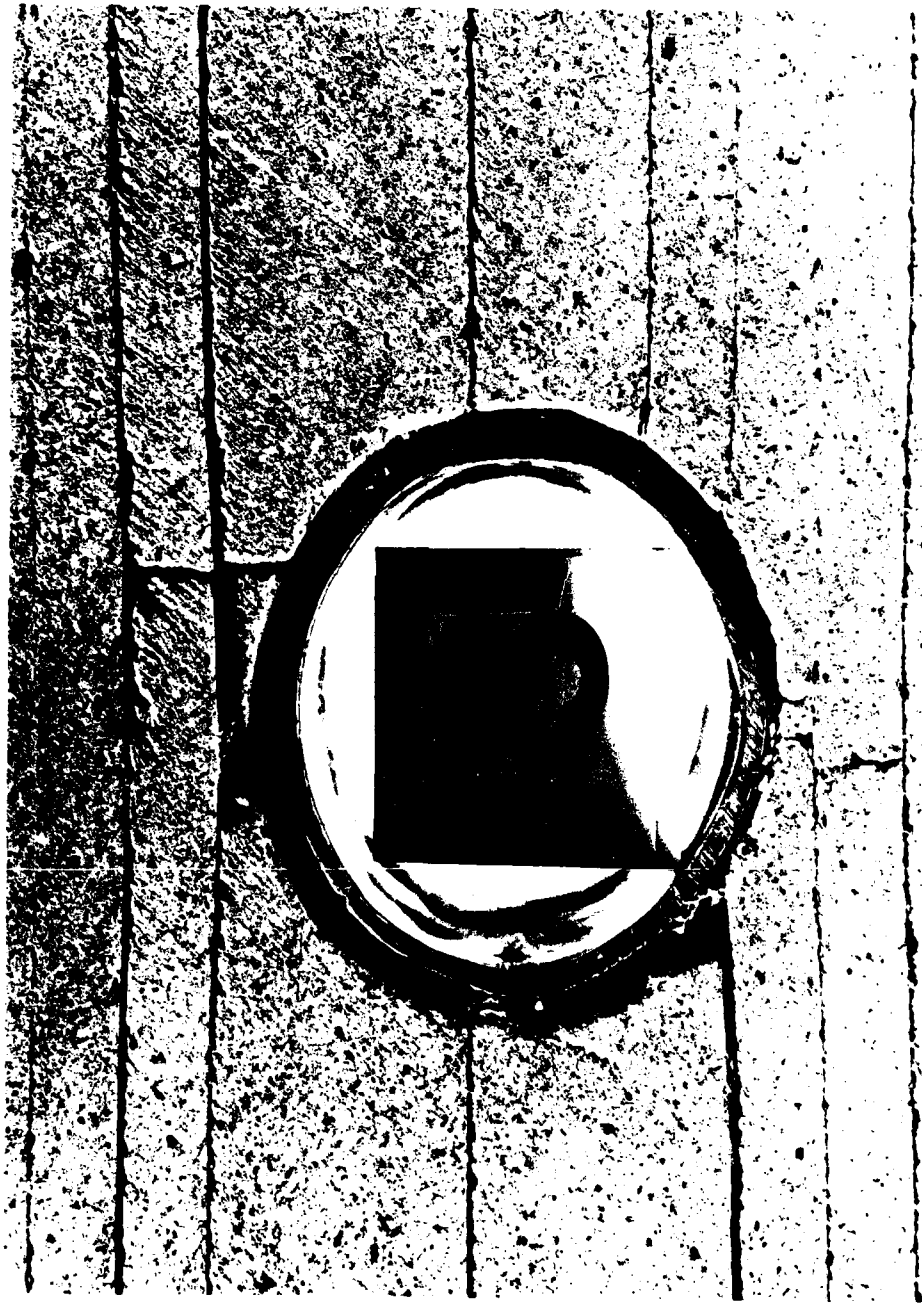
COMMENTS

The closure records are good. Liner strain records were obtained at the crown and one springline only. The specimen separated along joints through the tunnel during recovery. There was no evidence of block motion.



MP-5762-27

FIGURE A.2 SECTIONED SPECIMEN FROM TEST LSUX-13



MP-5762-29

FIGURE A.3 ENLARGEMENT OF TUNNEL REGION IN LSUX-13 SPECIMEN

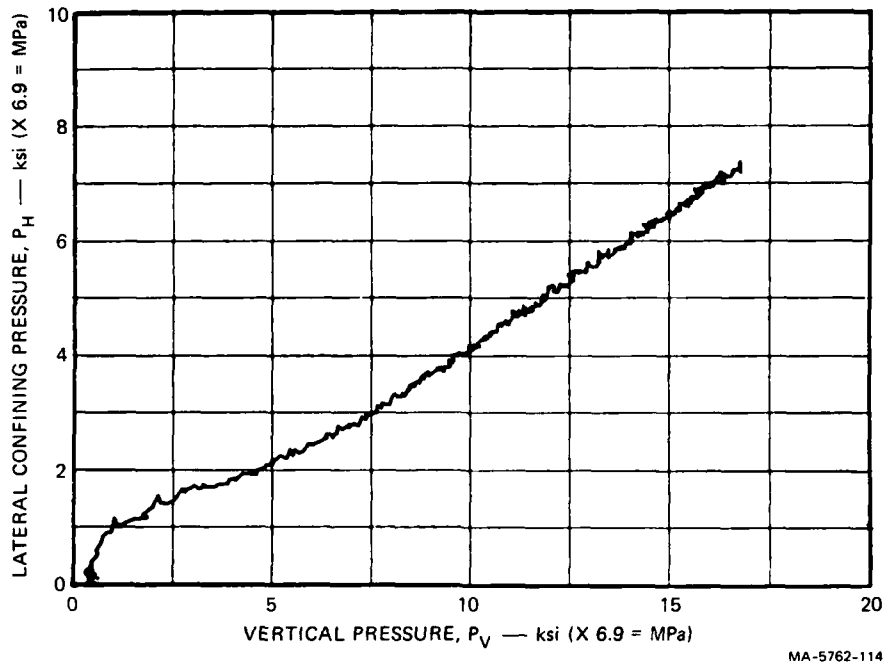


FIGURE A.4 LATERAL CONFINING PRESSURE VERSUS VERTICAL PRESSURE  
TEST LSUX-13

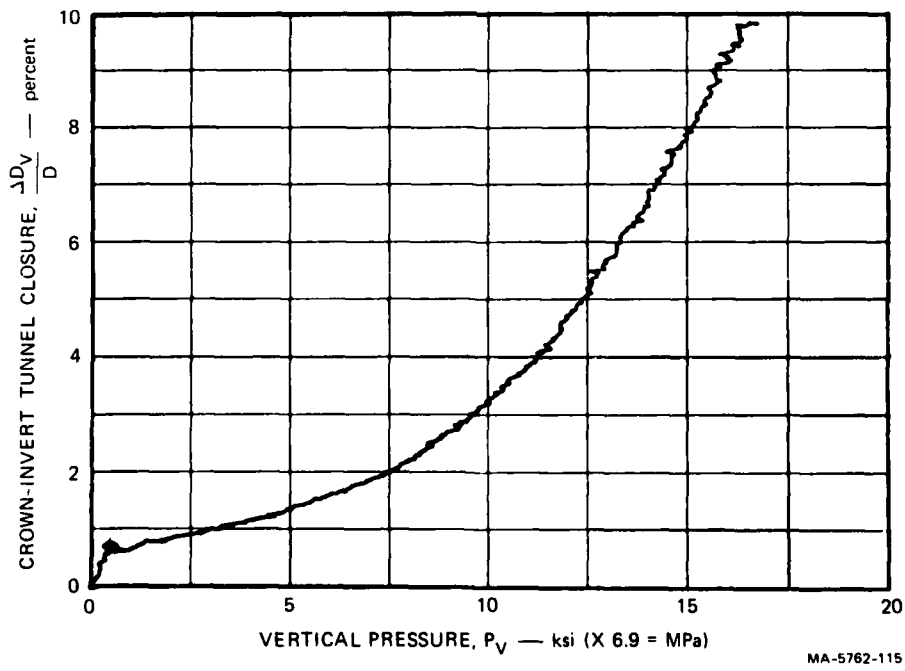


FIGURE A.5 CROWN-INVERT TUNNEL CLOSURE VERSUS VERTICAL PRESSURE  
TEST LSUX-13

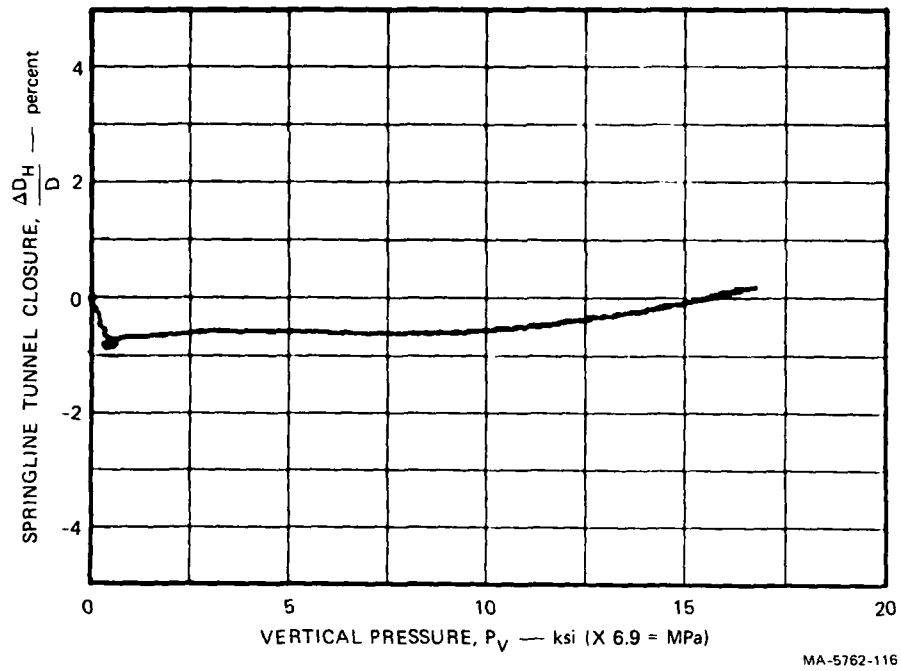


FIGURE A.6 SPRINGLINE TUNNEL CLOSURE VERSUS VERTICAL PRESSURE  
TEST LSUX-13

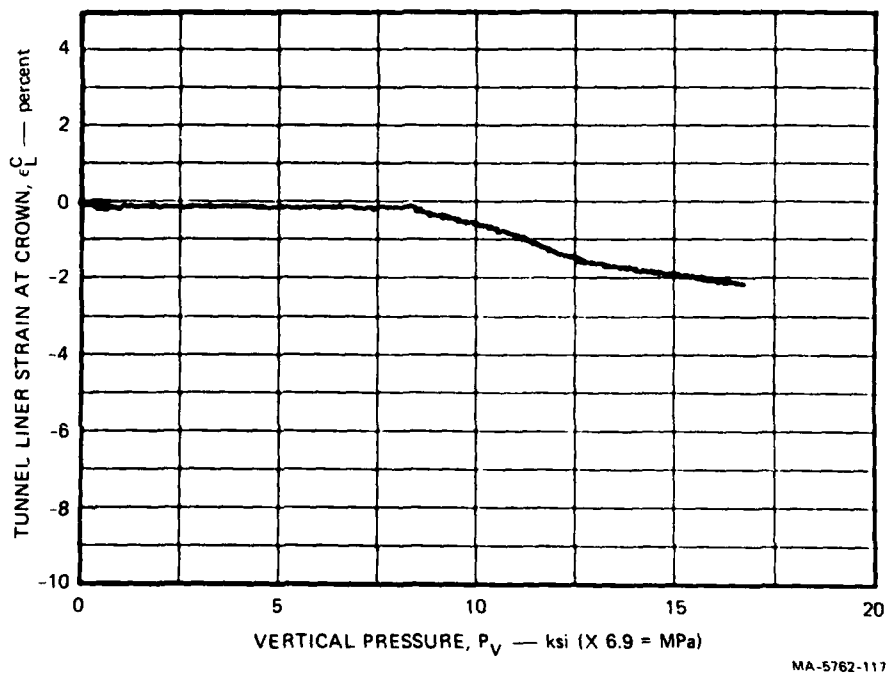
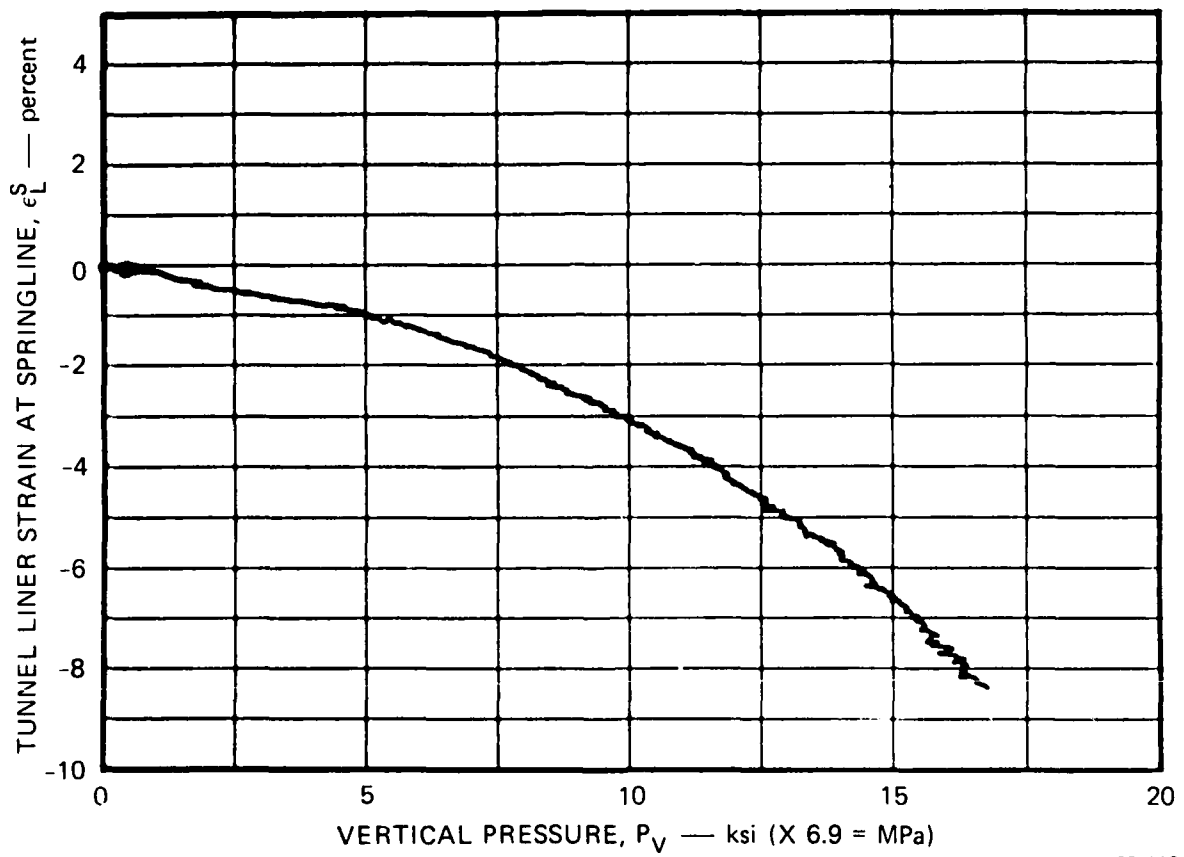


FIGURE A.7 TUNNEL LINER STRAIN AT CROWN VERSUS VERTICAL PRESSURE  
TEST LSUX-13



MA-5762-118

FIGURE A.8 TUNNEL LINER STRAIN AT SPRINGLINE VERSUS VERTICAL PRESSURE  
TEST LSUX-13

LSUX-14

LOAD-JOINT ORIENTATION ANGLE  $\beta$ :  $45^\circ$

TUNNEL-JOINT ORIENTATION ANGLE  $\gamma$ :  $0^\circ$

STRUCTURE: Direct contact 1015 steel liner,  $a/h = 12.5$

LOADING: Monotonic

COMMENTS

The closure records are good. No tunnel liner strain record was obtained at the invert. The specimen separated near the tunnel during recovery.



MP-5762-28

FIGURE A.9 SECTIONED SPECIMEN FROM TEST LSUX-14

AD-A088 912

SRI INTERNATIONAL MENLO PARK CA  
THEORETICAL AND EXPERIMENTAL STUDY OF DEEP-BASED STRUCTURES IN  
SEP 79 P E SENSENY; H E LINDBERG

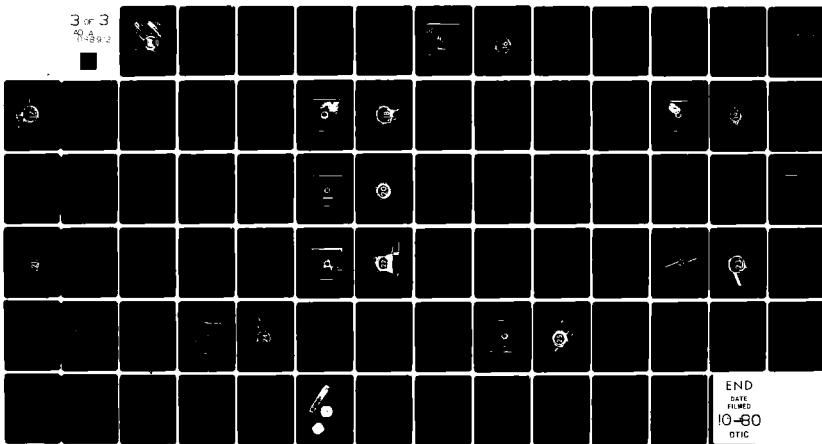
F/6 1 /13  
IN -- TC(U)  
DNA001-76-C-0385

UNCLASSIFIED

DNA-5208F

NL

3 of 3  
NOA  
7-89-2



END  
DATE  
FILMED  
10-80  
DTIC



MP-5762-30

FIGURE A.10 ENLARGEMENT OF TUNNEL REGION IN LSUX-14 SPECIMEN

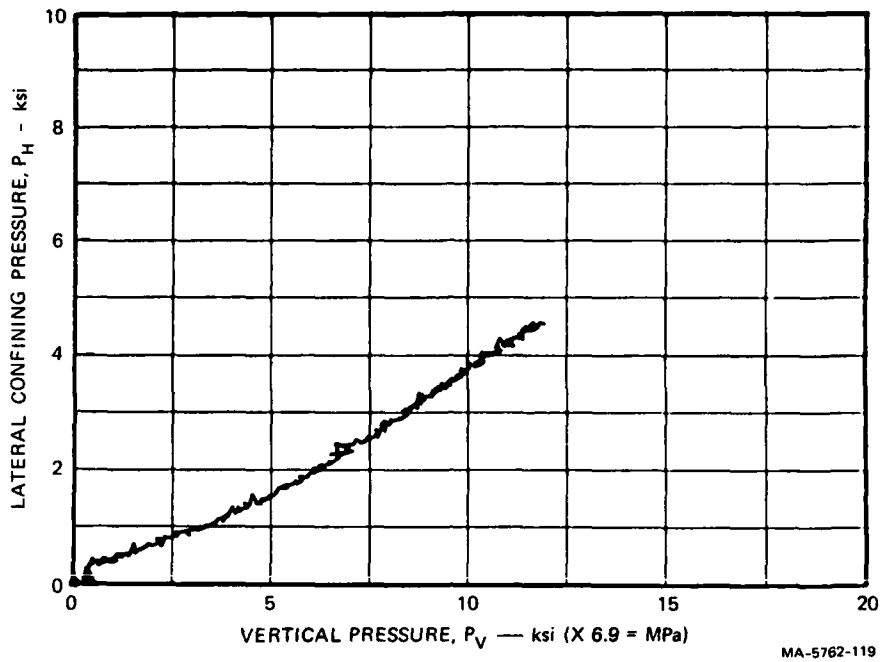


FIGURE A.11 LATERAL CONFINING PRESSURE VERSUS VERTICAL PRESSURE  
TEST LSUX-14

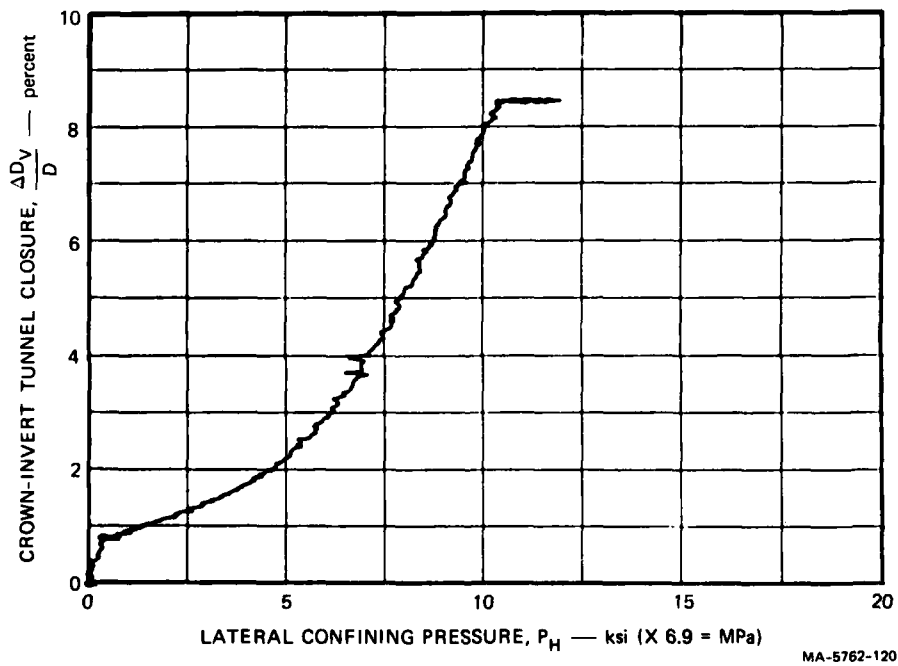
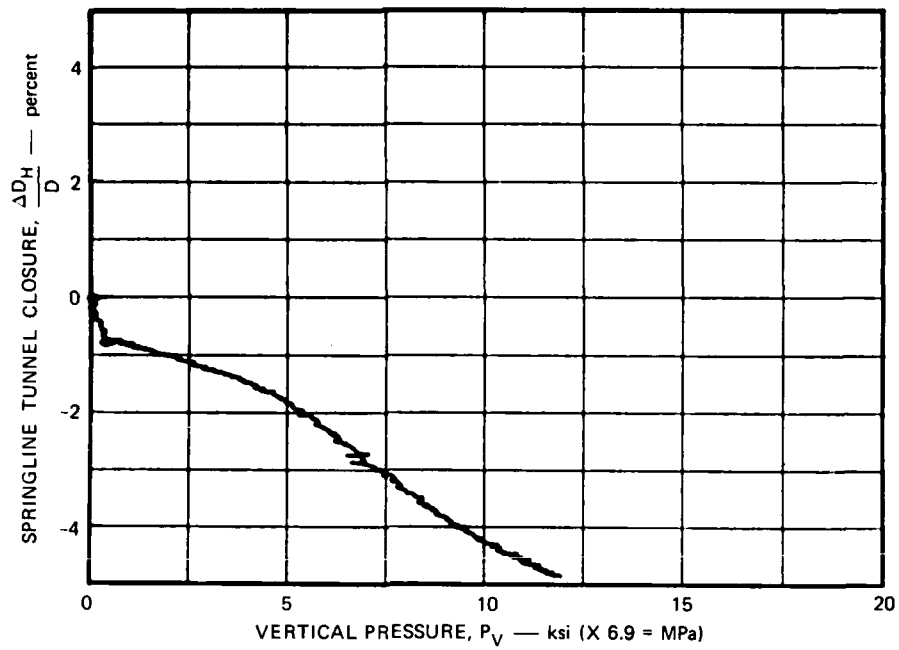
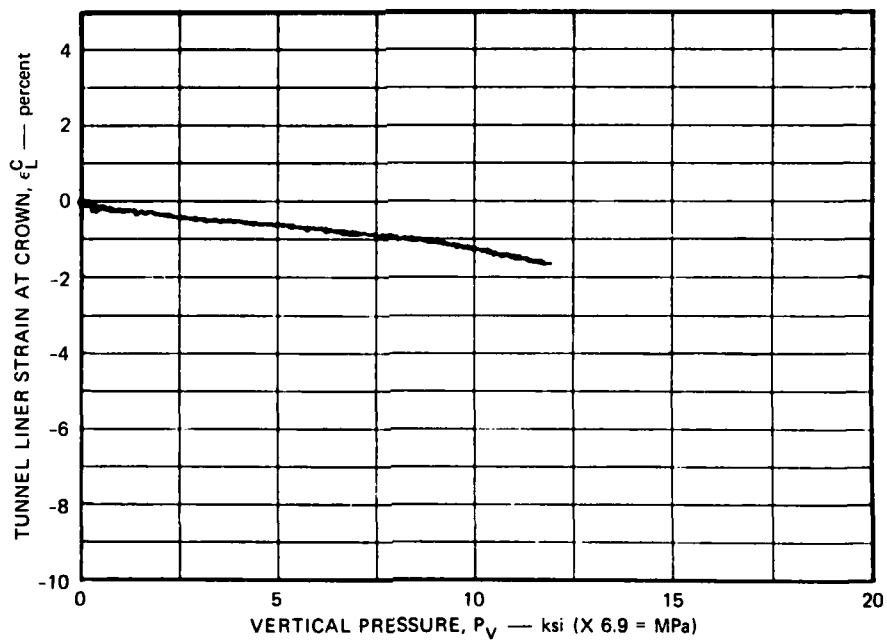


FIGURE A.12 CROWN-INVERT TUNNEL CLOSURE VERSUS VERTICAL PRESSURE  
TEST LSUX-14



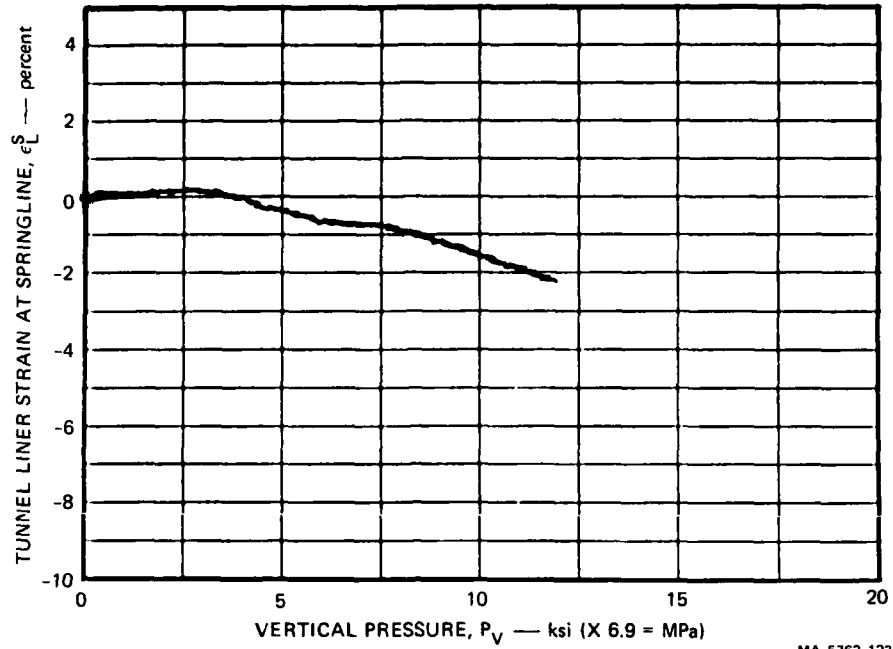
MA-5762-121

FIGURE A.13 SPRINGLINE TUNNEL CLOSURE VERSUS VERTICAL PRESSURE  
TEST LSUX-14



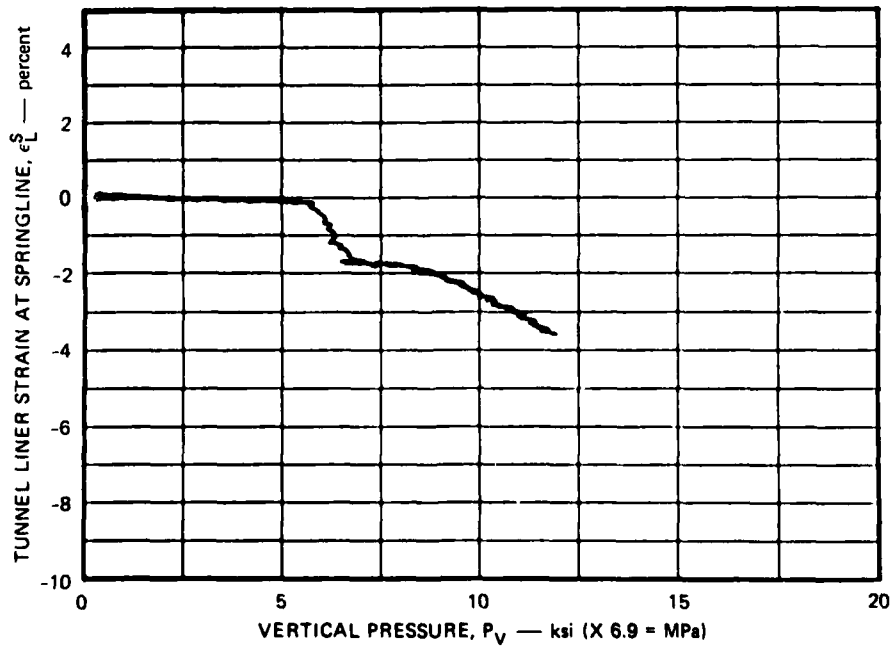
MA-5762-122

FIGURE A.14 TUNNEL LINER STRAIN AT CROWN VERSUS VERTICAL PRESSURE  
TEST LSUX-14



MA-5762-123

FIGURE A.15 TUNNEL LINER STRAIN AT LEFT SPRINGLINE VERSUS VERTICAL PRESSURE — TEST LSUX-14



MA-5762-124

FIGURE A.16 TUNNEL LINER STRAIN AT RIGHT SPRINGLINE VERSUS VERTICAL PRESSURE — TEST LSUX-14

LSUX-16

LOAD-JOINT ORIENTATION ANGLE  $\beta$ :  $30^\circ$

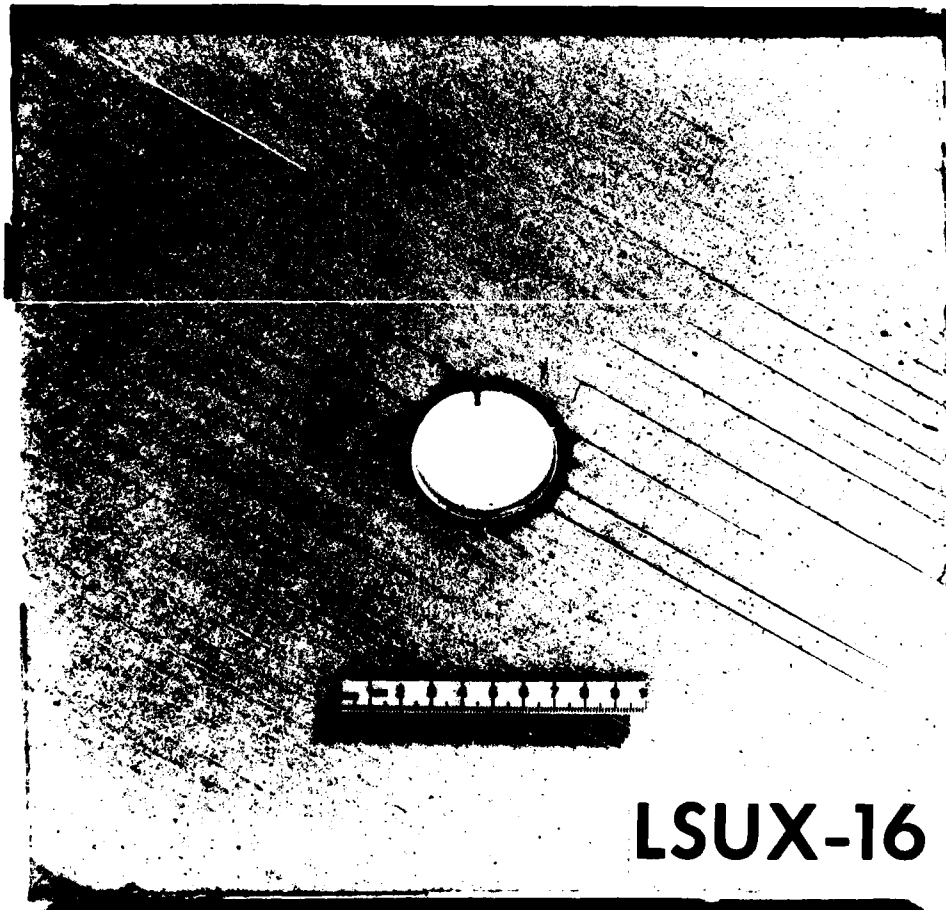
TUNNEL-JOINT ORIENTATION ANGLE  $\gamma$ :  $90^\circ$

STRUCTURE: Direct contact 1015 steel liner,  $a/h = 12.5$

LOADING: monotonic

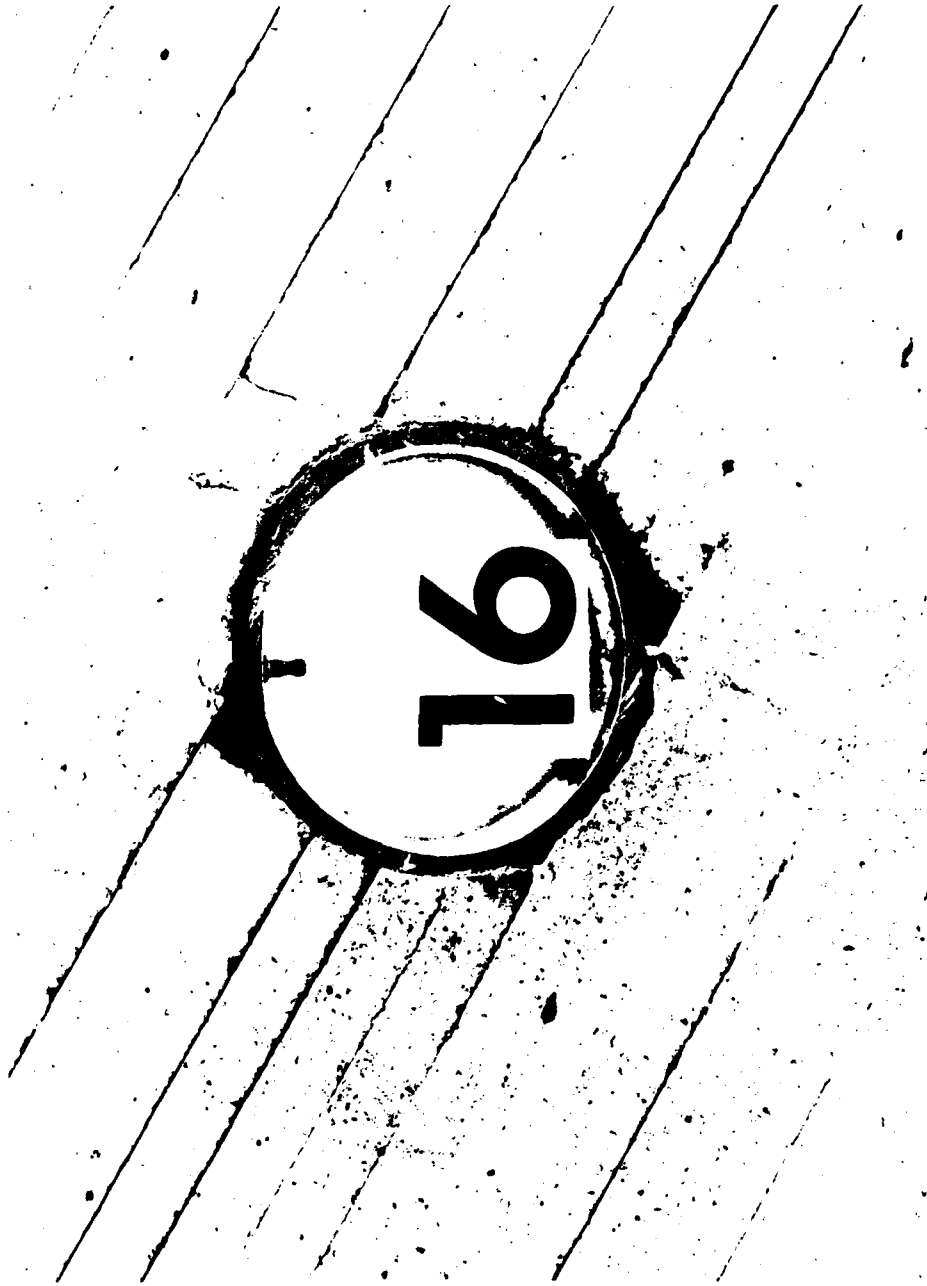
COMMENTS

The initial slopes of the tunnel closure versus vertical pressure curves,  $d(\Delta D/D)/dP_v$ , are much larger than expected, and the crown-invert closures are larger than would be predicted from the results of LSUX-13 ( $\beta = 0^\circ$ ) and LSUX-14 ( $\beta = 45^\circ$ ). The liner strain records are good. The specimen was recovered intact.



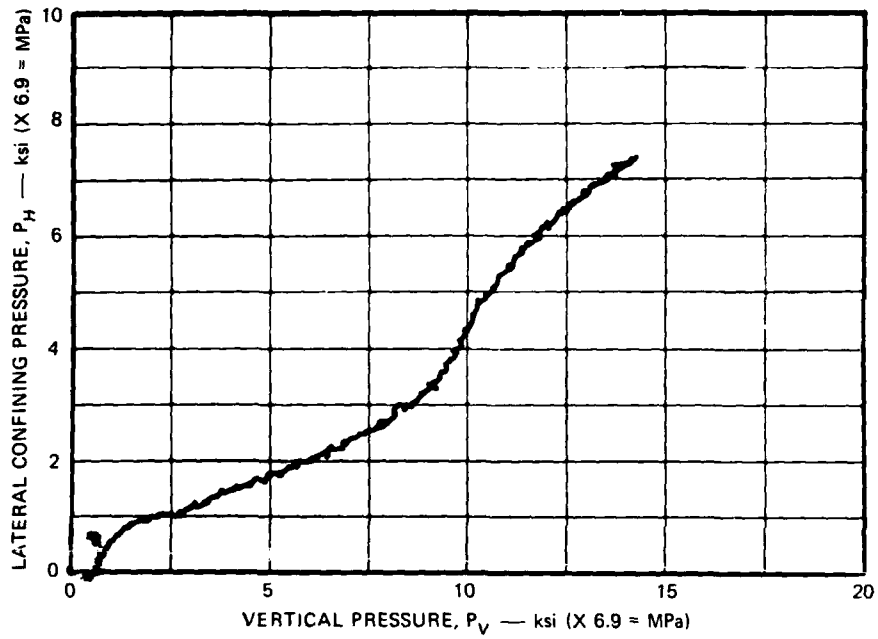
MP-5762-125

FIGURE A.17 SECTIONED SPECIMEN FROM TEST LSUX-16



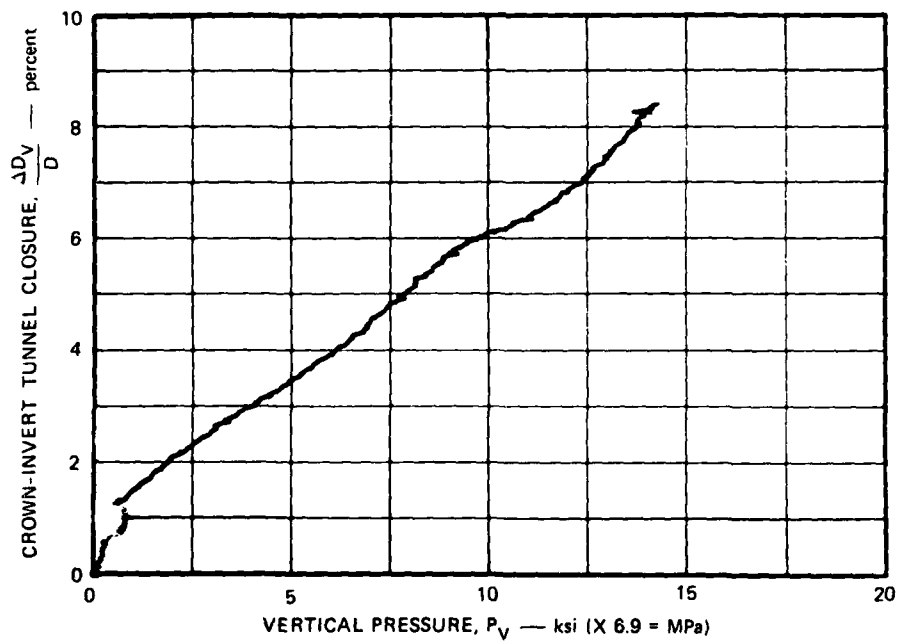
MP-5762-126

FIGURE A.18 ENLARGEMENT OF TUNNEL REGION IN LSUX-16 SPECIMEN



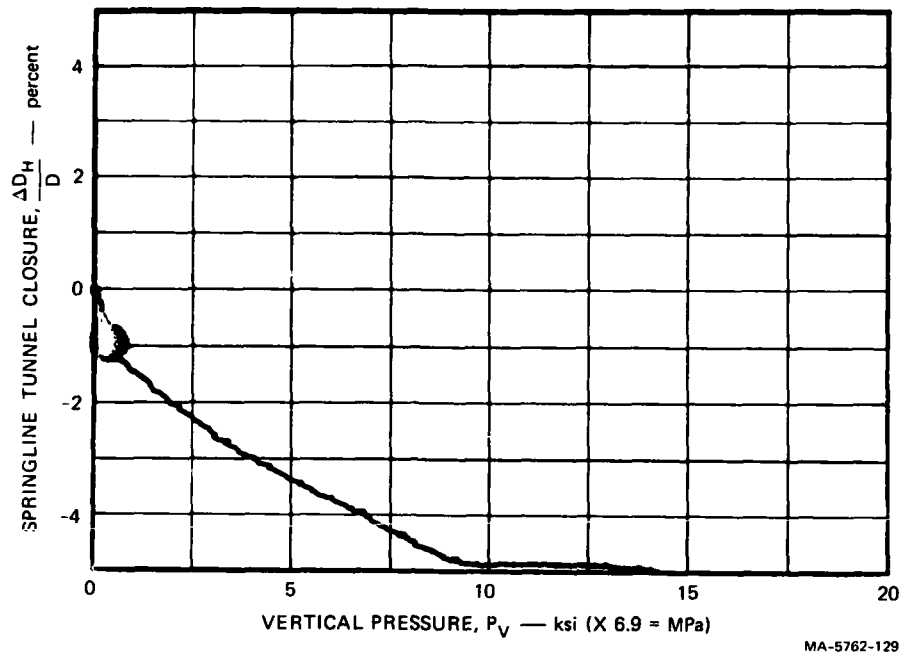
MA-5762-127

FIGURE A.19 LATERAL CONFINING PRESSURE VERSUS VERTICAL PRESSURE  
TEST LSUX-16



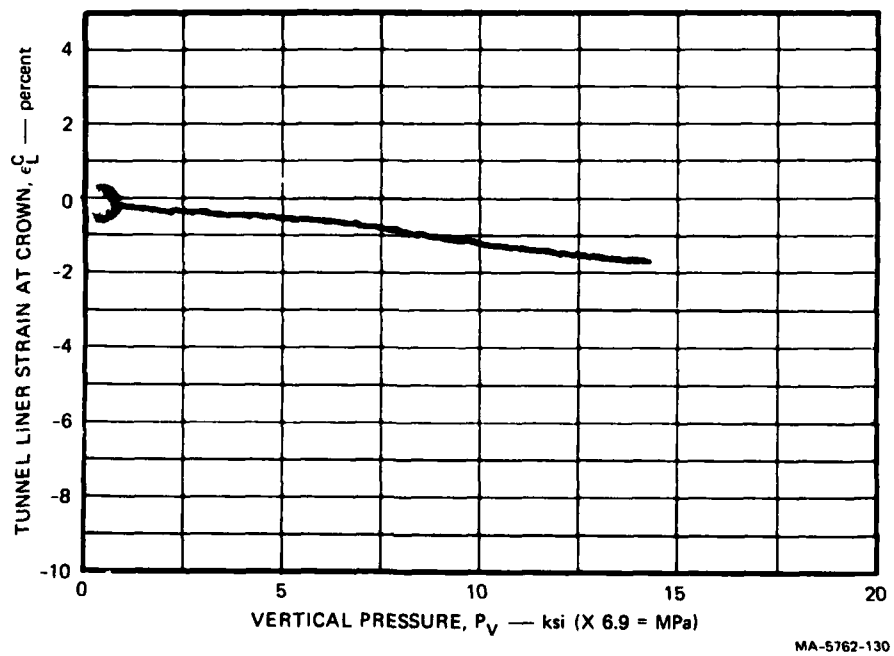
MA-5762-128

FIGURE A.20 CROWN-INVERT TUNNEL CLOSURE VERSUS VERTICAL PRESSURE  
TEST LSUX-16



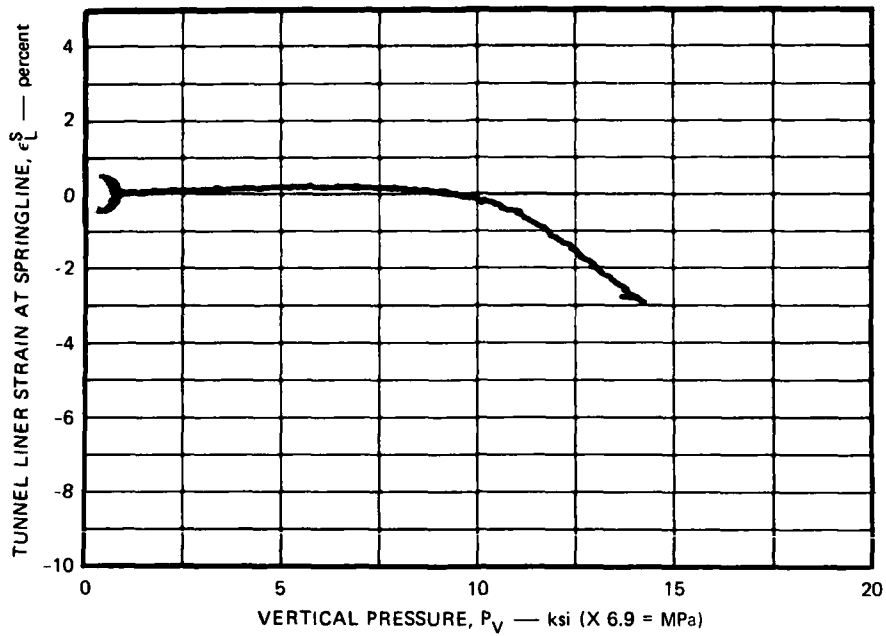
MA-5762-129

FIGURE A.21 SPRINGLINE TUNNEL CLOSURE VERSUS VERTICAL PRESSURE  
TEST LSUX-16



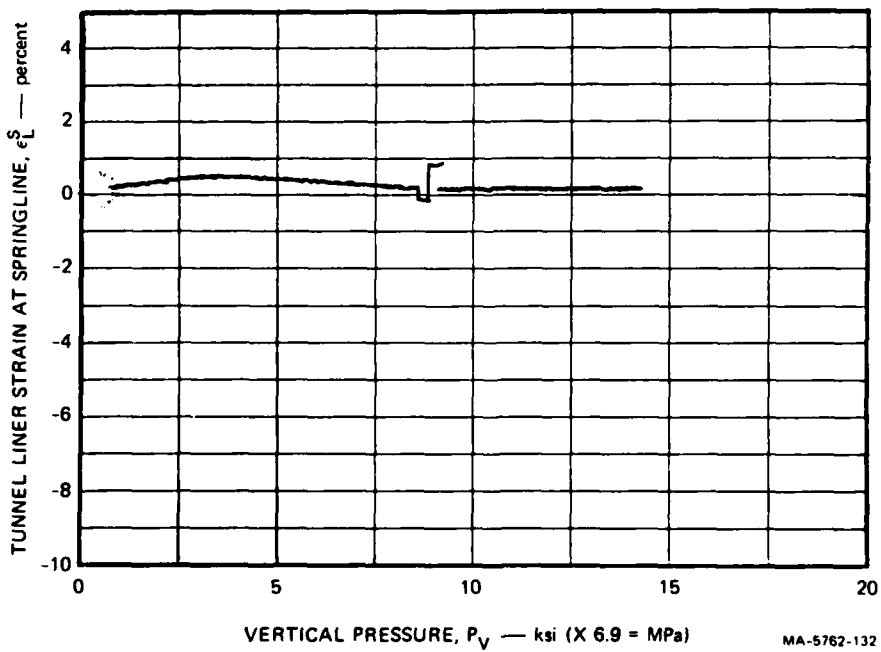
MA-5762-130

FIGURE A.22 TUNNEL LINER STRAIN AT CROWN VERSUS VERTICAL PRESSURE  
TEST LSUX-16



MA-5762-131

FIGURE A.23 TUNNEL LINER STRAIN AT LEFT SPRINGLINE VERSUS VERTICAL PRESSURE — TEST LSUX-16



MA-5762-132

FIGURE A.24 TUNNEL LINER STRAIN AT RIGHT SPRINGLINE VERSUS VERTICAL PRESSURE — TEST LSUX-16

LSUX-17

LOAD-JOINT ORIENTATION ANGLE  $\beta$ :  $0^\circ$

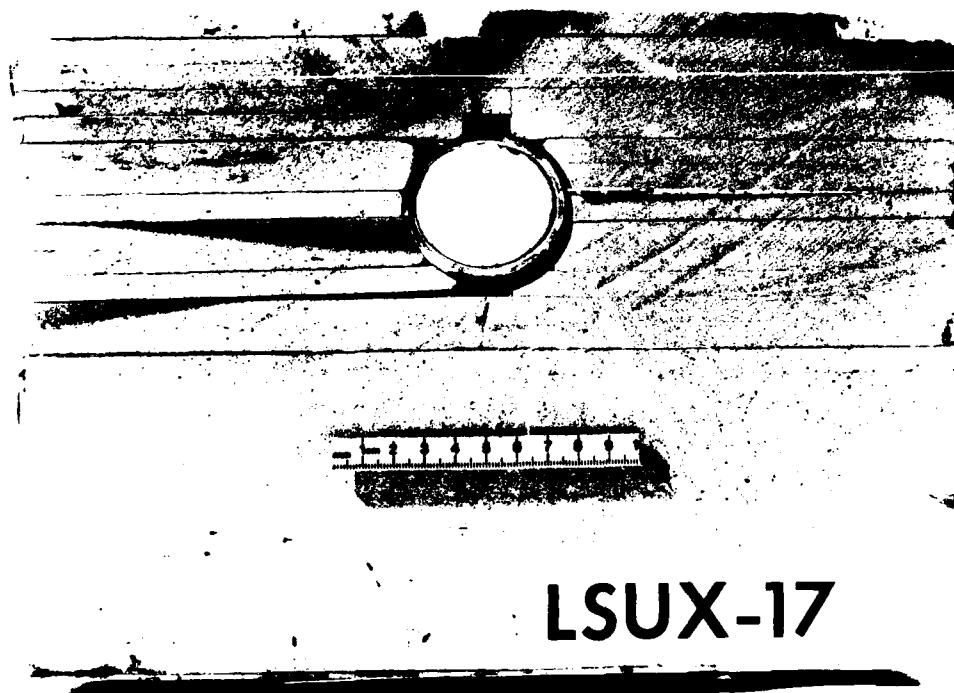
TUNNEL-JOINT ORIENTATION ANGLE  $\gamma$ :  $90^\circ$

STRUCTURE: Direct contact 1015 steel liner,  $a/h = 12.5$

LOADING: Cyclic

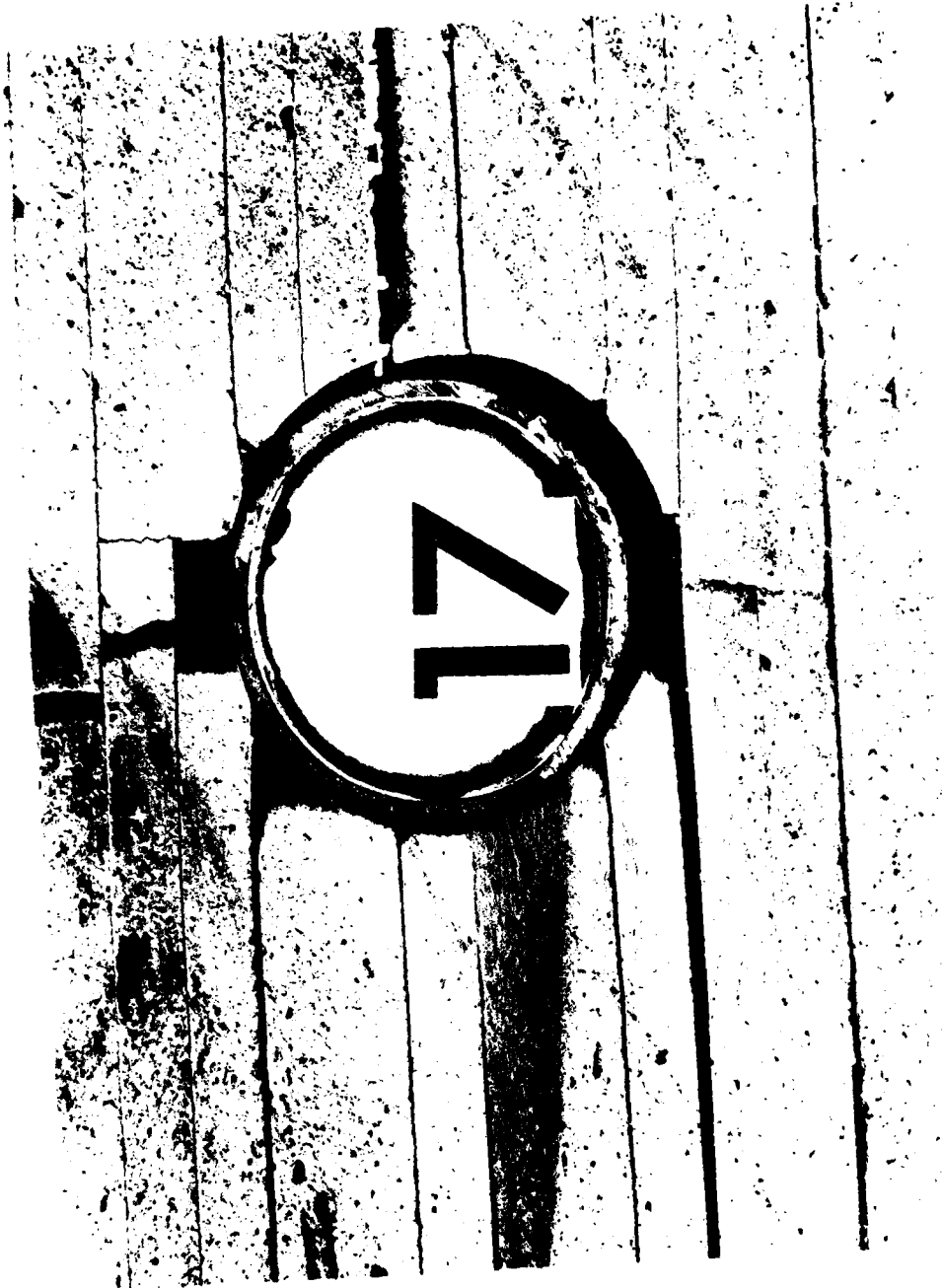
COMMENTS

The load was cycled at crown-invert closures of 2%, 3%, 5%, and 8%. Records of tunnel closure versus vertical pressure are similar to those obtained for cyclic loading of intact rock: unloading and reloading occur along the same lines, and additional closure is not obtained until the pressure is raised above the maximum pressure applied previously. Comparison with monotonic loading closure records from LSUX-13 ( $\beta = 0^\circ$ ) shows that cyclic loading does not degrade the load-carrying capability of the structure. Liner strain records at crown and one springline are good. The specimen could not be recovered intact because it expanded and locked into the machine: the top of the specimen was removed with a hammer and chisel.



MP-5762-133

FIGURE A.25 SECTIONED SPECIMEN FROM TEST LSUX-17



MP-5762-134

FIGURE A.26 ENLARGEMENT OF TUNNEL REGION IN LSUX-17 SPECIMEN

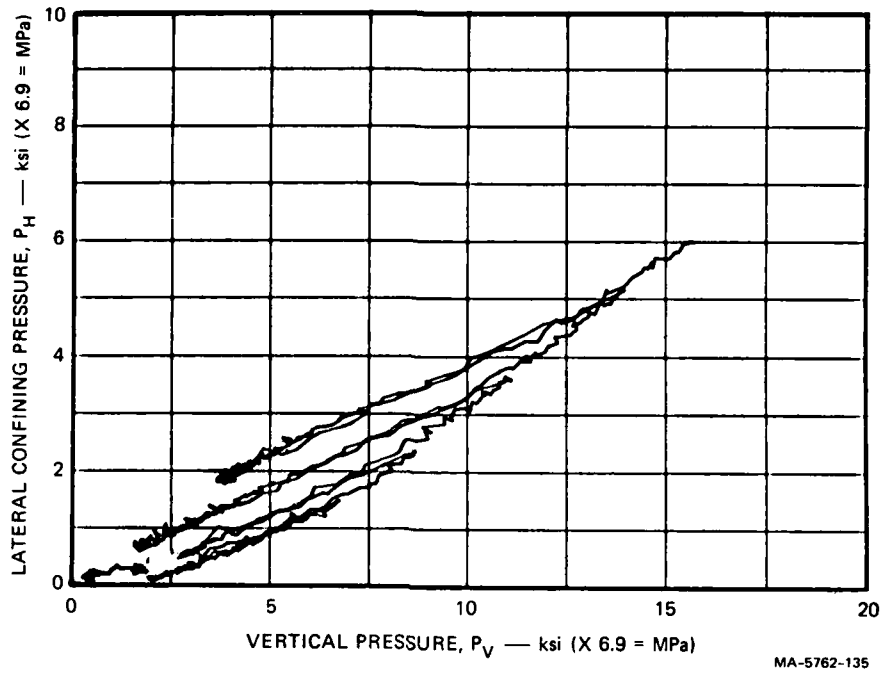


FIGURE A.27 LATERAL CONFINING PRESSURE VERSUS VERTICAL PRESSURE  
TEST LSUX-17

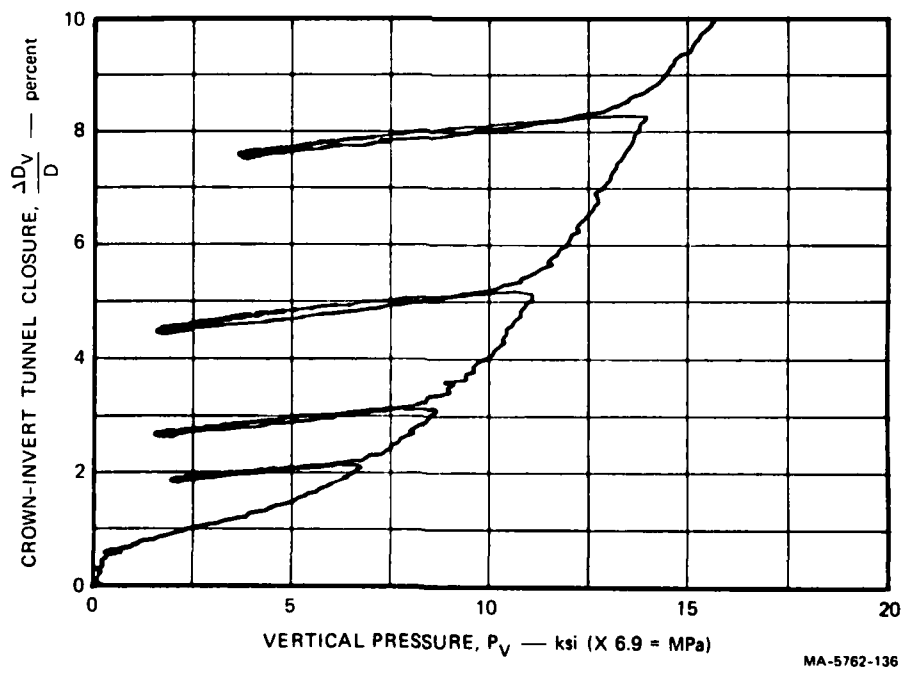


FIGURE A.28 CROWN-INVERT TUNNEL CLOSURE VERSUS VERTICAL PRESSURE  
TEST LSUX-17

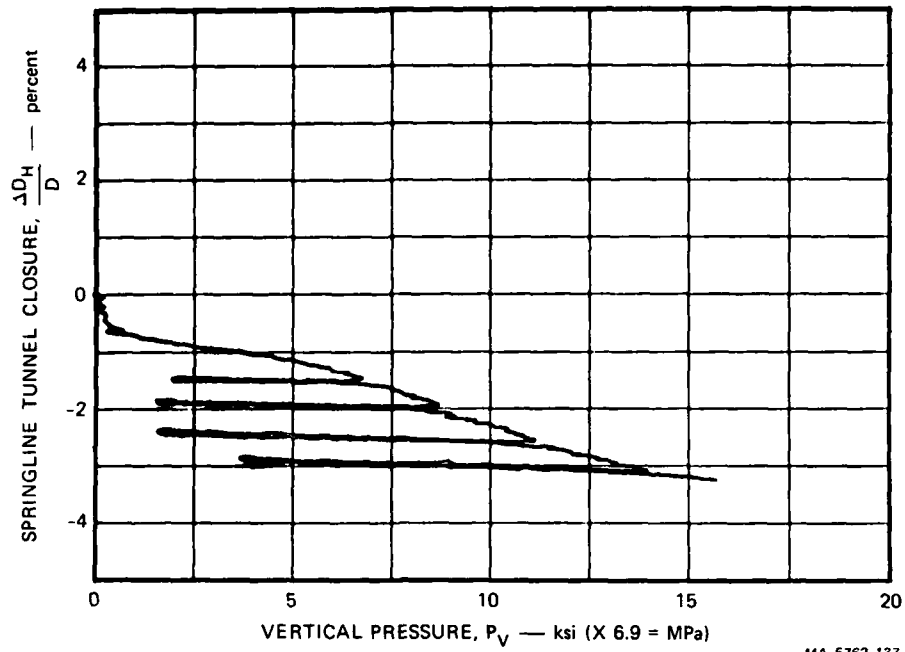


FIGURE A.29 SPRINGLINE TUNNEL CLOSURE VERSUS VERTICAL PRESSURE  
TEST LSUX-17

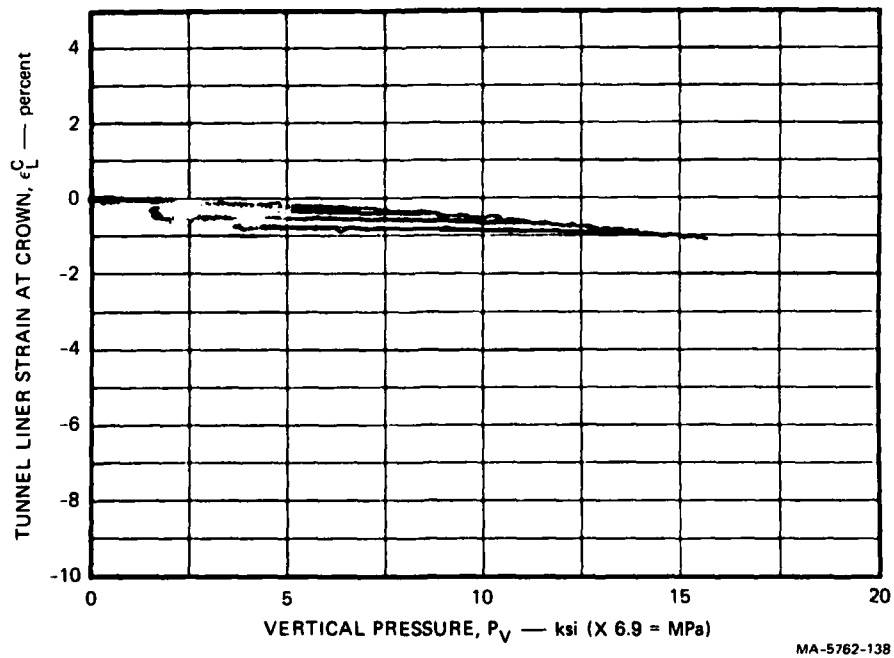
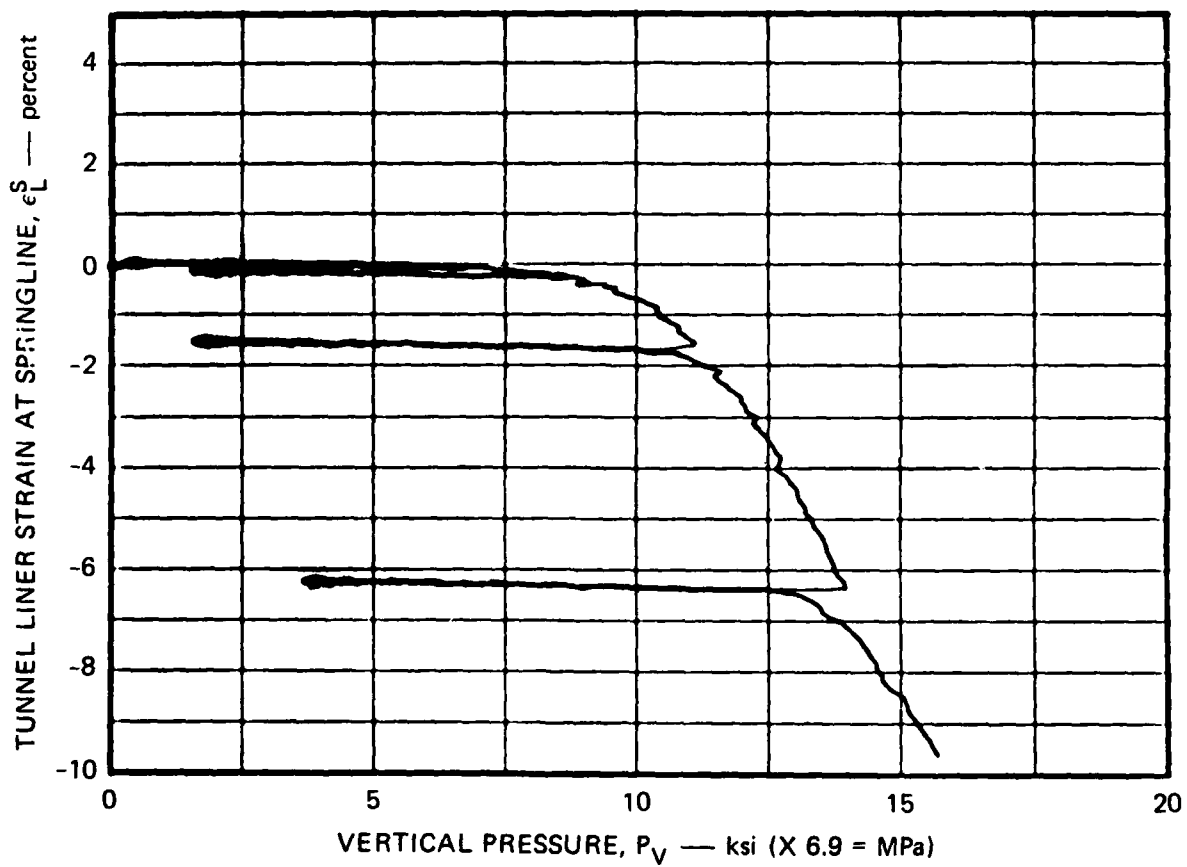


FIGURE A.30 TUNNEL LINER STRAIN AT CROWN VERSUS VERTICAL PRESSURE  
TEST LSUX-17



MA-5762-139

FIGURE A.31 TUNNEL LINER STRAIN AT SPRINGLINE VERSUS VERTICAL PRESSURE  
TEST LSUX-17

LSUX-18

LOAD-JOINT ORIENTATION ANGLE  $\beta$ : 45°

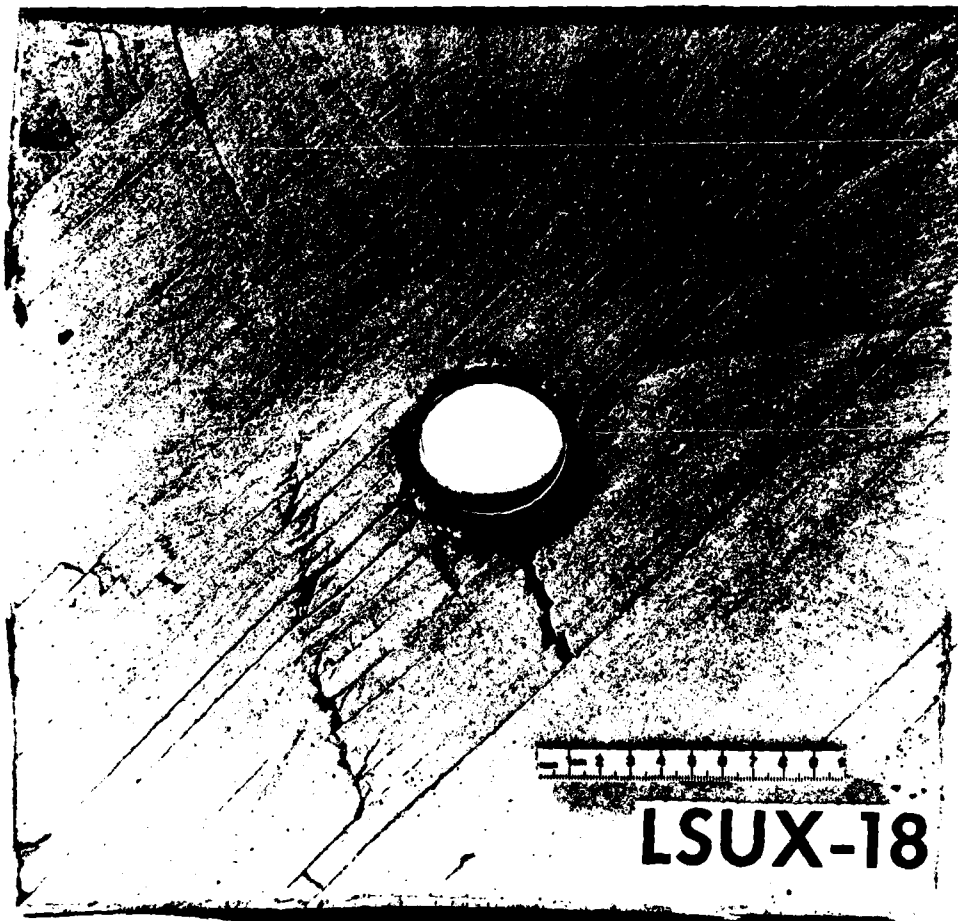
TUNNEL-JOINT ORIENTATION ANGLE  $\gamma$ : 90°

STRUCTURE: Direct contact 1015 steel liner, a/h = 12.5

LOADING: Cyclic

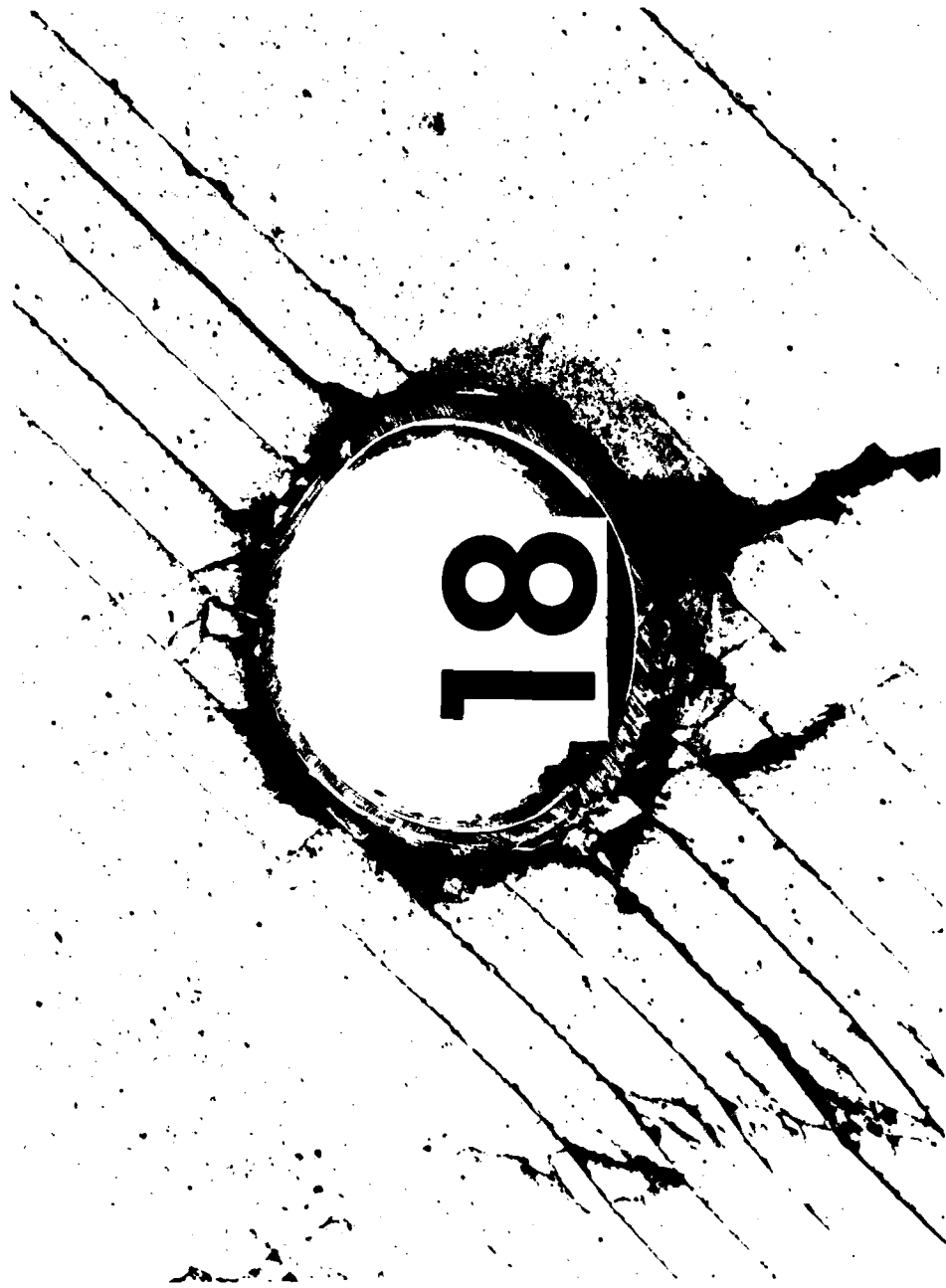
COMMENTS

The lateral confining pressure increased during loading to follow the specified path. However, because of an error in the load control program, the lateral confining pressure dropped rapidly during unloading. The confinement was reduced significantly during the unloading phase; hence, unloading and reloading tunnel closures do not lie along the same line. In fact, the lower confinement during unloading allowed tunnel closure to increase throughout most of the unloading phase. The specimen separated slightly during recovery. This caused the wide crack that runs downward from the tunnel. The line of cracks to the left of the tunnel is not thought to be the result of posttest handling.



MP-5762-140

FIGURE A.32 SECTIONED SPECIMEN FROM TEST LSUX-18



MP-5762-141

FIGURE A.33 ENLARGEMENT OF TUNNEL REGION IN LSUX-18 SPECIMEN

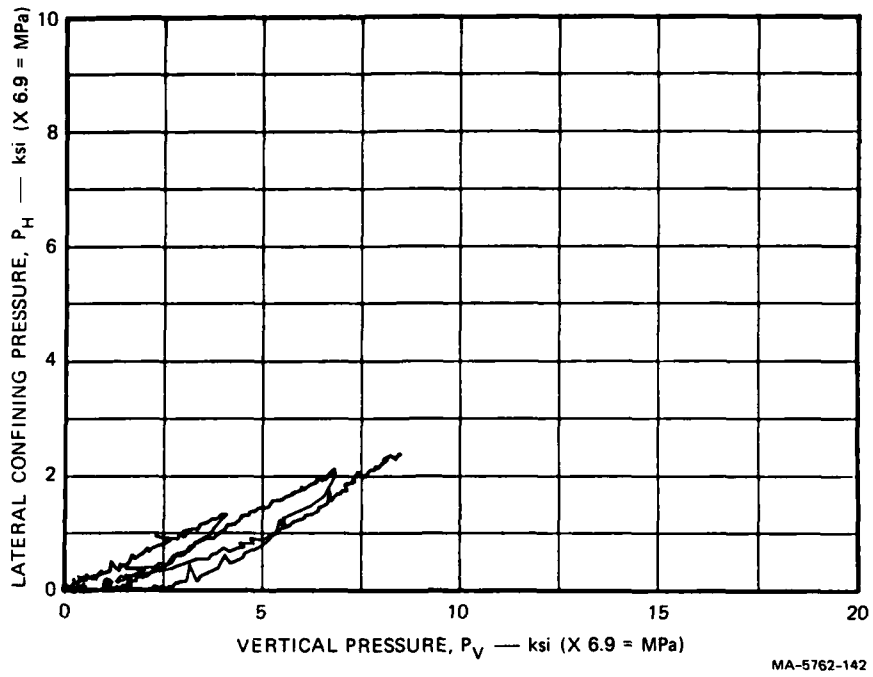


FIGURE A.34 LATERAL CONFINING PRESSURE VERSUS VERTICAL PRESSURE  
TEST LSUX-18

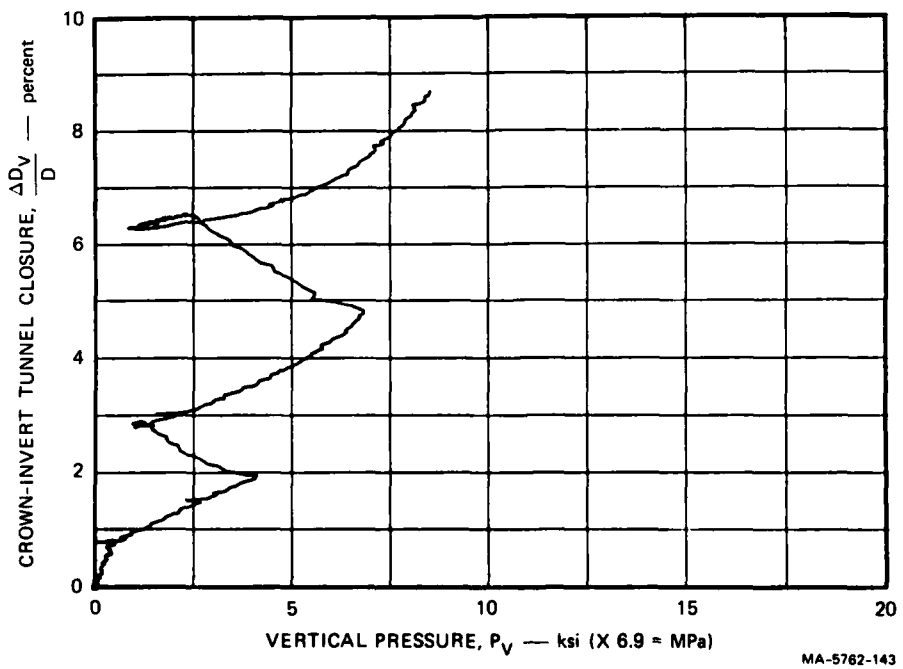


FIGURE A.35 CROWN-INVERT TUNNEL CLOSURE VERSUS VERTICAL PRESSURE  
TEST LSUX-18

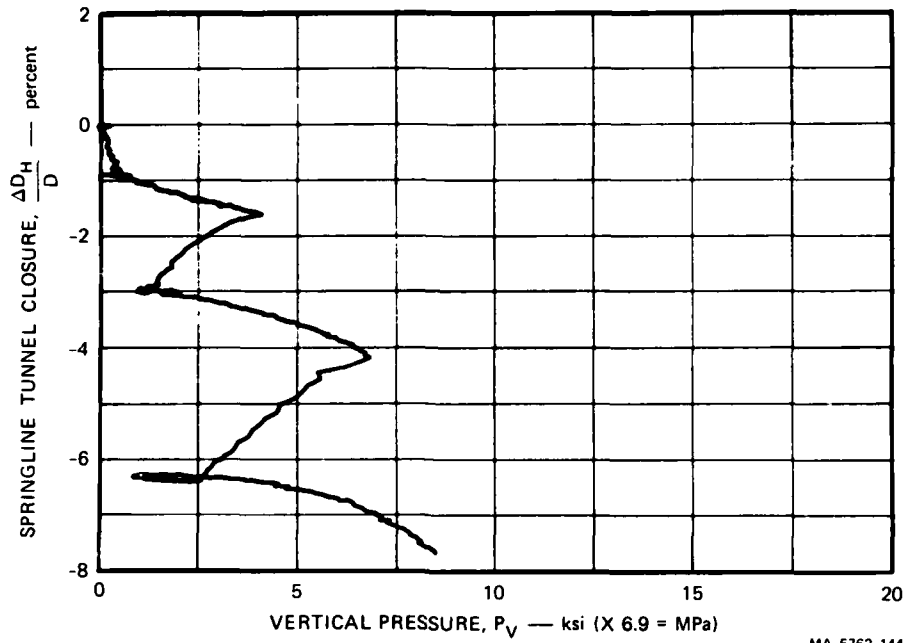


FIGURE A.36 SPRINGLINE TUNNEL CLOSURE VERSUS VERTICAL PRESSURE  
TEST LSUX-18

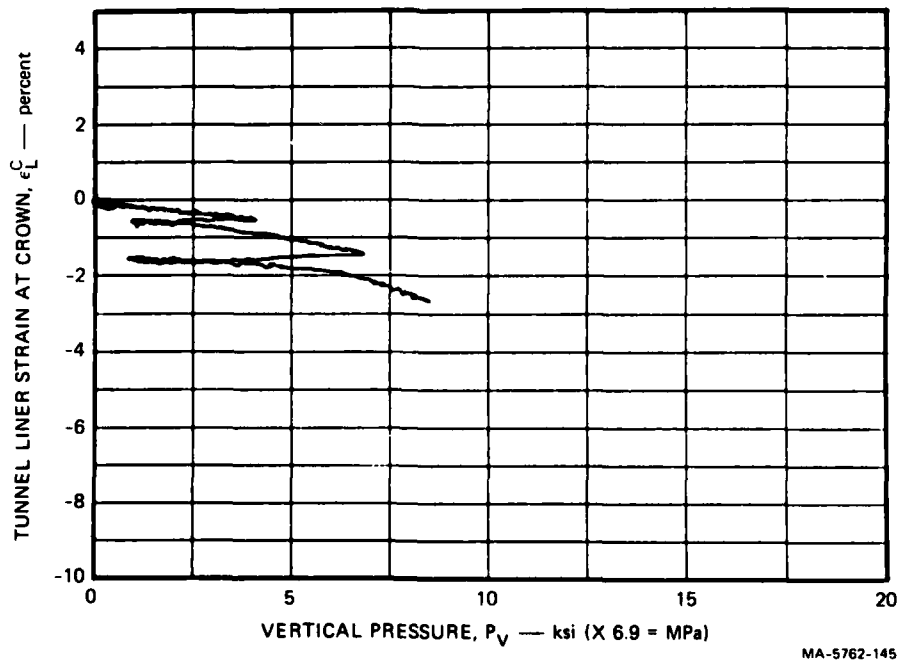
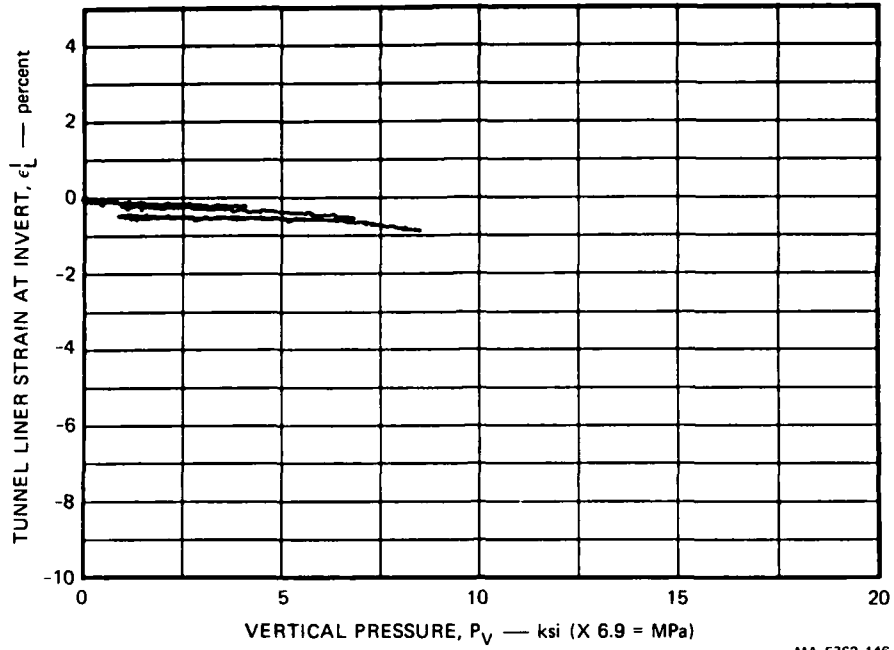
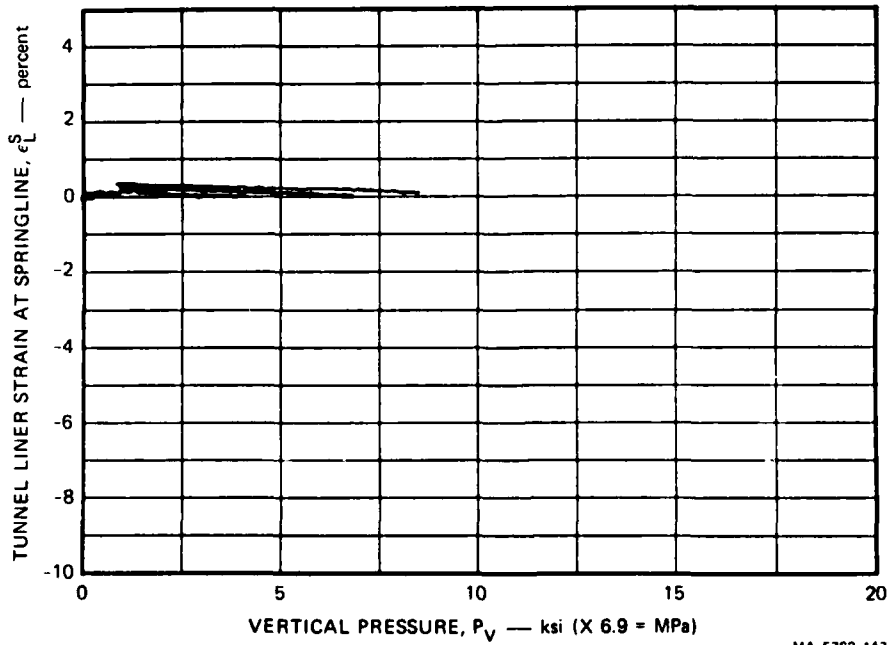


FIGURE A.37 TUNNEL LINER STRAIN AT CROWN VERSUS VERTICAL PRESSURE  
TEST LSUX-18



MA-5762-146

FIGURE A.38 TUNNEL LINER STRAIN AT INVERT VERSUS VERTICAL PRESSURE  
TEST LSUX-18



MA-5762-147

FIGURE A.39 TUNNEL LINER STRAIN AT SPRINGLINE VERSUS VERTICAL PRESSURE  
TEST LSUX-18

LSUX-19

LOAD-JOINT ORIENTATION ANGLE  $\beta$ : 30°

TUNNEL-JOINT ORIENTATION ANGLE  $\gamma$ : 90°

STRUCTURE: Backpacked 1015 steel liner, a/h = 12.5  
Polyurethane foam backpacking, R/h = 4.3

LOADING: Monotonic

COMMENTS

The press-fit interference between the backpacking and the rock cavity was too great. The drag of the backpacking along the tunnel wall caused misalignment of the rock-cavity closure transducers. This misalignment was probably the cause of the intermittent rock-cavity closures measured. In addition, the tight press fit deformed the structure so that the initial response was lost: change of structure diameters (transducer readings) during installation are:

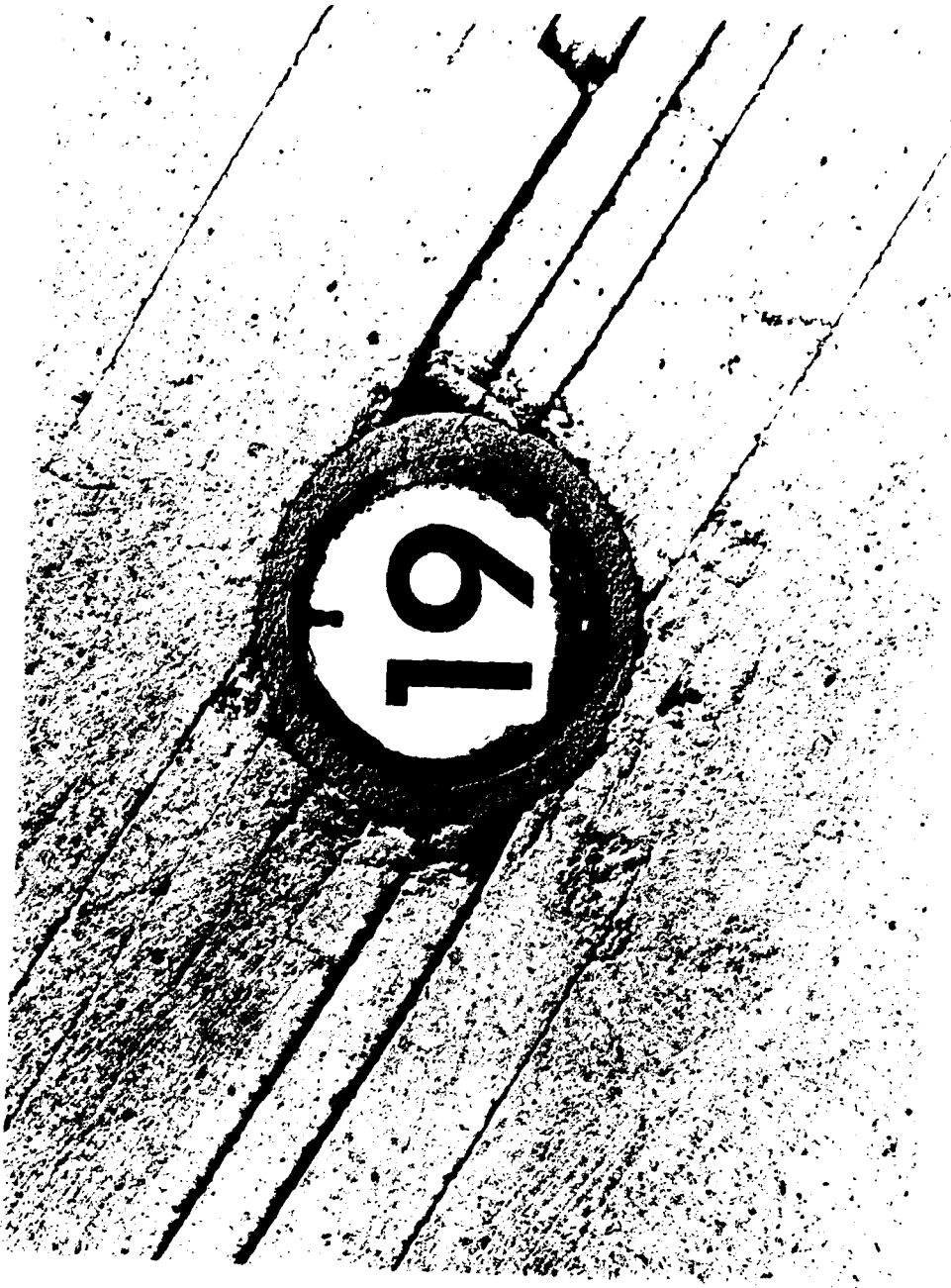
Rock Cavity:	Crown-invert	+1.75%
	Springline	-2.0%
Liner:	Crown-invert	+1.25%
	Springline	-.5%

Liner closure records are smooth and similar to those obtained for other backpacked structures. Liner strain records are good but slightly noisy because the sensitivity of the signal conditioning units was set too low. The specimen separated slightly during recovery.



MP-5762-149

FIGURE A.40 SECTIONED SPECIMEN FROM TEST LSUX-19



MP-5762-150

FIGURE A.41 ENLARGEMENT OF TUNNEL REGION IN LSUX-19 SPECIMEN

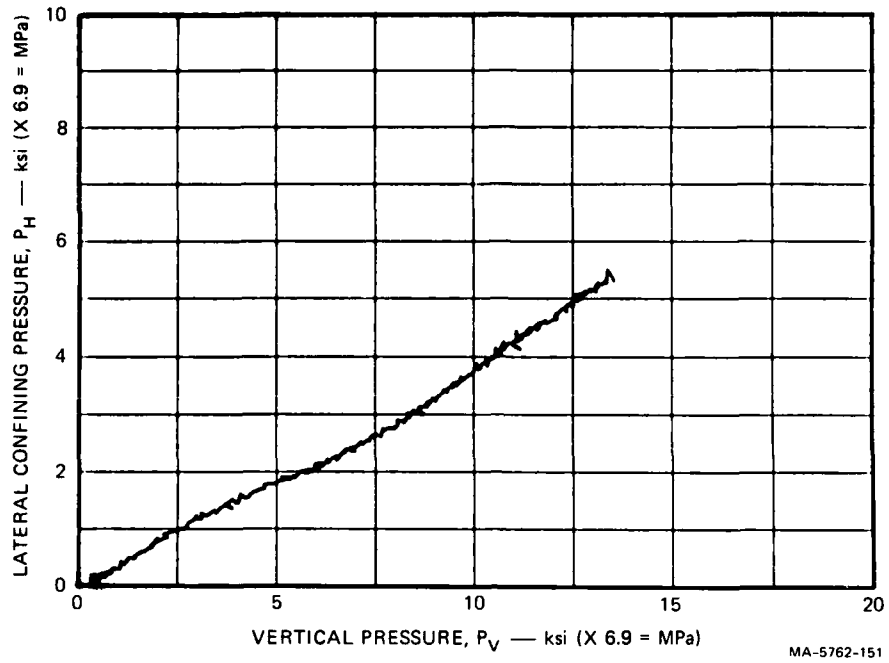


FIGURE A.42 LATERAL CONFINING PRESSURE VERSUS VERTICAL PRESSURE  
TEST LSUX-19

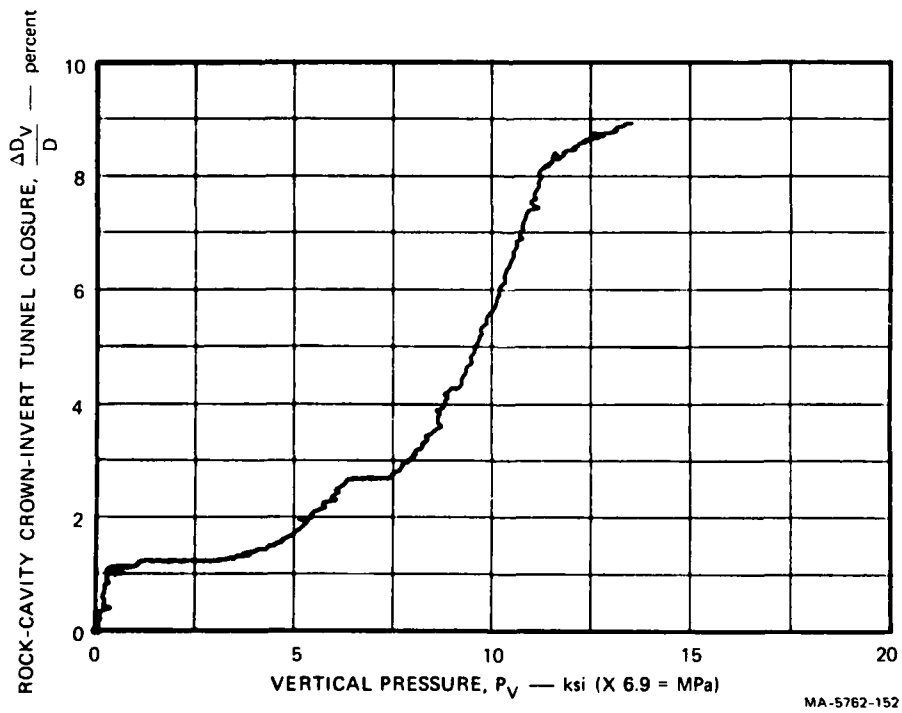


FIGURE A.43 ROCK-CAVITY CROWN-INVERT TUNNEL CLOSURE VERSUS VERTICAL PRESSURE — TEST LSUX-19

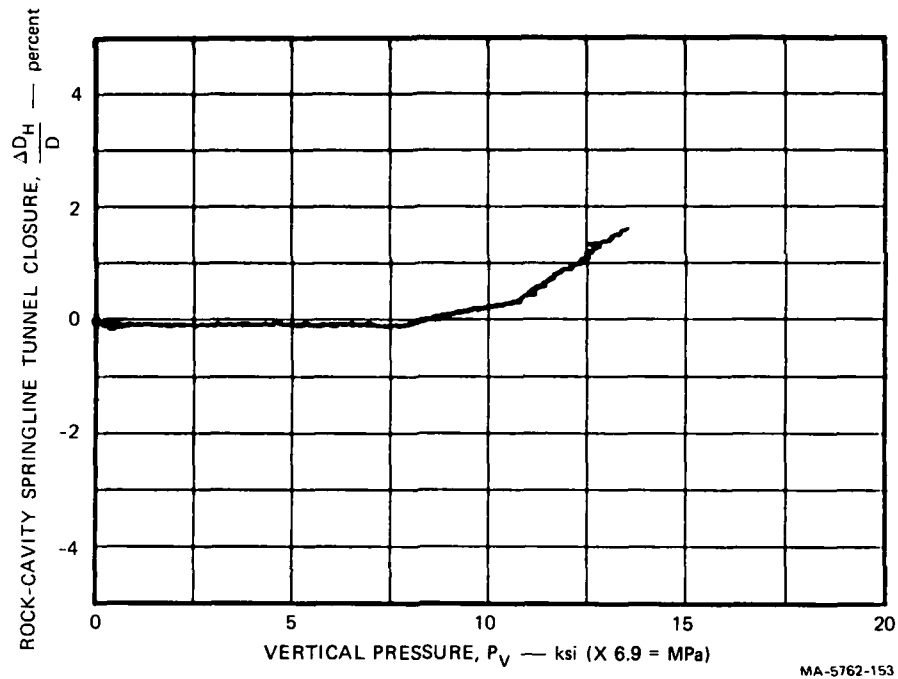


FIGURE A.44 ROCK-CAVITY SPRINGLINE TUNNEL CLOSURE VERSUS VERTICAL PRESSURE — LSUX-19

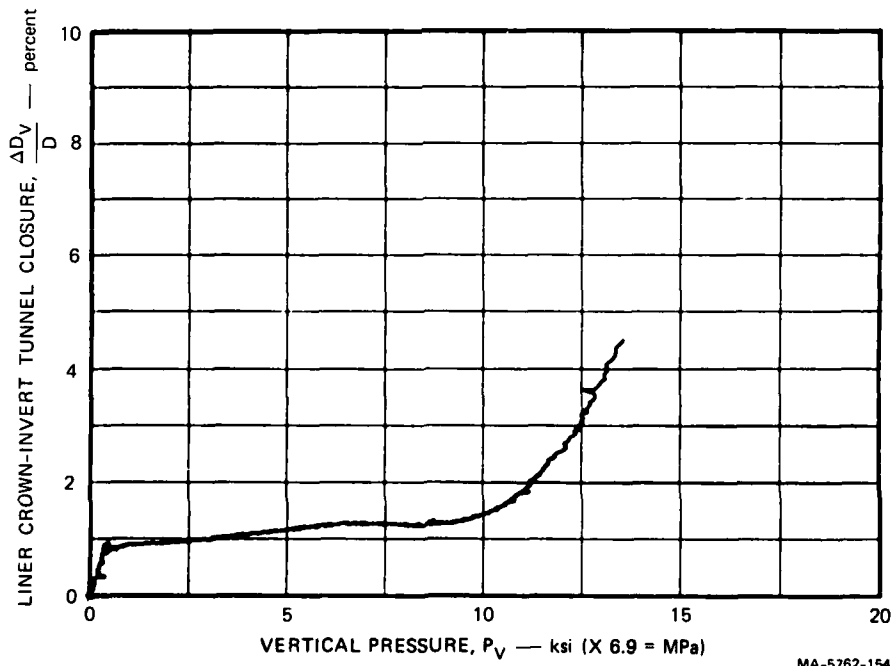
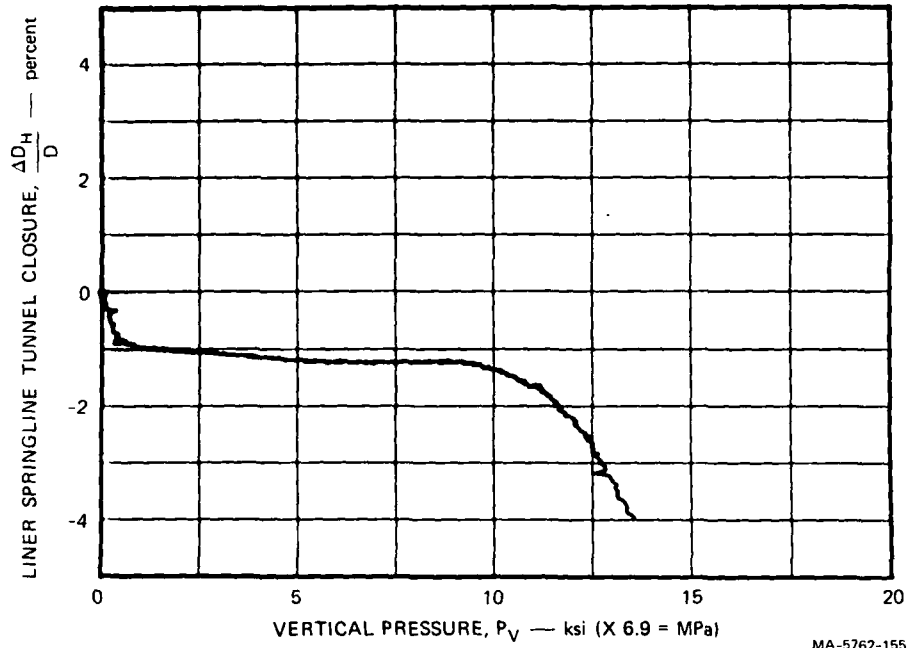
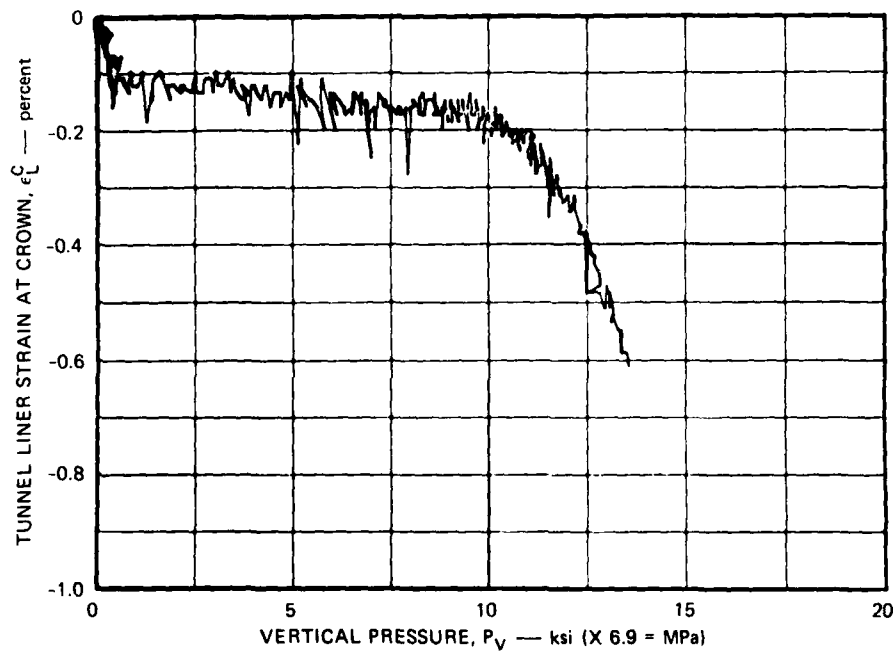


FIGURE A.45 LINER CROWN-INVERT TUNNEL CLOSURE VERSUS VERTICAL PRESSURE — TEST LSUX-19



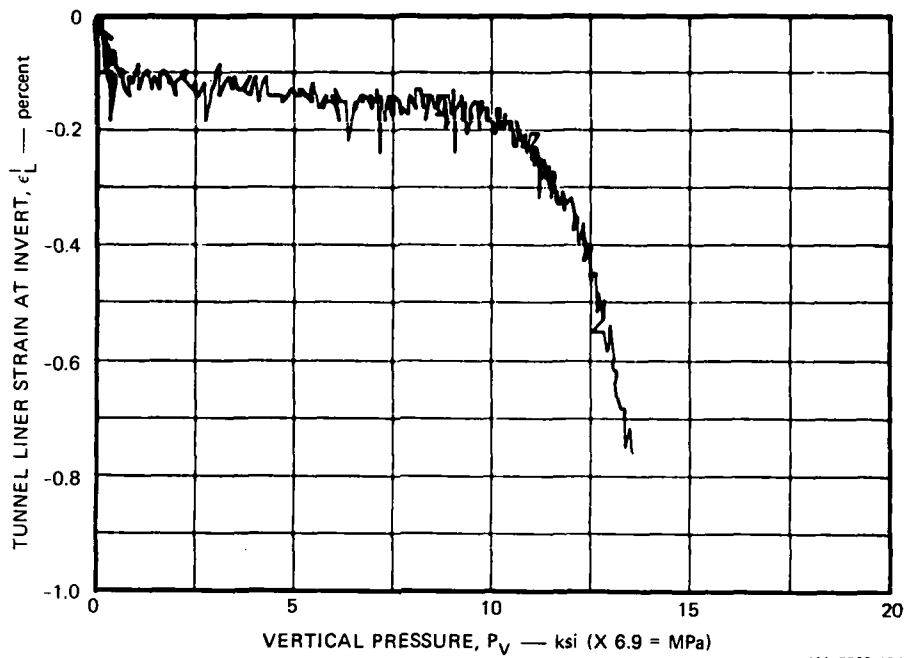
MA-5762-155

FIGURE A.46 LINER SPRINGLINE TUNNEL CLOSURE VERSUS VERTICAL PRESSURE — TEST LSUX-19



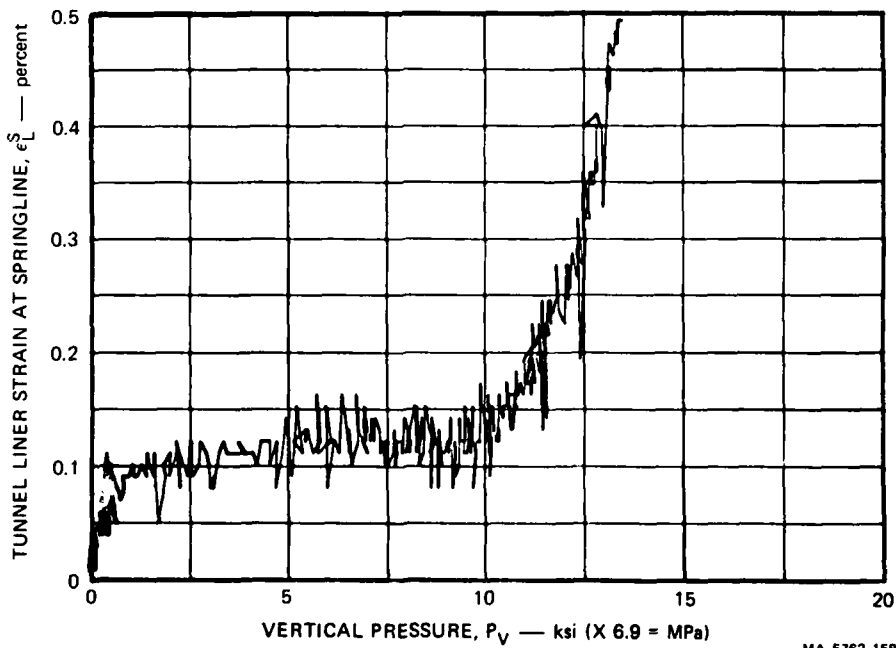
MA-5762-156

FIGURE A-47 TUNNEL LINER STRAIN AT CROWN VERSUS VERTICAL PRESSURE — TEST LSUX-19



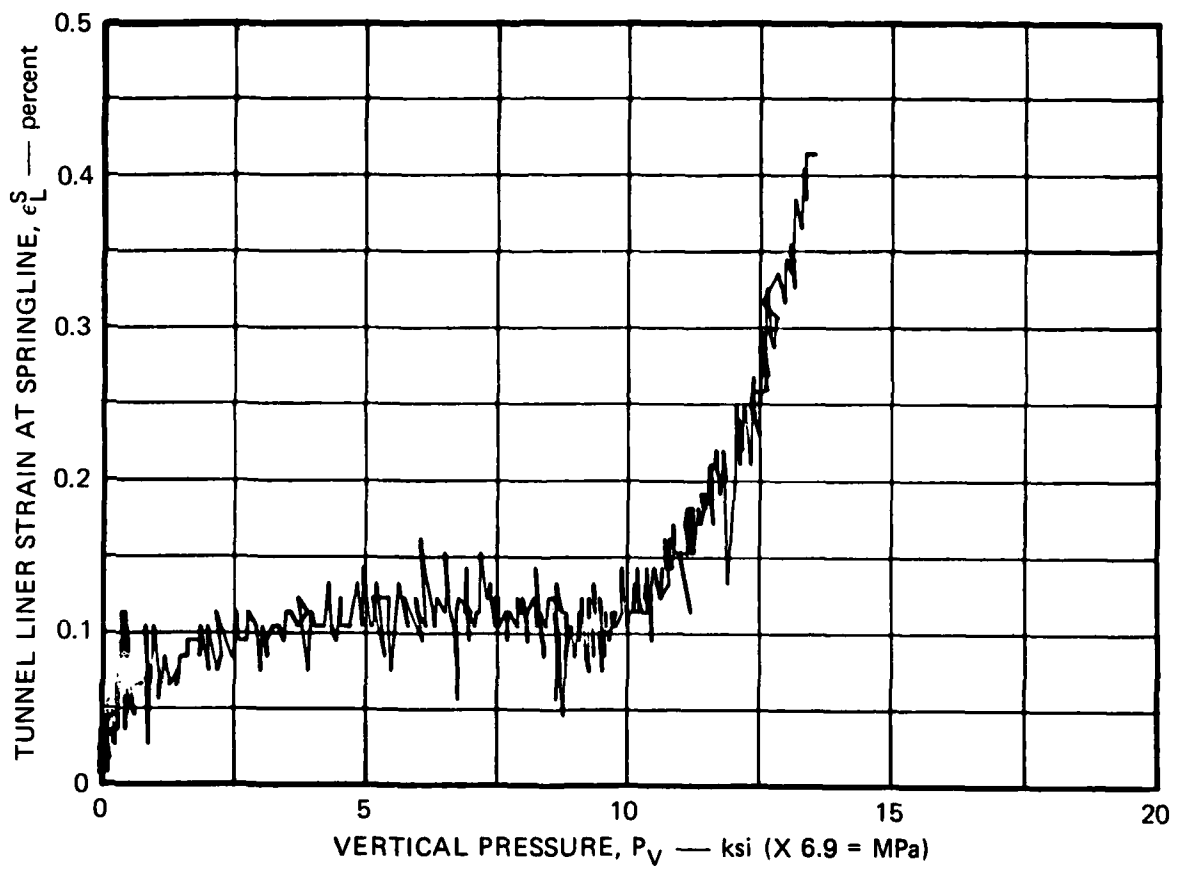
MA-5762-157

FIGURE A.48 TUNNEL LINER STRAIN AT INVERT VERSUS VERTICAL PRESSURE — TEST LSUX-19



MA-5762-158

FIGURE A.49 TUNNEL LINER STRAIN AT LEFT SPRINGLINE VERSUS VERTICAL PRESSURE — TEST LSUX-19



MA-5762-159

FIGURE A.50 TUNNEL LINER STRAIN AT RIGHT SPRINGLINE VERSUS VERTICAL PRESSURE — TEST LSUX-19

LSUX-20

LOAD-JOINT ORIENTATION ANGLE  $\beta$ :  $0^\circ$

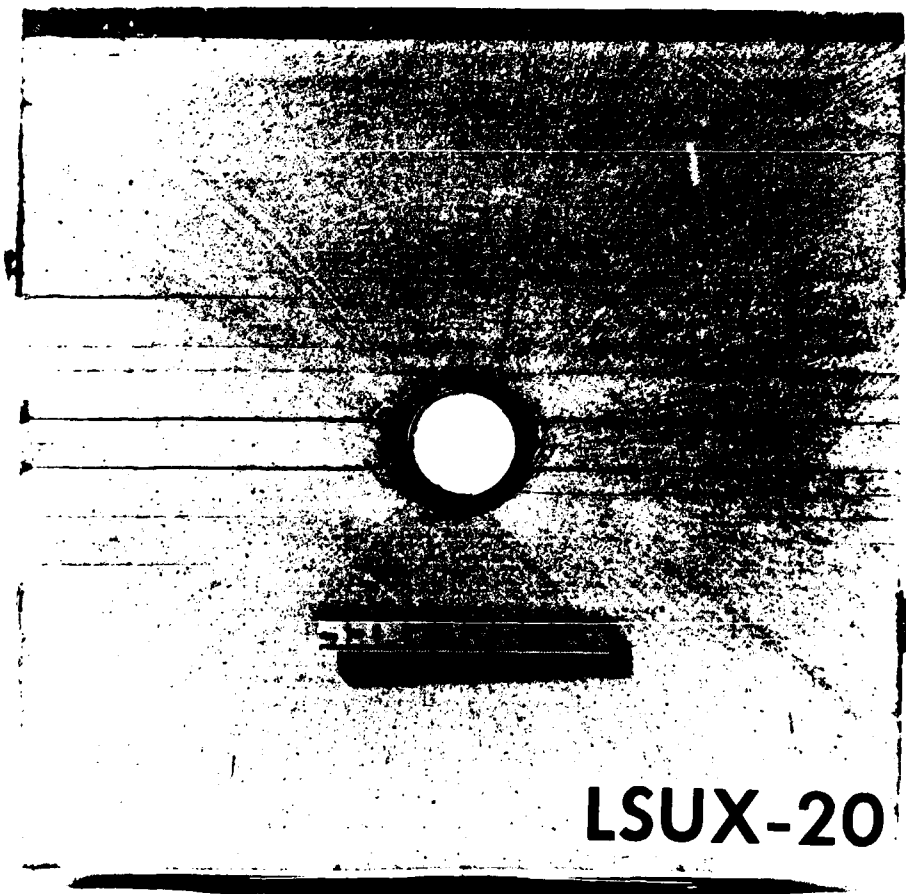
TUNNEL-JOINT ORIENTATION ANGLE  $\gamma$ :  $90^\circ$

STRUCTURE: Backpacked 1015 steel liner,  $a/h = 12.5$   
Polyurethane foam backpacking,  $R/h = 4.3$

LOADING: Monotonic

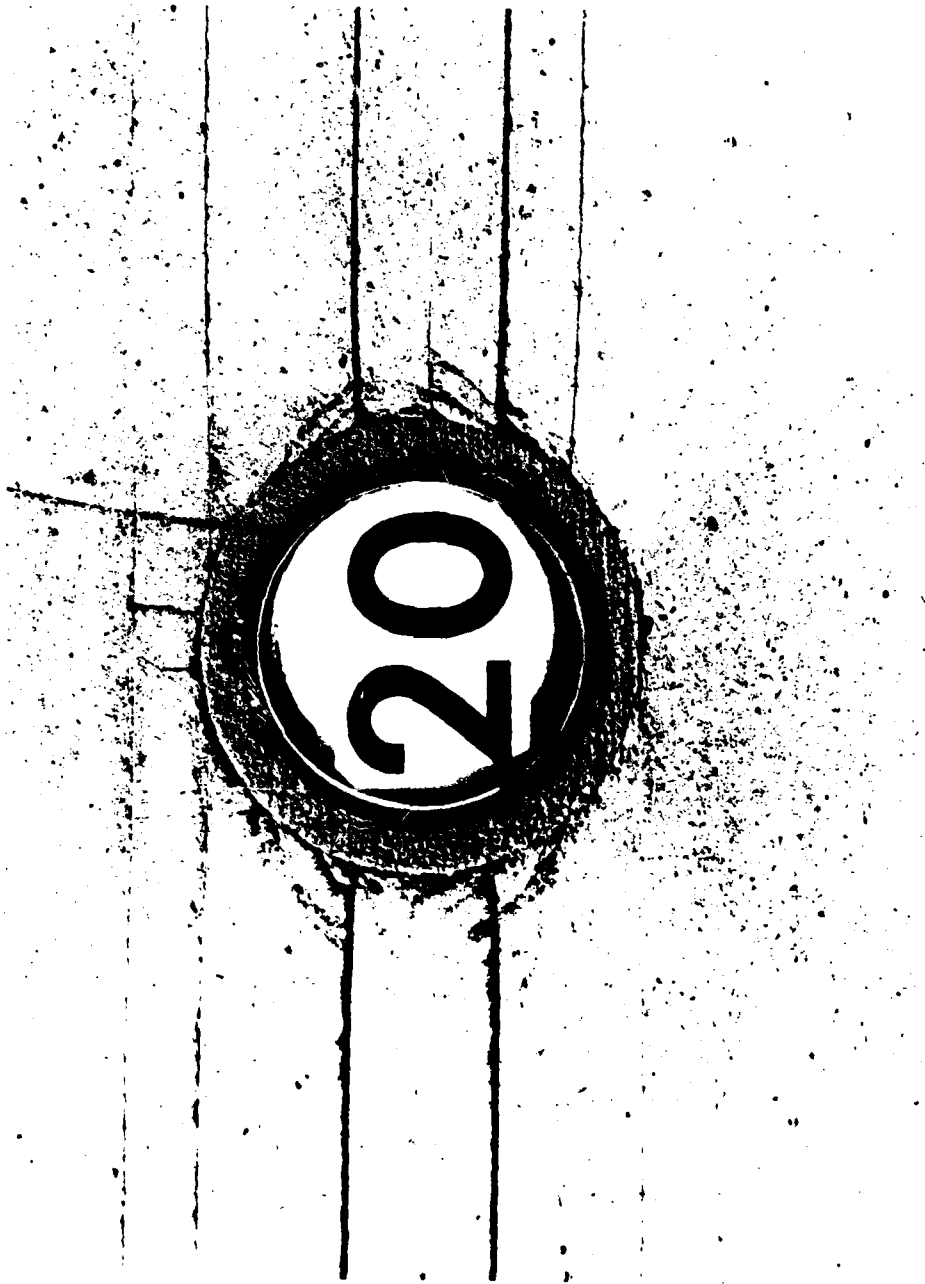
COMMENTS

The reinforcing structure fit well, so that there was no change in closure transducer readings during liner installation. Closure records are good, and liner closure records show the expected slight decrease in amplitude just before the backpacking began to crush at constant stress everywhere around the liner. Liner strain records are good. The specimen separated slightly during recovery. Examination of the rock around the springlines shows moderate shear cracking.



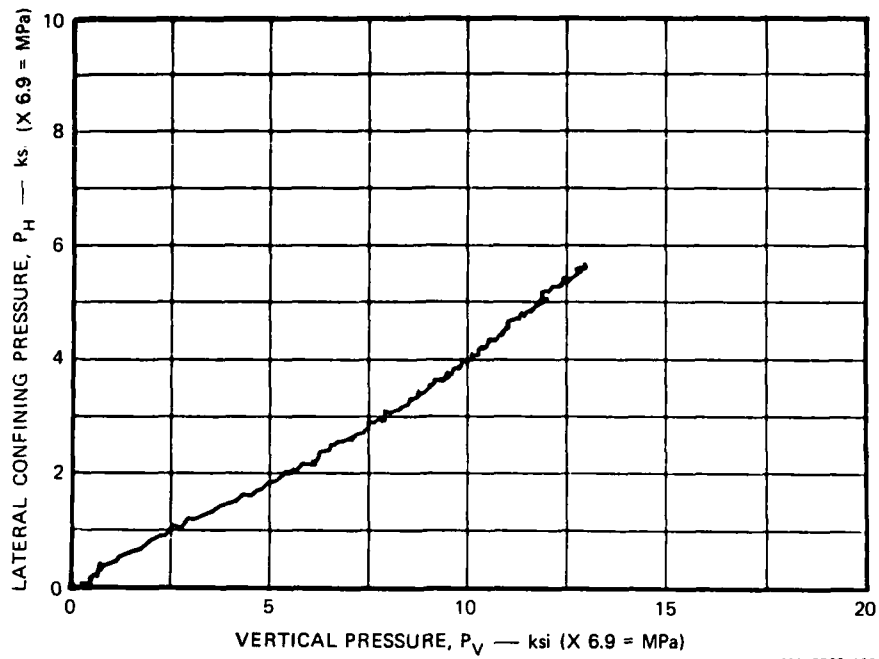
MP-5762-160

FIGURE A.51 SECTIONED SPECIMEN FROM TEST LSUX-20



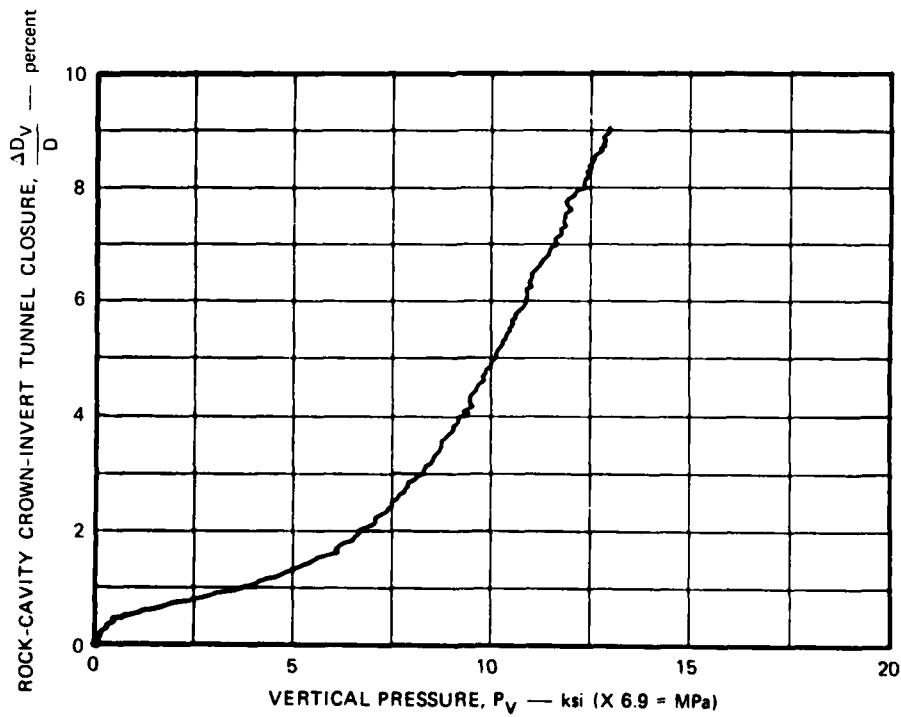
MP-5762-161

FIGURE A.52 ENLARGEMENT OF TUNNEL REGION IN LSUX-20 SPECIMEN



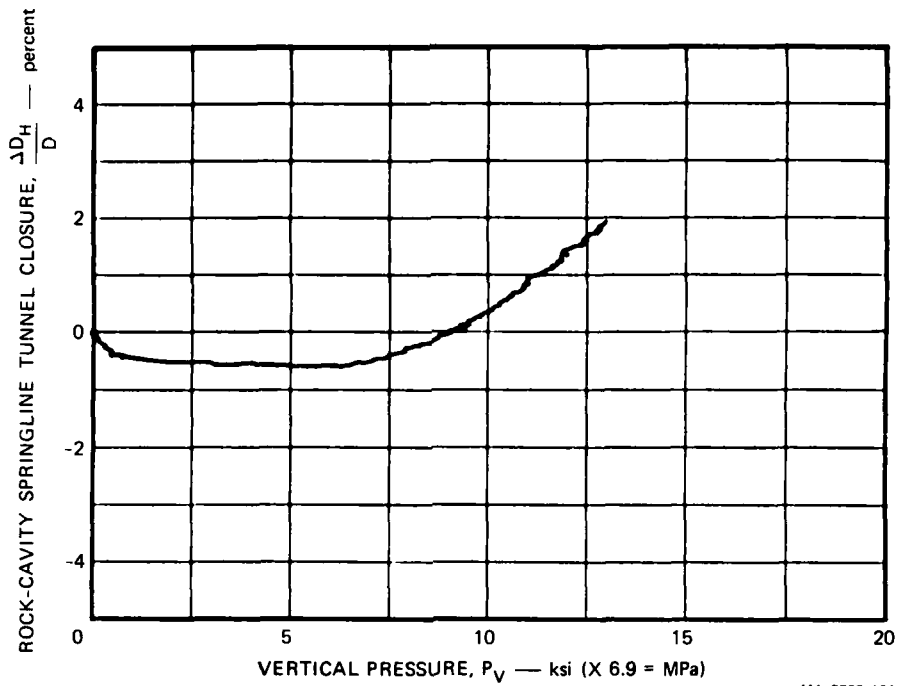
MA-5762-162

FIGURE A.53 LATERAL CONFINING PRESSURE VERSUS VERTICAL PRESSURE — TEST LSUX-20



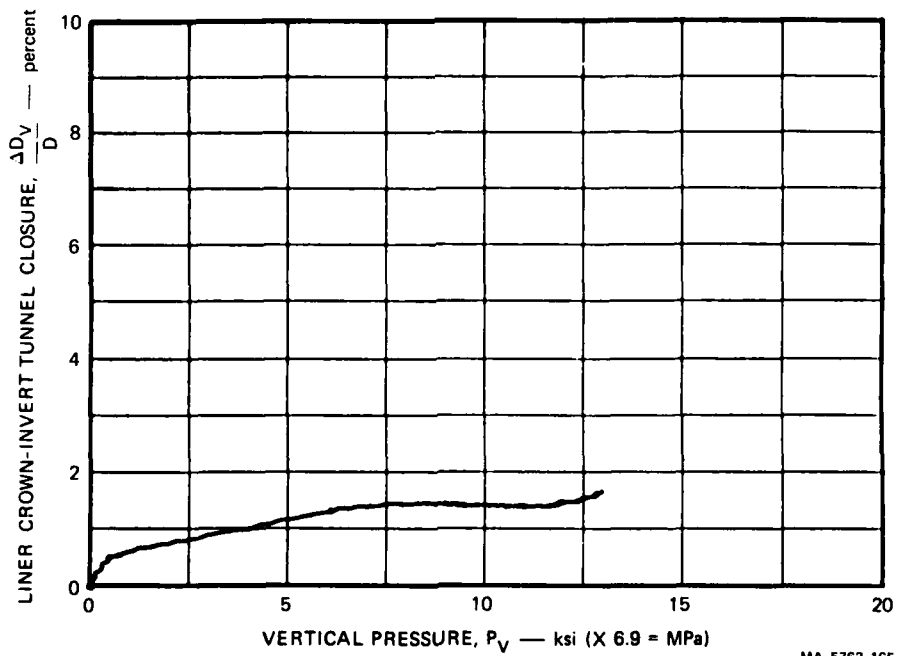
MA-5762-163

FIGURE A.54 ROCK-CAVITY CROWN-INVERT TUNNEL CLOSURE VERSUS VERTICAL PRESSURE — TEST LSUX-20



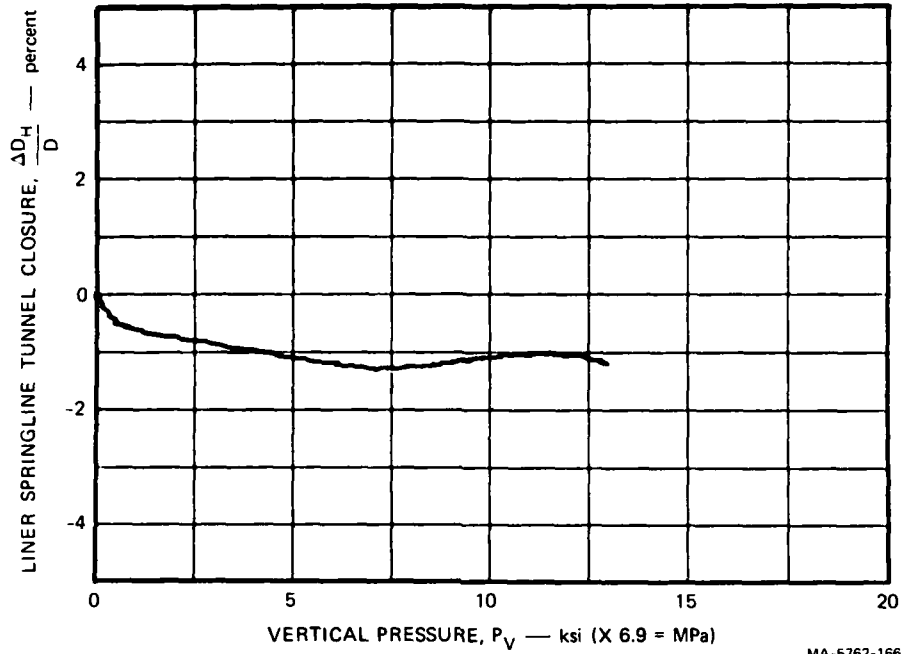
MA-5762-164

FIGURE A-55 ROCK-CAVITY SPRINGLINE TUNNEL CLOSURE VERSUS VERTICAL PRESSURE — TEST LSUX-20



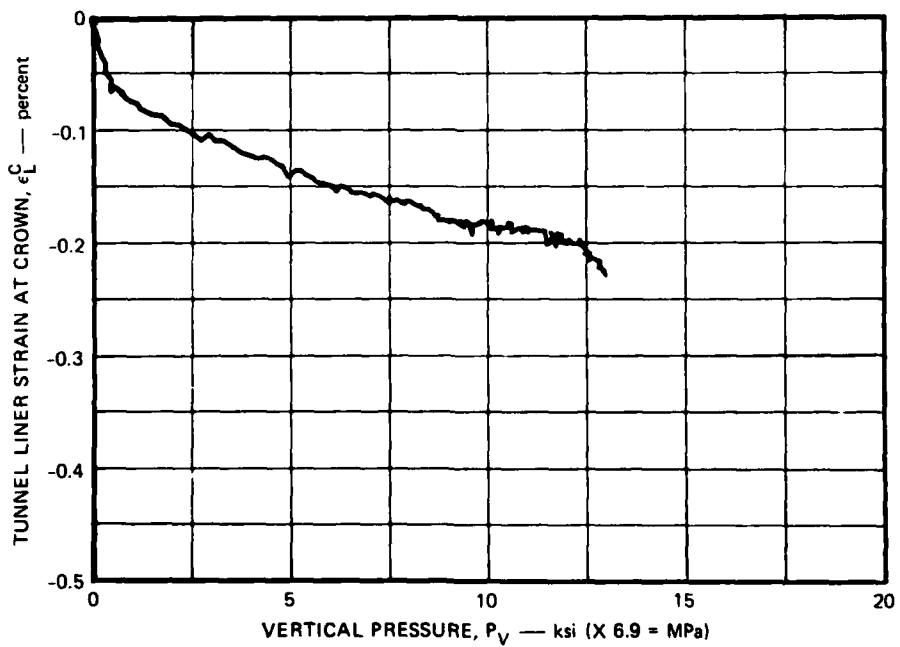
MA-5762-165

FIGURE A-56 LINER CROWN-INVERT TUNNEL CLOSURE VERSUS VERTICAL PRESSURE — TEST LSUX-20



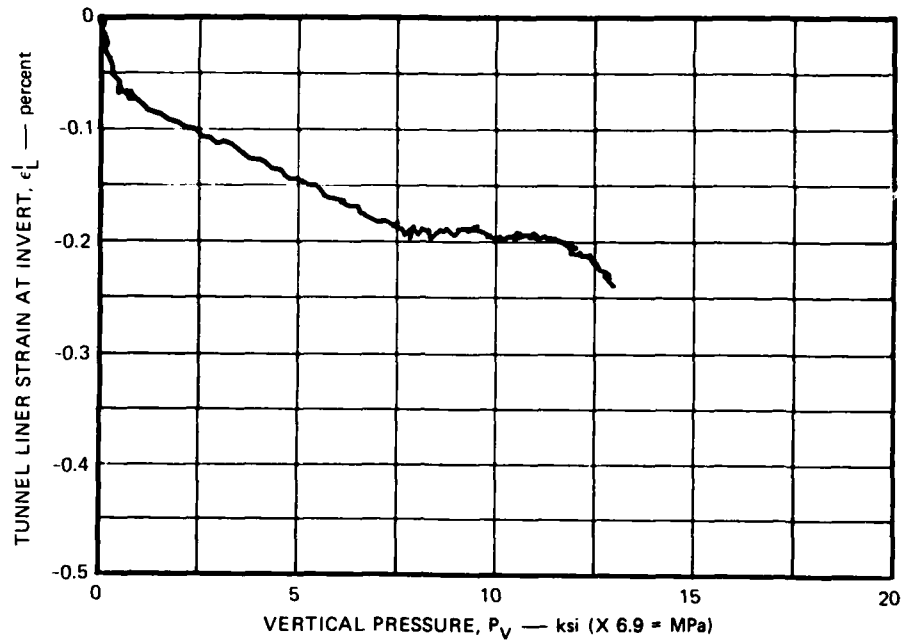
MA-5762-166

FIGURE A.57 LINER SPRINGLINE TUNNEL CLOSURE VERSUS VERTICAL PRESSURE — TEST LSUX-20



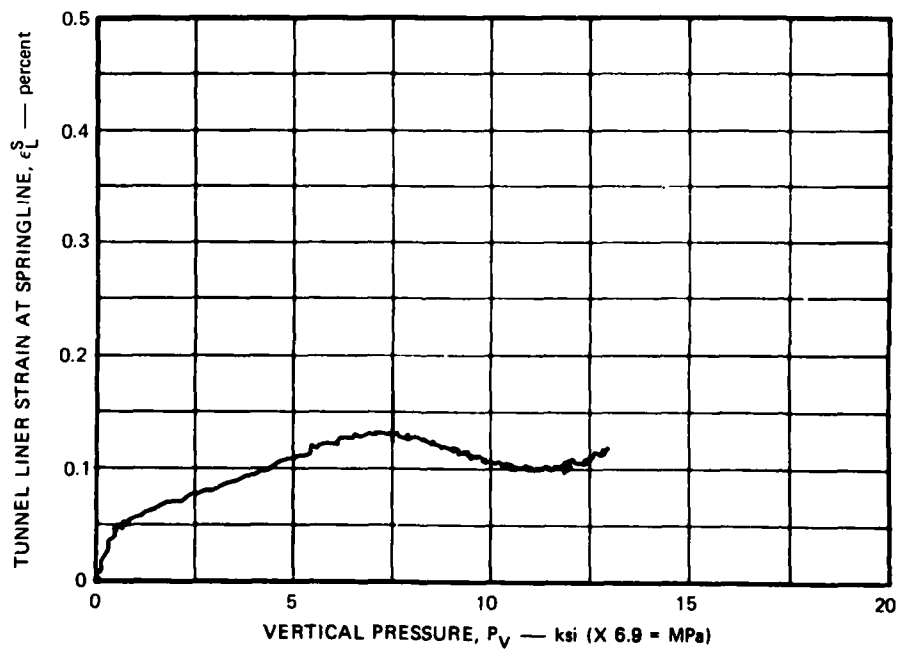
MA-5762-167

FIGURE A.58 TUNNEL LINER STRAIN AT CROWN VERSUS VERTICAL PRESSURE — TEST LSUX-20



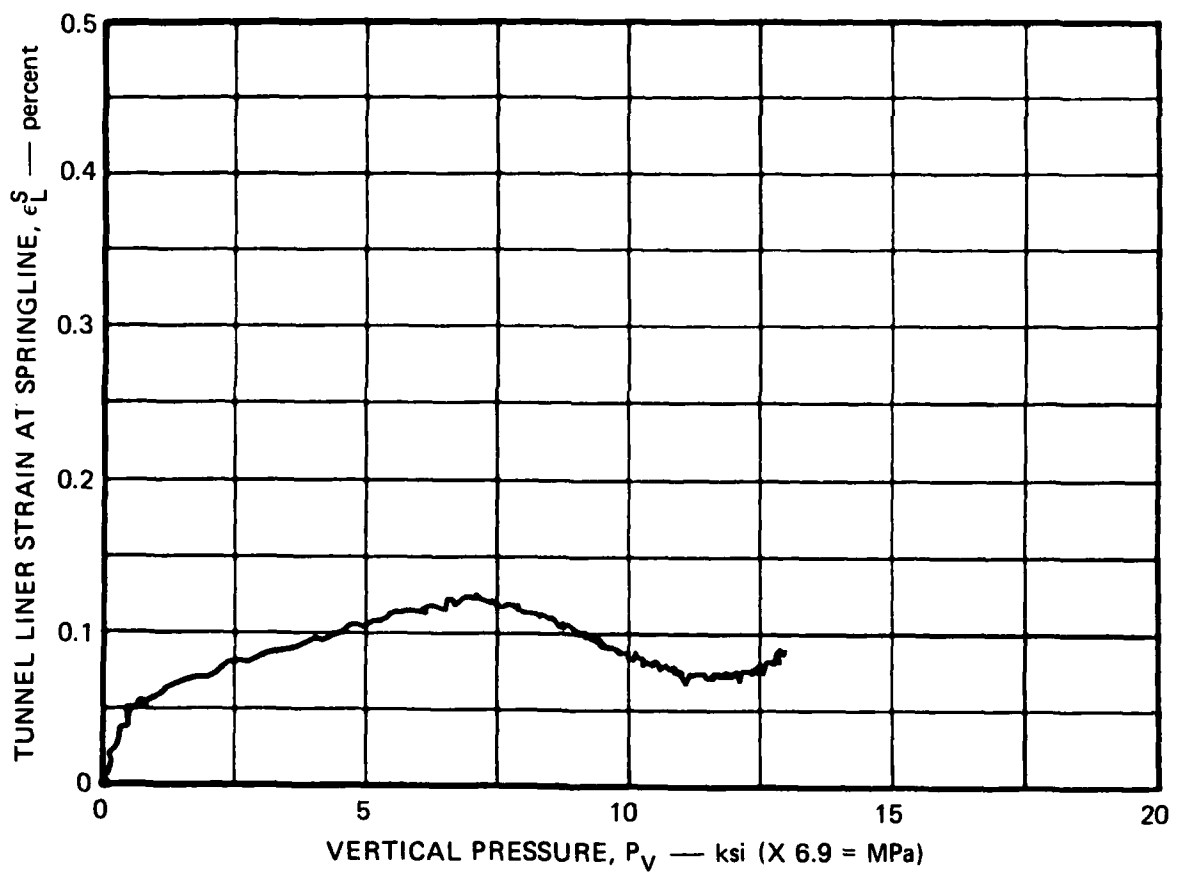
MA-5762-168

FIGURE A.59 TUNNEL LINER STRAIN AT INVERT VERSUS VERTICAL PRESSURE — TEST LSUX-20



MA-5762-169

FIGURE A.60 TUNNEL LINER STRAIN AT LEFT SPRINGLINE VERSUS VERTICAL PRESSURE — TEST LSUX-20



MA-5762-170

FIGURE A.61 TUNNEL LINER STRAIN AT RIGHT SPRINGLINE  
VERSUS VERTICAL PRESSURE — TEST LSUX-20

LSUX-21

LOAD-JOINT ORIENTATION ANGLE  $\beta$ : 45°

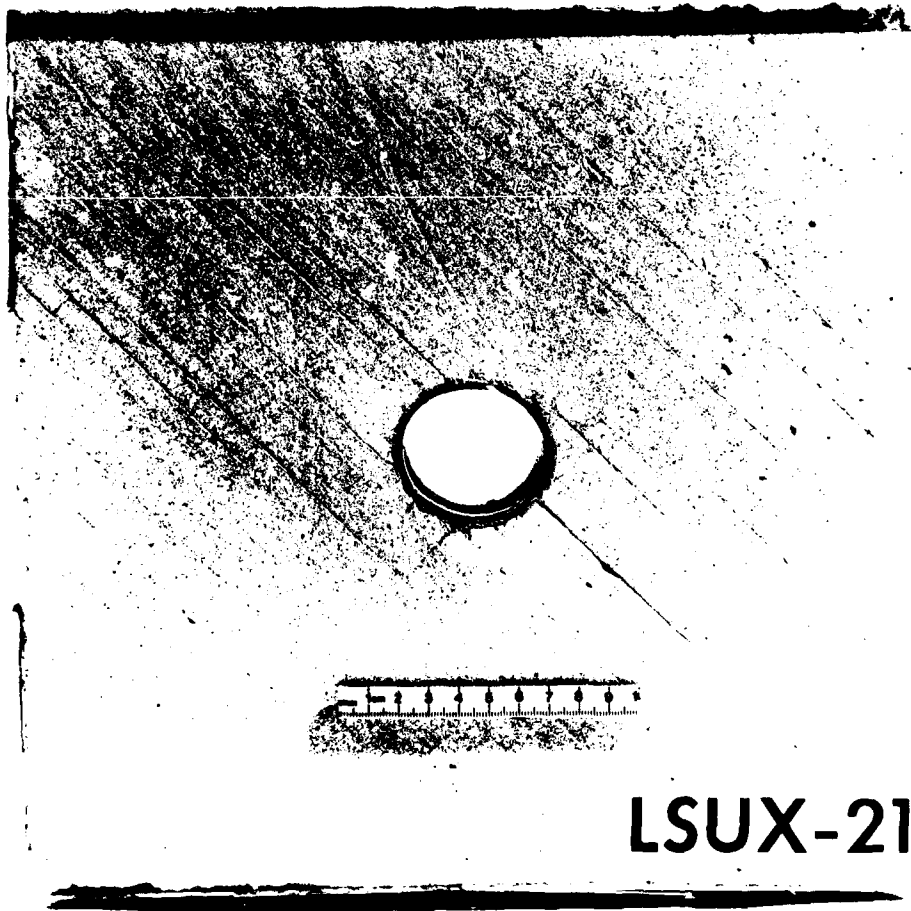
TUNNEL-JOINT ORIENTATION ANGLE  $\gamma$ : 90°

STRUCTURE: Direct contact 1015 steel liner,  $a/h = 12.5$

LOADING: Cyclic

COMMENTS

This test was a repeat of LSUX-18 except that we followed a common path in the  $P_H/P_V$  plane during loading and unloading. The load was cycled at crown-invert closures of 2%, 3%, 5%, and 8%. Records of tunnel closure versus vertical pressure are similar to those obtained for cyclic loading of intact rock: unloading and reloading occur along the same lines, and additional closure is not obtained until the pressure is raised above the maximum pressure applied previously. Liner strain records were obtained at the invert and one springline only. The specimen was recovered intact. Examination of the rock around the tunnel shows that cyclic loading produced no significant damage.



MP-5762-171

FIGURE A.62 SECTIONED SPECIMEN FROM TEST LSUX-21



MP-5762-172

FIGURE A.63 ENLARGEMENT OF TUNNEL REGION IN LSUX-21 SPECIMEN

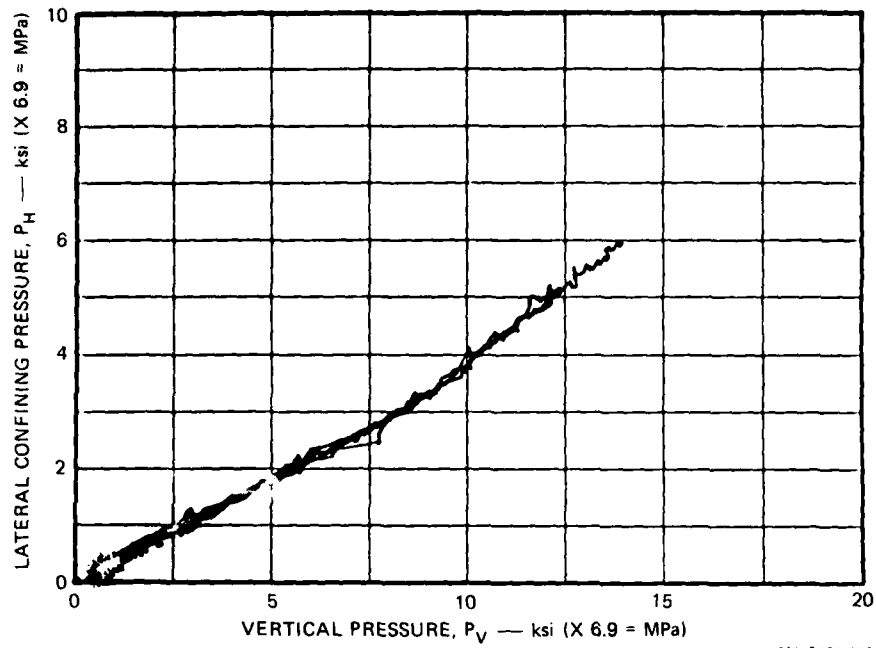


FIGURE A.64 LATERAL CONFINING PRESSURE VERSUS VERTICAL PRESSURE — TEST LSUX-21

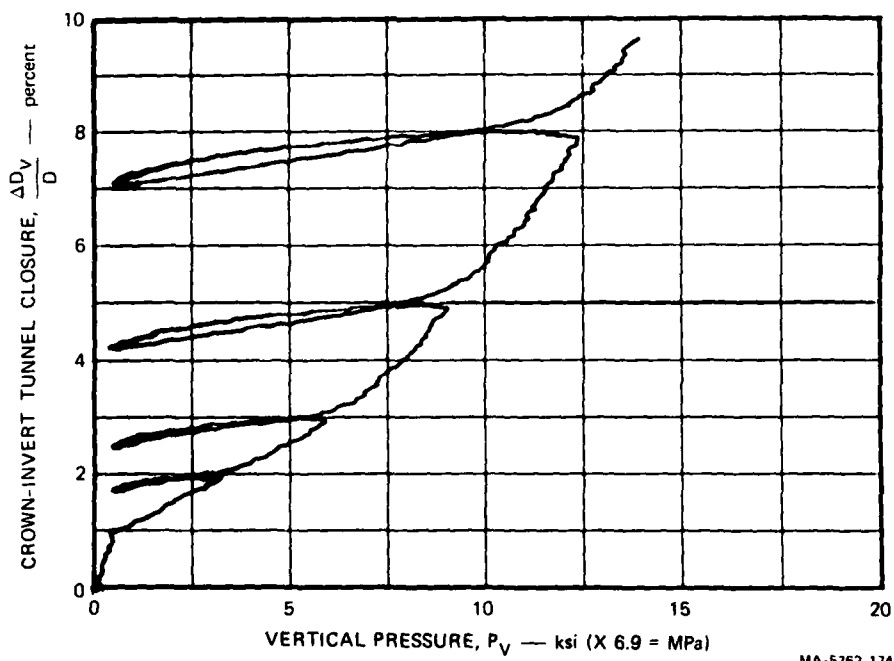
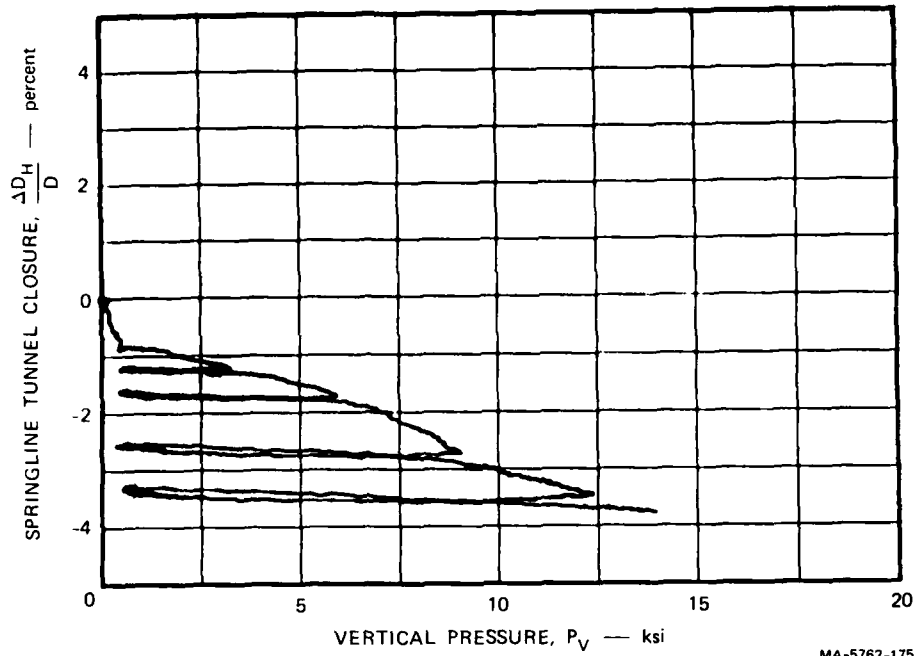
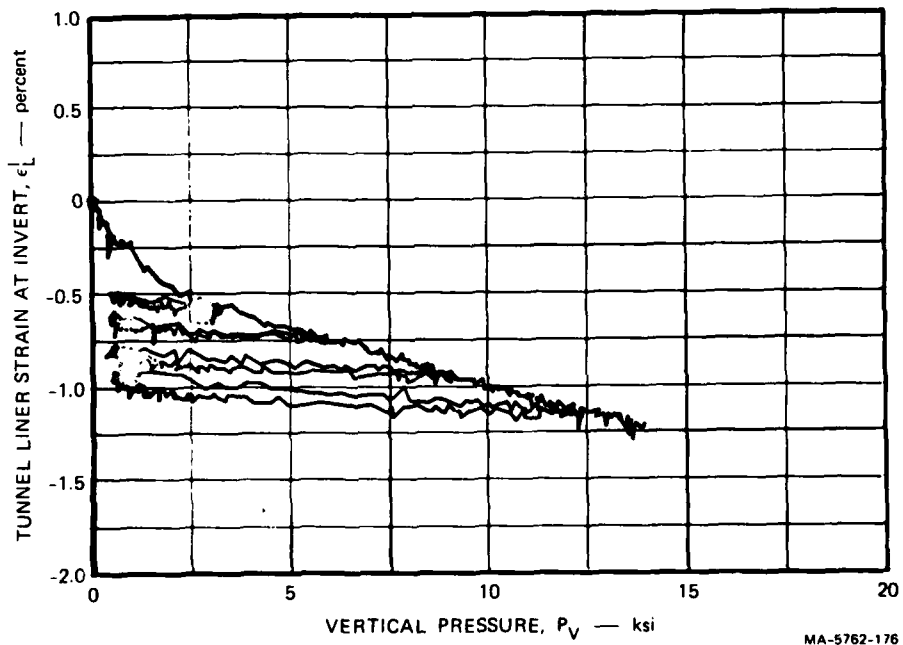


FIGURE A.85 CROWN-INVERT TUNNEL CLOSURE VERSUS VERTICAL PRESSURE — TEST LSUX-21



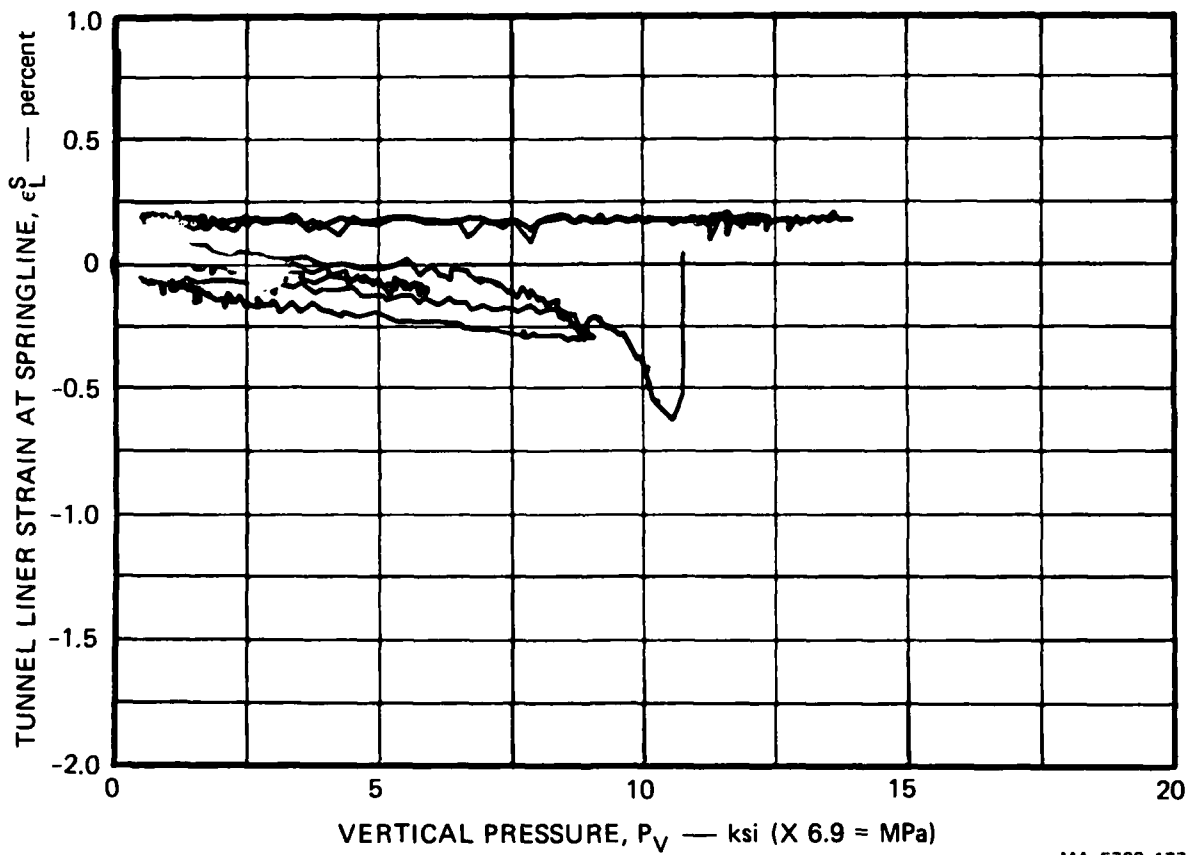
MA-5762-175

FIGURE A.66 SPRINGLINE TUNNEL CLOSURE VERSUS VERTICAL PRESSURE — TEST LSUX-21



MA-5762-176

FIGURE A.67 TUNNEL LINER STRAIN AT INVERT VERSUS VERTICAL PRESSURE — TEST LSUX-21



MA-5762-177

FIGURE A.68 TUNNEL LINER STRAIN AT SPRINGLINE VERSUS VERTICAL PRESSURE — TEST LSUX-21

LSUX-22

LOAD-JOINT ORIENTATION ANGLE  $\beta$ :  $30^\circ$

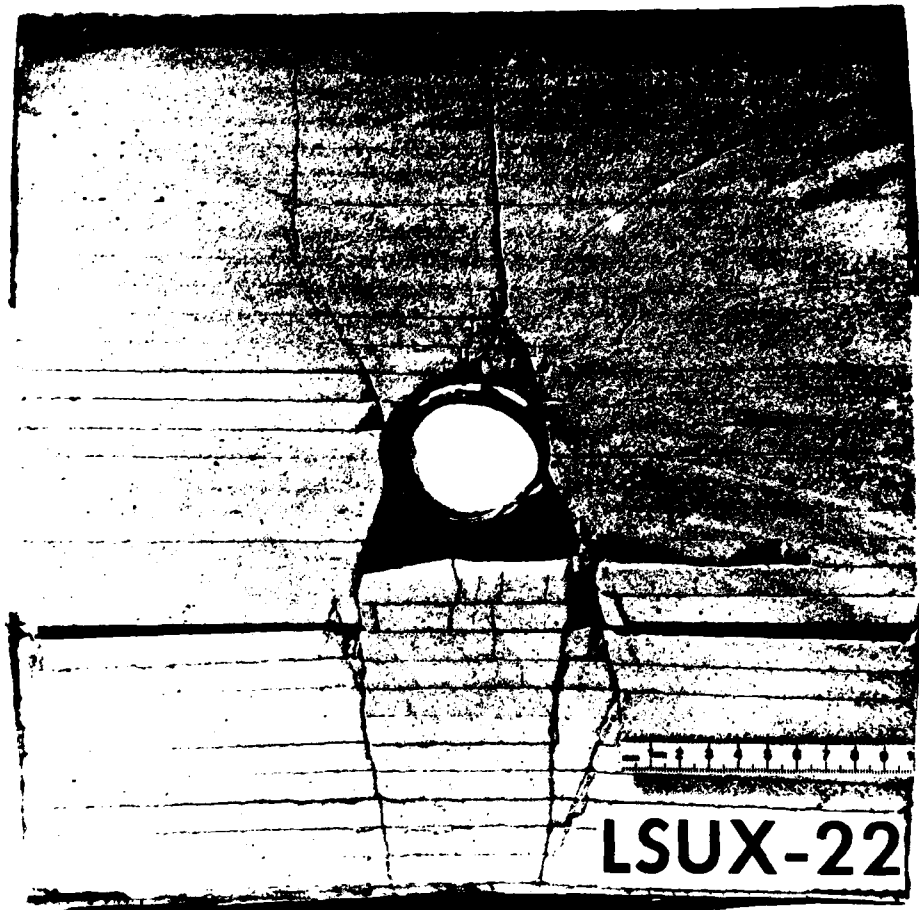
TUNNEL-JOINT ORIENTATION ANGLE  $\gamma$ :  $60^\circ$

STRUCTURE: Direct contact 1015 steel liner,  $a/h = 12.5$

LOADING: Monotonic

COMMENTS

In this test, we lost the seal between the vertical loading chamber and lateral loading chamber at  $P_v = 9.5$  ksi (65.5 MPa), when the crown-invert closure was about 4% and the springline closure was about -1.25%. The test was essentially completed at this level and closure records are good. Liner strain records, which were obtained at springlines only, were also good. The specimen was damaged heavily during recovery; however, the vertical cracks that intersect the tunnel are thought to be the result of tunnel deformation during the test.



MP-5762-178

FIGURE A.69 SECTIONED SPECIMEN FROM TEST LSUX-22



MP-5762-179

FIGURE A.70 ENLARGEMENT OF TUNNEL REGION IN LSUX-22 SPECIMEN

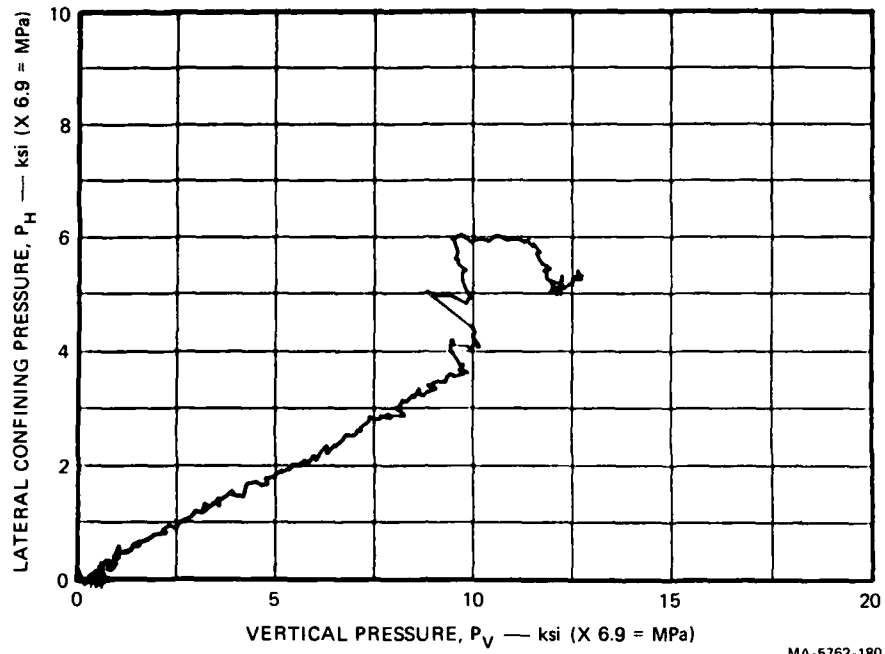


FIGURE A.71 LATERAL CONFINING PRESSURE VERSUS VERTICAL PRESSURE — TEST LSUX-22

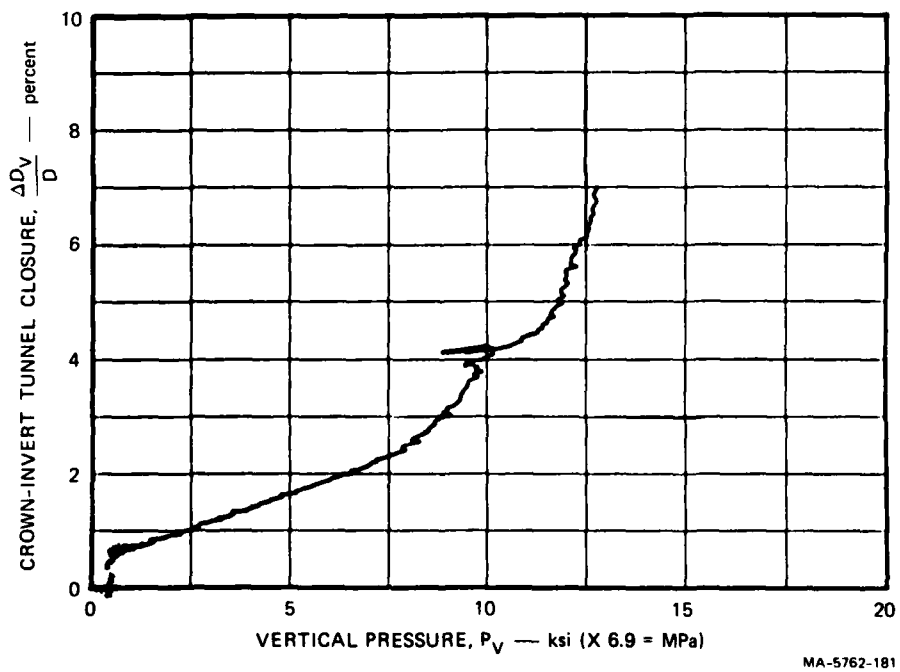
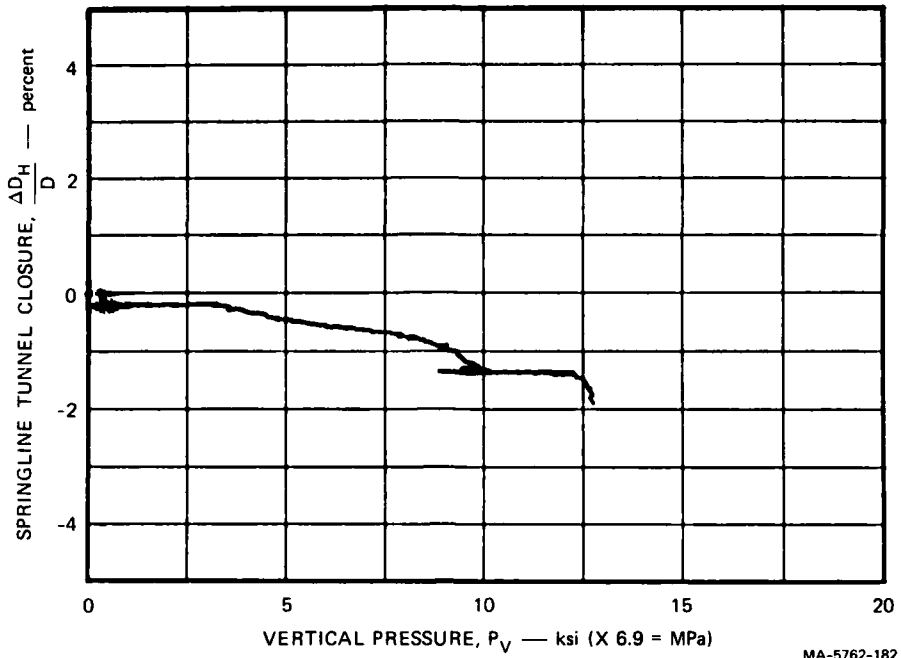
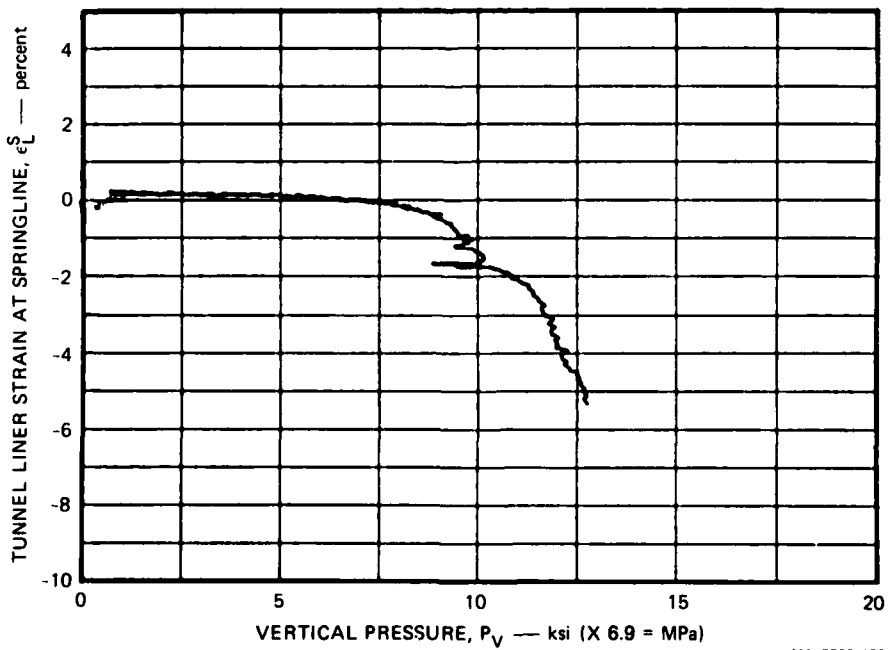


FIGURE A.72 CROWN-INVERT TUNNEL CLOSURE VERSUS VERTICAL PRESSURE — TEST LSUX-22



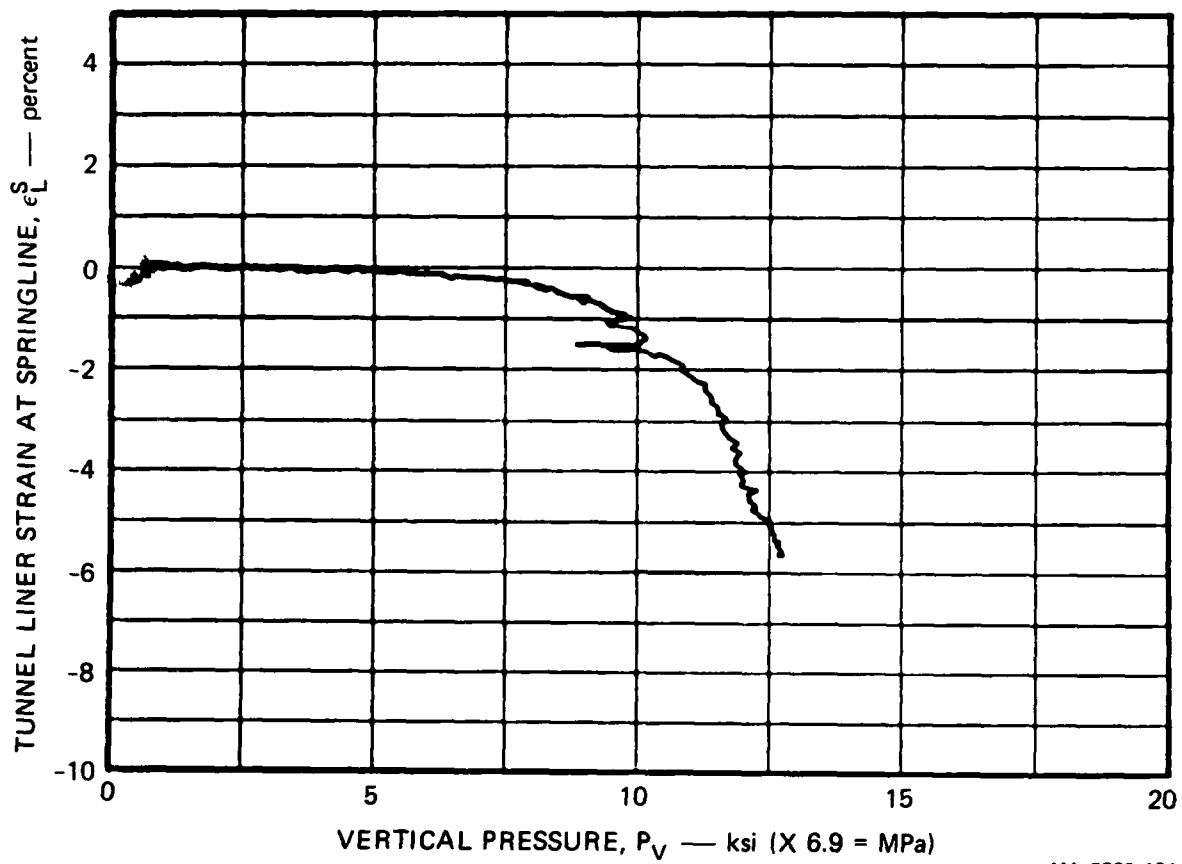
MA-5762-182

FIGURE A.73 SPRINGLINE TUNNEL CLOSURE VERSUS VERTICAL PRESSURE — TEST LSUX-22



MA-5762-183

FIGURE A.74 TUNNEL LINER STRAIN AT LEFT SPRINGLINE VERSUS VERTICAL PRESSURE — TEST LSUX-22



MA-5762-184

FIGURE A.75 TUNNEL LINER STRAIN AT RIGHT SPRINGLINE VERSUS VERTICAL PRESSURE — TEST LSUX-22

LSUX-23

LOAD-JOINT ORIENTATION ANGLE  $\beta$ : 30°

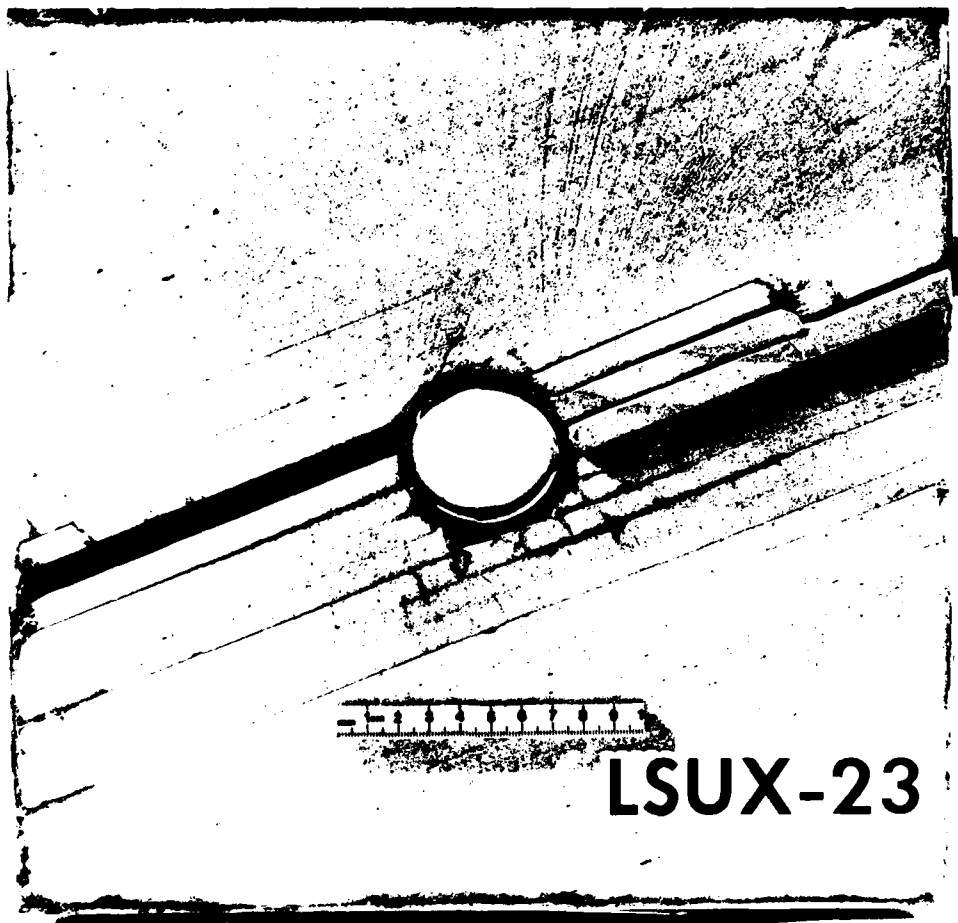
TUNNEL-JOINT ORIENTATION ANGLE  $\gamma$ : 69.3°

STRUCTURE: Direct contact 1015 steel liner, a/h = 12.5

LOADING: Monotonic

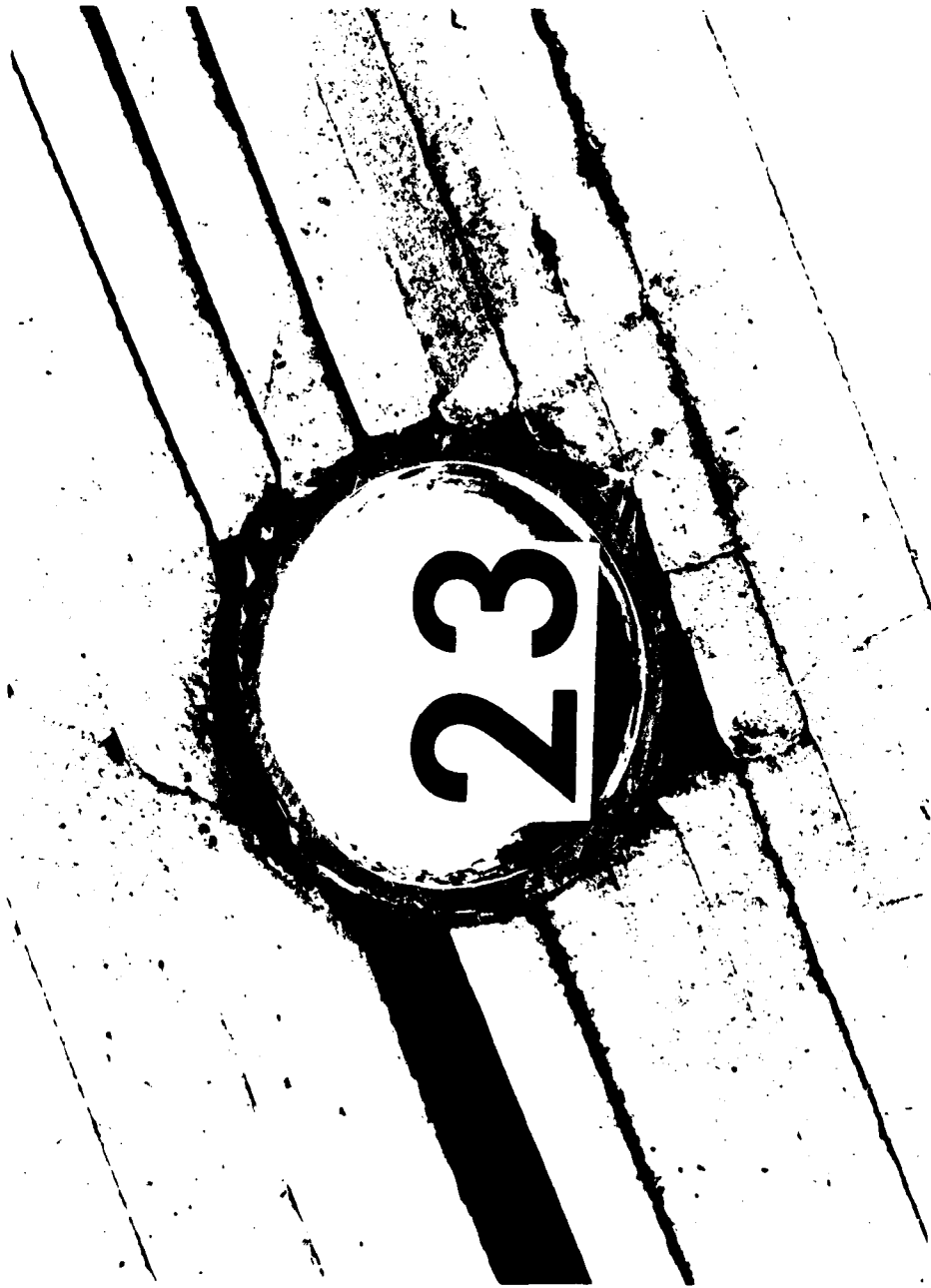
COMMENTS

Both tunnel closure and liner strain records are good. However, liner strain records were obtained at the crown and one springline only. The specimen separated slightly during recovery and several of the plates were broken.



MP-5762-185

FIGURE A.76 SECTIONED SPECIMEN FROM TEST LSUX-23



MP-5762-186

FIGURE A.77 ENLARGEMENT OF TUNNEL REGION IN LSUX-23 SPECIMEN

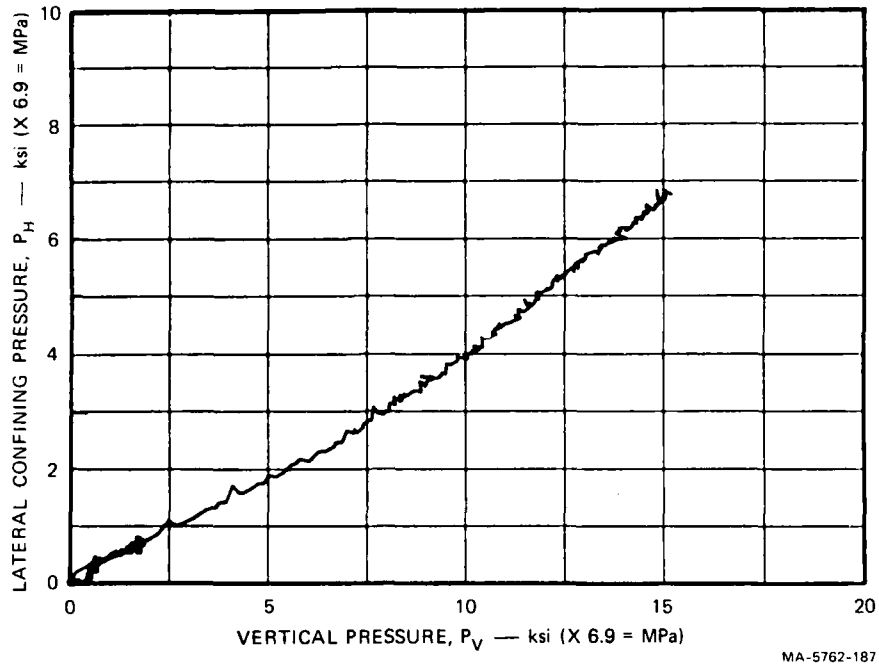


FIGURE A.78 LATERAL CONFINING PRESSURE VERSUS VERTICAL PRESSURE — TEST LSUX-23

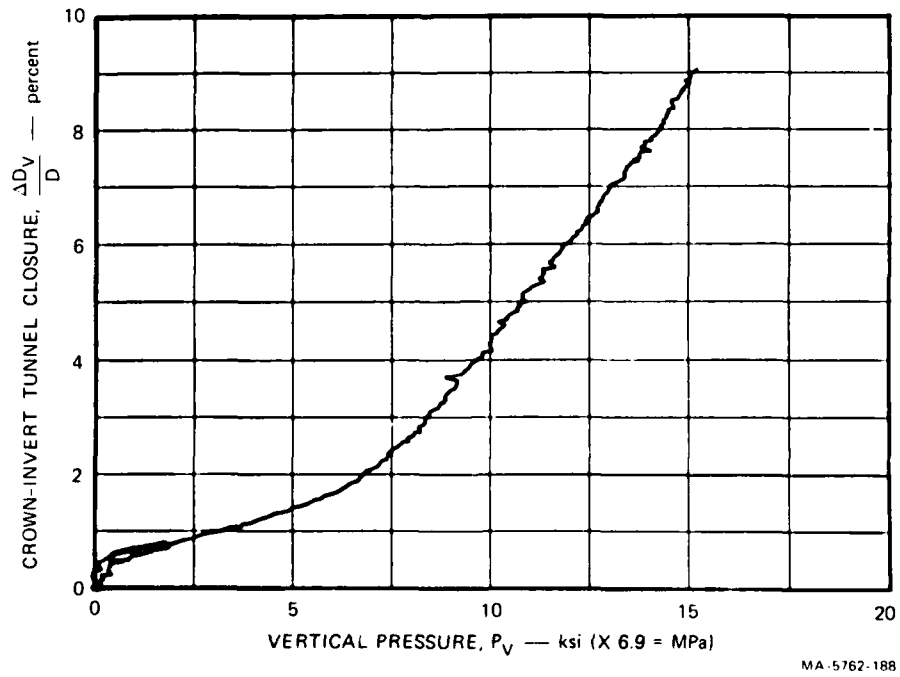


FIGURE A.79 CROWN-INVERT TUNNEL CLOSURE VERSUS VERTICAL PRESSURE — TEST LSUX-23

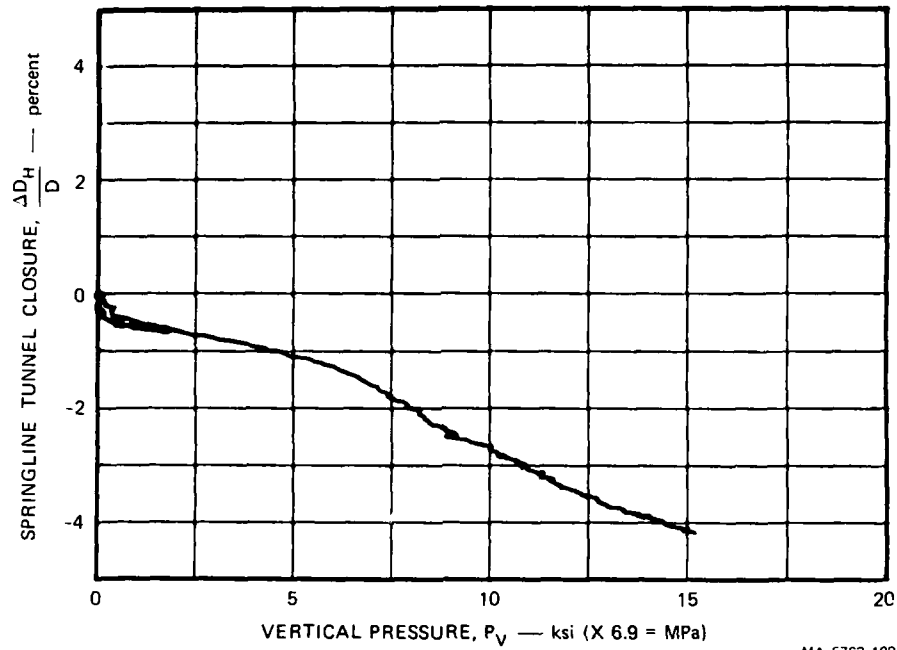


FIGURE A.80 SPRINGLINE TUNNEL CLOSURE VERSUS VERTICAL PRESSURE — TEST LSUX-23

MA-5762-189

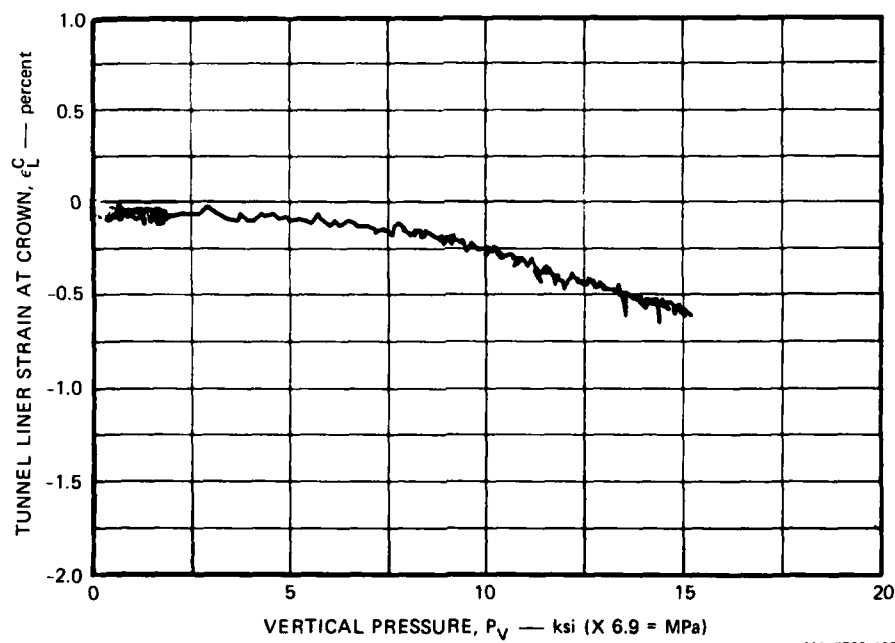
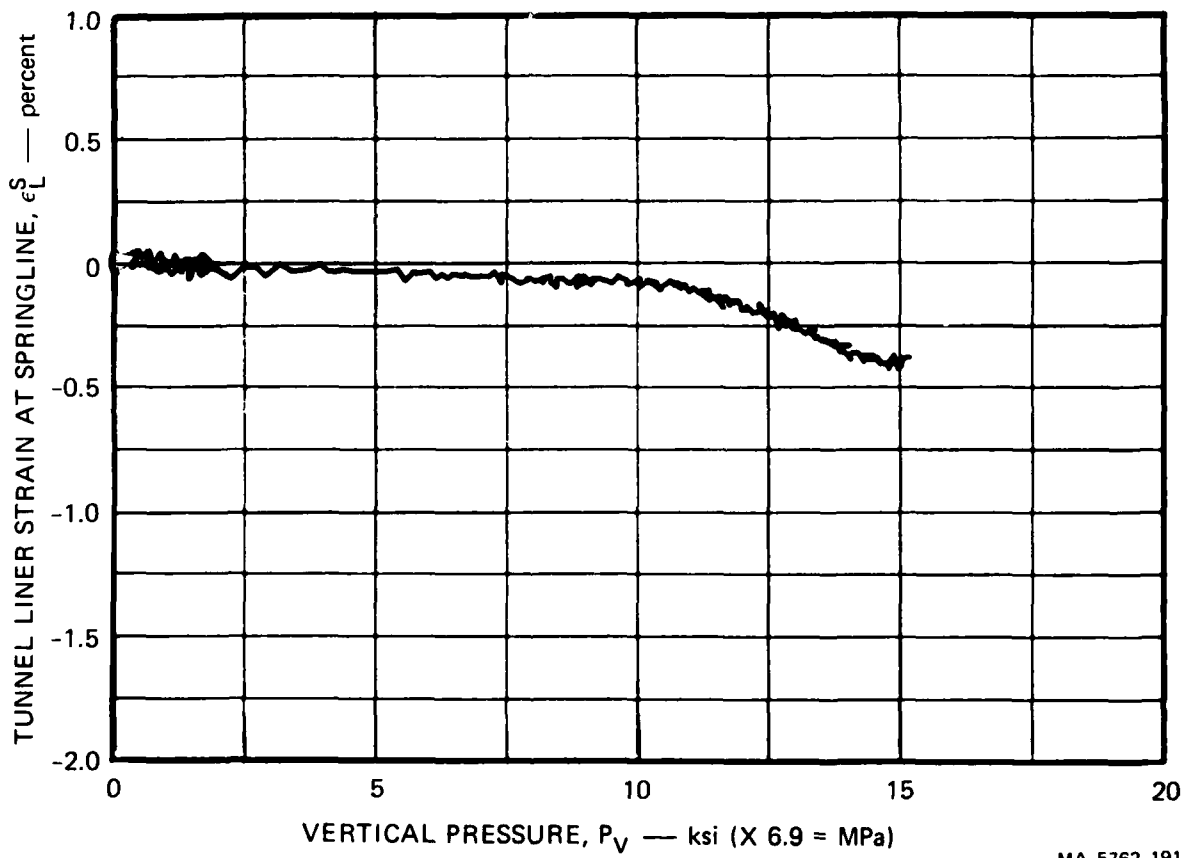


FIGURE A.81 TUNNEL LINER STRAIN AT CROWN VERSUS VERTICAL PRESSURE — TEST LSUX-23

MA-5762-190



MA-5762-191

FIGURE A.82 TUNNEL LINER STRAIN AT SPRINGLINE VERSUS VERTICAL PRESSURE — TEST LSUX-23

LSUX-24

LOAD-JOINT ORIENTATION ANGLE  $\beta$ : 30°

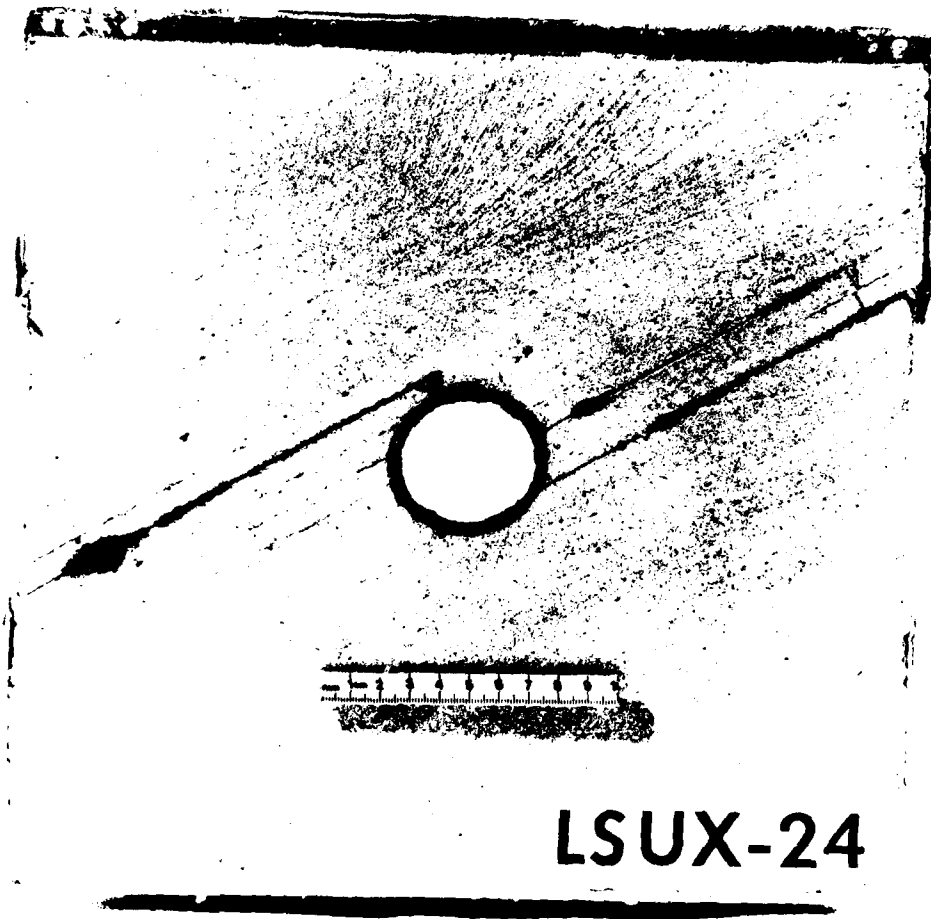
TUNNEL-JOINT ORIENTATION ANGLE  $\gamma$ : 90°

STRUCTURE: Direct contact 1015 steel liner,  $a/h = 12.5$

LOADING: Monotonic

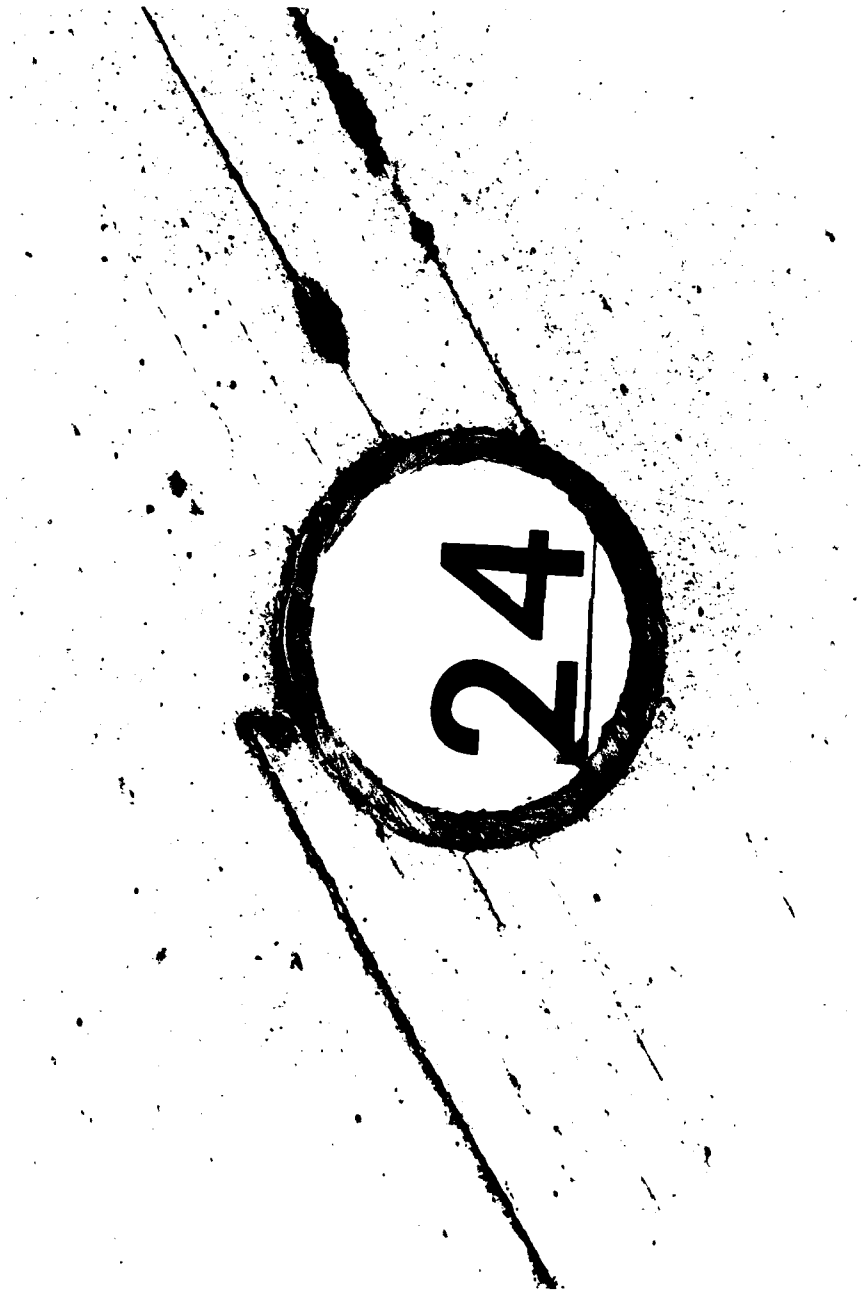
COMMENTS

No springline tunnel closure record was obtained. The test produced good liner strain records from the crown and from one springline location. The specimen separated during recovery along the joint passing through the tunnel. Dark spots in the photograph of the posttest cross section are stains made by epoxy used in putting the specimen together.



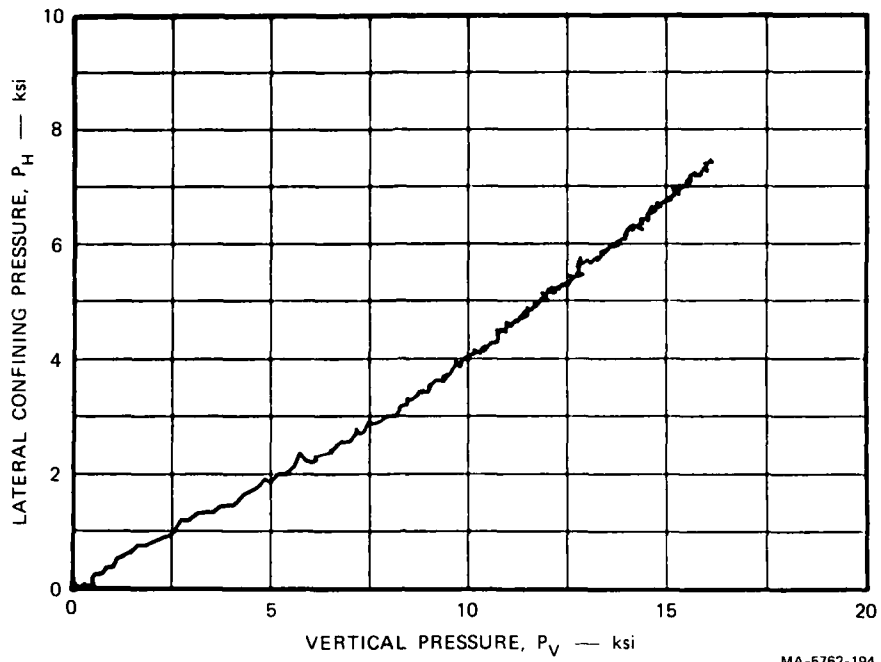
MP-5762-192

FIGURE A.83 SECTIONED SPECIMEN FROM TEST LSUX-24



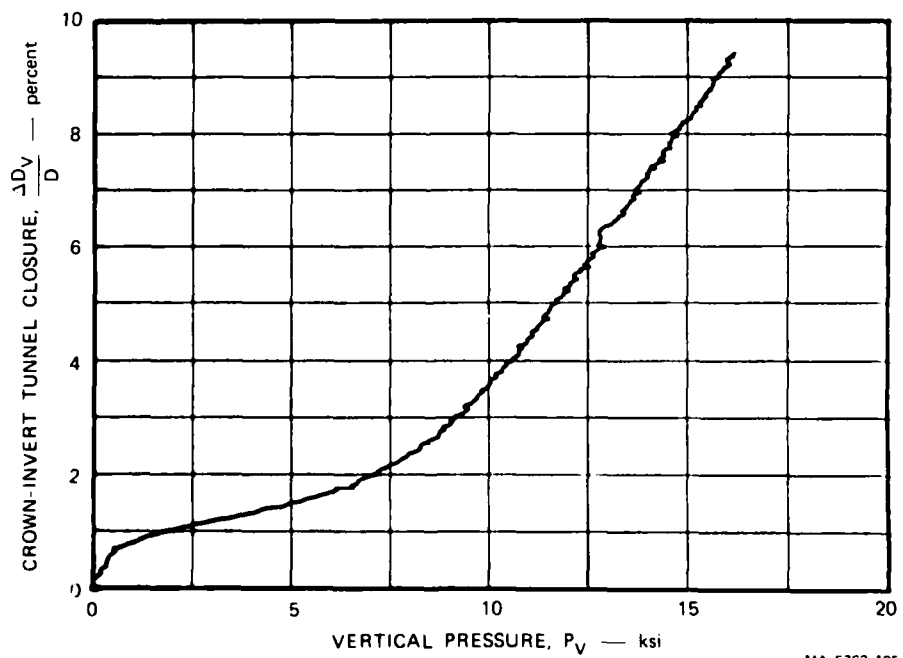
MP-5762-193

FIGURE A.84 ENLARGEMENT OF TUNNEL REGION IN LSUX-24 SPECIMEN



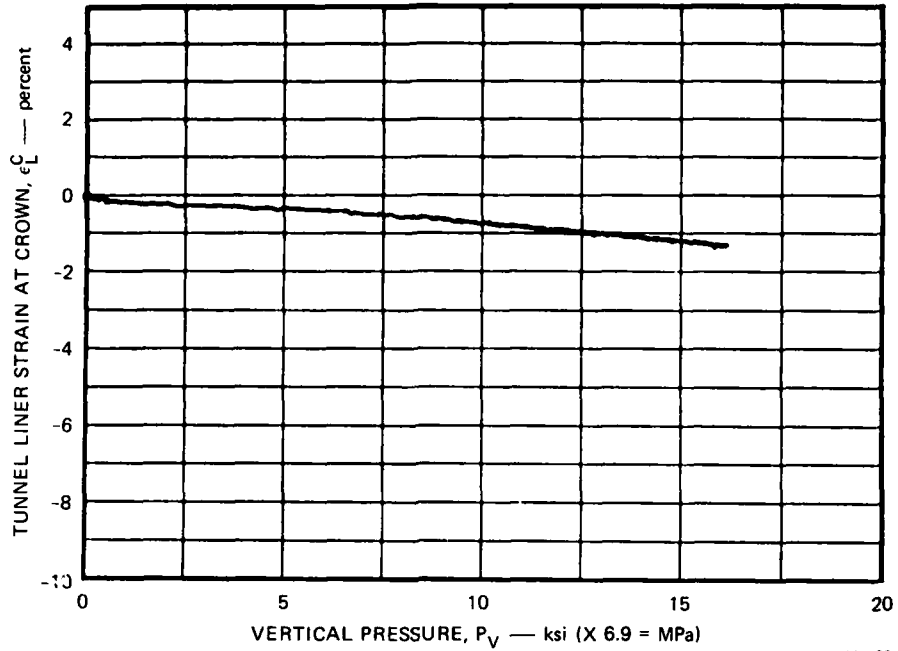
MA-5762-194

FIGURE A.85 LATERAL CONFINING PRESSURE VERSUS VERTICAL PRESSURE — TEST LSUX-24



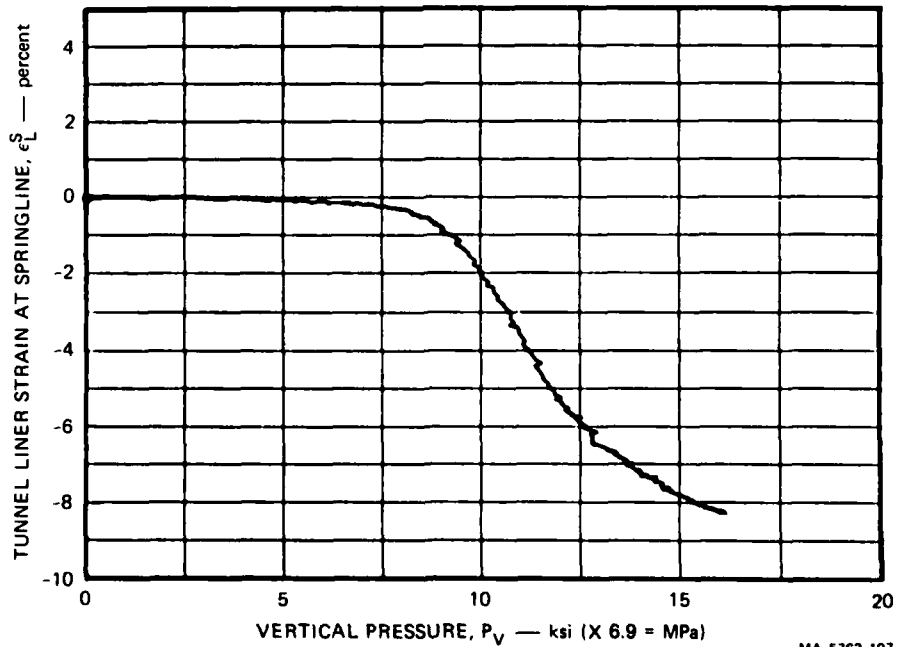
MA-5762-195

FIGURE A.86 CROWN-INVERT TUNNEL CLOSURE VERSUS VERTICAL PRESSURE — TEST LSUX-24



MA-5762-196

FIGURE A.87 TUNNEL LINER STRAIN AT CROWN VERSUS VERTICAL PRESSURE — TEST LSUX-24



MA-5762-197

FIGURE A.88 TUNNEL LINER STRAIN AT SPRINGLINE VERSUS VERTICAL PRESSURE — TEST LSUX-24

LSUX-25

LOAD-JOINT ORIENTATION ANGLE  $\beta$ :  $45^\circ$

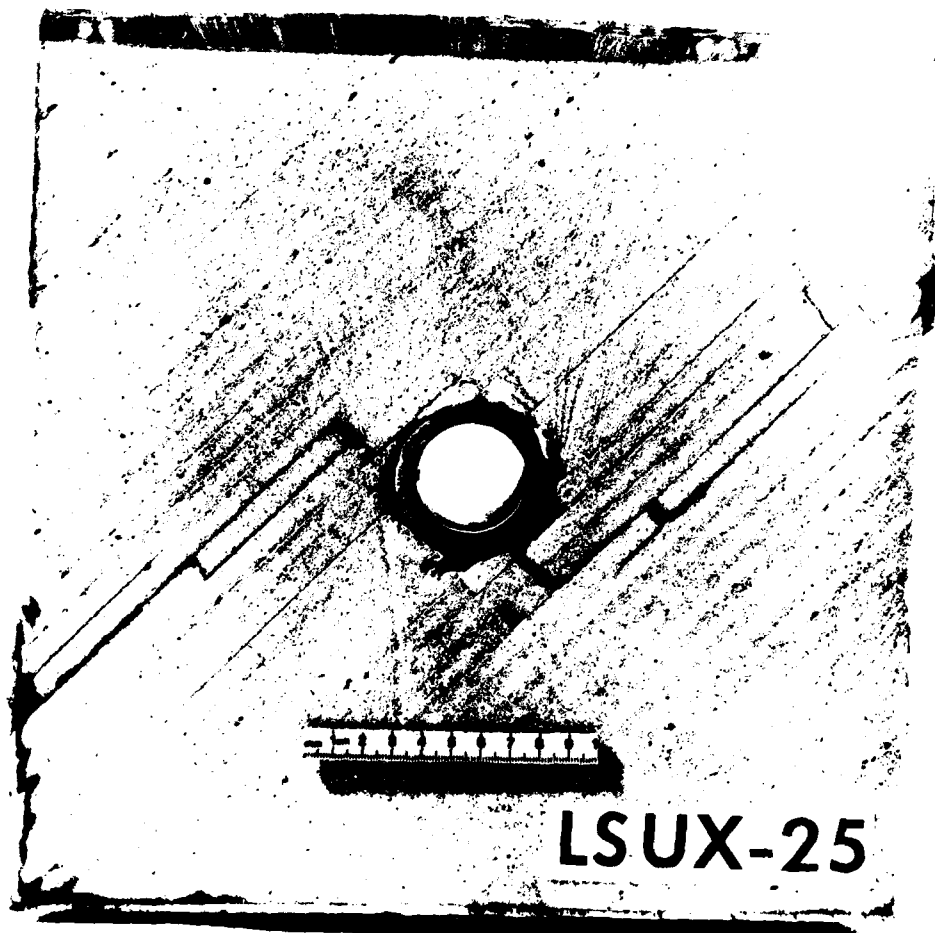
TUNNEL-JOINT ORIENTATION ANGLE  $\gamma$ :  $90^\circ$

STRUCTURE: Backpacked 1015 steel liner,  $a/h = 12.5$   
Polyurethane foam backpacking,  $R/h = 4.3$

LOADING: Monotonic

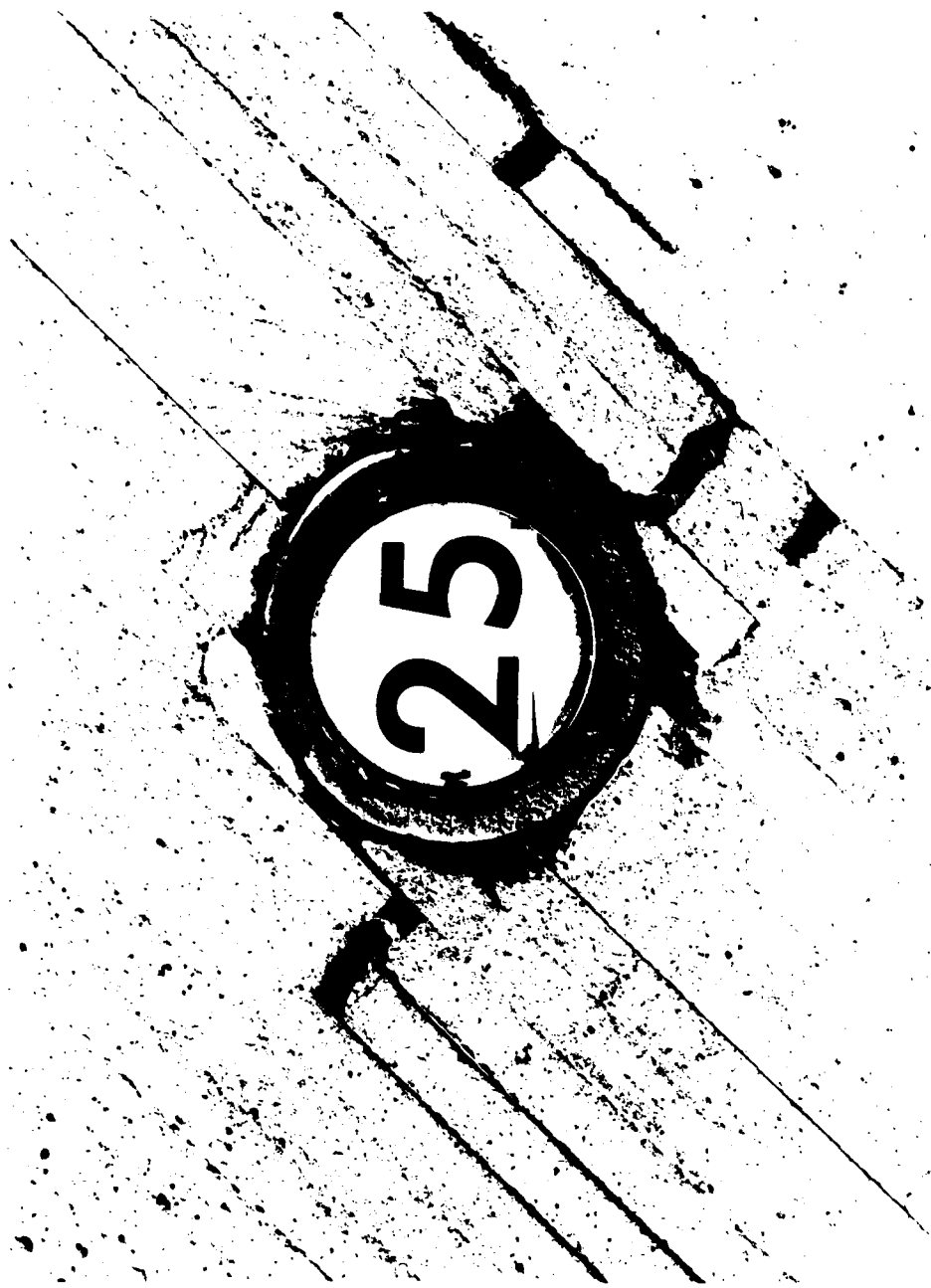
COMMENTS

Tunnel closure records are good. However, liner closure records show the closures as slightly larger than expected, because of improper closure transducer installation. Good liner strain records were obtained from the crown and both springline locations. The specimen separated into two halves during recovery.



MP-5762-198

FIGURE A.89 SECTIONED SPECIMEN FROM TEST LSUX-25



MP-5762-199

FIGURE A.90 ENLARGEMENT OF TUNNEL REGION IN LSUX-25 SPECIMEN

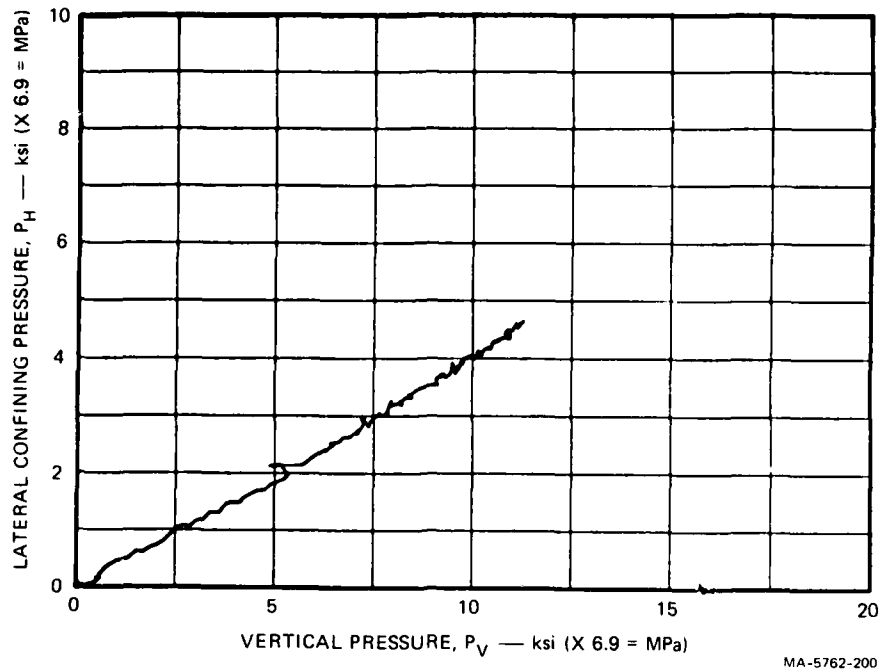


FIGURE A.91 LATERAL CONFINING PRESSURE VERSUS VERTICAL PRESSURE — TEST LSUX-25

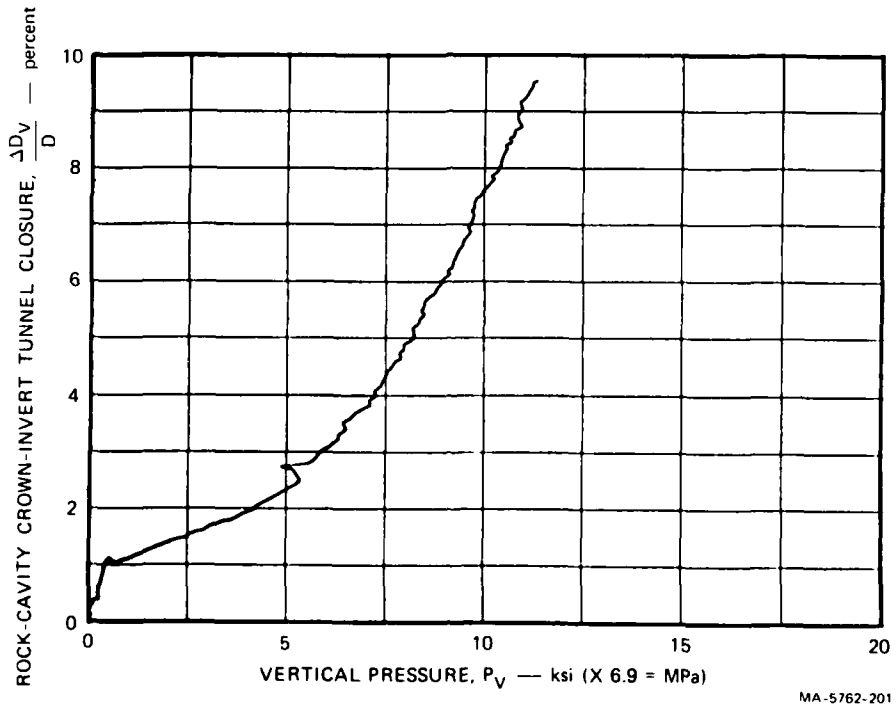


FIGURE A.92 ROCK-CAVITY CROWN-INVERT TUNNEL CLOSURE VERSUS VERTICAL PRESSURE — TEST LSUX-25

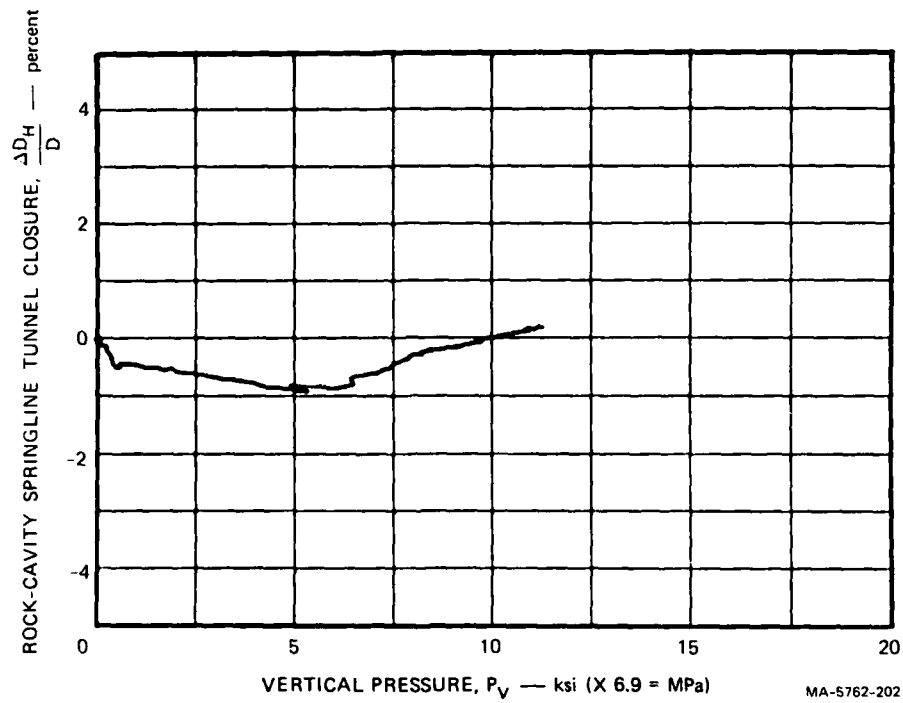


FIGURE A.93 ROCK-CAVITY SPRINGLINE TUNNEL CLOSURE VERSUS VERTICAL PRESSURE — TEST LSUX-25

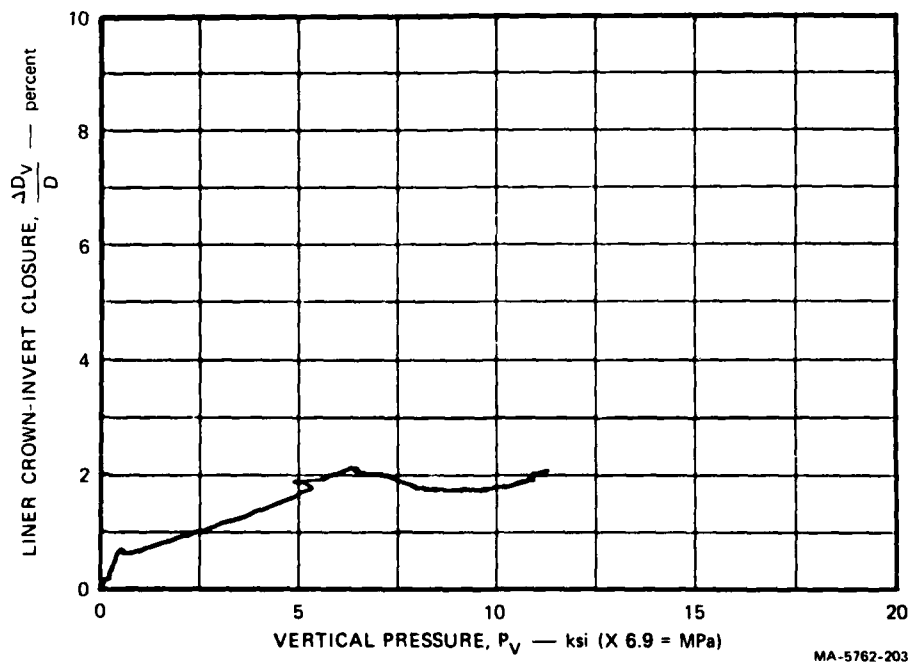
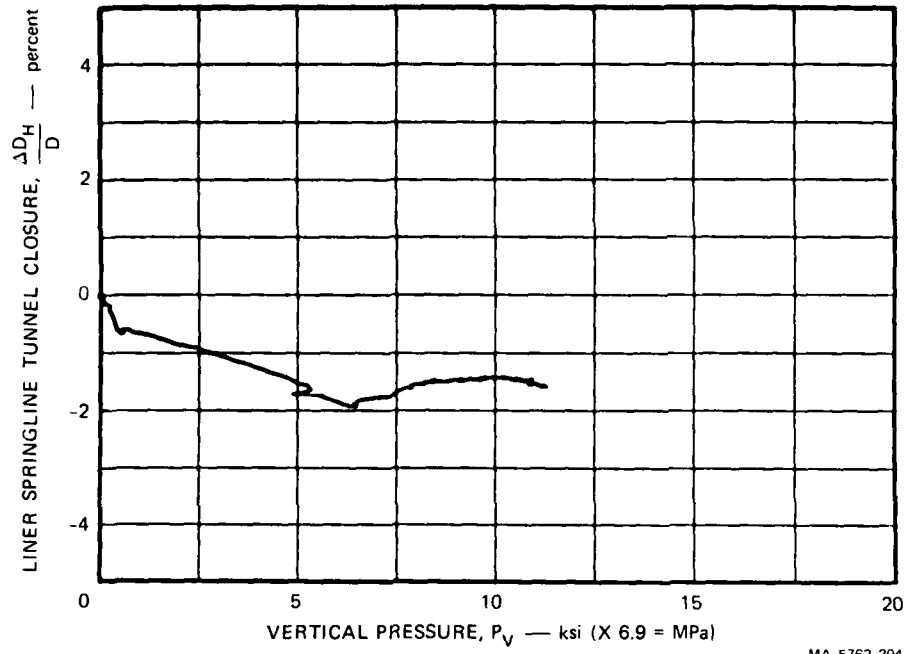
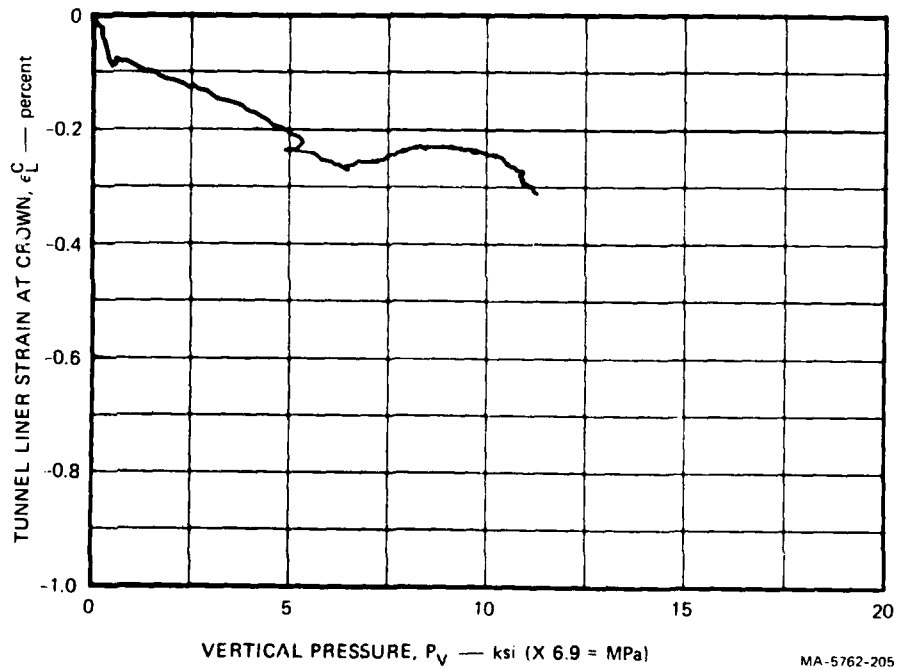


FIGURE A.94 LINER CROWN-INVERT TUNNEL CLOSURE VERSUS VERTICAL PRESSURE — TEST LSUX-25



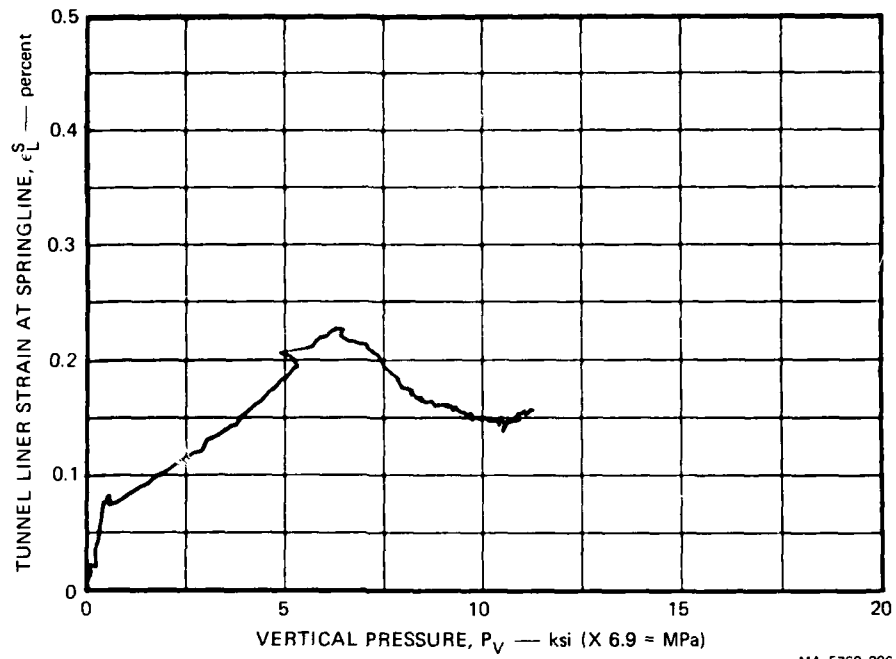
MA-5762-204

FIGURE A.95 LINER SPRINGLINE TUNNEL CLOSURE VERSUS VERTICAL PRESSURE — TEST LSUX-25



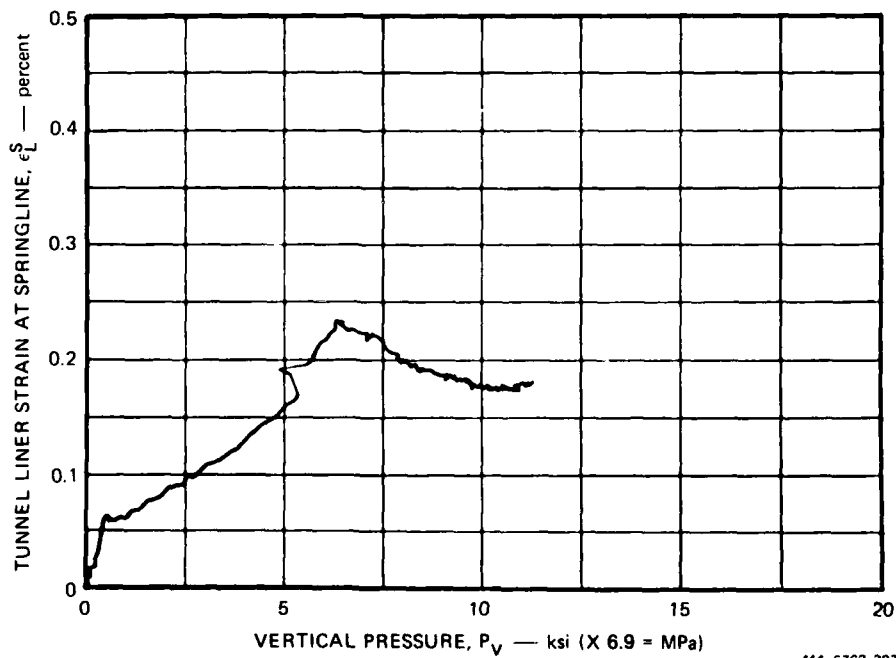
MA-5762-205

FIGURE A.96 TUNNEL LINER STRAIN AT CROWN VERSUS VERTICAL PRESSURE — TEST LSUX-25



MA-5762-206

FIGURE A.97 TUNNEL LINER STRAIN AT LEFT SPRINGLINE VERSUS VERTICAL PRESSURE — TEST LSUX-25



MA-5762-207

FIGURE A.98 TUNNEL LINER STRAIN AT RIGHT SPRINGLINE VERSUS VERTICAL PRESSURE — TEST LSUX-25

## Appendix B

### RESPONSE TO CYCLIC LOADING OF TUNNELS REINFORCED WITH BACKPACKED STRUCTURES

#### B.1 INTRODUCTION

This appendix describes tests performed to determine if tunnels reinforced with backpacked structures shake down as do tunnels reinforced with direct contact structures. We performed four static uniaxial-strain loading tests on 4-inch-diameter (0.1-m) specimens of saturated 16A rock simulant. The tunnels were reinforced with backpacked liners. In two tests the loading was monotonic, and in two the loading was cycled.

Because of the small tunnel size, 0.462 inch (11.8 mm) inside diameter in the 4-inch-diameter (0.1-m) specimens, only two closure transducers (dial indicator bore gages) could be inserted into the tunnel, one from each end. In the first monotonic loading test, SUX-117, we measured liner closure at the crown-invert and springline diameters. In the second, SUX-119, we measured rock-cavity closure at the same orientations. Similarly, in the cyclic loading tests we measured liner closure in the first test (SUX-118) and rock-cavity closure in the second (SUX-120).

Results of the four tests are similar to those obtained for direct contact structures in 6B and SRI RMG 2C2 simulants. When the specimen is loaded, unloaded, and then reloaded, little additional rock-cavity or liner closure occurs until the loading pressure exceeds the maximum pressure applied in the first loading.

#### B.2 TUNNEL REINFORCING STRUCTURE

The tunnel reinforcing structure was a 1015 steel monocoque cylinder backpacked with polyurethane foam. Figure B.1 shows a photograph of the structure, as well as the end fittings that connect the tunnel with

the access ports in the testing machine. The steel liner had a mean-radius-to-wall-thickness ratio  $a/h$  of 12.5 and a 0.500-inch (12.7-mm) outside diameter. The liner extended beyond the ends of the backpacking to join with the end fittings. The polyurethane backpacking for all four tests was machined from a single large casting. The inside and outside diameters of the backpacking were chosen to obtain about a 1-mil diametral interference fit with both the steel liner and rock cavity. The steel liner was pressed into the backpacking, crushing it slightly, and the entire structure was pressed into the tunnel.

The density of the polyurethane foam was 13.2 lb/ft<sup>3</sup> (211 kg/m<sup>3</sup>); its stress-strain curve for uniaxial strain loading is shown in Figure B.2. This curve is the average of eight tests on specimens taken from the foam immediately surrounding the block from which the backpacking was machined. The backpacking crush strength  $\sigma_{20}$  at 20% strain is 550 psi (3.8 MPa).

To measure closure of the steel liner, we simply oriented our closure transducers to measure changes in the liner diameter at the crown-invert and the springlines. To measure closure of the rock cavity, we inserted pins through tiny drill holes in the structure at the crown, the invert, and both springlines. The closure transducers were then positioned inside the liner so that they rested on these pins and would therefore indicate changes in the rock-cavity diameter. The pins were fabricated from common straight pins, and the holes through the structure were counterbored slightly so that the head of each pin was flush with the outside diameter of the structure.

### B.3 MONOTONIC LOADING RESULTS

Figure B.3 plots crown-invert and springline closure as a function of the applied vertical pressure for both the liner and the rock cavity. The closures for both liner and rock cavity are given as percentages of the original inside diameter of each. The rock-cavity crown-invert closure increases monotonically with the applied vertical pressure and reaches about 10% when the vertical pressure is 16 ksi (110 MPa) at

the end of the test. The rock-cavity springline closure, however, is first slightly negative (less than a 0.1% increase in the springline diameter) and then later becomes positive for pressures greater than 7 ksi (48 MPa), reaching a maximum closure of about 3.5% at the end of the test.

As expected, closure of the liner is much less than that of the rock cavity. For example, when the rock-cavity crown-invert closure is 10%, the liner crown-invert closure is only 0.6%. Both closures are positive throughout the test. In contrast to rock-cavity springline closure, however, liner springline closure is always negative and has about the same magnitude as the crown-invert closure at all vertical pressures. Figure B.3 also shows that the magnitudes of both the liner crown-invert and springline closures have a relative maximum at  $P_V = 10$  ksi (69 MPa) of about 0.7%. For pressures between 12 and 16 ksi (83 and 110 MPa), liner closure remains constant, and then the crown-invert closure increases while the springline closure decreases.

The deformation of the liner may be understood by examining the stress in the backpacking as it deforms. Initially, the pressure on the liner is asymmetric because of the asymmetric closure of the rock cavity and the corresponding asymmetric deformation of the backpacking. Because the backpacking strain is greater at the crown-invert than at the springlines, the liner becomes oval. As the strain in the backpacking at the crown and invert reaches about 10% at  $P_V = 10$  ksi (69 MPa), the pressure on the liner around these points becomes constant (see Figure B.2).<sup>\*</sup> However, the backpacking strain at the springlines is less than 10%, and the pressure at the springlines increases with further loading. Therefore, the springline closure increases and the

---

<sup>\*</sup> Strain in the backpacking  $\epsilon_{bp}$  can be calculated with the formula

$$\epsilon_{bp} = R/H [\Delta D_R/D_R - (D_L/D_R)(\Delta D_L/D_L)]$$

where  $\Delta D_R/D_R$  is rock-cavity closure,  $\Delta D_L/D_L$  is liner closure,  $D_L/D_R$  is the liner-to-rock-cavity diameter ratio, and  $R/H$  is the radius-to-thickness ratio of the backpacking.

crown-invert closure decreases. When the backpacking strain at the springlines reaches 10%, the pressure on the liner is constant around the circumference and the liner does not deform from its ovalled shape as the applied pressure and rock-cavity closure both increase. Finally, at about  $P_V = 16$  ksi (110 MPa), the backpacking at the crown-invert starts to lock up and the liner oval deformation resumes.

The liner crown-invert and springline closures are nearly equal and opposite because, unlike that for the rock cavity, liner deformation is almost entirely in the oval mode ( $n = 2$ ). The backpacking isolates the liner from hoop mode ( $n = 0$ ) deformation because by design the crushing stress of the backpacking ( $\sigma_{cr} \approx 550$  psi = 3.8 MPa) is much less than the yield pressure of the liner ( $p_y = \sigma_y h/a = 40,000$  psi/12.5 = 3200 psi = 22.1 MPa). Thus, liner hoop deformation is elastic and limited to values negligibly small on the scale of deformations in Figure B.3.

#### B.4 CYCLIC LOADING RESULTS

Figure B.4 plots crown-invert and springline closures as a function of applied vertical pressure for both the liner and the rock cavity. Closures during loading are shown as solid symbols and during unloading as open symbols. The specimens were loaded with unload-reload cycles at  $P_V = 7.5, 10,$  and  $18$  ksi (52, 69, and 124 MPa). Unloading was stopped at about 1.5 ksi (10 MPa) to preserve the testing machine tools.

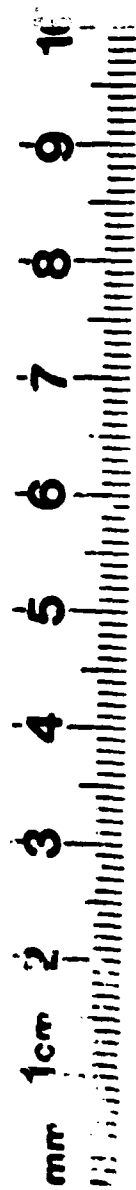
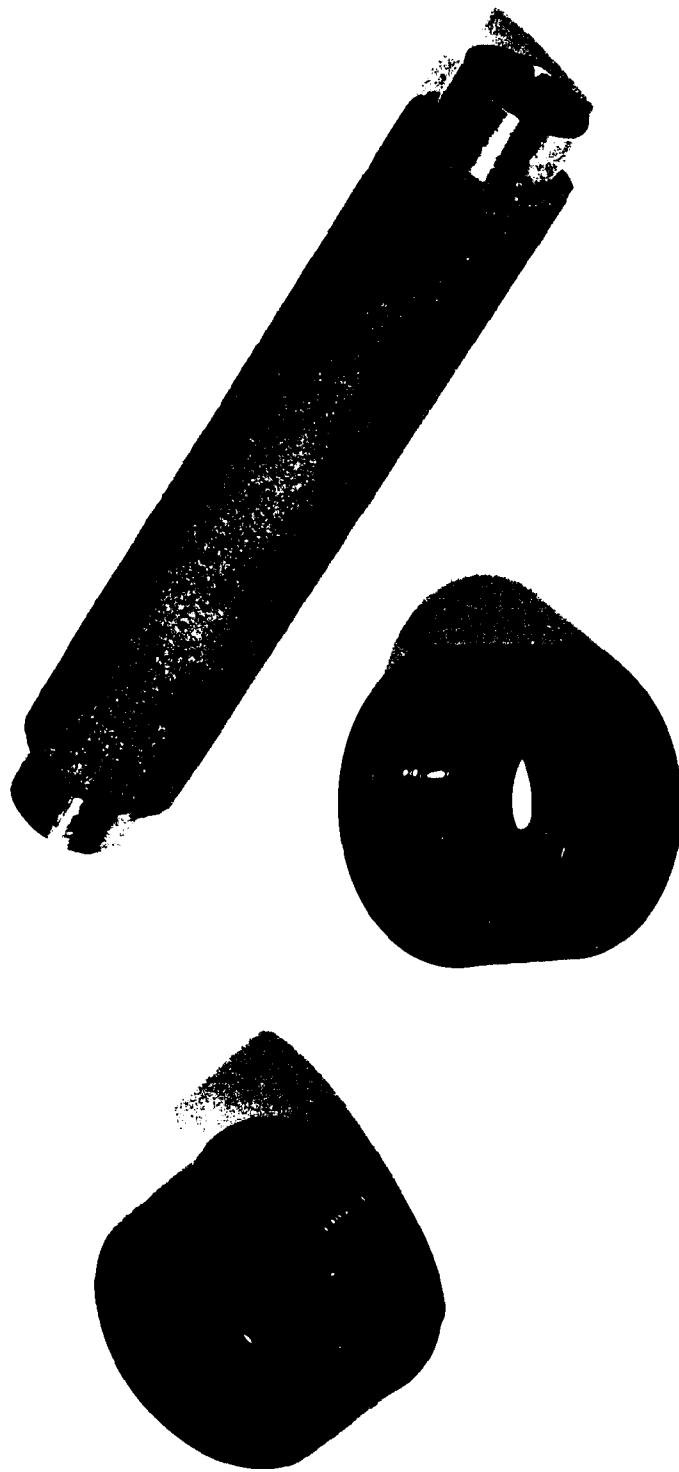
For comparison with the cyclic-loading closures, Figure B.4 also includes lines representing the monotonic loading data plotted in Figure B.3. The close proximity of the monotonic and cyclic loading data shows that cycling the load does not reduce the structure's load-bearing capacity; greater closure requires higher pressure, just as for monotonic loading. Furthermore, unloading and reloading occur along the same path. A minor deviation from this trend was found in the liner deformation during the reload portion of the cycle initiated at 18 ksi (124 MPa).

During the reload portion of this last cycle in load, the magnitude of the liner closure does not decrease at  $P_V = 10$  ksi (69 MPa), as it did for both monotonic loading and initial loading to 18 ksi (124 MPa) in this test. The reason for the difference is that loading to  $P_V = 18$  ksi (124 MPa) causes the backpacking to begin to lock up. This point is shown on the stress-strain curve for the backpacking material given in Figure B.2. Response to unloading is plotted as a dashed line in this figure. Reloading response also follows the dashed stress-strain path: stress increases monotonically with strain; there is no constant stress crush, as there is for monotonic loading. Therefore, the load on the liner and, consequently, the amplitude of the liner closures increase monotonically during reloading.

The resulting liner closure curves for reloading are not, however, simply the monotonic loading curves shifted backwards along the pressure axis by 8 ksi (55 MPa), because during the reloading part of the cycle the rock-cavity springlines are moving outward, whereas for monotonic loading they are moving inward. This difference in rock-cavity springline motion causes the backpacking to exert a different pressure on the liner springlines, and hence, gives slightly different liner response.

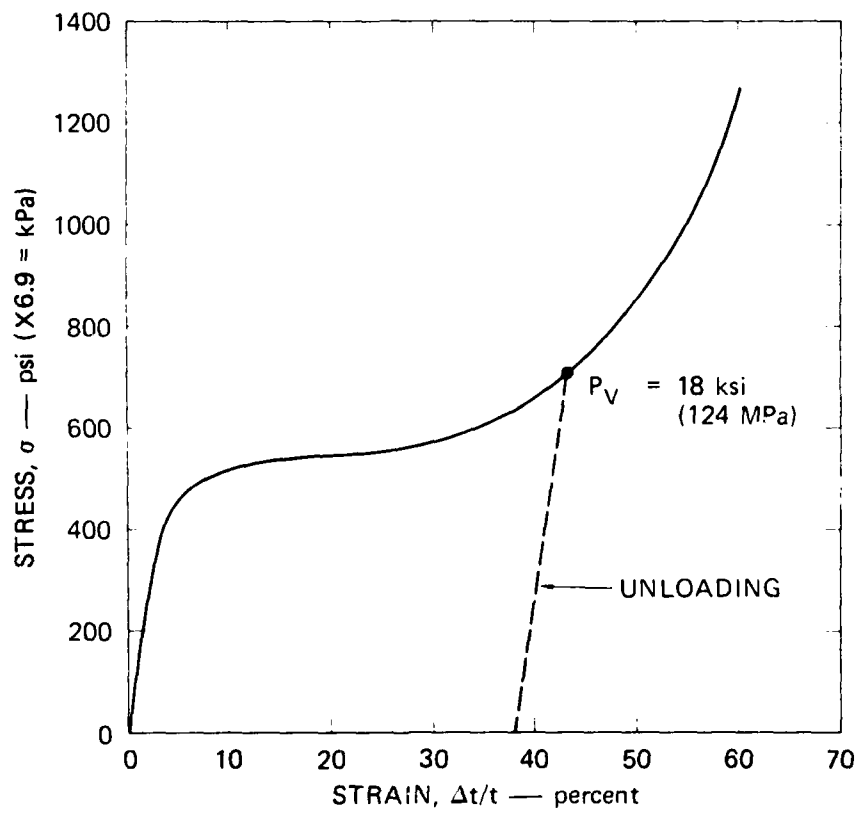
Although this last cycle in load did produce additional liner closure (less than 1% at the end of the cycle in load), it represents an extreme case where a cycle in load is initiated at a pressure above the design load. The design load for this backpacked structure is about 15 ksi (about 100 MPa). Figure B.4 shows that for this load the rock-cavity crown-invert closure is 5% and the liner closure is less than 1%. This design load falls in the middle of the pressure range over which liner closure remains constant. Cycles in load initiated at the design load would not be expected to produce additional liner closure because the backpacking would not have started to lock up.

These four tests show that a rock cavity reinforced with a backpacked structure shakes down in the same way as a similar cavity reinforced with an integral (or direct contact) structure. Also, the tests again demonstrate that backpacking effectively isolates the interior liner from the large rock-cavity closures.



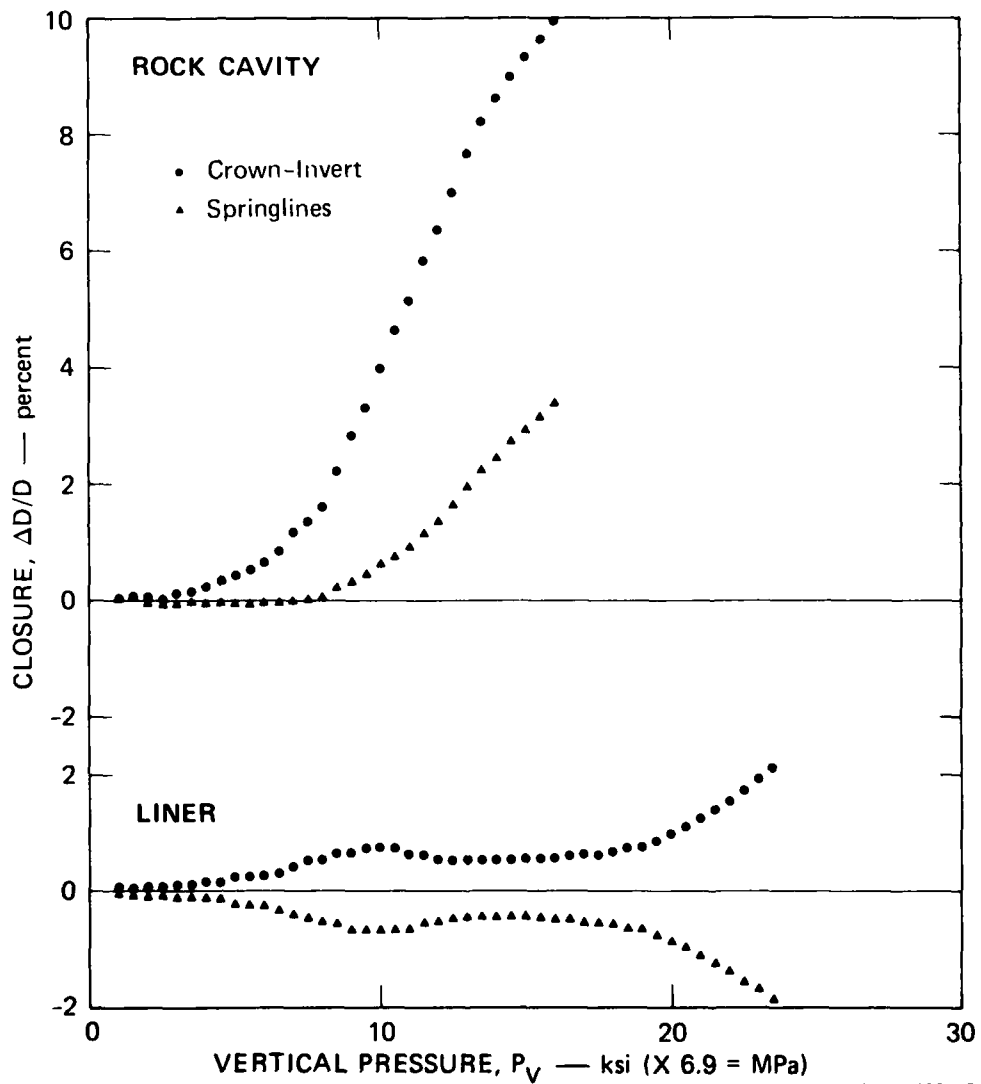
MP-5762-74

FIGURE B.1 BACKPACKED STRUCTURE AND END-FITTINGS



MA-5762-71A

FIGURE B.2 STRESS-STRAIN CURVE FOR UNIAXIAL STRAIN LOADING OF 13.2 lb/ft<sup>2</sup> (211 kg/m<sup>3</sup>) POLYURETHANE FOAM  
 $\dot{\epsilon} = 3.3 \times 10^{-2} \text{ s}^{-1}$



**FIGURE B.3 ROCK-CAVITY AND LINER CLOSURE FOR STATIC MONOTONIC UNIAXIAL STRAIN LOADING OF A BACKPACKED STRUCTURE IN 16A ROCK SIMULANT**  
 $a/h = 12.5$ ,  $R/H = 4.3$

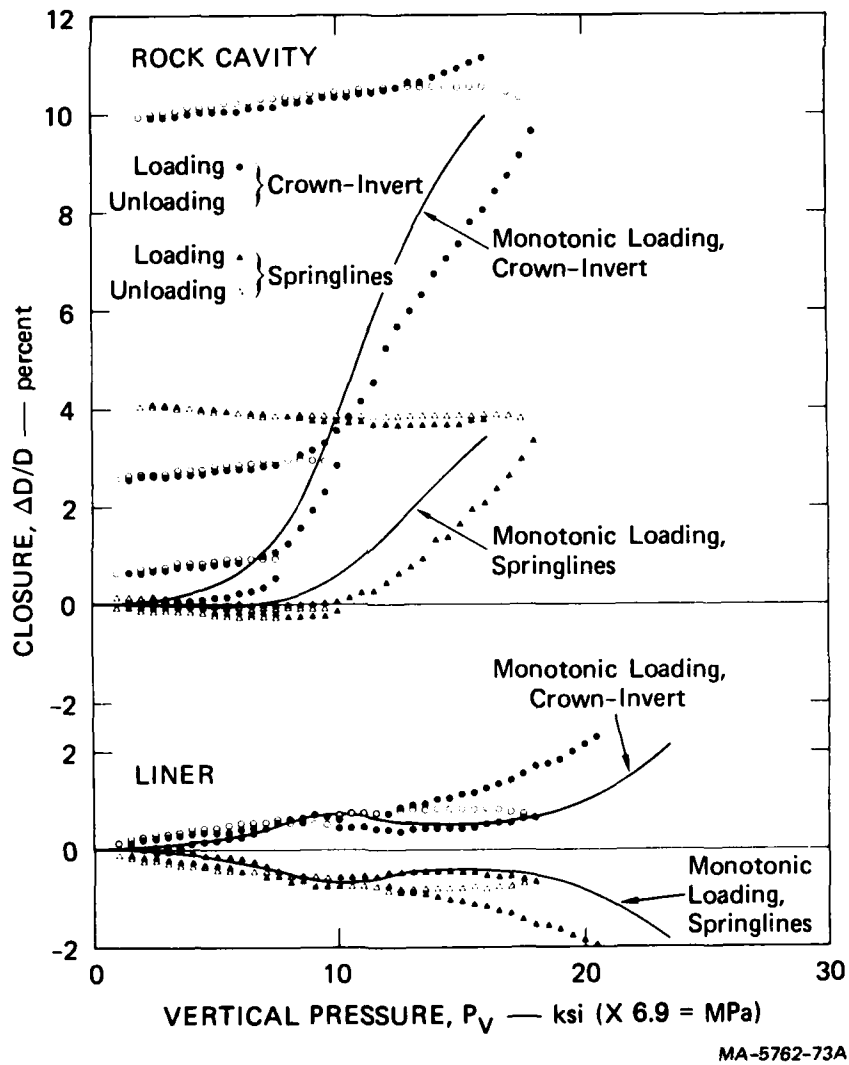


FIGURE B.4 ROCK-CAVITY AND LINER CLOSURE FOR CYCLIC AND MONOTONIC UNIAXIAL STRAIN LOADING OF A BACKPACKED STRUCTURE IN SATURATED 16A ROCK SIMULANT

DISTRIBUTION LIST

DEPARTMENT OF DEFENSE

Assistant to the Secretary of Defense  
Atomic Energy  
ATTN: Executive Assistant

Defense Advanced Rsch. Proj. Agency  
ATTN: TIO

Defense Intelligence Agency  
ATTN: RDS-3A  
ATTN: DB-4C2

Defense Nuclear Agency  
ATTN: STNA  
ATTN: RAEV  
3 cy ATTN: SPSS  
4 cy ATTN: TITL

Defense Technical Information Center  
12 cy ATTN: DD

Field Command  
Defense Nuclear Agency  
ATTN: FCPR  
ATTN: FCTMOF

Field Command  
Defense Nuclear Agency  
Livermore Division  
ATTN: FCPRL

Field Command Test Directorate  
Defense Nuclear Agency  
2 cy ATTN: FCTC, J. LaComb

Joint Strat. Tgt. Planning Staff  
ATTN: NRI-STINFO Library  
ATTN: JLA

Undersecretary of Defense for Rsch. & Engrg.  
ATTN: Strategic & Space Systems (OS)

DEPARTMENT OF THE ARMY

Chief of Engineers  
Department of the Army  
ATTN: DAEN-RDM  
ATTN: DAEN-MCE-D

Construction Engineering Rsch. Lab.  
Department of the Army  
ATTN: CERL-SOI-L

Deputy Chief of Staff for Ops. & Plans  
Department of the Army  
ATTN: MOCA-ADL

Harry Diamond Laboratories  
Department of the Army  
ATTN: DELHD-N-P

U.S. Army Ballistic Research Labs  
ATTN: DRDAR-TSB-S  
ATTN: DRDAR-BLT, W. Taylor  
ATTN: DRDAR-BLV  
ATTN: DRDAR-BLE, J. Keefer

DEPARTMENT OF THE ARMY (Continued)

U.S. Army Communications Command  
ATTN: Technical Reference Division

U.S. Army Engineer Center  
ATTN: DT-LRC

U.S. Army Engineer Dist., Omaha  
ATTN: MROED-D, C. Distefano

U.S. Army Engineer Div., Huntsville  
ATTN: HNDED-SR  
3 cy ATTN: C. Huang

U.S. Army Engineer Div., Ohio River  
ATTN: ORDAS-L

U.S. Army Engr. Waterways Exper. Station  
ATTN: WESSD, G. Jackson  
ATTN: Library  
ATTN: WESSE, L. Ingram  
ATTN: WESSA, W. Flathau  
ATTN: WESSS, J. Ballard  
ATTN: J. Day  
ATTN: J. Drake  
ATTN: P. Miakar

U.S. Army Nuclear & Chemical Agency  
ATTN: Library

DEPARTMENT OF THE NAVY

Chief of Naval Operations  
ATTN: OP-943

Naval Construction Battalion Center  
ATTN: Code L44, H. Haynes  
ATTN: Code L51, R. O'Dello  
ATTN: Code L08A  
ATTN: Code L51, S. Takahashi  
ATTN: Code L51, W. Shaw

Naval Electronic Systems Command  
ATTN: PME 117-211, B. Kruger

Naval Facilities Engineering Command  
ATTN: Code O9M22C

Naval Postgraduate School  
ATTN: Code 0142, Library

Naval Research Laboratory  
ATTN: Code 2627

Naval Surface Weapons Center  
ATTN: Tech. Library & Info. Services Branch

Naval War College  
ATTN: Code E-11

Strategic Systems Project Office  
Department of the Navy  
ATTN: NSP-43

DEPARTMENT OF THE AIR FORCE

Air Force Institute of Technology  
ATTN: Library

Air Force Weapons Laboratory  
Air Force Systems Command  
ATTN: NTE, M. Plamondon  
ATTN: NT, D. Payton  
ATTN: SUL

Assistant Chief of Staff  
Studies & Analyses  
Department of the Air Force  
ATTN: AF/SASM

Ballistic Missile Office  
Air Force Systems Command  
ATTN: MNNH  
ATTN: MNN

Deputy Chief of Staff  
Operations Plans and Readiness  
Department of the Air Force  
ATTN: AFXODC

Deputy Chief of Staff  
Research, Development, & Acq.  
Department of the Air Force  
ATTN: AFRDQSM

Foreign Technology Division  
Air Force Systems Command  
ATTN: NIIS, Library

Strategic Air Command  
Department of the Air Force  
ATTN: XPFS  
ATTN: NRI-STINFO Library

DEPARTMENT OF ENERGY CONTRACTORS

Lawrence Livermore National Laboratory  
ATTN: Technical Information Dept. Library  
ATTN: L-21, D. Oakley  
ATTN: H. Heard

Los Alamos National Scientific Laboratory  
ATTN: MS 364  
ATTN: L. Germaine  
ATTN: B. Killian  
ATTN: J. Johnson

Oak Ridge National Laboratory  
ATTN: Central Research Library

Sandia National Laboratories  
Livermore Laboratory  
ATTN: Library & Security Classification Div.

Sandia National Laboratories  
ATTN: 3141  
ATTN: L. Hill

OTHER GOVERNMENT AGENCIES

Department of the Interior  
Bureau of Mines  
ATTN: Technical Library

OTHER GOVERNMENT AGENCIES

Department of the Interior  
U.S. Geological Survey  
ATTN: W. Twenhofel  
ATTN: R. Carroll  
ATTN: D. Snyder

Department of the Interior  
U.S. Geological Survey  
ATTN: D. Roddy

DEPARTMENT OF DEFENSE CONTRACTORS

Aerospace Corp.  
ATTN: P. Mathur  
ATTN: Technical Information Services

Agabian Associates  
ATTN: C. Bagge  
ATTN: M. Balachanda  
2 cy ATTN: M. Agabian

Applied Theory, Inc.  
ATTN: J. Trulio

AVCO Research & Systems Group  
ATTN: Library, A830

BDM Corp.  
ATTN: T. Neighbors  
ATTN: Corporate Library

Boeing Co.  
ATTN: Aerospace Library  
ATTN: M/S 42/37, K. Friddell  
ATTN: R. Dyr Dahl  
ATTN: H. Leistner  
ATTN: J. Wooster  
ATTN: T. Berg

California Institute of Technology  
ATTN: D. Anderson

California Research & Technology, Inc.  
ATTN: Library  
ATTN: K. Kreyenhagen  
ATTN: S. Schuster

California Research & Technology, Inc.  
ATTN: D. Orphal

University of California  
ATTN: R. Goodman  
ATTN: N. Cook

Calspan Corp.  
ATTN: Library

Civil Systems, Inc.  
ATTN: J. Bratton

University of Denver  
ATTN: Sec. Officer for J. Wisotski

EG&G Washington Analytical Services Center, Inc.  
ATTN: Library

Electromechanical Sys. of New Mexico, Inc.  
ATTN: R. Shunk

DEPARTMENT OF DEFENSE CONTRACTORS (Continued)

Eric H. Wang  
Civil Engineering Rsch. Fac.  
ATTN: N. Baum

Foster-Miller Associates, Inc.  
ATTN: J. Hampson for E. Foster

General Electric Company-TEMPO  
ATTN: DASIAC

IIT Research Institute  
ATTN: M. Johnson  
ATTN: R. Welch  
ATTN: Documents Library

Institute for Defense Analyses  
ATTN: Classified Library

J. H. Wiggins Co., Inc.  
ATTN: J. Collins

Kaman Avidyne  
ATTN: Library

Kaman Sciences Corp.  
ATTN: Library

Lockheed Missiles & Space Co., Inc.  
ATTN: T. Geers  
ATTN: Technical Information Center

Massachusetts Inst. of Technology  
ATTN: W. Brace

Merritt CASES, Inc.  
ATTN: J. Merritt

Nathan M. Newmark Consult. Eng. Svcs.  
ATTN: A. Hendron  
ATTN: W. Hall  
ATTN: N. Newmark

City College of New York  
ATTN: C. Miller

Northwestern University  
ATTN: T. Belytschko

Pacifica Technology  
ATTN: G. Kent

Physics International Co.  
ATTN: F. Sauer  
ATTN: E. Moore  
ATTN: Technical Library

Pacific Sierra Research Corp.  
ATTN: H. Brode

R & D Associates  
ATTN: J. Lewis  
ATTN: R. Port  
ATTN: D. Rawson  
ATTN: C. MacDonald  
ATTN: D. Shrinivasa  
ATTN: Technical Information Center

DEPARTMENT OF DEFENSE CONTRACTORS (Continued)

Science Applications, Inc.  
ATTN: Technical Library

Science Applications, Inc.  
ATTN: Technical Library

Southwest Research Institute  
ATTN: W. Baker  
ATTN: A. Wenzel

SRI International  
ATTN: B. Holmes  
ATTN: H. Lindberg  
ATTN: G. Abrahamson

Systems, Science & Software, Inc.  
ATTN: R. Duff  
ATTN: Library  
ATTN: T. Bache  
ATTN: W. Wray  
ATTN: C. Archembeam  
ATTN: D. Grine

Terra Tek, Inc.  
ATTN: H. Pratt  
ATTN: Library

Tetra Tech, Inc.  
ATTN: Library

Texas A & M University System  
ATTN: J. Handin  
ATTN: Sec. Officer for A. Rychlik

TRW Defense & Space Sys. Group  
ATTN: P. Huff  
ATTN: Technical Information Center  
ATTN: N. Lipner

TRW Defense & Space Sys. Group  
ATTN: E. Wong  
ATTN: P. Dai

Universal Analytics, Inc.  
ATTN: E. Field

Weidlinger Assoc., Consulting Engineers  
ATTN: M. Baron  
ATTN: I. Sandler

Weidlinger Assoc., Consulting Engineers  
ATTN: J. Isenberg

Westinghouse Electric Corp.  
ATTN: W. Volz

William Perret  
ATTN: W. Perret

Rand Corp.  
ATTN: A. Laupa